5-2019

Investigation of Powder Recyclability and Liquid-Solid-Gas Interactions during Powder Bed Selective Laser Melting of Stainless Steel 316L

Daniel Walter Galicki
University of Tennessee, dgalicki@vols.utk.edu

Investigation of Powder Recyclability and Liquid-Solid-Gas Interactions during Powder Bed Selective Laser Melting of Stainless Steel 316L

A Dissertation Presented for the
Doctor of Philosophy
Degree
The University of Tennessee, Knoxville

Daniel Walter Galicki
May 2019

To Patricia, Pam, & Peter Galicki

ACKNOWLEDGEMENTS

Research is not conducted in a vacuum. I would like to thank the following individuals:

- My committee members, Professor Sudarsanam Suresh Babu, Professor Claudia Rawn, Professor Easo George, and Dr. Ryan DeHoff, for providing guidance and support during my PhD.

- Dr. Fred List III and Keith Carver for training me on the Renishaw AM 250 machine and patiently working with me to develop and conduct experiments.

- Tom Geer of the Materials Science and Technology Division of ORNL for etching so many of my samples, and for teaching me how to etch for myself.

- Fred C. Montgomery of the Nuclear Fuels Materials group at ORNL for measuring the powder size distributions of my powder samples.

- Shawn Reeves, Shirley Waters, and Andres Marquez of the Materials Science and Technology Division of ORNL for training me on the scanning electron microscopes and for helping me whenever I ran into problems while using them.

- Thanks to Dr. Ralph Dinwiddie for allowing me to use and for training me on the operation of the high-speed infrared camera. Thanks to Jake Raplee and Travis McFalls for the many hours of discussion related to infrared data analysis.

- Donald Erdman and Rick R. Lowden of the Materials Science and Technology division of ORNL for training me on the operation of and the use of their tensile testing frames.

- Collin Whitt, and Professor Michael Miller of the Ohio State University's Center for Electron Microscopy and Analysis for allowing access to and help with conducting TEM of powders.

- Dr. Mehdi Eizadjou, Dr. Keita Nomoto, and Professor Simon Ringer of the Australian Centre for Microscopy & Microanalysis for generous access to and help conducting atom probe tomography experiments.

- Dr. H.M. Meyer III of ORNL's Materials Science and Technology Division for conducting and teaching me about X-ray photoelectron spectroscopy.

- Dr. Bryan Chakoumakos and the Neutron Scattering Division of ORNL for collecting and analyzing single-crystal diffraction data.

- Dr. Zhili Feng and Alan Frederick of the Materials Science and Technology Division of ORNL for access to and help with tensile sample annealing.

- Dr. Kinjal Ganda and Dr. Niebedim Cajetan of Ames Laboratory, and Dr. Orlando Rios of ORNL for help with collection and analysis of magnetic measurements, DSC, and TGA of powders.

- Dr. Michael Kohler of the Joint Institute for Advanced Materials (JIAM) Diffraction Facility, located at the University of Tennessee, Knoxville for help collecting high-temperature powder x-ray diffraction data.

- Jamie Stump for writing MatLab code that removes moving spatter signature from high-speed IR data of the SLM process.

- Derrick Morrin, Roland Fields, and Chris Hayes of Y12 for their mentorship and funding of my PhD research.

- Dr. John Vitek for teaching an informal class on how to use ThermoCalc and DICTRA.

- Dr. Avinash Prabhu, Dr. Niyanth Sridharan, Dr. Ben Shassere, Dr. Alex Plotkowski, Dr. Naren Raghavan, Michel Haines, Travis McFalls, for the many stimulating conversations and various good times.

- Rita Ayers and Anita Monroe for the absolutely necessary administrative support and for always having a solution to whatever problem I could cook up.

- My dad, Peter Galicki for his many encouraging phone calls and for inspiring me to go down the path of engineering.

- My lovely wife, Patricia Galicki who moved states with me and stood by me and supported me through the many rough patches along the way.

- Dr. William Sames, who suggested that I apply for a PhD student position as part of Dr. Babu's research group.

ABSTRACT

This dissertation pertains to the fundamental understanding of powder degradation and the dissolution of gas, specifically interstitials such as oxygen, into metal alloy powders and parts during selective laser melting (SLM) additive manufacturing (AM) and their impact on defect generation, microstructure, and mechanical properties of parts built using this process.

A powder recyclability experiment was conducted to investigate the effect that powder re-use has on bulk powder and build properties. Mechanical testing and analysis of parts produced during the experiment showed higher than normal yield strengths and provided evidence of powder re-use affecting the ductility of SLM parts.

A heat affected zone experiment was conducted to investigate the local property changes in unmelted powder. Local oxidation in unmelted powder near melt zones was observed and characterized. The size of the melt zone adjacent to the unmelted powder bed was shown not to be a contributing factor to the extent of local oxidation.

A variable oxygen environment experiment was conducted to investigate the effect of elevated levels of atmospheric oxygen on stainless steel 316L builds. Mechanical testing results indicate that the mechanical properties of additively manufactured 316L parts are insensitive to significant variation of cover gas O_2 concentration in the build chamber during processing.

A cooling rate study was conducted in an effort to use laser processing parameters to manipulate the microstructure/mechanical properties of as-built parts. High-speed infrared (IR) data was analyzed and representative cooling rates of the parts and the surrounding powder bed as a function of build height were obtained.

Finally, stainless steel 316L spatter material was observed to solidify as single-crystal ferrite. This is unusual behavior considering that the composition of stainless steel 316L usually causes it to solidify as austenite. The single-crystal nature of the ferritic spatter particles is particularly interesting and suggests that the particles solidify at rapid velocities and that conditions exist that allow for the nucleation of ferrite to outcompete that of the austenite phase.

TABLE OF CONTENTS

LIST OF TABLES

LIST OF FIGURES

CHAPTER 1 INTRODUCTION & BACKGROUND

1.1. Recyclability Studies in Additive Manufacturing

It has been shown that the recycling of powder feedstock in electron beam melting (EBM) additive manufacturing processes can affect some of the material properties of subsequently built parts [1]–[3]. Researchers at Oak Ridge National Laboratory (ORNL) have demonstrated how oxygen pickup, even while within allowable specifications, can affect the intrinsic properties of materials built using EBM (Figure 1.1) [1]. Published research conducted by Tang et. al. supports the ORNL findings [3]. They show in Figure 1.2 how oxygen content in Ti-6Al-4V powder increases as a function of reuse. They also present in Table 1-1 the tensile properties of Ti-6Al-4V test samples manufactured using the EBM process and recycled powder feedstock where the yield and ultimate tensile strengths increase as a function of powder reuse and oxygen content.

Additive manufacturing machines that use laser melting processing operate under very different conditions than electron beam additive manufacturing machines (i.e. no vacuum, limited preheat temperatures, increased time b/w thermal cycles, non-sintered powder bed). Renishaw™ conducted an SLM recyclability study using Ti-6V-4Al feedstock. Over 38 builds cycles, researchers observed that while oxygen and nitrogen levels in the builds increased as a function of re-use, the ultimate tensile strengths of the parts made during each cycle exhibited a slight increase as a function of powder re-use [4]. Thus, they concluded that their build parameters were valid from the beginning to the end of the experiment. The Ti-6Al-4V mechanical properties measured by Renishaw™ agrees with the electron beam data collected by Tang.

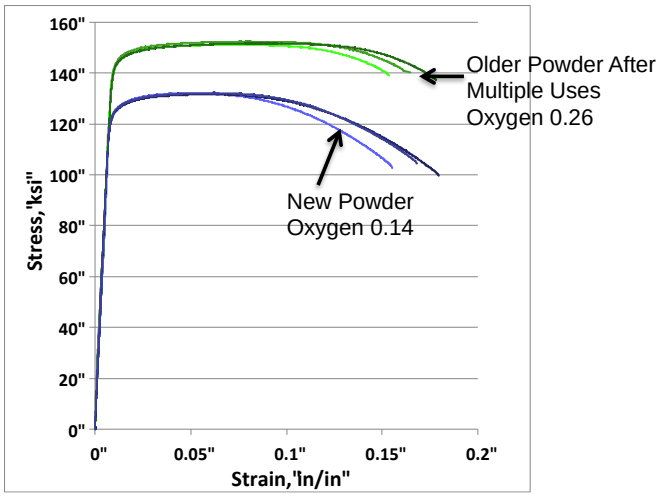

Figure 1.1: Engineering stress-strain curves of Ti-6Al-4V builds made with powder feed stock in the fresh condition and after multiple uses. The builds were made using the same processing conditions, in the same machine. The increase in strength is attributed to stabilization of alpha (HCP) phase due to oxygen pick up [1].

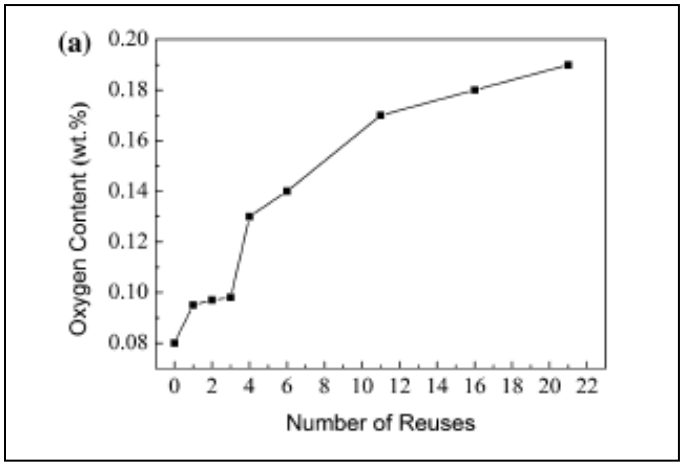

Figure 1.2: Ti-6Al-4V powder oxygen composition versus number of reuse times. The measurement uncertainty is ±0.001 wt% [3].

Table 1-1: Tensile Properties of Ti-6Al-4V additively manufactured from recycled powder. Reproduced from ref [3].

Powder reuse times	Powder oxygen (wt.%)	Yield strength (MPa)	Ultimate tensile strength (MPa)	Tensile elongation (%)	Reduction in area (%)	Density (g/cm^{-3})
0	0.080	834 ± 10.0	920 ± 10.0	16.0 ± 0.3	54 ± 3.0	4.410 ± 0.004
2	0.097	870 ± 8.0	970 ± 10.0	15.0 ± 0.3	46 ± 3.0	4.410 ± 0.004
6	0.14	822 ± 25.0	910 ± 20.0	13.5 ± 1.0	53 ± 4.0	4.411 ± 0.004
11	0.17	891.5 ± 4.5	986.5 ± 3.5	17.8 ± 0.8	50.0 ± 1.0	4.428 ± 0.003
16	0.18	939.6 ± 3.6	1028.1 ± 4.1	15.3 ± 1.8	42.1 ± 4.1	4.380 ± 0.018
21	0.19	960 ± 30.0	1039.3 ± 2.7	15.5 ± 0.9		4.381 ± 0.019

A different type of powder quality experiment was conducted by Liu et. al. [5], stainless 316L steel virgin powder feedstock was mixed with spatter particles and processed via SLM. Their mechanical property results can be compared to the tensile properties of base metal and weld metal samples tested and tabulated by Idaho National Lab researchers (Figure 1.3) [6]. Parts that were made with fresh powder mixed with spatter particles show a large reduction in ductility (from 30% down to 10%), however the researchers did not attempt to explain the reason behind the increase in tensile properties and the corresponding decrease in ductility. The property changes could be an effect brought on by differences between the powder's virgin, as-received state and its state after being processed and sieved. Nandwana et. al. have demonstrated that cyclic loading and unloading of powder through a powder bed additive manufacturing process can induce chemical and morphological changes, as well as change the powder size distribution [7]. These types of powder changes are thought to result from direct and indirect contact with the energy source (laser/electron beam) and/or the melted regions of the powder bed, in conjunction with environmental variables such as the presence of oxygen or other reactive gases within the build chamber during processing.

It should be noted that some finished part property changes that result as a function of powder degradation have been observed to be mitigated or eliminated entirely by manipulation of machine melting parameters or by post-processing of the finished parts [8]. However, neither of these solutions attempts to explain the whole mechanism of how powder degradation induces property change within additively manufactured parts. At the beginning of this work, little research had been conducted on how the properties of additively manufactured parts vary as a function of powder reuse. In addition, almost all of the current research on powder recyclability and reuse focused on the electron-beam process exclusively. The current work attempts to quantitatively identify, explain, and predict how powder degradation as a function of re-use affects parts created using the SLM process.

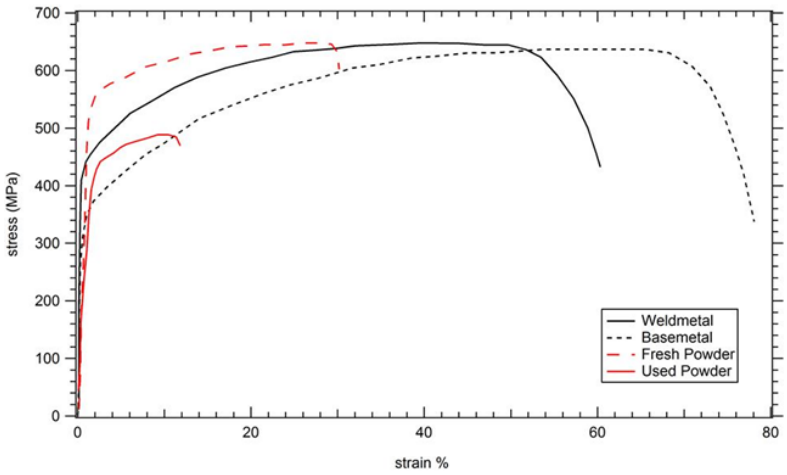

Figure 1.3: Stress-strain diagram of SLM manufactured stainless 316L compared to standard 316L base metal and welded regions. Reproduced here using data from references [5], [6].

1.2. Solidification

Metal additive manufacturing is similar to traditional welding in many ways. Both processes utilize a heat source to locally melt a substrate and welding also often utilizes a moving heat source and filler material to create a continuous weld, much like metal additive manufacturing. Because of this similarity, welding literature can be called upon to understand much of the physical science behind the solidification of metal alloys during additive manufacturing processes. In stainless steel alloy systems, two of the major influencers affecting solidification are the chemical composition of the alloy system, and the cooling rate/solidification rate of the melt. Researchers have been able to describe the effects of both of these influences in both an empirical manner as well as with theoretical equations.

1.2.1. Influence of Chemical Composition

Stainless steel typically solidifies as austenite (FCC), ferrite (BCC), or some combination of the two phases (dual phase). Further heat treatment and cooling processes can create other phases as well, particularly martensite and precipitation hardened phases, but this section will focus on compositional effects on the FCC/BCC phase fractions in stainless steels. For decades, metallurgists and welders have been developing process maps that predict phase fractions of interest in particular steel alloy systems. These maps have historically been developed by fitting experimental data. They began with Strauss and Maurer's nickel-chromium microstructure diagram developed in 1920 [9] and have been modified and tweaked as new understanding of different alloying elements came to light. The most reliable and accurate diagram available today is the WRC-1992 diagram shown in Figure 1.4 with a red box denoting the compositional region that the virgin 316L powder feedstock introduced in the following sections of this report resides in [10], [11]. The WRC-1992 plots the ferrite number (FN) as a function of nickel-equivalent and chromium-equivalent. Nickel/chromium equivalents are equations that add the relative effects of like-phase promoting elements into one, easy to plot number. Ferrite promoting alloying elements would be added to the chromium equivalent number while austenite promoting, or stabilizing alloying elements would be added to the nickel equivalent number. however, it is again worth mentioning that these types of compositional diagrams were developed using data obtained from arc welds and therefore are associated with relatively slow cooling rates (10^3 K/s). In high-power beam process such as electron beam and laser beam welding it is common to see cooling rates on the order of 10^4 to 10^6 K/s. The WRC-1992 diagram and others like it do not predict the ferrite values well at these high cooling rates.

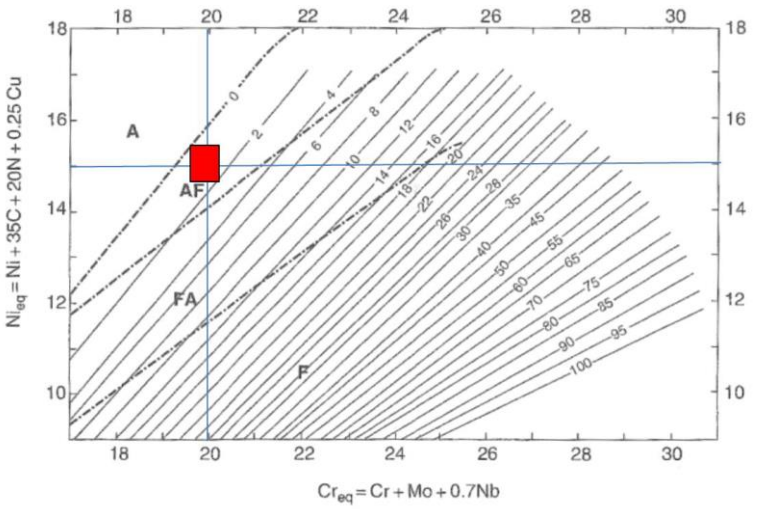

Figure 1.4: The WRC-1992 constitutional diagram predicting ferrite number as a function of nickel and chromium alloying equivalents. A red box marks the compositional area into which the 316L powder feedstock in this study falls.

1.2.2. Influence of Cooling Rate

During rapid solidification, the primary mode of solidification may change, the microstructural features are much finer, and solute segregation patterns may be greatly altered [12]. Researchers recognized this effect and approached the problem with different techniques. Elmer et. al. performed cooling rate experiments on seven high-purity Fe-Cr-Ni alloys with 59 wt% iron and Cr/Ni ratios that varied from 1.15 to 2.18. Cr is a strong ferrite (F) stabilizer in iron-alloy systems, while Ni is a strong austenite (A) stabilizer. To measure the cooling rates of the welds that they produced, they utilized the linear relation between cooling rate and dendrite arm spacing (DAS) discovered by Katayama and Matsunawa for 310 stainless steel [13].

$$\lambda_1 = 80(\varepsilon)^{-0.33} \quad (1\text{-}1)$$

$$\lambda_2 = 25(\varepsilon)^{-0.28} \quad (1\text{-}2)$$

where λ_1 is the primary dendrite arm spacing (PDAS), λ_2 is the secondary dendrite arm spacing (SDAS), and (ε) is the cooling rate.

They found that stainless steel can solidify in five modes (A, AF, E, FA, F) and twelve morphologies (cellular dendritic A, cellular A, interdendritic F, intercellular F, eutectic, intercellular A, vermicular F, lacy F, blocky A, Widmanstatten A, massive A, and cellular F). Their work incorporated the effect of cooling rate during solidification as well as varying the Cr/Ni ratio.

In 2003, Vitek et. al. developed and trained a neural network on the same database that was used to develop the WRC-1992 diagram, as well as their own set of high cooling rate experimental data [14], [15]. Their ORFN neural network demonstrated a marked improvement over the WRC-1992 when predicting ferrite number in welds performed at any cooling rate (Figure 1.5).

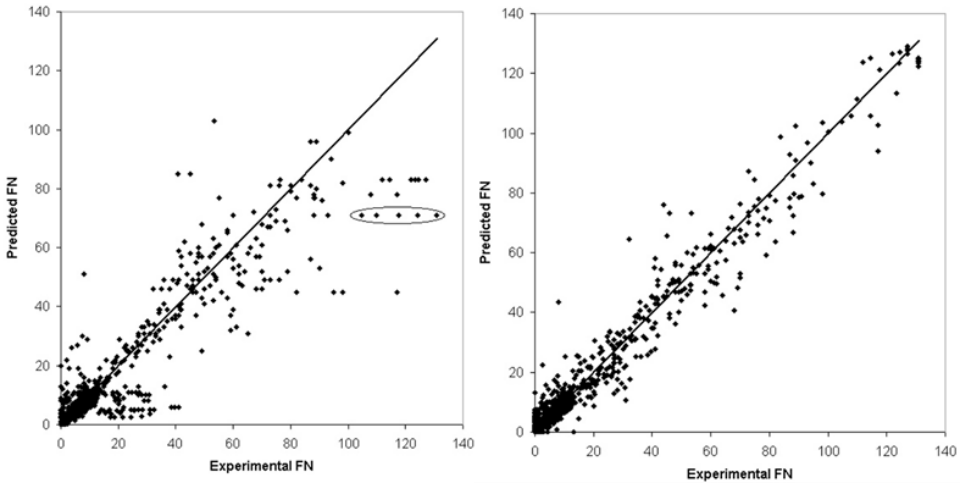

Figure 1.5: (left) WRC-1992 and (right) ORFN predicted ferrite number compared to experimental data.

1.2.3. Interface Response Function

In addition to the empirical results described in the previous section, researchers have also developed theoretical equations to try and predict the solidification mechanism of alloys. Kurz and Fisher described a general theoretical framework to relate the dendrite tip radius, solid/liquid interface undercooling, and primary dendrite arm spacing in alloy growth in positive temperature gradients [16]. They gave equations to predict primary arm spacing for both low and high growth velocities. This work led to the development of Kurz, Giovanola, and Trivedi's seminal KGT modal for directional solidification which is valid under high growth velocity conditions [17]**.** They coupled an appropriate stability criterion with the solute trapping effect to predict microstructural features such as primary solidification phase and cell/dendrite morphology as a function of growth velocity. The effects of undercooling (diffusion coefficient as a function of temperature) as well as the partition coefficient (as a function of velocity and temperature) and liquidus slope (a function of temperature), and their individual effects on the solid/liquid interface curvature and solute composition in the solid is considered within the model. The following equations make up the KGT model and can be used to iteratively solve either dendrite tip or planar front temperatures, as a function of growth velocity. With these equations and the appropriate inputs, it is possible to estimate the primary solidification phase to be the phase with the highest dendrite tip or planar temperature at a particular growth velocity.

Velocity dependent partition coefficient:

$$k_V^i = \frac{k_o^i + a_o(V_s/D_i)}{1 + a_o(V_s/D_i)} \tag{1-3}$$

Velocity dependent liquidus slope:

$$m_V^i = m_o^i \left[\frac{1 - k_V^i\left(1 - \ln\left\{k_V^i/k_o^i\right\}\right)}{1 - k_o^i}\right] \tag{1-4}$$

Dendrite tip liquid concentration:

$$c_l^{i*} = \frac{c_o^i}{1 - (1 - k_V^i)\,\mathrm{Iv}\{P^i\}} \tag{1-5}$$

Dendrite tip temperature:

$$T_d = T_l + \sum_i \left(c_l^{i*} m_V^i - c_o^i m_o^i\right) - \frac{2\Gamma}{R} - \frac{V_s}{\mu} - \frac{GD}{V_s} \tag{1-6}$$

Planar front temperature:

$$T_{planar} = T_s + \sum_i c_o^i \left(\frac{m_V^i}{k_V^i} - \frac{m_o^i}{k_o^i}\right) - \frac{V_s}{\mu} \quad (1\text{-}7)$$

where k_o^i is the equilibrium partition coefficient for element *i*, a_o is the characteristic diffusion distance, D_i is the solute diffusivity of element *i*, V_s is the solid-liquid interface velocity, m_o^i is the equilibrium liquidus slope of element *i*, Γ is the Gibbs-Thompson coefficient, P^i is the Peclet number for element *i*, c_o^i is the liquid equilibrium liquid concentration for alloying element *i*, $\mathrm{Iv}\{P^i\}$ is the Ivantsov function, T_l is the liquidus temperature of the initial ally composition, and μ is the interface kinetic coefficient.

1.3. Oxidation of Stainless Steels

1.3.1. Solid-State Oxidation

Ellingham diagrams reveal that Cr_2O_3 oxides are the most thermodynamically stable of the metal oxides and are therefore predicted to form first before all other oxides. Cr_2O_3 forms at an oxygen partial pressure of just 10^{-13} mbar at the melting temperature of 316L steel (1400 ^oC). It is followed in stability by FeO (10^{-9} mbar), Fe_3O_4 (10^{-4} mbar), NiO (10^{-3} mbar), and Fe_2O_3 (10^2 mbar) [18]. Alloying elements within stainless steel 316L can also form oxides at this temperature: MnO at 10^{-15} mbar, and SiO_2 at 10^{-17} mbar O_2 partial pressure. SLM machines operate at oxygen partial pressures of 10^{-3} – 10^{-2} mbar (see section 4.1.1), indicating that some amount of oxide formation both within the weld pool and in the powder feedstock itself is likely during the SLM process, with the oxide amount dependent on the kinetics of oxide formation and growth. Reviews of low and high temperature oxidation of metals can be found in references [19] and [20].

Traditional oxidation studies of steel measure the weight gain or loss of the steel over time while exposed to oxidizing temperatures and environments over a time span of hours. These continuous studies allow for the study and definition of the complete kinetic record of the oxidizing reaction at a specific temperature.

Stainless steel oxidation literature reveals that a range of oxides may form (Cr_2O_3, FeO, Fe_2O_3, Fe_3O_4, NiO, and spinel) [21], [22]. Kinetics of these oxide growths is complicated by the various diffusion rates of metal and oxygen ions through the different oxide phases, and the varying degrees of solubility of the oxides in one another [23]. Tarabay et. al. investigated the oxidation of a 304L stainless steel, water atomized powder via thermogravimetric analysis held at 800^{o}C under a helium oxygen mixture for 6 to 20 hours, and found that it oxidized akin to conventual stainless steel plate, exhibiting parabolic like behavior and chromium-oxides forming at early stages of oxidation, and iron-oxides forming at later stages of oxidation [24].

The amount of time that unmelted steel powder is exposed to high temperatures during the SLM process is typically on the order of seconds as opposed to the minutes or hours, making the measurement of these oxides by traditional methods difficult and the development of a predictive model preferable. This work attempts to develop a simple model using simple well-known formulas like the Rosenthal heat equation in conjunction with widely available thermodynamics and kinetics software like ThermoCalc and DICTRA.

1.3.2. Oxidation Phenomenon During Welding

Hibiya and Debroy have calculated the change in surface tension gradient of molten iron as a function of oxygen partial pressure above as well as the oxygen addition to the melt pool [25], [26]. As oxygen is added to the weld pool, the surface tension gradient of molten iron experiences a negative to positive shift in sign value. This sign shift in surface tension gradient can affect the convective flow pattern within the melt pool and can consequently affect the melt pool aspect ratio. In selective laser melting, the consequences of a changing weld pool width and depth could be realized as decreased overlap between melt tracks and/or decreased bonding between melt layers. Both of these consequences have the potential to increase lack of fusion porosity in the final part. Louvis et. al. has shown that pre-existing aluminum oxides can affect the solidification of the weld pool during SLM processing of aluminum alloys [27]. Thin oxide layers that form at the initial liquid-solid interface during SLM solidification can interfere with epitaxial solidification of the weld pool, reducing the bond strength between melt layers. In SLM, it is conceivable that oxide seeds could be introduced into the melt pool via the breakup of surface oxides on the metal powder feedstock. Since it is preferable to reduce inclusions, a strong motivation exists to limit the extent of oxide formation both on the powder prior to SLM processing and the powder/part system during SLM processing. This forms the motivation for the current research. Our specific focus is related to the observing and explaining the oxide formation in the heat-affected-zone (HAZ) regions of the powder bed near to the part perimeter.

1.4. Present Investigation

1.4.1. Objectives

The goal of this investigation was to investigate the liquid-metal-gas interactions between the melt pool, metal powder, and gaseous environment during the SLM processing of 316L stainless steel.

Industry sectors like automotive and aerospace have been among the first adopters of metal additive manufacturing for use in production environments. One of powder bed metal additive manufacturing’s attractive features is the potential to re-use any unmelted feedstock in a bid to offset the higher cost of the initial feedstock purchase. However,

without a reasonable level of knowledge of how re-used, or recycled, powder can change as a function of re-use, industry is more likely to forego recycling in the name of caution By elucidating how changes within the powder feedstock have the potential to affect built-part quality, industry members will be able to make better informed decisions that will reduce the cost of additively manufactured parts and increase part quality and reproducibility.

1.4.2. Approach

During the course of this research effort, several experiments were designed and implemented to investigate individual phenomena of the selective laser melting of stainless steel 316L powder, such as part property and powder characteristic variability as a function of powder re-use, local powder bed oxidation, and the effects of operating at higher than normal oxygen containing environments. Additional experiments were conducted with the goal of influencing spatter production characteristics and as-built microstructures in selective laser melting via instrument parameter selection.

All of the experiments described in the following sections and chapters were conducted using a Renishaw AM250 selective laser melting additive manufacturing machine located at the Manufacturing Demonstration Facility of Oak Ridge National Laboratory. Section 2.1 of Chapter 2 provides an overview of the Renishaw machine and its operating principles. Section 0 of Chapter 2 is dedicated to detailing the experimental design, conditions, and procedures implemented at each major stage of the research process. Section 0 of Chapter 2 details the data collection categories and techniques of the feedstock virgin powder and each experiment.

In Chapter 3 the discovery of unusual single-crystal ferrite (BCC) spatter particles is documented and characterized using EBSD, SCXRD, HTXRD, inert gas fusion, and APT. The cooling rates of the particles are estimated by etching the austenitic (FCC) spatter particles and measuring the dendrite arm spacings. A rationalization of the solidification mechanism of the BCC phase in these particles is introduced at the end of this chapter.

0 details a novel heat-affected-zone experiment that was conducted to investigate any local property changes in unmelted powder as a function of distance from a melt region. A simple heat transfer model based on Rosenthal's heat transfer equation was developed and used as input into a DICTRA oxide growth model. The oxide growth model was compared against experimental data. The knowledge gained from this experiment would be beneficial in the design of future powder re-use experiments for laser powder bed additive manufacturing.

Chapter 5 presents and discusses the results from an experiment designed to investigate the effect of elevated levels of atmospheric oxygen on builds using a stainless steel 316L powder feedstock. The design of the experiment was also such that

the effect of melting powder contaminated with naturally occurring spatter could be compared against that of powder containing no spatter particles. Mechanical testing of the parts built during this experiment was conducted and compared against the results obtained from the recyclability experiment in Chapter 6.
Chapter 6 describes the design and implementation of a powder recyclability experiment. This experiment was conducted to investigate the effect(s) that powder re-use has on stainless steel 316L powder and built-part properties. A “built volume” approach was used to conduct the recyclability experiment, wherein a single geometry was built as tall as the initial loading of virgin powder feedstock would permit. The same geometry was then re-built using only the remaining powder feedstock from the first build. This pattern was repeated until such a time when the volume of remaining powder feedstock from a previous build cycle would not permit the start of the next build cycle. Powder samples were taken and characterized at stage of the recyclability experiment, and mechanical testing was conducted on the built-parts themselves to determine if any mechanical property variation exists as a function of powder re-use.

Chapter 7 presents and discusses results obtained from an experiment designed to influence the cooling rates of as-built parts by implementing a laser pre-scan step prior to melting. Current industry selective laser machine selections do not offer the ability or make it difficult for users to design pre-heat scans into build files. This pre-heat ability may prove useful, however, in influencing the amount of residual strain originating from thermal stresses developed within as-built parts during the build process. The influence of differing sets of laser pre-heat parameters was observed via the collection and analysis of infrared intensity over time using a high-speed infrared camera.

Chapter 8 serves as a summary of the results and concepts that were developed during this investigation. These concepts relate primarily to how stainless-steel powder feedstock interacts with and reacts to varying environments during the selective laser melting process brought about as functions of laser parameters, cover gas makeup, and temperature profiles.

CHAPTER 2 EXPERIMENTAL PROCEDURES & DATA COLLECTION

This chapter describes in detail the experimental design, conditions, and procedures conducted during the course of this body of research, as well as the data collection methods and techniques that were employed.

2.1. The Renishaw AM-250 Instrument

The Renishaw AM250, manufactured by Renishaw™, is a machine that utilizes a single 200W Nd:YAG laser, operating in pulsed mode, to selectively melt and bond a thin, 50-micron thick powder layer to an underlying substrate material. By repeatedly melting and bonding fresh deposits of powder to previously melted layers, the Renishaw AM250 can produce a near-net-shape metal part of almost any desired geometry. The process takes place inside of a non-reactive, argon-gas-filled build chamber (Figure 2.1). The argon in the build chamber is constantly removed, passed through a filter, and re-introduced back into the chamber using a fan system. The filter removes evaporated material (soot) as well as submicron powder particles that are produced as a byproduct of the selective laser melting process.

The build chamber is kept at positive pressure relative to the outside of the machine and has oxygen sensors (located just after the filter and again just after the fan that powers the gas flow) that instruct the machine to stop the build (if one is building) and purge the system with argon if oxygen levels within the chamber climb to higher than desired levels. Proprietary Renishaw software used the values from these sensors to report oxygen content in units of parts per million (ppm). The oxygen partial pressure (p_{O_2}) was calculated from the measured chamber pressure and oxygen ppm values. The oxygen data presented in this thesis was collected from the “bottom” sensor, as it measures the gas coming directly from the build chamber (before filtration) and is therefore considered a truer indicator of the actual O_2 value within the build chamber cover gas than the sensor located in the “top” position.

At every layer, the substrate is mechanically lowered by 50 microns to allow room for the next layer of powder to be deposited. The machine uses a silicon wiper blade, positioned nearly flush to the build substrate, to push powder from underneath a gravity-fed powder hopper and onto the waiting substrate at the beginning of each layer.

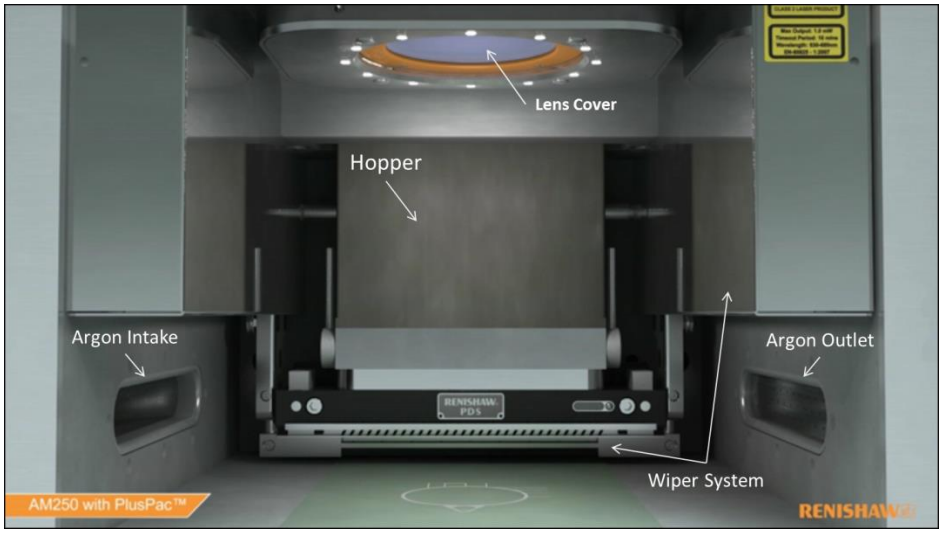

Figure 2.1: Rendering of the Renishaw AM250 build chamber obtained from the Renishaw™ website.

The Renishaw AM250 has many parameters which can be optimized and tuned to produce a part with the correct level of desired quality. Some of the most important and most commonly varied parameters in this study are: laser power (P), spot distance (d_s), exposure time (t_e), focus offset (FO), and hatch spacing (h). The Renishaw AM250 differs from many commercial SLM machines in that it utilizes a spot-mode (pulse-mode) laser instead of the more common continuous laser. Renishaw™ reasons that the pulsed-mode laser provides more uniformity and control to the melting process as well as providing for better dimensional accuracy in as-built parts. As such, the distance between each spot weld (d_s), as well as for how long the laser remains firing at each spot weld position (t_e) are parameters that are not seen in systems using continuous lasers. Laser power (P), focus offset (FO), and the distance between laser raster scans (h) are parameters that are also used in systems with continuous lasers.

Any stainless-steel powder that is re-used is first sieved using a 66-micron sieve to remove any large particles that may have been introduced to the powder bed during the selective laser melting process via the spattering process. The sieving process is driven by a vibrating motor that shakes the sieve and allows powder to fall through the sieve holes. The sieved powder falls into a waiting stainless steel receptacle. When the receptacle is full, the opening is closed with a flange and the receptacle is then connected to the hopper via flanges. The sieved powder is then allowed to fall into the hopper. The sieving and hopper reloading processes were conducted in an ambient lab environment where relative humidity levels were typically around 30%. Attempts were made to limit the amount of time that re-used powder was exposed to air during the sieving and reloading process.

2.2. Experimental Procedures

2.2.1. Recyclability Study Experimental Plan

A 3-dimensional geometry, shown in Figure 2.3, was designed using SolidWorks and exported as an STL file. The geometry consisted of six tensile bars of dimension 1.3x10.2x1.3 cm and four “filler” bars of dimension 1.3x10.2x(variable) cm. Lacking guidance from literature, it was decided that the degree to which the powder feedstock would be affected by the laser melting process would likely be based upon the volume fraction of melted powder in the powder bed. On this assumption, four filler bars were added to the geometry in order to allow for a continuous volume of melt past the point when the tensile bars had finished building. During the building of the tensile bars, the build geometry volume comprised 21.22% of the total build volume. After completion of the tensile bars, the filler bar geometry volume comprised 8.49% of the build volume until completion of the build. It is important to report the melt volumes relative to the powder bed volume, as it is assumed that the number of spatter particles generated is directly proportional to the volume of powder melted.

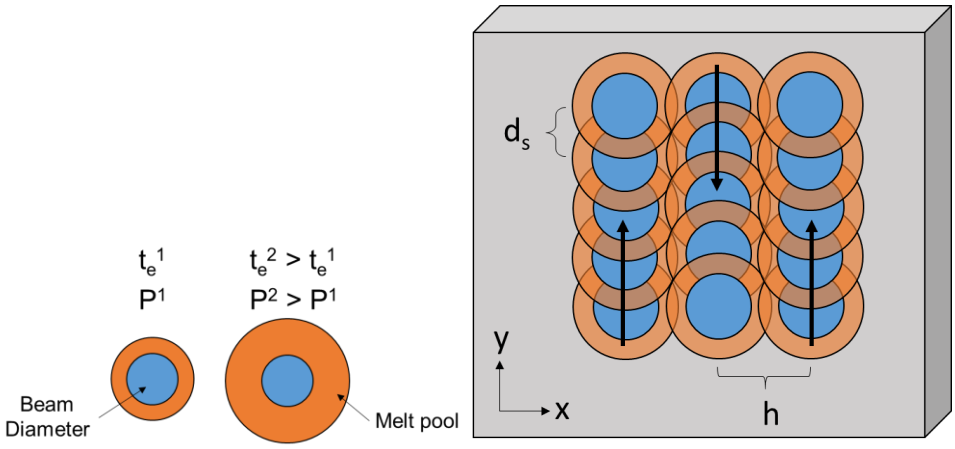

Figure 2.2: (left) Effect of exposure time (t_e) and/or laser powder (P) on weld pool diameter. (right) Top-down view of three lines of a raster scan pattern utilizing pulsed-laser melting. Spot distance (d_s) is the distance between spots melts, and hatch spacing (h) is the distance between raster scan lines.

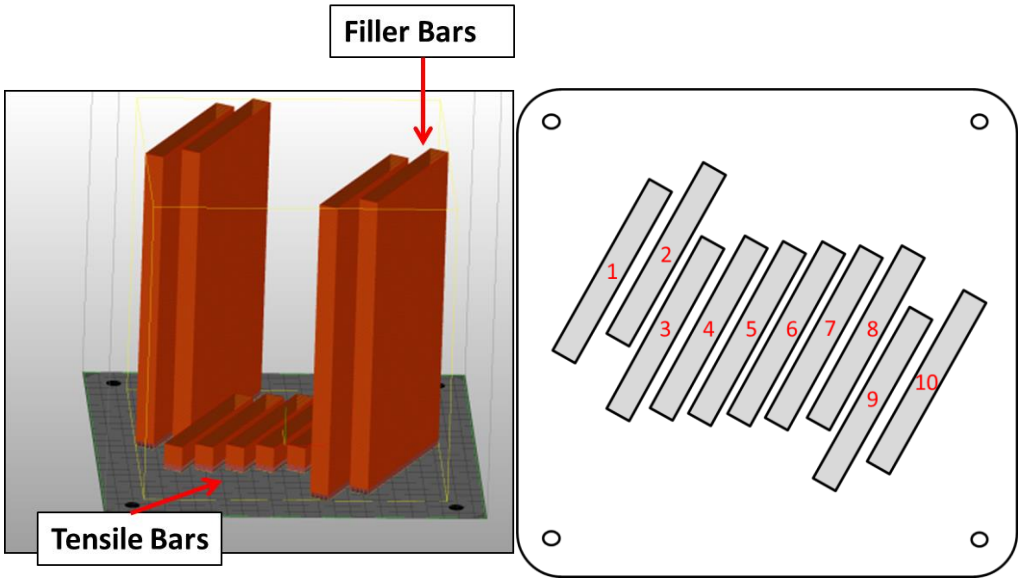

Figure 2.3: (a) Isometric-view representation of the geometry that was built during the recyclability experiment. (b) Top-down view of the positions of all 10 parts on the base plate. All 10 parts rested on 4mm high support structures to aid in their removal from the base substrate.

All of the bars were supported above and attached to the 250x250x15 mm tool steel base plate by 4 mm tall support structures. The supports were included in order to facilitate removal of the bars from the built plate upon completion of the build. The STL file was imported into Renishaw's AutoFab software where the geometry was virtually oriented on the build plate and geometry slicing took place. The sliced file was then loaded into the Renishaw™ AM250's machine software. This geometry was built four times, with each build utilizing the unmelted powder from the previous cycle as feedstock.

An initial powder mass of 104.35 kilograms of virgin 316L stainless steel powder was loaded into the hopper of the Renishaw™ AM250 machine. The term "virgin" refers to the state of the powder as-received from Renishaw™. The powder was sourced from Renishaw™ who, at the time of the experiment, sourced their powder from LPW. LPW sources their powder from multiple manufactures and blends powder batches together in order to meet customer powder specifications. Because of this sourcing process, neither a detailed history nor an ultimate powder manufacturer for the feed stock powder can be cited.

The loaded geometry was then built until the hopper ran out of powder, as evidenced by visually observing a lack of powder released during the powder dosing sequence. During processing, a continuous stream of argon gas was blown across the powder bed at a height determined by Renishaw™ as to not physically disturb the powder bed. The argon flow was controlled by setting the speed of a recirculating fan to 17 Hz. The actual argon flow rate is unknown. This argon stream inerted the build chamber and served to carry some of the molten droplets ejected from the melt pool away from the powder bed (see Figure 2.4).

These molten droplets solidify in flight and collect in a pile at the base of the left wall of the chamber, (see Figure 2.7). This ejected material is referred to in this document as "downstream" powder because its position is downstream relative to the argon gas stream. The general morphology of downstream/spatter is shown in Figure 2.5. The argon stream also serves to redirect some of the melt vapors away from the optical lens located at the top of the build chamber and towards the system's filter which is connected inline to the gas recirculation system. The system's filter was changed approximately every 72 hours during the build, which required a temporary pause (~5 minutes) in the build while filters were being swapped.

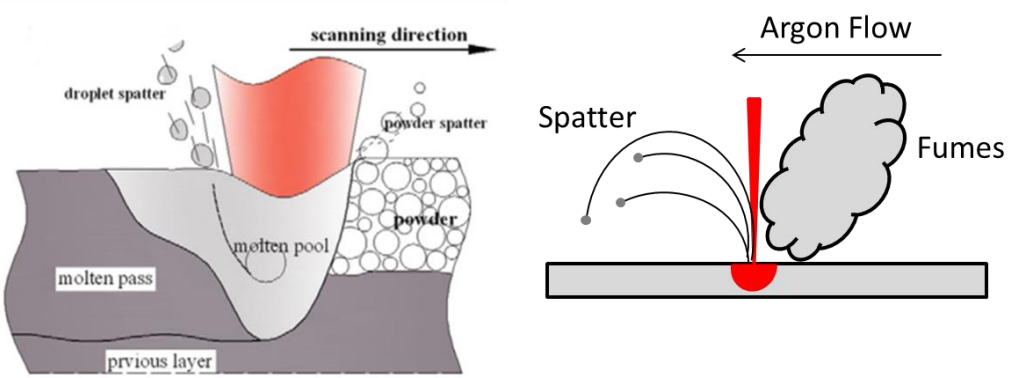

Figure 2.4: Spatter particles fall back into the powder bed and vaporized metal emerges from the melt pool [5].

This pattern of building and reusing the unmelted powder was repeated until the remaining unmelted powder in the powder bed was insufficient to build the entirety of the tensile bars. A fifth build was conducted using legacy powder. This legacy powder was known to have been used as feedstock for multiple projects and was assumed to have undergone more than the three reuse cycles that our experiment was limited to. The fifth build was intended as a reference point with which to compare results from the first four cycles. Data logs of the argon line pressure, elevator temperature, chamber temperature, chamber pressure, oxygen levels, and the number of layers were collected after the completion of each build (see Appendix B).

2.2.2. Heat Affected Zone Experimental Plan

A Renishaw AM250 instrument with a maximum laser power of 200W was used to conduct three heat-affected-zone experiments (HAZ1, HAZ2, and HAZ3). The Renishaw AM250 build process uses a pulsed laser to selectively melt regions of a metal powder bed. Melting bonds the powder layer to either the tool steel build plate or previously melted layers. Virgin stainless steel 316L powder purchased from Renishaw was used as the feedstock in all of the HAZ experiments. Before starting the process, the build chamber was evacuated and refilled with a non-reactive argon cover gas. A purge and refill cycle was conducted until the chamber oxygen content measured below 0.02 mbar. During the SLM process, the argon cover gas was constantly recirculated over the powder bed surface and through a filter using a fan set at a recirculating speed of 22 Hertz. The volumetric flow rate of the chamber gas as well as the type of flow over the powder bed (laminar vs turbulent) is unknown. A full list of machine parameters used during each build can be found in Appendix A. Parameter selection and slicing of the CAD part was conducted using AutoFab v1.8.

The heat-affected-zone experiments were designed to provide information from the unmelted powder bed regions, measured as close as possible to a melted region during selective laser melting. All three of the HAZ experiments were designed to have walls of processed material spaced at regular intervals to each other. This spacing created channels where un-melted powders were retained. The number of channels for a given spacing was chosen to keep the total volume of powder (~1cm^3) contained within the channels approximately constant across each channel spacing value. As the spacing between the channel walls decreased, the fraction of unmelted powder within the channel that was exposed to the heat given off by the melting of the channel walls increased. Powder samples collected from the channels post process were analyzed for phase change, oxygen content, and powder size distribution change. The designs of the three experiments were necessarily focused on gradual changes. It was found during powder collection that the 100 µm wide channel walls in the HAZ1 experiment (Figure 2.8) were too thin and would break and mix with the powder during collection of the 150 µm channel powder, contaminating the sample.

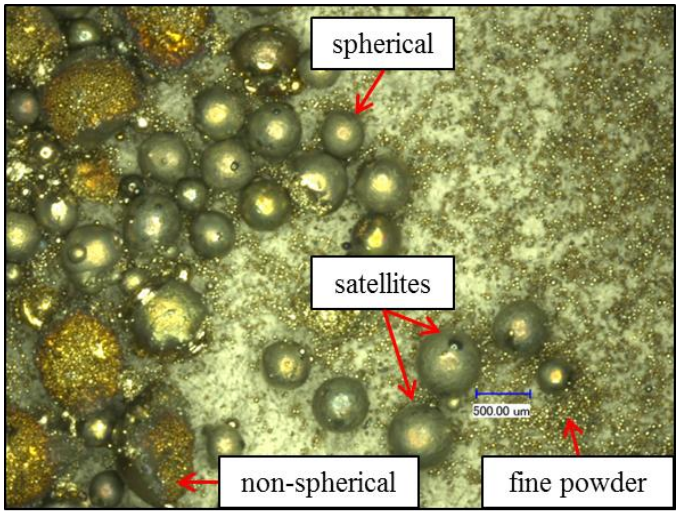

Figure 2.5: Images confirm that (unsieved) ejected molten particles are much coarser (> 200 µm) compared to the fresh powder (27 µm). Ejected particles exhibit all shapes including spherical, near spherical, non-spherical, and with satellites.

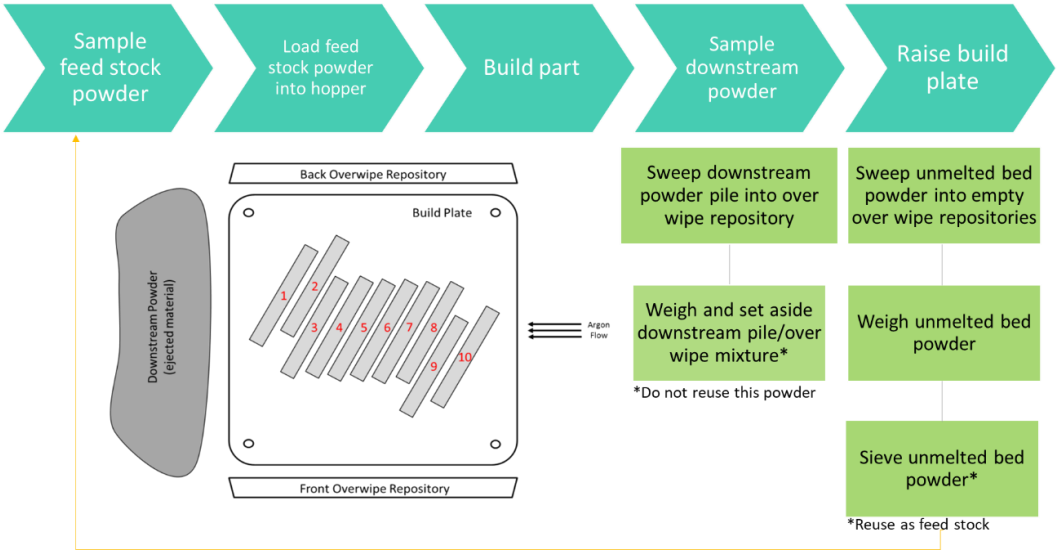

Figure 2.6: Flow chart of the recyclability experiment process.

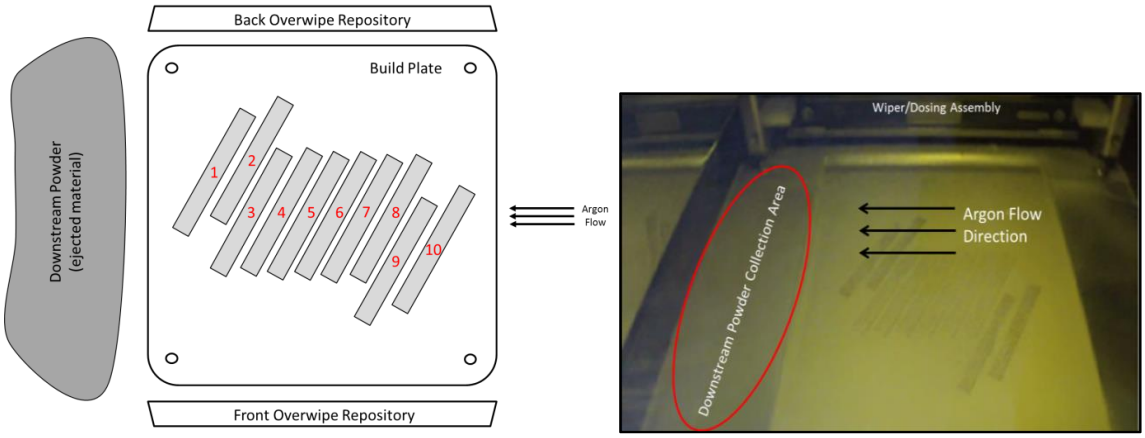

Figure 2.7: Top-down schematic of the recyclability experiment build geometry in relation to other features of the build chamber.

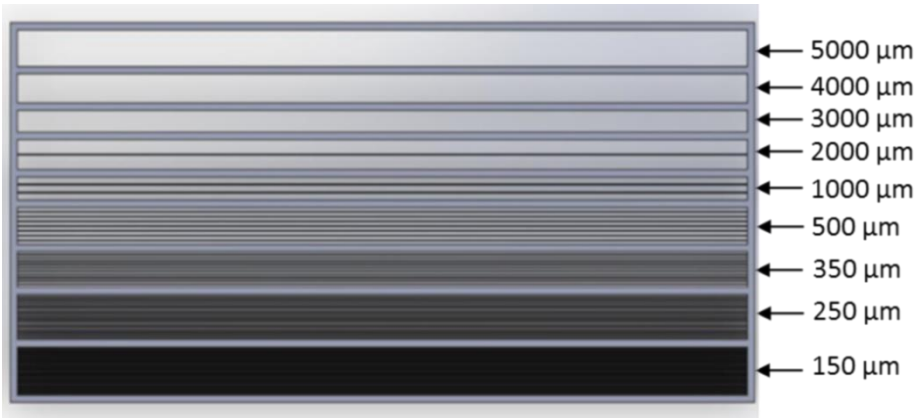

Figure 2.8: Top-down view of heat-affected-zone experiment #1: 5mm, 4mm, 3mm, 2mm, 1mm, 500 µm, 350 µm, 250 µm, and 150 µm wide channels separated internally by 100µm thick walls.

The HAZ1 experiment was redesigned and repeated in the HAZ2 experiment shown in Figure 2.9. The HAZ2 design featured channel walls of 150 µm thickness that did not break during sample collection. The HAZ2 design also physically spaced channel sections from each other in order to eliminate any contributing heat effects between channel sections.

The HAZ3 experiment was designed to investigate the effect of channel wall thickness on the heat-affected-zone within the channels. This experiment chose two extremes in both channel wall thickness (150 µm; 2000 µm) and channel width (150 µm; 5000 µm) and combined them into the four distinct sections shown in Figure 2.10.

Powder samples were collected from each channel width section of all three experiments by covering all of the non-collection channels with an aluminum plate that had a rubber pad glued onto one face, and then turning the entire baseplate upside down to allow powder to flow out of the open channel and onto an aluminum foil sheet. C-clamps were used to ensure that the rubber pad made a strong seal against the channel wall surfaces, thereby preventing the mixing of powders between channels during powder removal. Powder samples were stored in separate glass vials designated by their experiment number (HAZ1, HAZ2, or HAZ3) and channel widths/wall thicknesses.

2.2.3. Variable Oxygen Environment Experimental Plan

A 3-dimensional geometry, shown in Figure 2.11a and Figure 2.12, was designed using SolidWorks and exported as an STL file. The geometry consisted of 2 groupings of 3 sets of tensile bars of dimension 0.95x0.95x5.8 cm, for a total of 18 tensile bars. Each individual set consisted of 3 tensile bars stacked in the build-direction and separated from each other in the build-direction by 4 mm of support material. In the x-direction, each set was separated by a distance of 8 mm. The sets were labeled A through F and, beginning with bars nearest to the base plate and counting in the z-direction, the 3 tensile bars within each set were labeled 1, 2, and 3. For example, sample 2E would be the middle of the three stacked bars in the stack of tensile bars designated as stack E in Figure 2.11.

Powder bed samples were collected at each cover gas oxygen level by building three open troughs, shown in Figure 2.11 (b). Each trough was built on supports. The supports raised the bottom of each trough to the build layer corresponding to the beginning of each level of tensile bars.

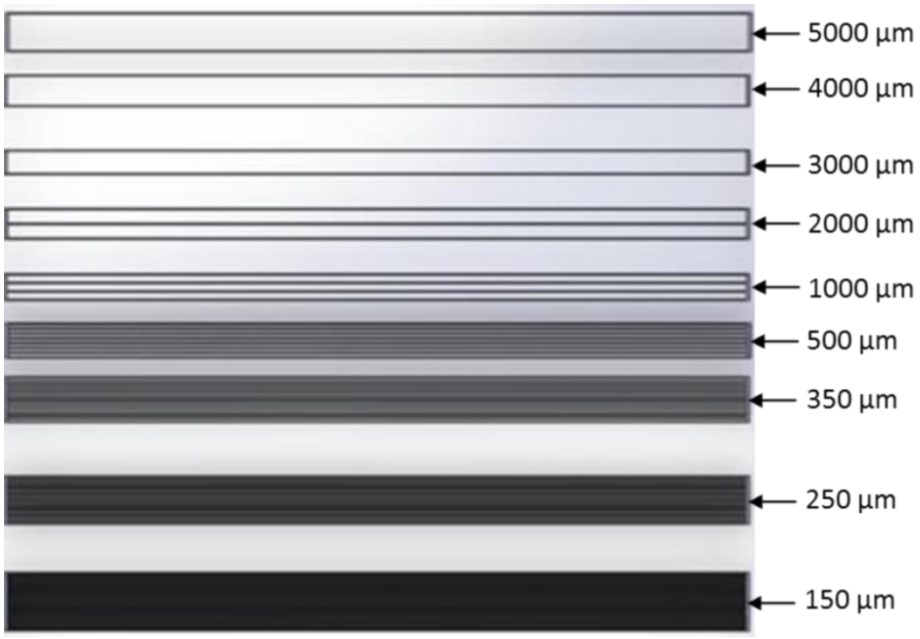

Figure 2.9: Top-down view of heat-affected-zone experiment #2: 5mm, 4mm, 3mm, 2mm, 1mm, 500um, 350 µm, 250 µm, and 150 µm wide channels separated internally by 150 µm thick walls.

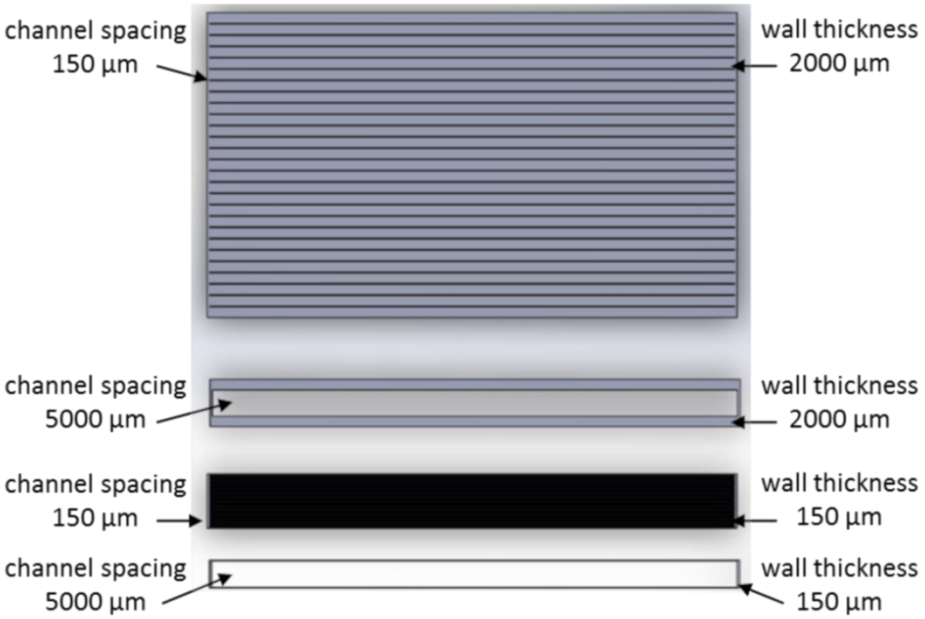

Figure 2.10: Heat-affected-zone experiment #3: 5mm wide channel with 150 µm thick walls, 5mm channel with 2mm thick walls, 150 µm channels with 150 µm thick walls, and 150 µm channels with 2 mm thick walls.

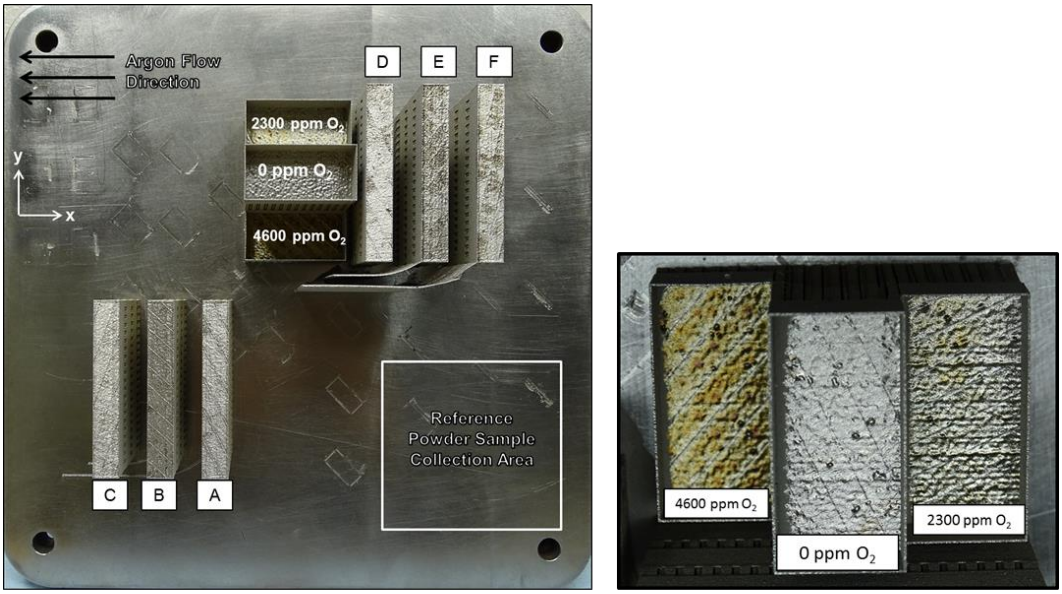

Figure 2.11: Top view of (a) completed oxygen experiment build geometry and (b) spatter particle receptacles.

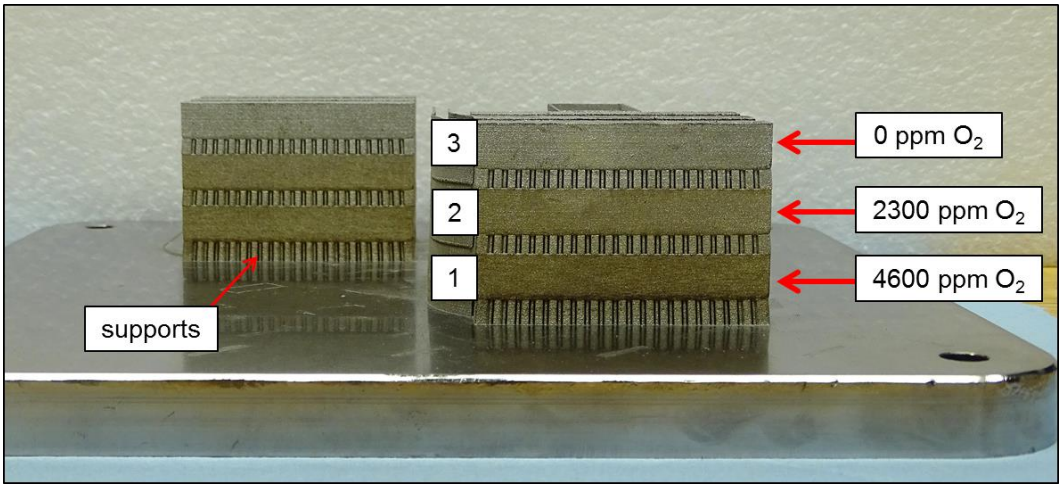

Figure 2.12: Side view of completed oxygen experiment build showing how tensile bars were stacked on top of support structures.

The AM250 machine default is to melt parts from left to right as they are positioned on the build plate. Thin walls, or “tails”, were added to the geometry and connected to sets E and F in order to control the order of melting so that F melted before E and E melted before D. This was done so that spatter originating from the melting of F may have had the opportunity to fall into the bed powder at locations that would be subsequently melted to build sets E and D. The same reason applies to the tail attached to set E; which resulted in set D being effectively exposed to twice the amount of spatter contamination as set E. This principle is applied in reverse to sets A through C; set C melts first, set B melts second, and set A melts third. In this fashion, the spatter originating from sets B and A have the opportunity to fall onto the already melted and solidified surface of set C, and the spatter from set A has the opportunity to fall onto the melted and solidified surfaces of both sets B and C. However, unlike the spatter contamination that fell onto sets D and E, the spatter from set A and B has a new layer of fresh powder deposited by the wiper before melting of those areas occurs again. It is unknown if the wiper is capable of moving or removing spatter particles in the powder bed during the wiping process.

Oxygen content within the build chamber was monitored by machine sensors and logged every 15-20 seconds throughout the build (see Appendix B). Oxygen was introduced into the system by the manual throttling of a needle valve installed in line with the gas recirculation system inside the Renishaw™ AM250 machine. The needle valve opened to the lab atmosphere and allowed the introduction of ambient air into the gas recirculation system when throttled open. Using the AM250 instrument control panel, a limit point of 5000 ppm oxygen was set, beyond which the system would automatically pause the build and purge with argon until the oxygen content again read below 5000 ppm. It should be noted that the AM250 had a slow pressure leak throughout the experiment (~1 mbar/hr) and would periodically introduce argon to recover lost pressure (~every 9 hours). This periodic introduction of argon would, over time, deplete the oxygen levels within the chamber, which required the operator to remain on hand to throttle the needle valve open or closed in order to remain at the desired build chamber oxygen levels of 4600 ppm for the first layer of tensile bars, 2300ppm for the second layer of tensile bars, and 0ppm for the third layer of tensile bars.

Three thin walled receptacles (see Figure 2.11b) were also built alongside the grouping of sets D, E, and F in order to collect the spatter originating from the melting of these three sets at each oxygen level tested. The bottom of each receptacle began level in height with the bottom of the tensile bars (layers 1, 2, or 3) that it was meant to collect spatter from. The walls were built to match the height of their respective tensile bars, i.e. 0.95 cm. The receptacles were left open faced with the intent that excess powder above the zone of interest collected by each receptacle would flow away during the raising of the build plate and removal of the finished build from the powder bed.

2.2.4. Cooling Rate Study Experiment Plan

An experiment was designed to influence the cooling rate of a melted part by preheating the powder in and surrounding the melt area of each layer. Because of the low packing density of the powder bed, conduction of heat away from the melted part through the powder bed is slower than it would be through a fully dense portion of the same material. Preheating powder directly adjacent to the melt region slows down the heat transfer further by decreasing the local temperature gradient between the part and the powder bed. However, should the preheating of the powder bed result in sintering of the powder particles, the opposite effect may be achieved, where the thermal conductivity of the preheated portion of the powder bed is increased via sintering and therefor allowing heat to move away from the melted region more rapidly than if the powder bed had not been sintered.

By decreasing the rate of heat transfer away from the melt zone, the balance of energy input from the laser and the energy leaving the melt zone via conduction is affected, effectively producing a preheated substrate for the next melt event. When melt parameters are optimized for use on a non-heated substrate, the effect of a preheated substrate will likely increase the likelihood that a key holing condition will be met and increase the chance that spatter from key holing will form during processing. By the same logic, if thermal conductivity through the powder bed is increased via sintering, the resulting temperature of the melted and resolidified region may remain more stable throughout the build process and the likelihood of keyholing and spatter production may be reduced. By reducing the amount of spatter originating from the melt pool it is reasoned that any inclusions or defects introduced into parts by spatter falling into the powder bed would also be reduced. The instrument used to conduct the spatter experiment was the Renishaw™ AM250, 200-Watt SLM system located at the Manufacturing Demonstration Facility, a part of ORNL.

An experiment made up of 180 cylindrical posts, 5 mm in diameter and 5 mm in height, was designed in the Magics software and built on a using a size-reduced baseplate composed of 316L stainless steel and with dimensions of 6x6x0.25 inches. The experiment was designed so that prior to the melting of each post, a 7 mm diameter circular area of the powder encompassing the post was processed using the parameter combinations shown in the left side of Figure 2.13. This prior processing is referenced here as a ‘preheat’. The parameters used to melt the posts after the preheat were the default parameters provided by Renishaw™. These parameters (see Appendix A) were updated by Renishaw™ from those used in the recyclability and HAZ experiments and were considered as representative of industry standards at the time the experiment was performed.

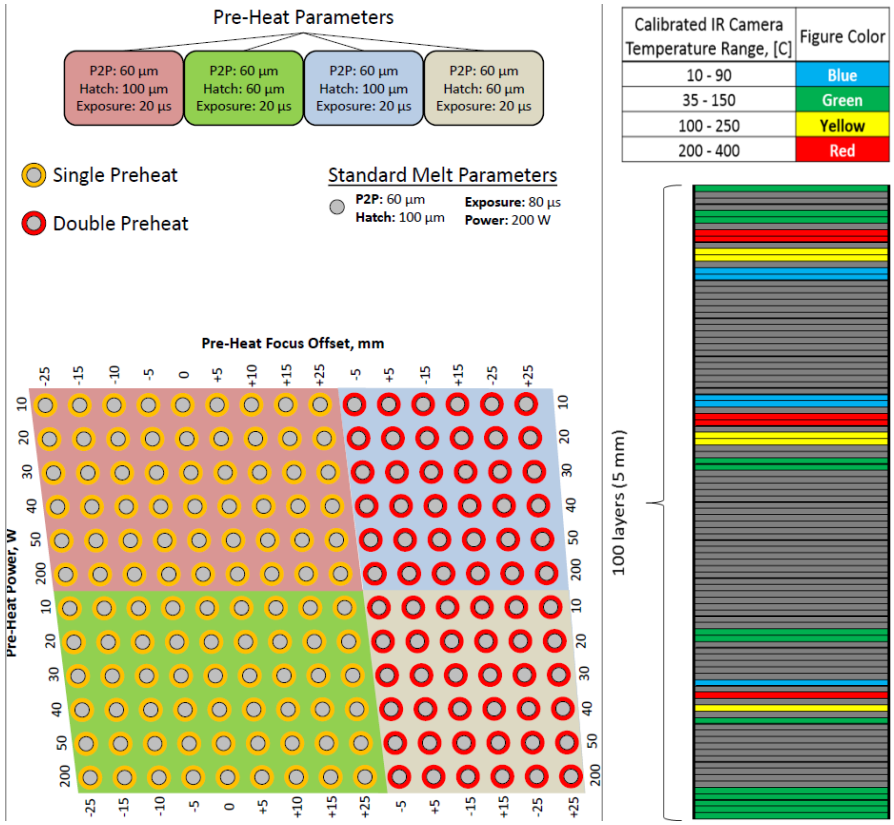

Figure 2.13: (left) Top down view of the build plate geometry and (right) a visualization of the build layers for which IR data was collected.

2.3. Data Collection

A variety of techniques were utilized to characterize the powder feedstock, printed parts, and spatter material that are integral to the discoveries and hypotheses presented in this thesis. Details of the following characterization techniques can be found in Appendix H.

Powder density and unconstrained flow properties were measured by following the standards set forth in ASTM B212-13 and ASTM B213-13.

X-ray photoelectron spectroscopy (XPS), electron-backscatter diffraction (EBSD), powder size distributions (PSD), and powder x-ray diffraction (XRD) data were all collected using instruments owned by ORNL's Material Science & Technology Division.

High-temperature x-ray diffraction (HTXRD) was conducted at the Joint Institute for Advanced Materials (JIAM) Diffraction Facility, while single-crystal x-ray diffraction (SCXRD) was conducted at the Neutron Scattering Division of ORNL.
Elemental chemistry analysis of both powder and part samples was conducted by Luvak Laboratories using the methods described in ASTM E1019-11, E1019-12, E1097-12, and E1447-09.

Magnetic measurements, differential scanning calorimetry (DSC), and thermogravimetric analysis (TGA) of powder samples were conducted by Ames Laboratory using Quantum Design Versa Lab VSM and NETZCH STA 449 F3 Jupiter instruments.

Transmission electron microscopy (TEM) was conducted using Tecnai T20 and Tecnai T30 instruments at the Center for Electron Microscopy and Analysis (CEMAS) at the Ohio State University (OSU).

2.3.1. Virgin Powder

All experiments were conducted using stainless steel 316L feed stock supplied by Renishaw™ in powder form. Due to existing non-disclosure agreements between Renishaw™ and its powder manufacturers, the precise origin and manufacturing details of the received powder feedstocks are not known. Discussions with persons knowledgeable of the metal powder production business point to the likelihood that many different batches of powder from several different powder manufacturers may have been blended together prior to shipping.

Section 2.3.1 is dedicated to the characterization the virgin powder feedstock. Results found in this section will referenced to in later chapters.

2.3.1.1. Chemical Analysis

The elemental weight percentages of both virgin powder feedstock, and a well-worked powder that was used in Cycle 5 of the recyclability experiment, are given in Table 2-1 and Table 2-2.

2.3.1.2. Hall Flowmeter, Apparent/Tapped Densities

Table 2-3 lists the powder's apparent and tapped densities, as well as its flow performance.

2.3.1.3. Powder Size Distribution

The powder size distribution of the virgin stainless 316L powder is shown in Figure 2.14. Table 2-4 provides the mean, median, mode and 10%, 50%, and 90% volume particle size diameters for each powder sample analyzed.

2.3.1.4. X-Ray Diffraction

Figure 2.15 shows the normalized X-ray diffraction patterns collected from the virgin 316L powder. Both batches of virgin powder are composed of fully FCC particles, with no BCC phase visible in the patterns.

2.3.1.5. Electron Back-Scatter Diffraction

Figure 2.16, depicting EBSD analysis of the virgin powder, shows the crystal structure the powder be primarily polycrystalline FCC (gamma phase) with only one small particle showing as BCC (alpha phase) detected.

2.3.1.6. Magnetic Measurements

Figure 2.17 shows that the virgin powder exhibits a mostly paramagnetic contribution to the M-H loop, as evidenced by the high saturation magnetization value (>30 kOe), and little to no magnetic retentivity.

2.3.1.7. Differential Scanning Calorimetry & Thermogravimetric Analysis

Figure 2.18 shows the heat flow of the powder as a function of temperature with a dashed line indicating the presence of a possible phase change at 1000^{o}C, as evidenced by the change in slope at this temperature. Samples were allowed to cool naturally after heating. The direction of heat flow away from the sample during cooling is opposite that of the heat flow into the sample during heating. The cooling curve has a shallower slope than the heating curve because the samples were allowed to cool naturally, in contrast to the forced heating during the heating cycle.

Table 2-1: Virgin stainless steel 316L feedstock powder elemental weight percentages.

Elemental ID	Cr	Ni	Mo	Mn	S	Si	C	P	N	O	H
*Standard	16-18	10-14	2-3	2.00	0.030	1.00	0.030	4.5E-2	0.10	-	-
Virgin	17.73	12.45	2.22	1.44	0.005	0.66	0.015	6.6E-3	0.10	0.032	9E-4
Error [+/-]	0.3	0.2	0.05	0.03	5E-4	0.01	0.005	1E-03	0.005	0.002	2E-5

*ASTM A276/276M-16a

Table 2-2: Cycle 5 feedstock 316L feedstock powder elemental weight percentages

Elemental ID	Cr	Ni	Mo	Mn	S	Si	C	P	N	O
*Standard	16-18	10-14	2-3	2.00	0.030	1.00	0.030	0.0450	0.10	-
Cycle 5 Feedstock	17.86	13.13	2.38	1.27	0.007	0.67	0.025	0.02	0.089	0.038
Error [+/-]	0.36	0.26	0.02	0.03	0.002	0.01	0.002	0.001	0.005	0.002

*ASTM A276/276M-16a

Table 2-3: Apparent and tapped densities of virgin stainless 316L powder, as well as the unconstrained flow of the powder as measured by ASTM B213-13.

Virgin Stainless Steel 316L Powder	
Apparent Density [g/cc]	5.470
Tapped Density [g/cc]	6.100
Hall Flow Test [s/50g]	16.668

Table 2-4: Virgin powder size characterization conducted by laser diffraction using ORNL's Horiba la950 V2 instrument.

Virgin Powder Manufacturer	median [µm]	mean [µm]	mode [µm]	variance [µm^2]	st. dev. [µm]	D(v,0.1) [µm]	D(v,0.5) [µm]	D(v,0.9) [µm]
Carpenter	31.775	32.916	31.908	74.626	8.639	23.281	31.775	43.839
Renishaw	28.621	29.759	28.105	66.568	8.159	20.563	28.621	40.116

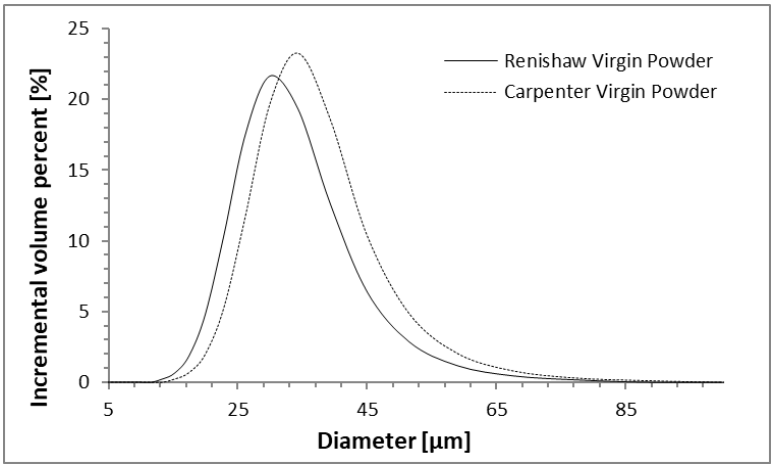

Figure 2.14: Virgin powder size characterization conducted by laser diffraction using ORNL's Horiba la950 V2 instrument.

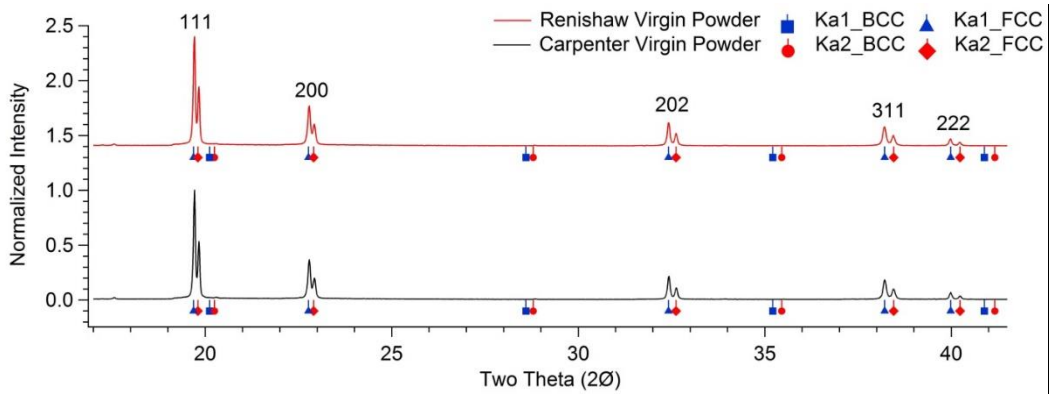

Figure 2.15: Powder x-ray diffraction pattern showing that virgin 316L powder has an austenitic (FCC) crystal structure with no evidence of ferrite (BCC).

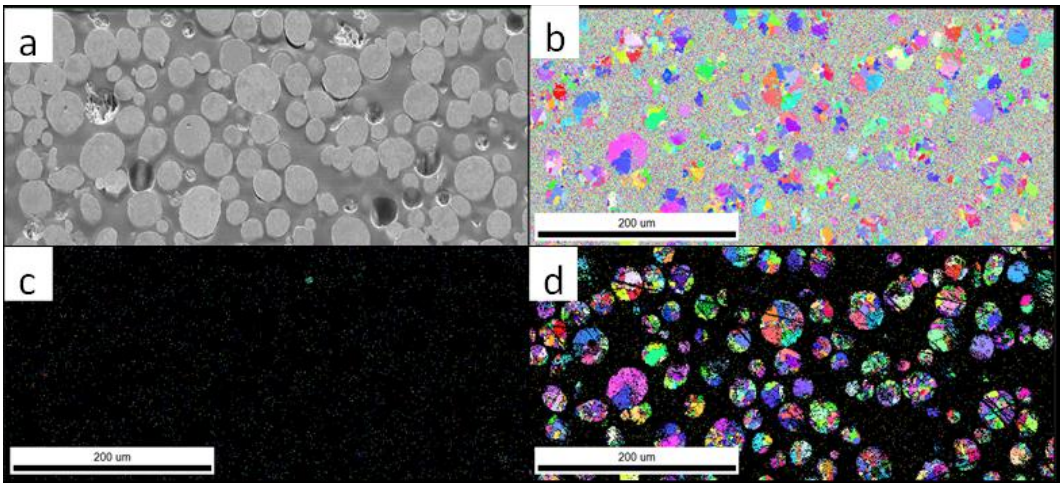

Figure 2.16: *(a)* SEM image of virgin stainless 316L powder, mounted in conductive epoxy and polished. *(b)* EBSD of virgin powder showing alpha (BCC) and gamma (FCC) phases together. *(c)* EBSD of virgin powder showing only alpha (BCC) phase. *(d)* EBSD of virgin powder showing only gamma (FCC) phase.

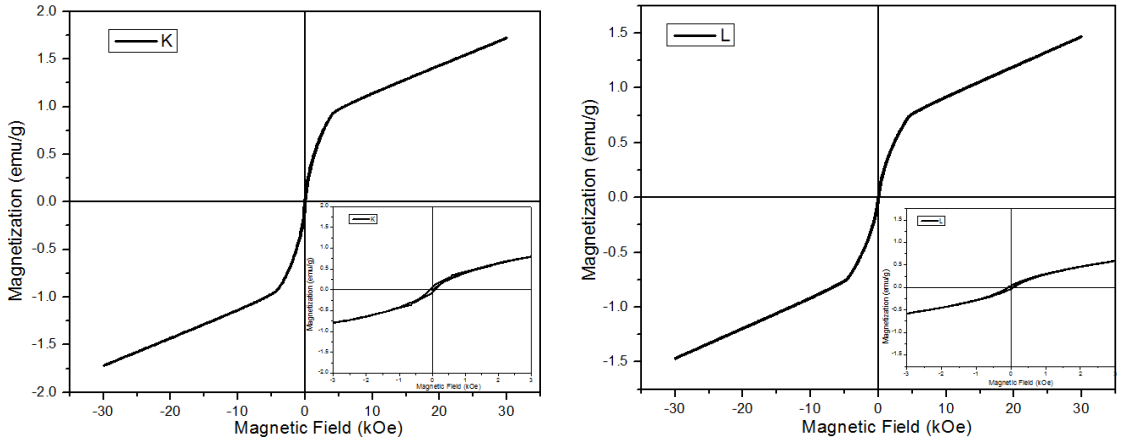

Figure 2.17: Hysteresis curves of Renishaw™ (K) and Carpenter (L) virgin powder.

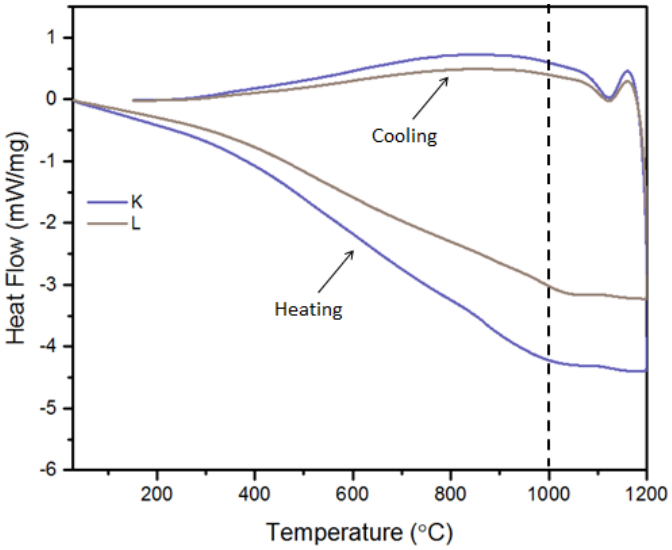

Figure 2.18: Differential scanning calorimetry (DSC) of Renishaw™ (K) and Carpenter (L) virgin powder. The dotted line indicates the presence of a phase change occurring at approximately 1000 °C.

Figure 2.19 shows the mass change of the virgin powder as it is heated from room temperature to 1200ºC while exposed to a magnetic field. A Faraday balance was used to measure the apparent mass change of the samples. The sudden drop in mass of the Renishaw virgin powder indicates a possible Curie temperature near 525ºC. The Curie of temperature Iron(II,III) oxide (FeO, Fe_2O_3) (575-585ºC) is close to this value, indicating the possible presences of iron-oxide within the powder.

2.3.1.8. Transmission Electron Microscopy

Transmission electron microscopy of virgin Renishaw™ powder was conducted at the Center for Electron Microscopy and Analysis (CEMAS) at the Ohio State University (OSU). The powder was mounted in a conductive epoxy and polished before a TEM foil sample was extracted using focused ion beam milling. Figure 2.20 depicts a powder particle selected for sample preparation, as well as the lift-out of the extracted foil. Figure 2.21 shows the ion beam polished TEM foil ready for imaging using TEM. Several micron-sized grains are seen to be present in the foil sample.

Several interesting features were identified within the virgin powder FIB foil and are shown in Figure 2.22. Two types of oxides/precipitates were found to be present in the foil. One type of precipitate was rich in Cr, Mn, and Mo (Figure 2.23) and was only found at the top of the foil, near the interface between the Pt covering and the sample itself (Figure 2.22a,e). The second type of precipitate is rich in Si, Mn, and O and was present mainly along grain boundaries (Figure 2.22d). Some Si-rich precipitates were surrounded by a Cr, Mo, S, and P rich region which presented as a bright area surrounding the dark oxides (Figure 2.22b). When viewed on-zone, dislocations could be seen to be tangled around some of the oxides (Figure 2.22c).

Selected area diffraction (SAD) was performed on each of the two types of precipitates found within the virgin powder FIB foil. Figure 2.24 shows that even when using the smallest selected area aperture available, a diffraction pattern of the Si-rich precipitate could not be obtained. Only the diffraction pattern of the FCC matrix is visible. It is possible that the amount of matrix above, below, and surrounding the precipitate dominated the diffraction and overpowered the precipitate's diffraction. In contrast, selected area diffraction of the Cr-rich precipitate produced overlapping diffraction patterns, one from the metal matrix and one from the precipitate itself.

2.3.1.9. X-Ray Photoelectron Spectroscopy

The major photoemission peak for each element identified during the surface composition of the as-received ad well-sputtered virgin powder are labelled in Figure 2.26. All other peaks are minor transitions of these same elements. It can be seen that the oxygen signature has decreased dramatically in the well-sputtered plot and the iron and chromium peaks have increased.

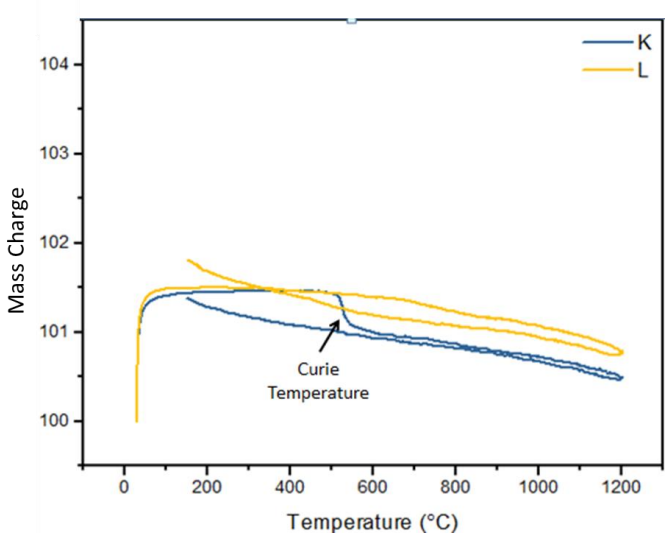

Figure 2.19: Thermogravimetric analysis of Renishaw™ (K) and Carpenter (L) virgin powder.

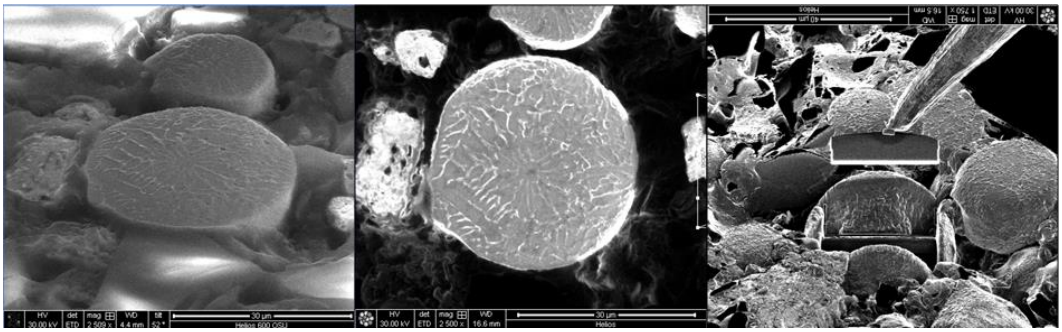

Figure 2.20: (left, middle) SEM images of virgin powder particle, embedded in epoxy and polished. (right) SEM image of the FIB foil lift-out.

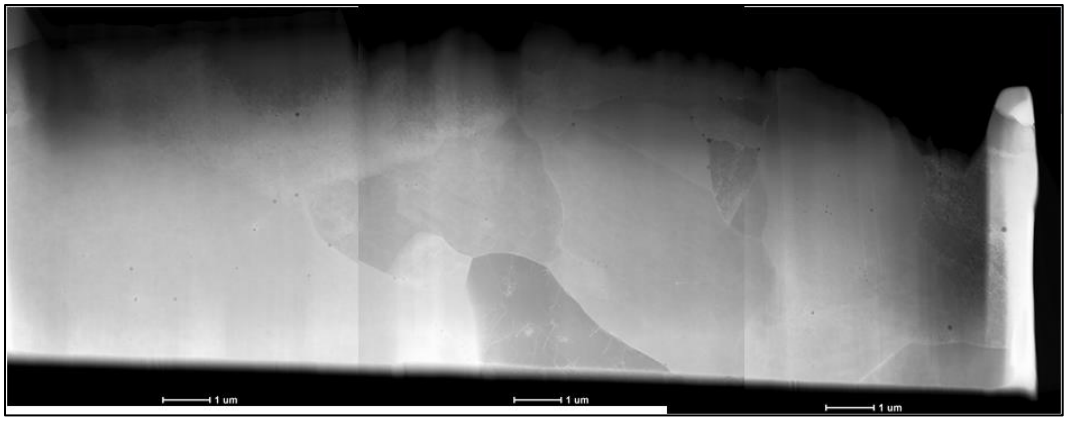

Figure 2.21: High angle annular dark field (HADF) TEM image of virgin powder TEM foil after undergoing thinning by focused ion beam.

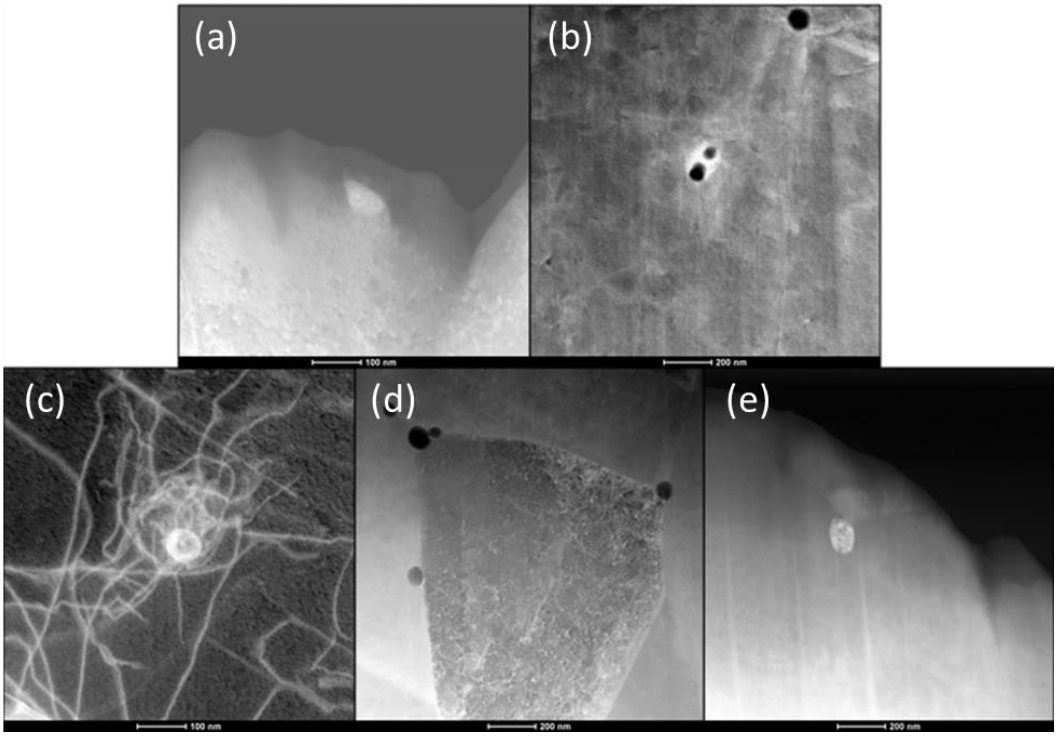

Figure 2.22: (a,e) Cr, Ni, Mo rich, non-spherical precipitates residing in the foil-Pt interface region. (b,d) Si, Mn, O rich, spherical precipitates located primarily along grain boundaries. (c) dislocation entanglement around an oxide.

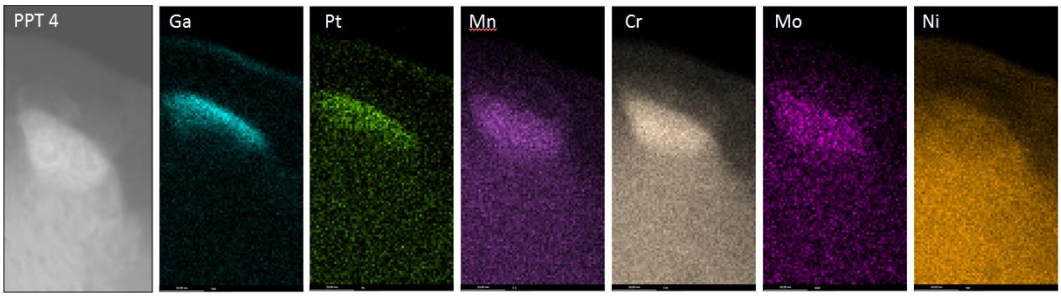

Figure 2.23: EDS map of the foil-Pt interface precipitate seen in Figure 2.22*a*.

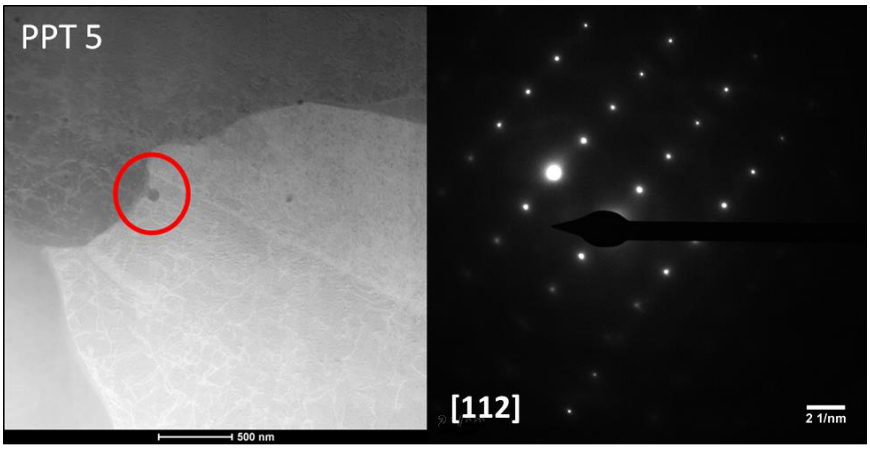

Figure 2.24: Selected area diffraction pattern of suspected oxide. Only the surrounding [112] matrix diffraction pattern is visible.

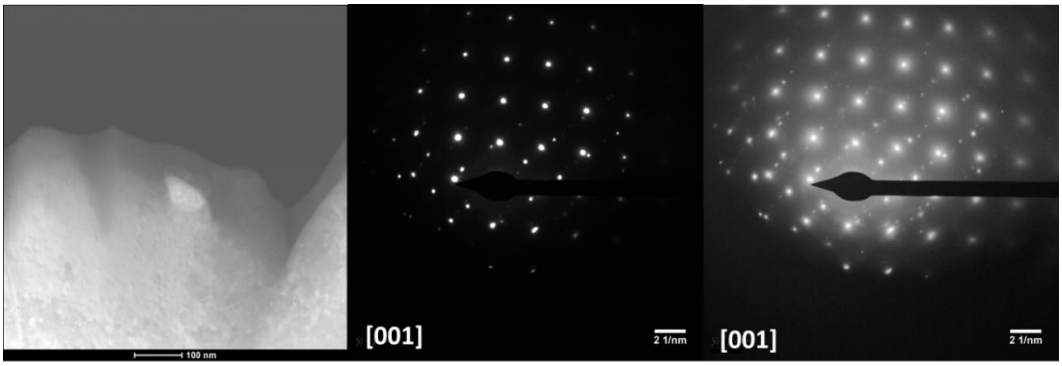

Figure 2.25: (left) TEM image of Cr-rich precipitate residing in the foil-Pt interface region. (center) Selected area diffraction pattern of the precipitate. (right) enhanced contrast image of the precipitate's selected area diffraction pattern .

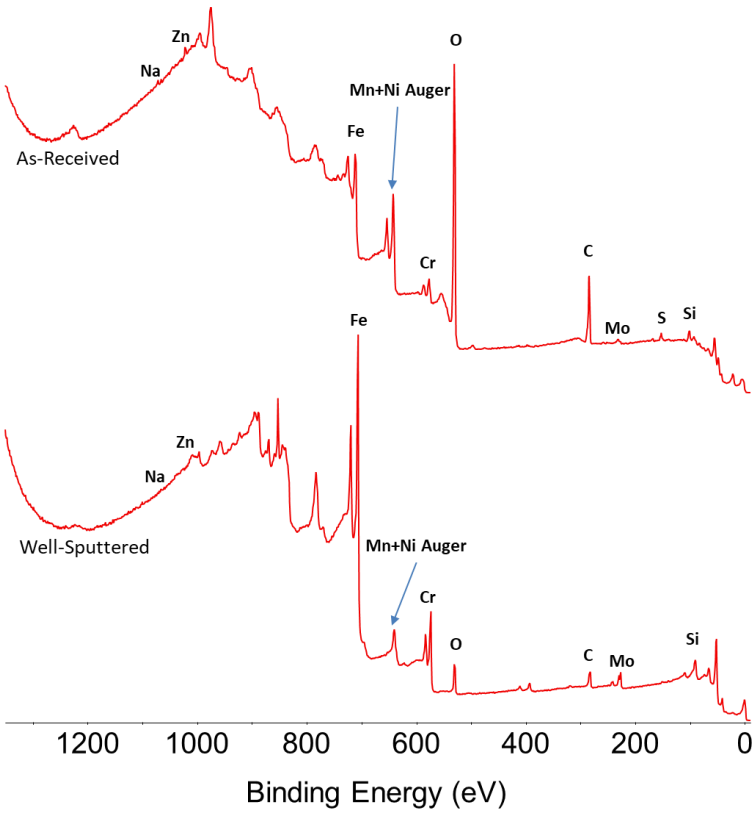

Figure 2.26: As-received and well-sputtered XPS elemental binding energy plot of virgin powder.

The depth profile data for the virgin powder is shown in Figure 2.27. The upper plot shows the total signals for C, Fe, Cr, Mn, Mo, and O. Ni was not followed, but the fact that the Mn level is so high once the outer layer (which consists primarily of C and metal oxides) is passed is due to the overlap with a Ni feature. Figure 2.27 shows that the surface carbon is removed quickly, but that the C-signal dies more slowly as sputtering proceeds. Likewise, the outermost layer of the powder particles is made up primarily of Fe- and Cr-oxides with an enrichment of Mn. By about 400 sec of etching (approximately equivalent to 80 nm) the O signal has decreased to ~20% of its initial value and the Fe and Cr signals are primarily metallic. The lower plot shows an example of peak fitting both the C 1s and Fe 2p signals to de-convolute them into surface adsorbed C, carbide C, metal Fe, and oxide Fe. The O 1s is also re-plotted. It is clear that as the Fe metal appears, the carbide starts to grow and likely indicates that carbide is being formed by gettering C-containing species from the residual gas within the measurement chamber.

2.3.2. Recyclability Experiment Data Collection

2.3.2.1. Powders

A 3.5 mL vial of downstream powder, as well as 20 mL and 3.5 mL vials of powder bed powder were collected after each cycle throughout the experiment. The downstream powder was collected by dragging the vial through the downstream collection pile by hand. Powder bed samples were collected by submerging the vial into the sieved, collected bed powder and allowing powder to flow into the vial.

Powder samples were analyzed using XRD and EBSD to detect any amounts of phase change or contaminants, as well as to characterize the grain structure. Samples of these powders were also analyzed for chemical content and compared against virgin powder. Powder size distributions of the powder bed powder and downstream powder after each reuse cycle were also measured.

2.3.2.2. Tensile Bars

MACHINING

The tensile bars (numbering 3 through 8 in Figure 2.3b) were removed from the base plate, using a band saw to cut through the support structures, and machined into tensile specimens following the specifications for sub sized tensile specimens set forth in ASTM E8M-04, reproduced here in Figure 2.28. Since no thickness is specified in ASTM E8M-04, a thickness of 5mm was specified during machining of the tensile specimens. Most of the as-built tensile bars contained enough material to extract two tensile specimens; a top and a bottom specimen as depicted in Figure 2.29. Specimens were labeled by their build cycle number (1 through 5), position on the build plate (3 through 8), and whether they were a top (T) or a bottom (B) specimen. For example:

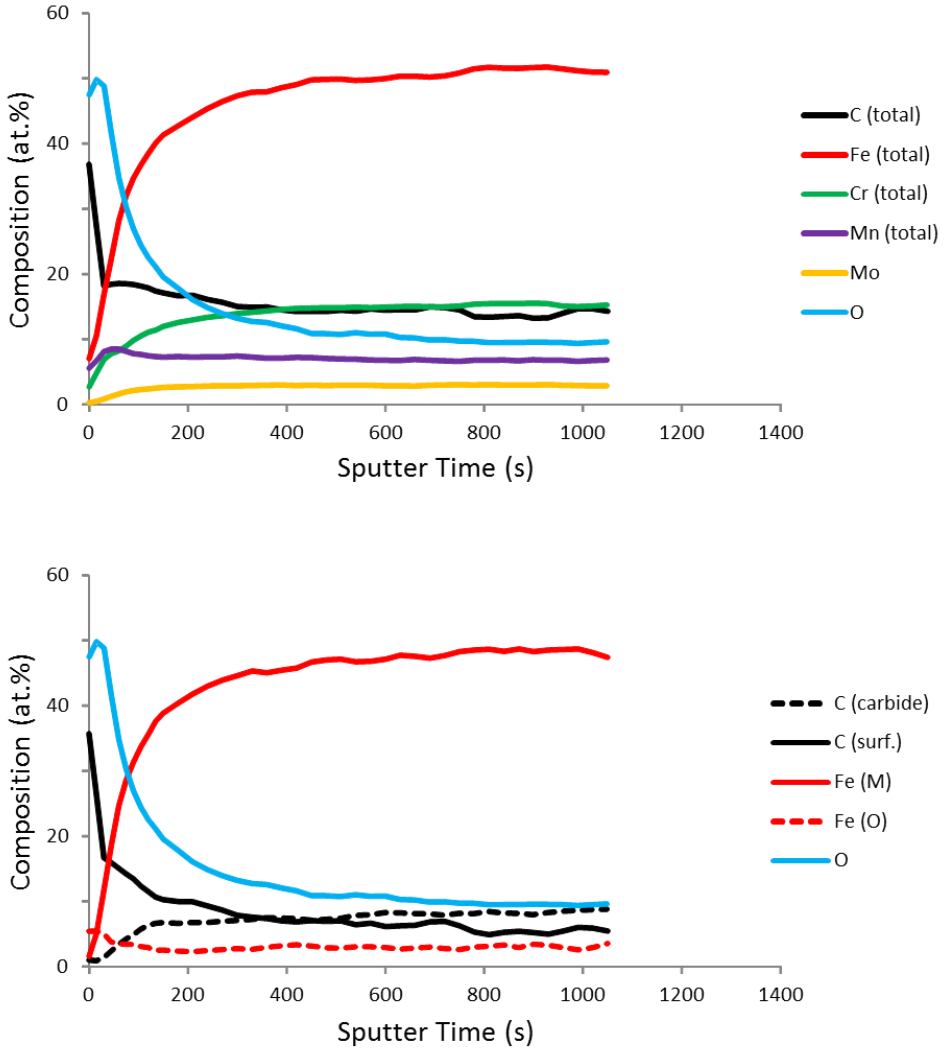

Figure 2.27: (top) Elemental depth profile of virgin powder. (bottom) Elemental depth profile of virgin powder oxides.

E 8M – 04

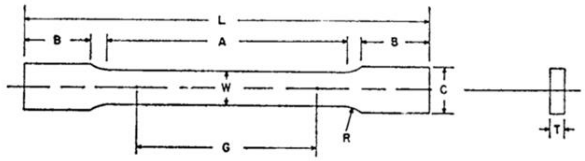

Dimensions, mm			
Nominal Width	Standard Specimens		Subsize Specimen
	Plate-Type 40 mm	Sheet-Type 12.5 mm	6 mm
G— Gage length (Note 1 and Note 2)	200.0 ± 0.2	50.0 ± 0.1	25.0 ± 0.1
W— Width (Note 3 and Note 4)	40.0 ± 2.0	12.5 ± 0.2	6.0 ± 0.1
T— Thickness (Note 5)		thickness of material	
R— Radius of fillet, min (Note 6)	25	12.5	6
L— Overall length, (Note 2, Note 7 and Note 8)	450	200	100
A— Length of reduced section, min	225	57	32
B— Length of grip section, (Note 8)	75	50	30
C— Width of grip section, approximate (Note 4 and Note 9)	50	20	10

Figure 2.28: ASTM E8M-04 standard for machining of sub-size tensile specimens.

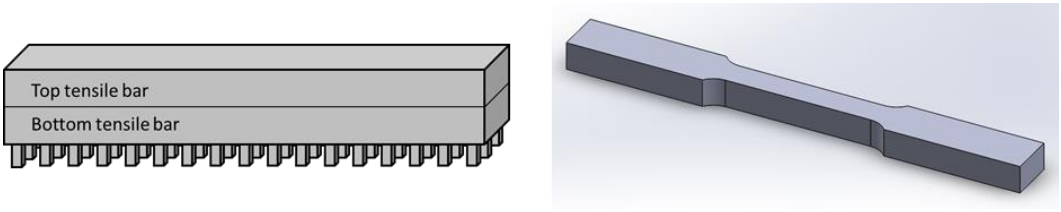

Figure 2.29: Schematic showing how two tensile specimens were obtained from a single, as built tensile bar.

sample 1-6B refers to the bottom tensile specimen machined out of the tensile bar 6 in Figure 2.3b, and also built during the first cycle of the recyclability experiment.

ANNEALING

Three tensile bars (3-3B, 3-3T, and 3-4T) in the machined state were selected for heat treatment by vacuum annealing. Sample 3-3B was annealed at 600^{o}C for 1 hour, sample 3-4T was annealed at 1095^{o}C for approximately 15 minutes, and sample 3-3T was annealed at 1250^{o}C for 7 hours to achieve a well-annealed microstructure. The respective heating/cooling cycles for samples 3-4T and 3-3T are provided in Figure 2.30 and Figure 2.31 below. Annealing was conducted via induction heating in an argon environment. Samples were placed in an alumina boat before being placed into the furnace and temperatures were measured via a thermocouple attached to the alumina crucible.

The annealed tensile specimens were tested at a crosshead speed of 0.001 in/sec until failure. Strain was recorded via a 1" MTS® extensometer attached to the sample's gage length. Reduced area (RA) values were obtained after testing by manually measuring with a caliper the widths and thicknesses of the failed specimens at the necking point.

After annealing and tensile testing, the grip sections of the annealed tensile bars were bisected along the XY plane, as shown in Figure 2.32, mounted in conductive epoxy, and polished. EBSD was used to search for grains oriented along a known set of directions (in this case the (110) directions) using ORNL HTML's JEOL 6500 scanning electron microscope and EBSD detector. Choosing grains that align to a known direction limits the amount of sample tilting required during TEM. The location of the desired grains, once found, were marked on the sample by allowing a 'scan burn' to develop in area as shown in Figure 2.33.

STEM sample foils were prepared by Focused Ion Beam (FIB) at The Ohio State University's Center for Electron Microscopy and Analysis (CEMAS). The high angle annular dark field (HAADF) STEM images of the prepared FIB foils were taken using CEMAS's Tecnai T20 instrument and are presented in Figure 2.34 and Figure 2.35. Three large precipitates are present in Figure 2.35. Two of the precipitates lie along a grain boundary while the third resides within the matrix of the foil.

2.3.2.3. Filler Bars

The filler bars (numbering 1, 2, 9, and 10 in Figure 2.3) were removed from the base plate using a band saw to cut through the support structures, sectioned into approximately 2.5x2.5x1.3cm samples (see Figure 2.36), mounted in epoxy, polished (See Appendix G), and in some cases, etched using a glyceregia etchant. The XZ planes of the samples were imaged using a LEICA optical microscope to determine porosity content and distribution in the build direction, as well as microstructure. Some of the samples were also analyzed via EBSD to gain salient information about grain size and grain shape, in addition to crystal phase and orientation.

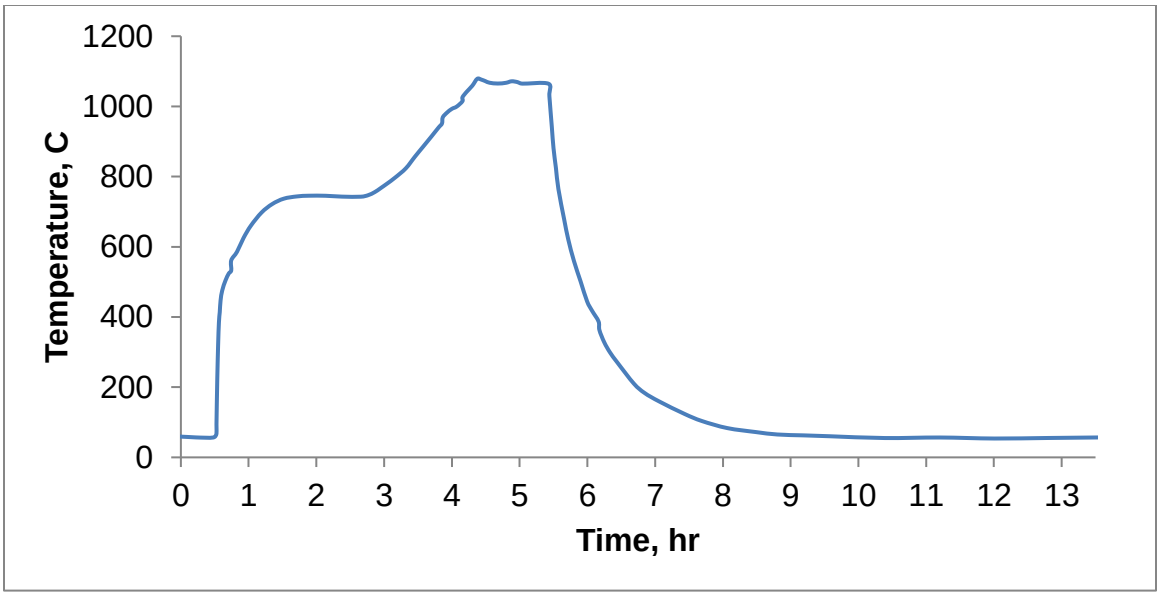

Figure 2.30: Annealing cycle experienced by tensile sample 3-4T.

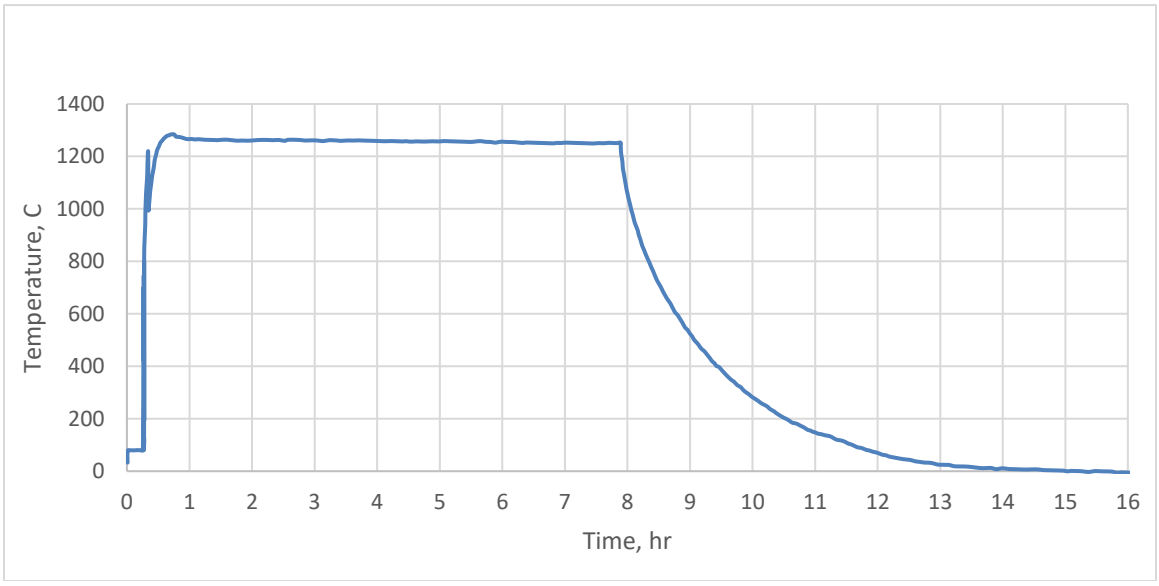

Figure 2.31: Annealing cycle experienced by tensile sample 3-3T.

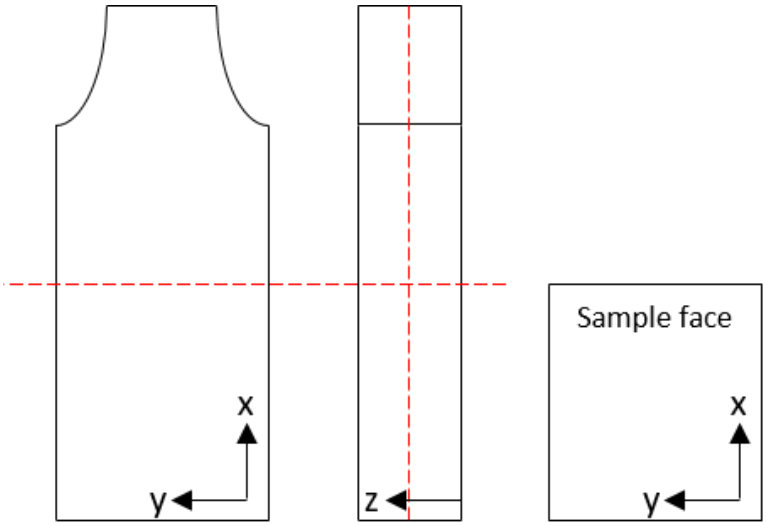

Figure 2.32: Schematic of annealed tensile bar grip section and cutting scheme.

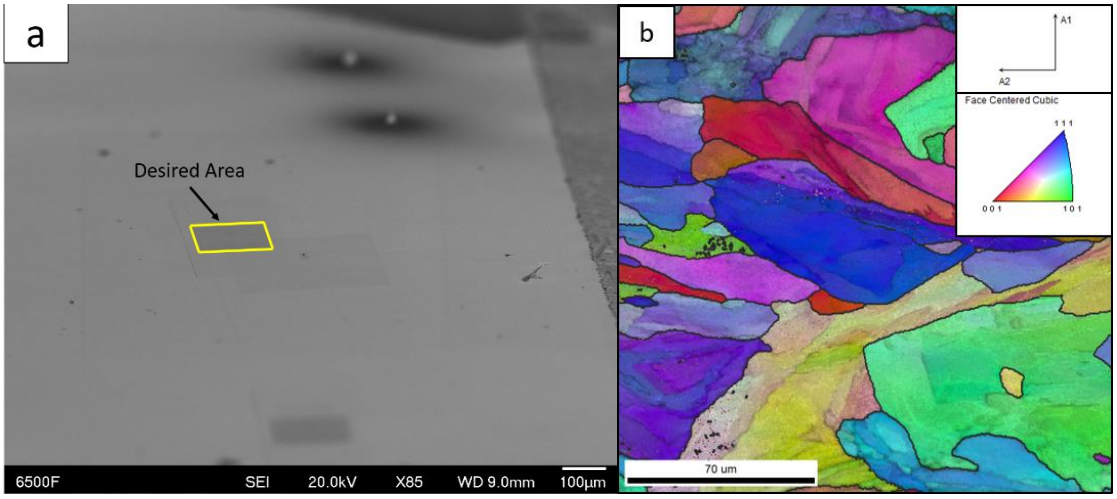

Figure 2.33: Locating area for TEM foil extraction: (a) EBSD scan of desired area and (b) inverse pole figure of scanned area. Green represents grains oriented in the desired (101) direction.

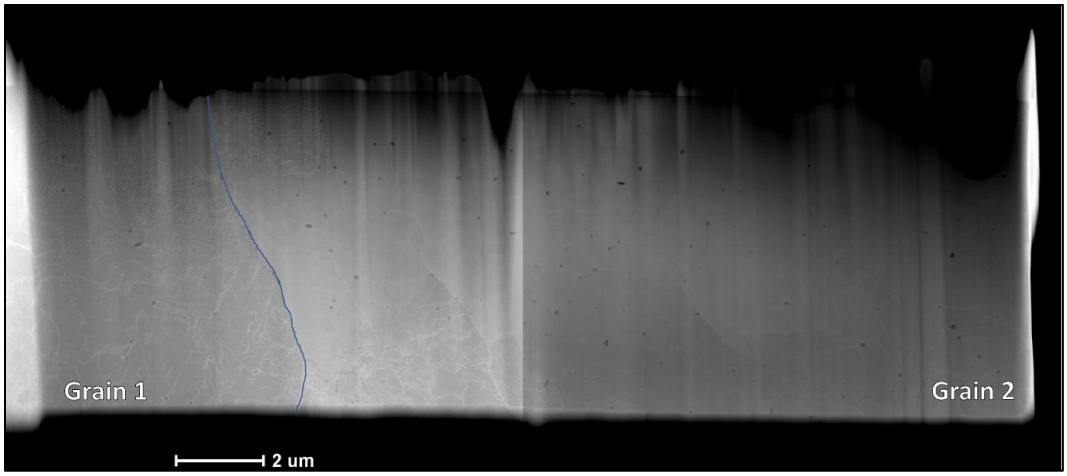

Figure 2.34: FIB foil of sample 3-4T annealed at 1095°C for 15 minutes, post-tensile test.

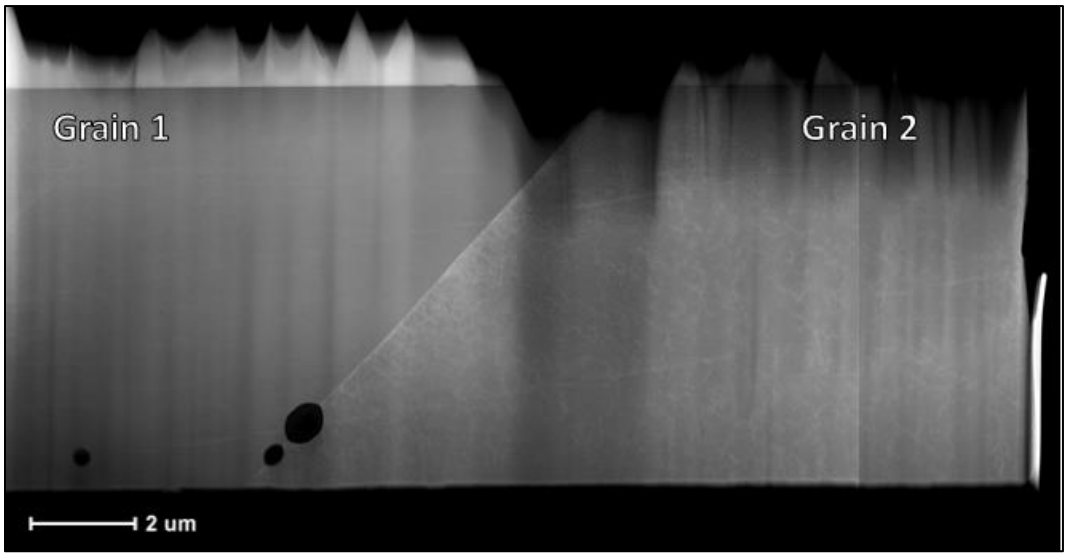

Figure 2.35: FIB foil of sample 3-3T annealed at 1250°C for 7 hours, post-tensile test.

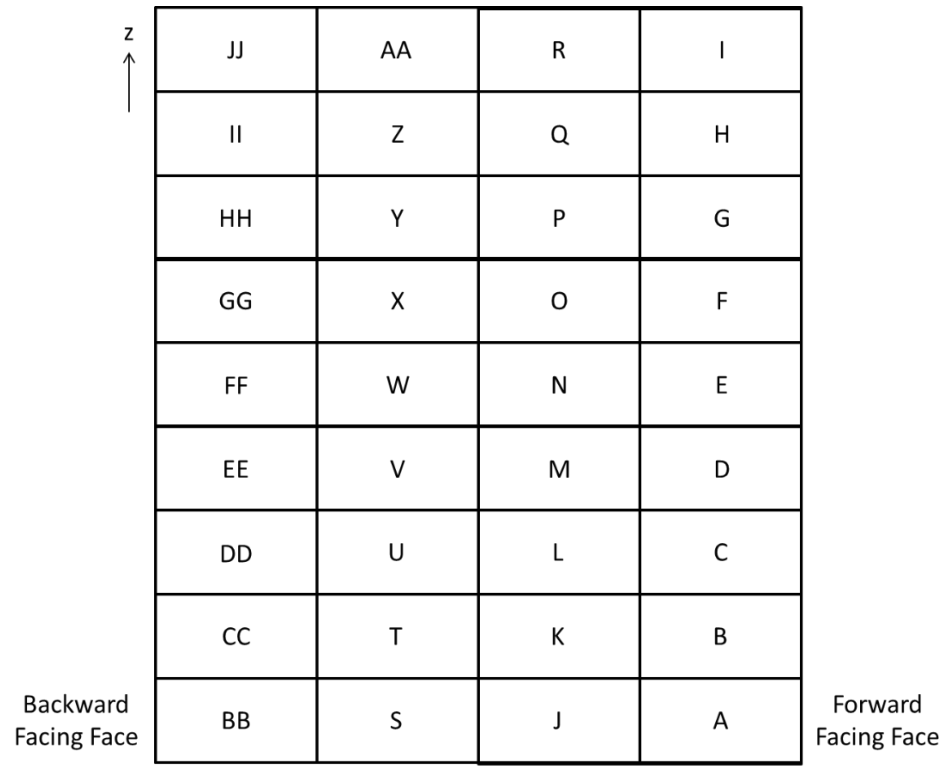

Figure 2.36: The sectioning and labeling scheme for cycle 1 filler bars. The forward facing plane faces the door of the build chamber, and the backward facing planes faces the back of the build chamber (see Figure 2.1 & Figure 2.7). z indicates the build direction and height of the part.

Figure 2.37 show a schematic of filler bar 10, built during the second cycle of the recyclability experiment. Two transmission electron microscope samples were extracted from random areas from near the center of filler bar sample 2-10K on its XZ face. The first sample was electropolished and imaged using the ORNL LAMDA facility's FEI Talos F200X S/TEM equipped with four silicon-drift detector (SDD) X-EDS system and FEI XFEG high brightness source. The second sample was extracted and polished by FIB and imaged at The Ohio State University's CEMAS center (Figure 2.38).

2.3.3. Heat Affected Zone Data Collection

Build chamber gas partial pressure was monitored and X-ray diffraction for phase analysis, laser diffraction for size distribution, bulk chemical analysis for oxygen content, and X-ray photoelectron spectroscopy for surface composition were performed on the heat-affected-zone powder samples in an attempt to identify a heat-affected-zone within the un-melted powder directly adjacent to melt zones.

2.3.3.1. X-Ray Diffraction

X-ray diffraction was performed on the 150μm, 500μm, and 5000μm channel width powder samples from the first two heat-affected-zone experiments as well as all four of the channel width/wall thickness combinations in the third heat-affected-zone experiment.

HAZ samples were analyzed using a Cu x-ray source while virgin powder was analyzed using a Mo x-ray source. To more easily compare the results resulting from two different x-ray sources (Cu, Mo), the 2-theta range of the Mo source was converted to a Cu 2-theta range using the conversion equation

$$\theta_{\mathrm{Cu}} = \arcsin\left[\frac{\lambda_{\mathrm{Cu}}^{\mathrm{avg}} \sin(\theta_{\mathrm{Mo}})}{\lambda_{\mathrm{Mo}}^{\mathrm{avg}}}\right] \quad (2\text{-}1)$$

where θ_{Cu} is the converted detection angle for a copper x-ray source, λ_{Cu}^{avg} is an average of the two Kα x-ray wavelengths emitted by the copper source, θ_{Mo} is the measured detection angle from molybdenum x-ray source XRD measurements, and λ_{Mo}^{avg} is the average of the two Kα x-ray wavelengths emitted by the molybdenum source.

2.3.3.2. Powder Size Distribution

The size distributions of powder collected from the 150μm, 250μm, 350μm, 500μm, and 1000μm channels from the HAZ2 experiment, and all four sections from the HAZ3 experiment were collected. Powder samples from the HAZ1 experiment were not measured for size distribution due to their expected similarity to powder collected from the HAZ2 experiment, but also because broken pieces of the channel wall had contaminated the 150μm channel powder HAZ1 sample.

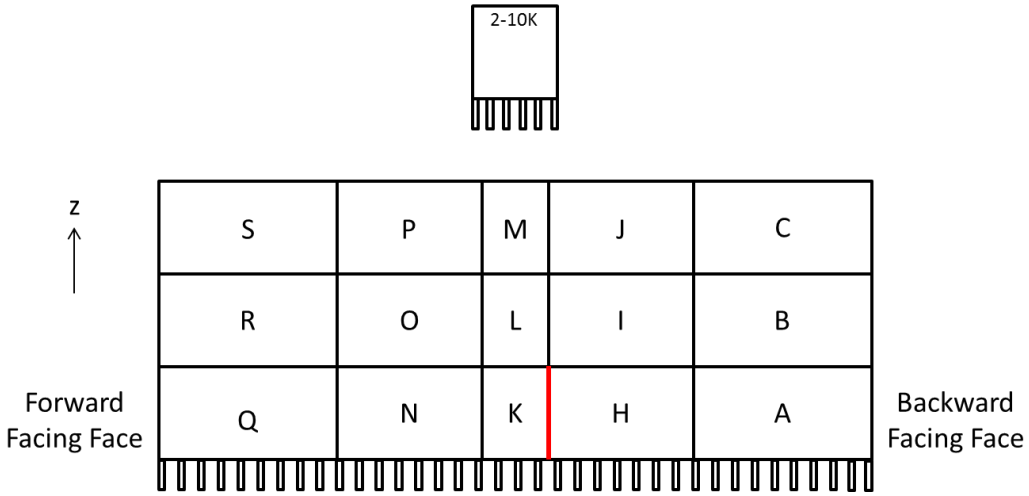

Figure 2.37: The sectioning and labeling scheme for cycle 2-10 filler bar. Of special notice is that the front and backward facing faces are reversed in this figure compared to Figure 2.36.

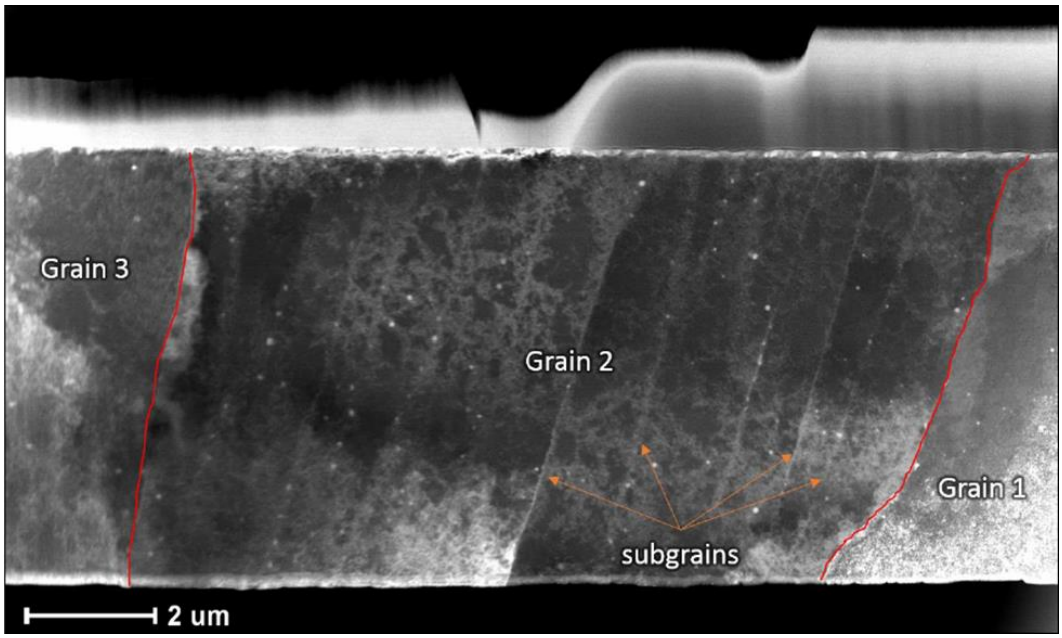

Figure 2.38: TEM foil extracted from the XZ face of sample 2-10K.

2.3.3.3. Chemical Analysis

Samples taken from powder originating in the 150µm, 500µm, and 5000µm channels from the HAZ1 and HAZ2 experiments, as well as all four of the channel width/wall thickness combinations in the HAZ3 experiment, were analyzed for bulk chemistry. Oxygen analysis results from the HAZ1 150µm channel width powder sample (see section 0) could be considered suspect if the oxygen content of the broken wall contaminants differ from that of the adjacent powder.

2.3.4. Variable Oxygen Environment Study Data Collection

2.3.4.1. Powder

After the build was complete and before removal of the part, 3.5 mL vials of powder were collected from both the downstream pile (see Figure 2.7) and the reference area of the powder bed, shown in Figure 2.11. The part was then removed from the build chamber and all of the powder collected in each receptacle was collected and labeled separately. Magnetic powder particles were separated from non-magnetic powder particles by pouring the powder from each sample onto a clean sheet of paper and manually passing a magnetic thorough the sample and removing and storing the particles that collected on the magnet, as shown in Figure 2.39. This process was repeated for each powder sample until the magnet was no longer picking up any particles.

X-RAY PHOTOELECTRON SPECTROSCOPY

Powder samples sampled from the reference area of the powder bed, shown in Figure 2.11 and magnetically partitioned were examined using XPS to differentiate between the surface chemistries of magnetic vs non-magnetic powder.

ATOM PROBE SPECTROSCOPY

Spatter powder collected from the downstream pile within the Renishaw AM250 was analyzed using atom probe tomography at The University of Sydney's Material Science department using a CAMECA LEAP 3000 Si operating in voltage mode and which has a detector efficiency of 57%. Figure 2.40 shows how the spatter was mounted and a coarse EBSD scan was used to identify FCC versus BCC particles.

Figure 2.41 shows how a focused ion beam was used to cut a wedge out of a BCC particle, which was then sectioned to create 5 APT tips.

APT tips were also created out of an FCC particle (Figure 2.42). The foil that the APT tips were created from was taken from the edge of the particle rather than from the interior (as in Figure 2.41) in an attempt to capture the thin oxide layer present on the surface of the powder. Only one tip remained unbroken throughout the data collection process. It is thought that stresses within the FCC APT samples created by the high voltage pulsing caused the bulk of the samples to crack along their grain boundaries

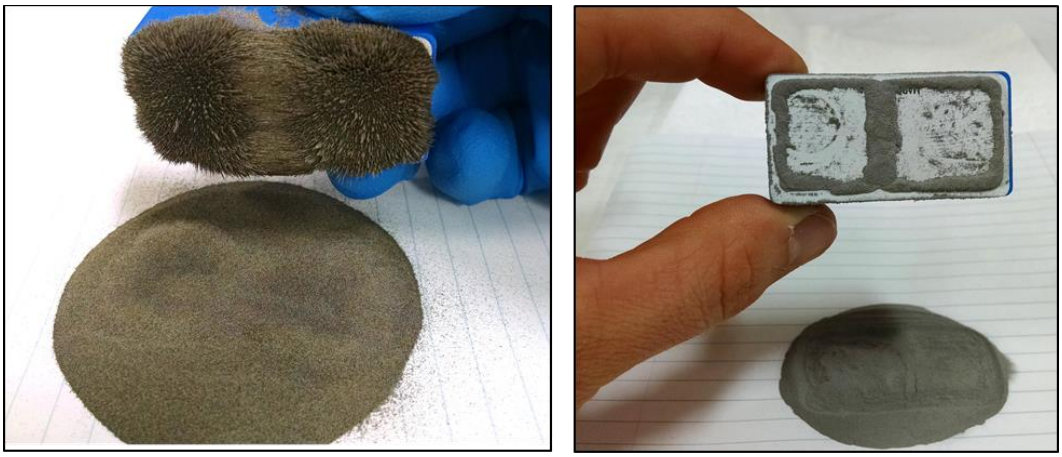

(a) (b)

Figure 2.39: (a) A first pass of the magnet through a collected powder sample compared to (b) many passes later where much of the magnetic powder has already been removed from the sample.

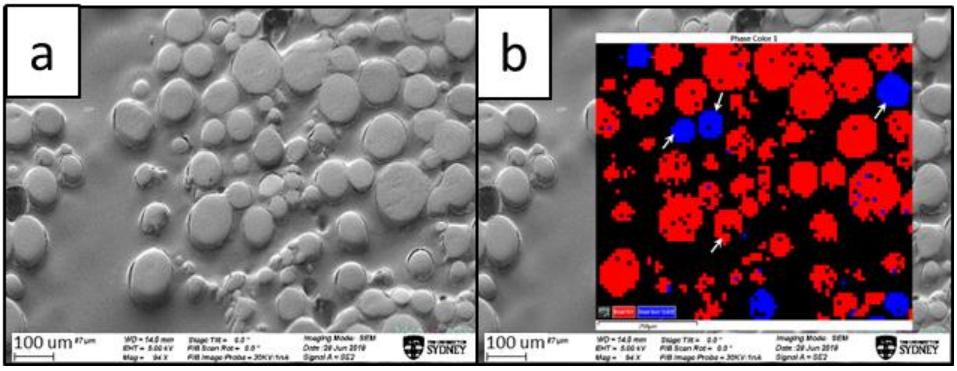

Figure 2.40: (a) SEM image of mounted and polished spatter particles. (b) Same SEM image with a coarse EBSD scan image identifying FCC and BCC particles overlaid.

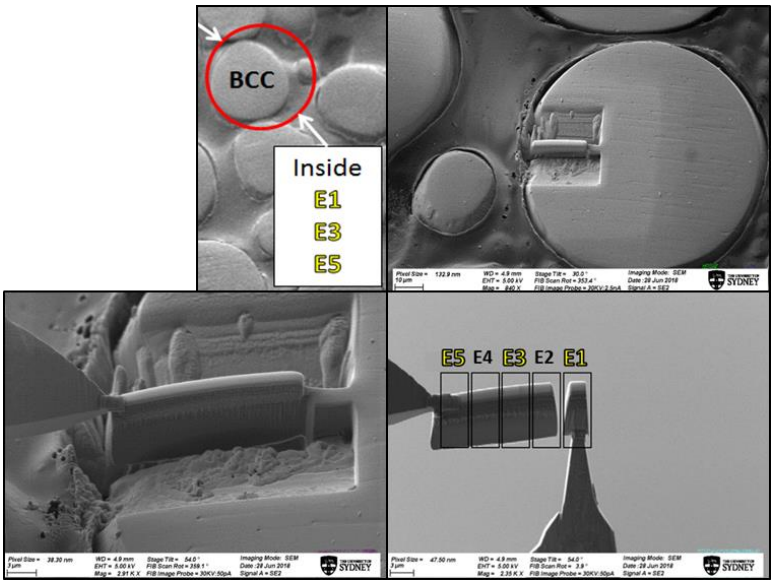

Figure 2.41: SEM images of the selection of a BCC particle for APT analysis, a top-down view of the selected particle prior to foil lift-out, connecting the Omni probe to the foil for lift-out, and sectioning of the foil prior to APT tip FIB polishing.

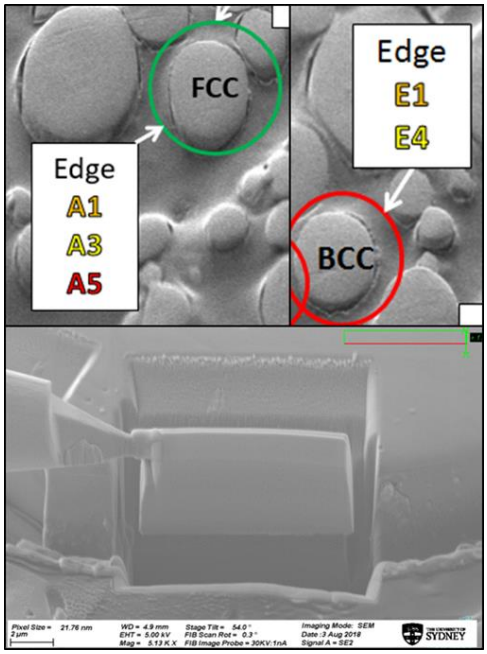

Figure 2.42: (top) SEM images of the FCC and BCC particles selected for chemical comparison. (bottom) SEM image of the lift-out of a foil from the edge of the FCC particle.

during the data collection process. This problem was not seen when collected APT data from the BCC tips because they were all single-crystal samples with no grain boundaries.

X-RAY DIFFRACTION

Powder x-ray diffraction was performed on the magnetically separated bed powder to investigate any phase differences within the powder that may contribute to their differing magnetic properties.

Single-crystal x-ray diffraction was performed on the magnetically separated spatter powder sampled from the downstream region of the build chamber. An individual BCC spatter particle was mounted in the manner of single-crystals, using a 300 μm diameter Molecular Dimensions LithoLoop with a drop of Paratone oil. A grouping of three BCC spheres was mounted in the same manner as the single particle and rotated while the diffraction data were collected.

High-temperature x-ray diffraction was also performed on the magnetically separated spatter powder sampled from the downstream region of the build chamber to investigate the phase stability of powder phases as function of temperature. Details are provided in Appendix H.

A graph depicting the entire heating/cooling cycle during HTXRD is shown in Figure 2.43. The programmed heat cycle differs from the actual heat cycle because extra collection time was programmed at the points where the heating/cooling rates changed, in case the instrument took longer than expected to reach each temperature point.

2.3.4.2. Tensile Bars

Samples 1C, 1A, 1D, 1F, 3A, and 3F were sectioned using a rotating saw and mounted in epoxy according to the cutting and mounting scheme shown in Figure 2.44. EBSD imaging was performed on the XY plane of sample 1F using the ORNL HTML's JEOL 6500 SEM microscope.

Hardness maps of the XZ and XY planes of the samples were conducted using a hardness mapping instrument. A load of 200 grams was used to indent and the indent grid parameters for each sample are shown in Table 2-5.

Tensile test pieces were machined out of tensile bars 1A, 1C, 1D, 1F, 3A, 3B, 3C, 3D, 3E, and 3F. The size of the as-built tensile bars precluded the use of ASTM standard dimensions. They were machined into custom tensile test pieces with the dimensions shown in Figure 2.45, using electrical discharge machining. Each tensile bar half produced 2 tensile test pieces, a top and a bottom specimen as depicted in Figure 2.45, which were labeled as 1A(1), 1A(2), 1C(1), 1C(2), etc., where the numbers 1 and 2 represent top and bottom respectively. Tensile specimens were tested at a crosshead speed of 0.001 in/sec until failure. Strain and stress values were recorded throughout

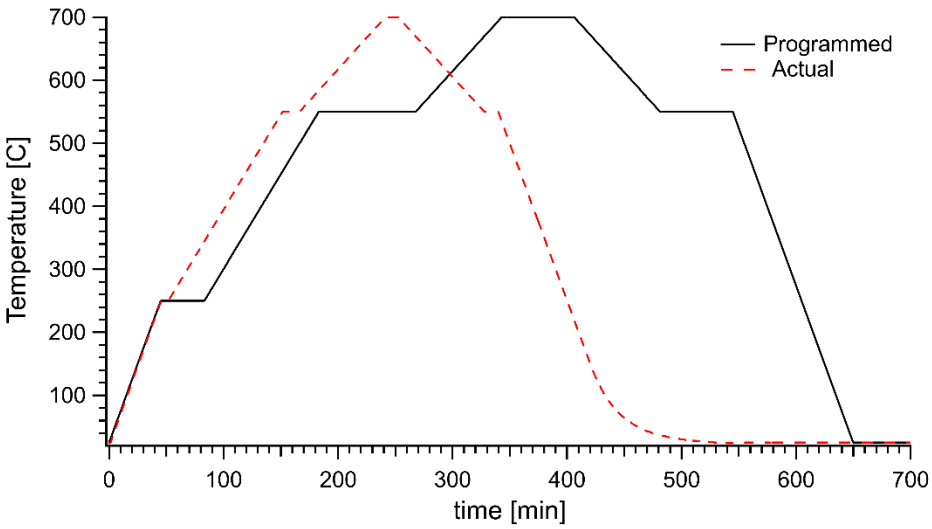

Figure 2.43: Temperature history of the high temperature powder x-ray diffraction sample during data collection.

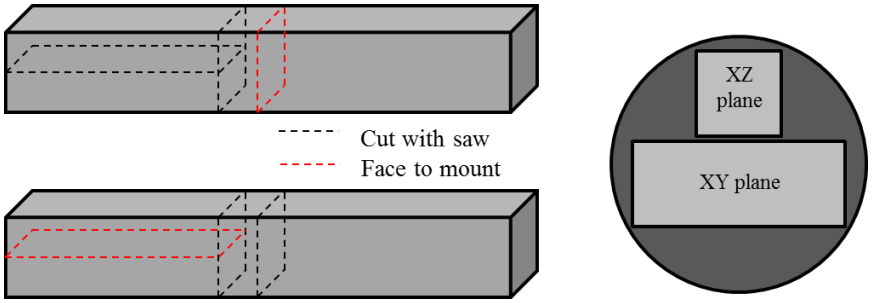

Figure 2.44: Cutting and mounting scheme for oxygen experiment tensile bar samples 1A and 3A.

Table 2-5: X & Y offset values dictating the spacing of the grid indent points for each sample tested.

	XZ Plane		*XY Plane*	
Sample	**X offset, µm**	**Y offset, µm**	**X offset, µm**	**Y offset, µm**
1C	1500	200	2000	200
1A	200	200	1925	200
1D	200	200	1950	500
1F	1500	200	1925	200
3A	200	200		
3F	1825	200	2015	200

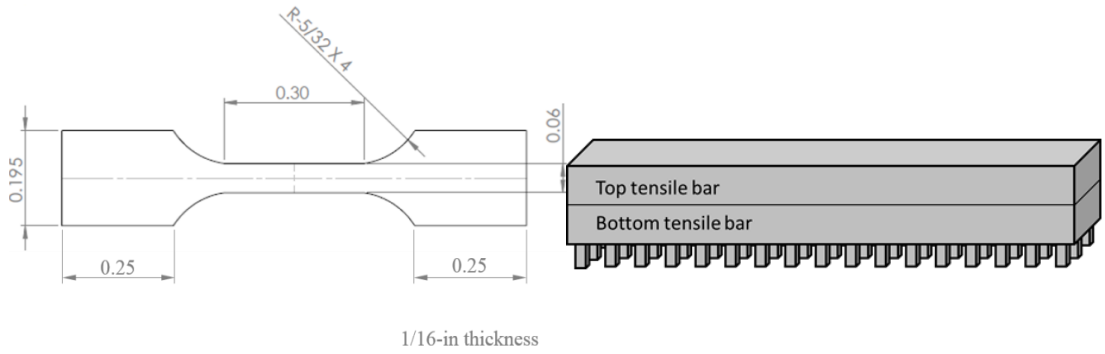

Figure 2.45: Schematic of oxygen experiment tensile bar dimensions

the testing period using National Instruments NImax sensor input software linked to custom LabVIEW software. Strain was recorded via a 1” extensometer attached to the sample’s gauge length.

A scanning transmission electron microscope foil of sample 1A was prepared by focused ion beam in the same manner as described in section 2.3.2.2. The location of the desired (110) grains, once found using EBSD, were marked on the sample by allowing a ‘scan burn’ to develop in area as shown in Figure 2.46 The high angle annular dark field STEM image of the prepared FIB foil is shown in Figure 2.47.

2.3.5. Cooling Rate Study Data Collection

For the cooling rate study experiment, in-situ IR data of the powder bed and build surfaces were collected using a custom camera setup. The setup consisted of a highly reflective mirror suspended from the ceiling of the build chamber at an angle which allowed light from the build surface to reflect up through a sapphire window and into the IR camera lens, as shown in Figure 2.48 and Figure 2.49.

The FLIR^{TM} SC800 high speed infrared (IR) camera was equipped with a 25 mm lens containing no filter. This configuration allowed for a resolution of 200 microns per pixel. For the cooling rate study, the IR camera was used to collected data during 28 layers out of the 100 build layers of the experiment (Figure 2.13). The IR camera was operated at approximately 217 frames per second (Hz) and manually started and stopped at the beginning and end of each of each build layer selected for observation.

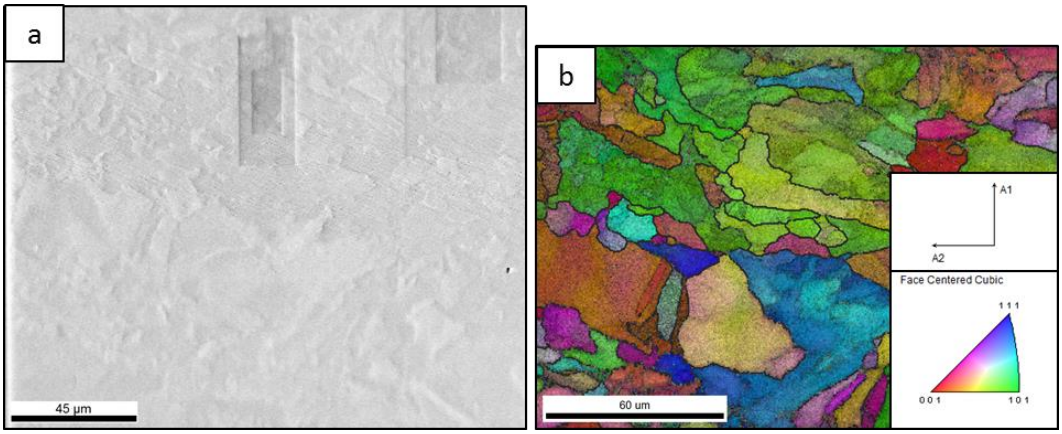

Figure 2.46: Locating area for TEM foil extraction: (a) EBSD scan of desired area and (b) inverse pole figure of scanned area. Green represents grains oriented in the desired (101) direction.

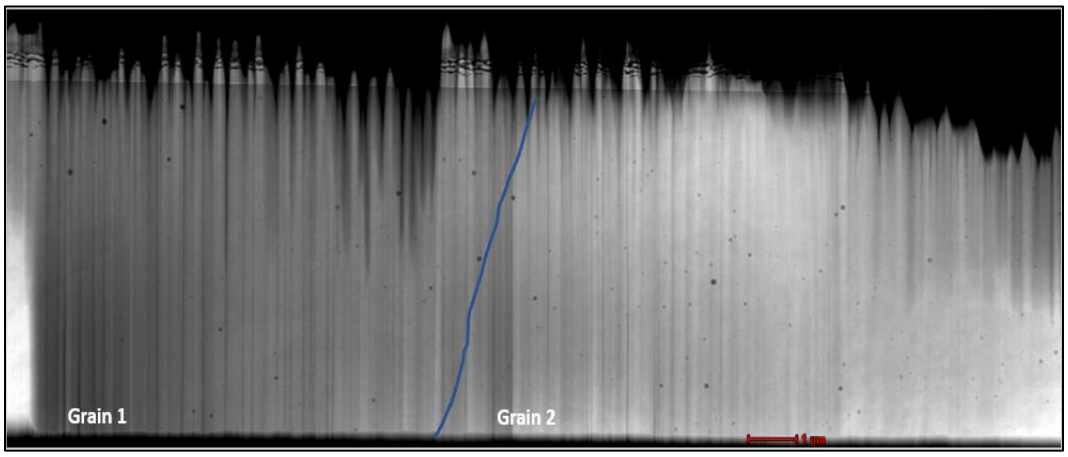

Figure 2.47: TEM foil extracted from sample 1A.

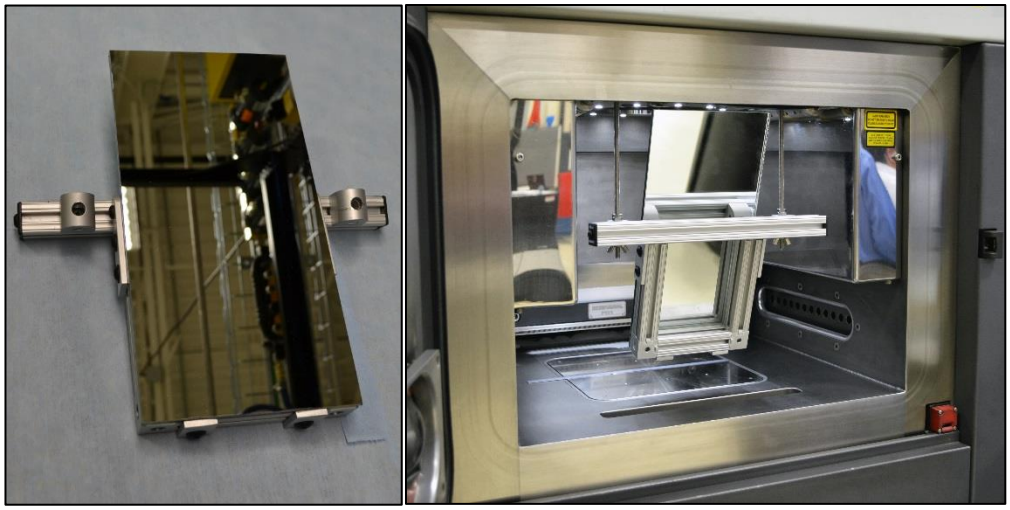

Figure 2.48: (left) Mirror mounted on aluminum frame. (right) Renishaw AM250 build chamber with mirror inserted for collection of infrared data.

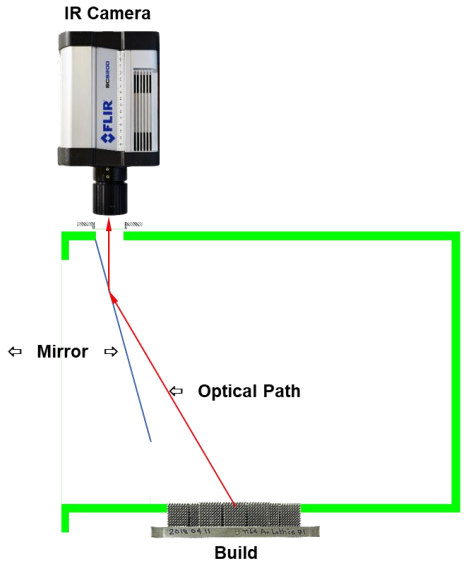

Figure 2.49: Schematic depicting the path taken by infrared light from the surface of the build, to the mirror, and into the lens of the high-speed infrared camera.

CHAPTER 3 SPATTER CHARACTERIZATION & SOLIDIFICATION RATIONALIZATION

ThermoCalc was used to conduct a Scheil calculation using the alloy composition gained from chemical analysis of both virgin powder as well as that of as-built parts. It was seen that when considering chemical composition alone under equilibrium conditions, the BCC phase never solidifies.

This chapter presents the discovery of fully single crystal BCC particles residing within samples of spatter powder as well as a rationalization as to their formation.

3.1. Spatter Characterization

Stainless steel 316L spatter powder was collected from the downstream area of the Renishaw AM250 build chamber (see section 2.2.1) after every experiment conducted in this study. These samples were fully characterized, and the data collected from characterization helped lead to a rationalization for the formation of the BCC phase.

3.1.1. Electron Backscatter Diffraction (EBSD)

The presence of the BCC phase within spatter powder samples was first observed using powder x-ray diffraction, where the presence of the BCC phase can clearly be seen in the spatter powder samples collected from downstream in Figure 3.1 compared to powder samples taken from the powder bed.

Spatter powders were then mounted in conductive epoxy and polished for observation using electron backscatter diffraction. EBSD revealed not just the presence of the BCC phase within the powder particles, but of what seemed to be fully single-crystal BCC particles. Figure 3.2 and Figure 3.3 show the relative amount of FCC and BCC phases residing in virgin powder and spatter powder respectively. Each color in the plots represents a specific crystal orientation. Each FCC particle is made up of many differently colored regions, indicating that they are polycrystalline in nature. Each BCC particle is made up of only one single color, indicating a single grain oriented in a particular direction.

A clear increase can be seen in the amount of the BCC phase in the spatter sample. It can also be seen from the sizes of some of the FCC particles in the spatter sample that some fraction of liquid spatter ejected from the weld pool solidifies as FCC. The large particle in top-center of the FCC EBSD image is too large to fit through the sieve screen used to filter out large particles before processing begins. Therefore, it must be a large particle that solidified after having been ejected from the weld pool as spatter during processing. For particles with diameters allowing them to fit through the sieve mesh, is not possible from the EBSD image to differentiate between molten then resolidified

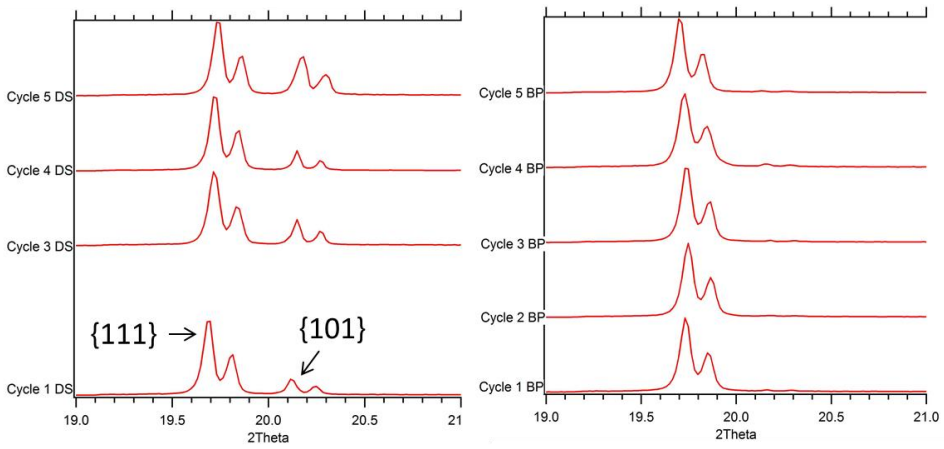

Figure 3.1: Comparison of bed and downstream powders by XRD shows slight shift to the right of peaks in the downstream powder and a slight increase in BCC phase in the bed powder as a function of reuse. Cycle 5 used a separate feedstock of highly worked powder with no known history.

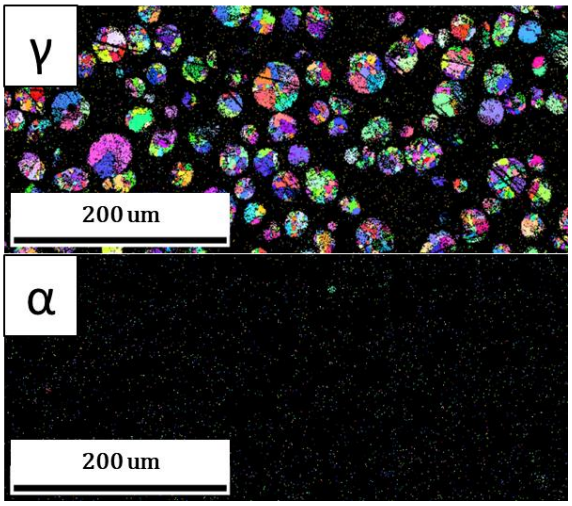

Figure 3.2: EBSD inverse pole figure images of virgin powder, mounted in conductive epoxy and polished. Virgin powder is composed almost entirely of polycrystalline austenite.

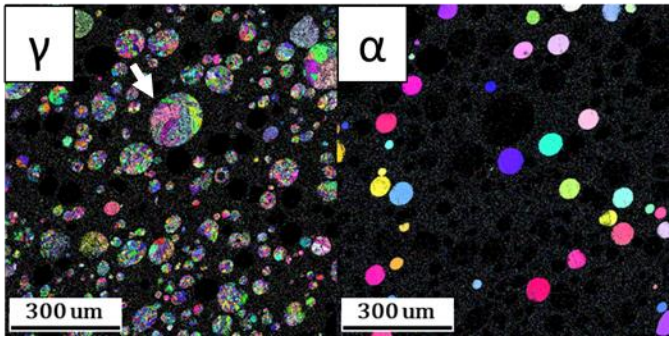

Figure 3.3: EBSD inverse pole figure images of spatter powder collected after cycle 3 of the recyclability experiment, mounted in conductive epoxy and polished. Spatter powder is composed of a mix of polycrystalline, austenitic particles and single-crystal, ferritic particles.

particles, and bed powder that was removed by pressure differentials caused by the laser melting process.

3.1.2. Single-Crystal X-ray Diffraction (SCXRD)

To confirm that the BCC particles were indeed fully single crystal and not an artifact of the 2D nature of mounted polished samples, single crystal x-ray diffraction was employed. An individual BCC spatter particle was mounted in the manner of single-crystals, using a 300 μm diameter Molecular Dimensions LithoLoop with a drop of Paratone oil, shown in Figure 3.4. Reciprocal lattice plane images were extracted from the 3D diffraction data, as shown in Figure 3.4.

A grouping of three BCC spheres was mounted in the same manner as the single particle and rotated while the diffraction data were collected. Those data and flat plate detector images were integrated to produce a 1D powder diffraction pattern suitable for analysis using the Rietveld method [28] and General Structure Analysis System (GSAS II) software package [29] to obtain the refined lattice parameter shown in Figure 3.5.

Figure 3.5 demonstrates that the BCC spatter particles are indeed single crystal with no FCC grains hiding within the particles. The Reitveld refined lattice parameter of 2.8761(3) Angstroms also shows that the BCC phase observed is a true BCC phase and not martensite.

3.1.3. High Temperature XRD (HTXRD)

To investigate the thermodynamic stability of the observed BCC phase, magnetically separated stainless steel 316L spatter powder collected from the variable oxygen environment study (see section 2.3.4) was analyzed using high temperature powder x-ray diffraction. Details of the analysis can also be found in section 2.3.4. A long scan was conducted under vacuum at room temperature both before heating and after cooling. Figure 3.6 confirms the presence of the BCC phase within the powder before heating, and the absence of the BCC phase within the sample after cooling back to room temperature.

Figure 3.7 depicts the heating portion of the thermal cycle experienced by the powder and shows that the (110) peak representing the BCC phase begins to decompose at a temperature of 550^{o}C and is largely absent by the time the sample reaches 650^{o}C. Both the (111) and (110) peaks appear to travel to the left in 2theta as the sample is heated as a result of the lattice parameters between atoms lengthening as the sample experiences thermal expansion. Both k-alpha and k-beta Cu x-ray wavelengths were used during the experiment. The presence of both wavelengths explains the split nature of the BCC (110) signature in Figure 3.7 and Figure 3.8.

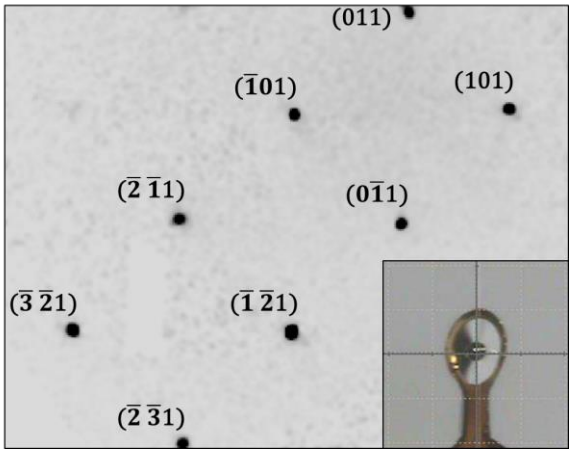

Figure 3.4: Reciprocal lattice place image of the (hk1) plane collected using single-crystal x-ray diffraction. (inset) Single BCC particle mounted in a Molecular Dimensions LithoLoop using Paratone oil.

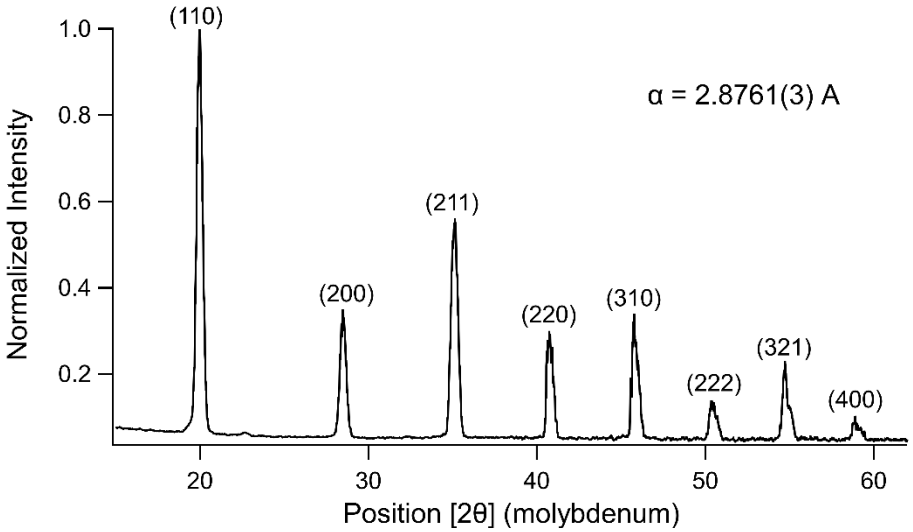

Figure 3.5: 1D artificial powder diffraction pattern created by integrating the single-crystal diffraction data obtained by rotating three single-crystal BCC particles.

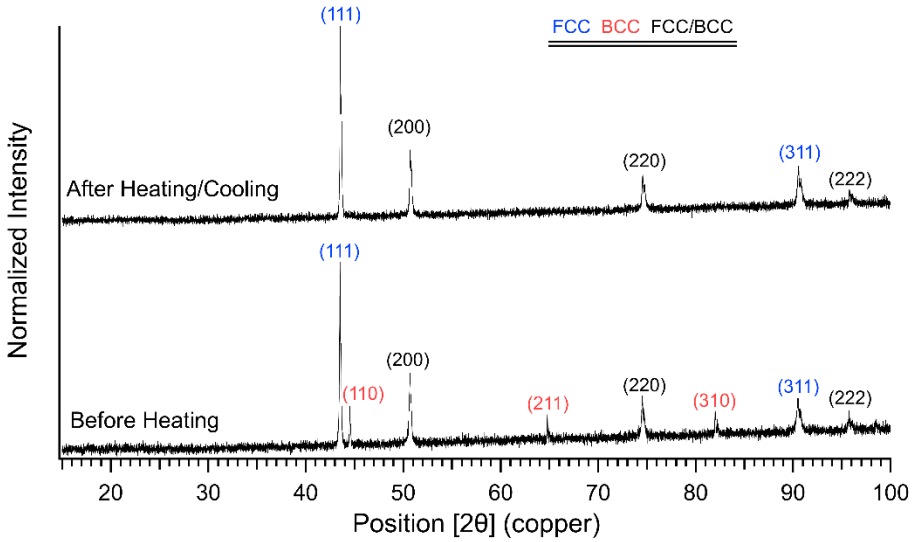

Figure 3.6: Powder diffraction pattern of magnetically separated magnetic stainless steel 316L powder before and after a heat cycle is applied.

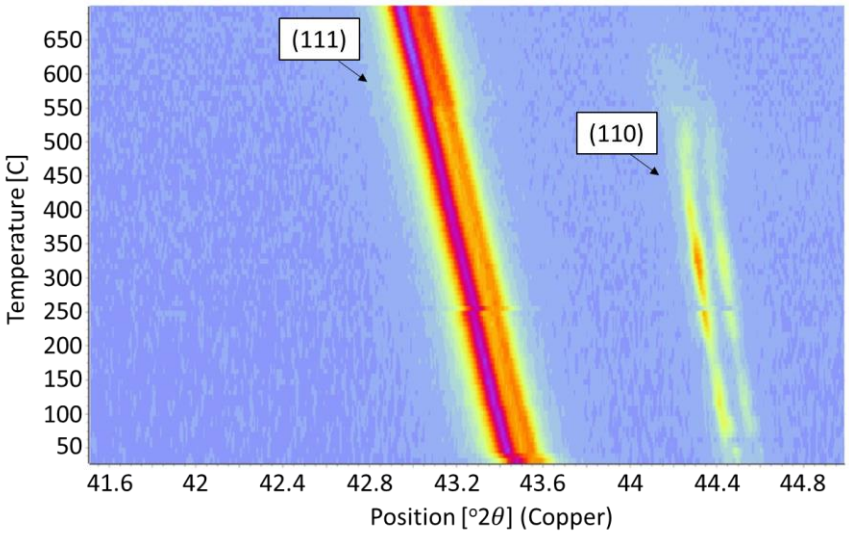

Figure 3.7: Multiple 1D powder x-ray diffraction patterns of magnetically separated magnetic powder combined and plotted as a function of temperature during the heating portion of a heating/cooling cycle.

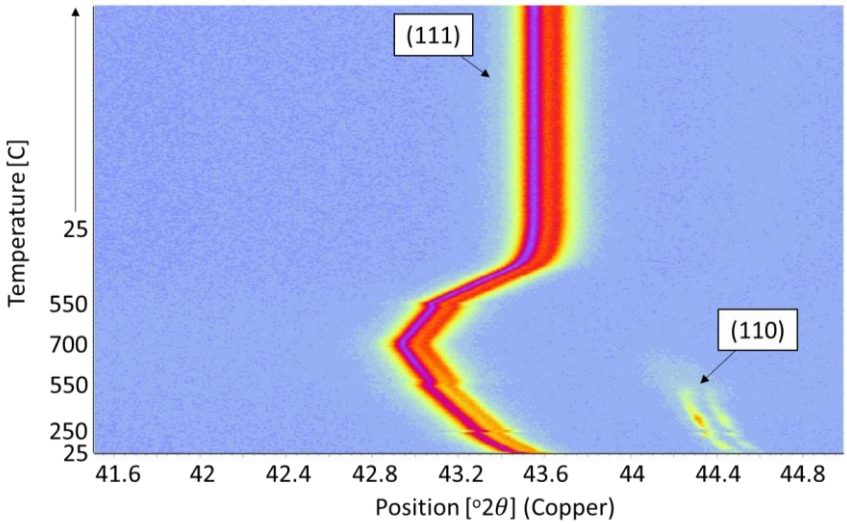

Figure 3.8: Multiple 1D powder x-ray diffraction patterns of magnetically separated magnetic powder combined and plotted as a function of temperature during the entire heating/cooling cycle.

Figure 3.8 depicts both the heating and cooling portions of the thermal cycle experienced by the powder sample. During cooling, the (110) peak representing the BCC phase does not reappear, suggesting that the BCC phase observed at room temperature and during heating was a metastable phase that transformed into FCC once the Ac1 temperature of the alloy was reached.

3.1.4. Chemical Composition

3.1.4.1. Bulk composition

The average chemical composition of the spatter powder was analyzed according to specifications laid out in ASTM E1019-11, E1019-12, E1097-12, and E1447-09. Figure 3.9 compares the chemical composition of the spatter powder with that of virgin powder and as-built parts. The only chemical differences between virgin and spatter powder are their relative amounts of oxygen and phosphorous, with oxygen being the largest mismatch.

To confirm that the high oxygen content within the spatter particles was not an artifact resulting from retained moisture at the surface of the particles, the sample was dried in an oven for 1 hour at 110^{o}C before being measured. The resulting oxygen content of the dried sample did not differ from the non-dried sample, ruling out retained moisture as the cause of increase oxygen content within the spatter powder.

3.1.4.2. Electron Diffraction Spectroscopy

Qualitative electron diffraction spectroscopy was conducted on individual spatter particles, one FCC and the other BCC to compare the local chemistry between the two phases. EBSD was used to confirm the phases of the particles before EDS was employed (Figure 3.10). Quantitative EDS data would have required the use of a known standard to calibrate against, and no known standard was available.

Figure 3.11 shows that qualitatively, there is no chemical difference between the FCC and BCC phases within the spatter particles.

3.1.4.3. Atom Probe Tomography

Because EDS was qualitative, APT was employed to quantitatively compare the composition of the BCC phase with the FCC phase in the spatter. Details of the APT data collection process can be seen in section 2.3.4.1.

The weight percents of O, C, P, Co, S, Cu, N, V, Mn, Si, and Mo were evaluated for three of five tips obtained from a BCC particle. The results are plotted in Figure 3.12. It can be seen that chemical homogeneity extends from the edge of the powder particle at least a third of the way towards the center of the particle.

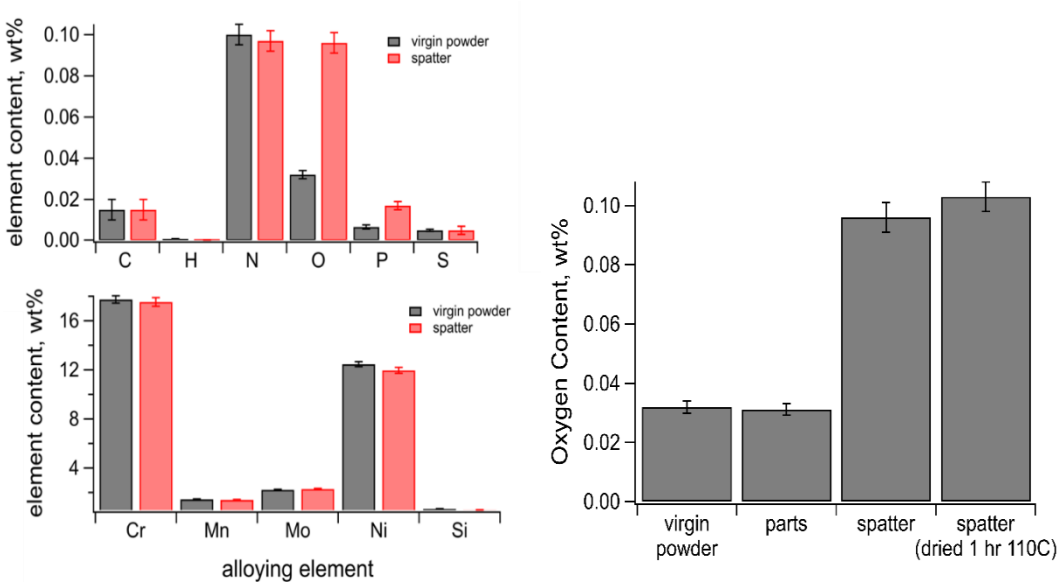

Figure 3.9: (left) Comparison of the chemical composition of virgin and spatter powder samples. (right) Comparison of the oxygen content within virgin powder, as-built parts, spatter powder, and spatter powder that has been baked in an oven to remove adsorbed water molecules.

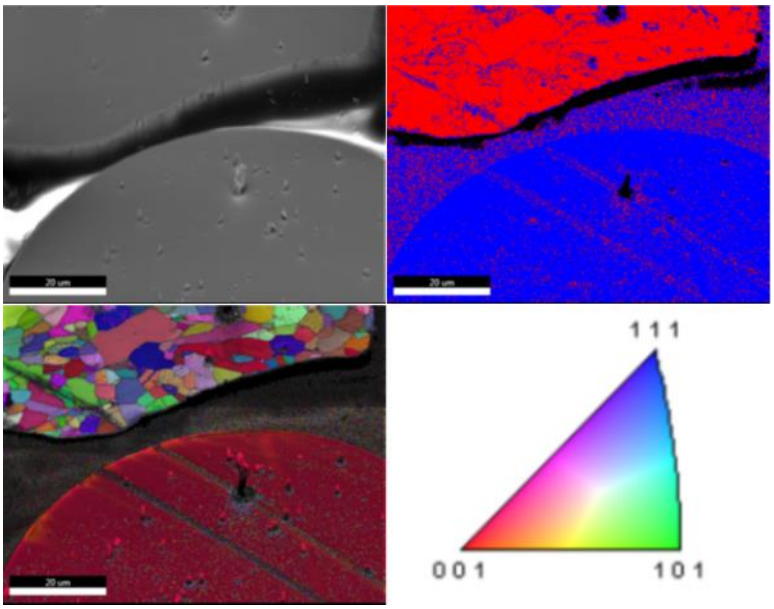

Figure 3.10: (top-left) SEM image of two powder particles selected for EDS analysis, (top-right) EBSD image of identified phases, (bottom) EBSD inverse pole figure image with associated color map.

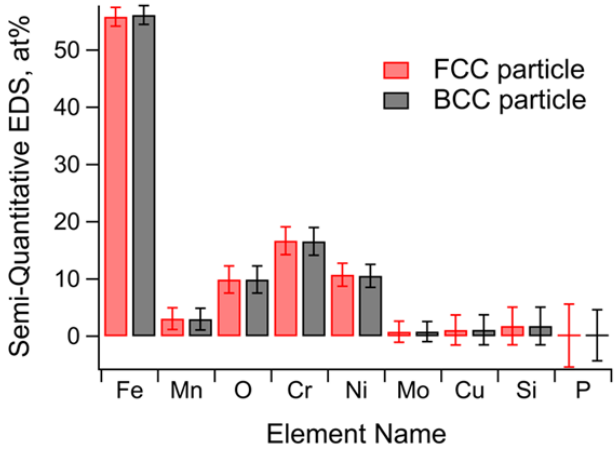

Figure 3.11: Qualitative EDS results comparing the relative chemical composition of an FCC vs a BCC spatter particle.

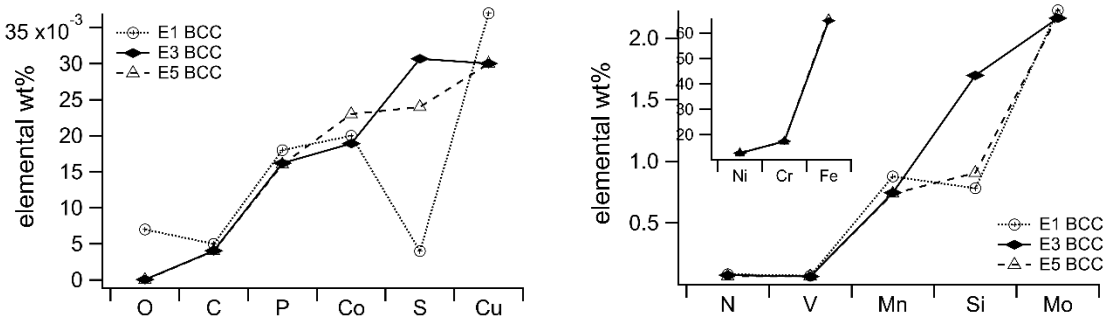

Figure 3.12: Quantitative chemical composition obtained using atom probe tomography of 3 samples taken from a single BCC particle. E1 being closest to the center of the particle, and E5 being closest to the edge of the particle.

The data collected from an FCC APT sample is compared with that of a BCC particle in Figure 3.13. No chemical difference exists between the two samples.

3.1.5. Optical Imaging

The relationship between cooling rate and dendrite arms pacing introduced in section 0 was used to estimate the cooling rate experienced by virgin powder as well as powder particles collected from the downstream area within the Renishaw build chamber. The downstream area is where the majority of spatter particles are assumed to collect during processing, having been carried there by the cover gas flow. The powder samples were mounted in a conductive epoxy, and electrochemically etched using 10% oxalic and a voltage of 6.3V for 5.5 minutes (Figure 3.14 and Figure 3.15).

3.2. Discussion

3.2.1. Oxygen Content

Palmer et. al. showed that nitrogen concentrations in pure iron samples held at high temperatures and exposed to a low-pressure nitrogen plasma increased significantly. They used this finding to explain increased nitrogen contents in welding results found in literature [30][31]. Rather than diatomic nitrogen, atomic nitrogen existed in higher than equilibrium quantities within the plasma, allowing a higher concentration of atomic nitrogen to dissolve into the iron metal/weld liquid.

It is hypothesized here that a similar effect was occurring during selective laser melting of stainless steel 316L. However instead of nitrogen, residual oxygen in the build chamber was assumed to break apart within the plasma above the weld pool and dissolve preferentially into the weld liquid. This would create an oxygen gradient with in the weld pool as shown in Figure 3.16. The oxygen rich region of the weld pool would exhibit a lower surface tension than oxygen free melt [25]. The liquid with lowered surface tension would have less resistance to being ejected from the weld pool, creating the oxygen-rich spatter observed via bulk chemical characterization.

The above is an elegant hypothesis; however, the APT experiments showed quantitatively that both the FCC and BCC particles lacked significant amounts of oxygen within their bulk. XPS experiments of powder within the powder bed (see section 2.3.1.9) suggest that much of the oxygen measured in powder samples resides in the form of oxides formed at the surface of the particle. APT experiments only measure a very small volume of material (50x50x100nm) and it is possible that the observed data is not representative of all spatter particles. It is also possible that the oxygen diffused to the surface of the molten spatter droplet in-flight and formed an oxide shell prior to the solidification of the rest of the droplet. This hypothesis relies on the assumption that the

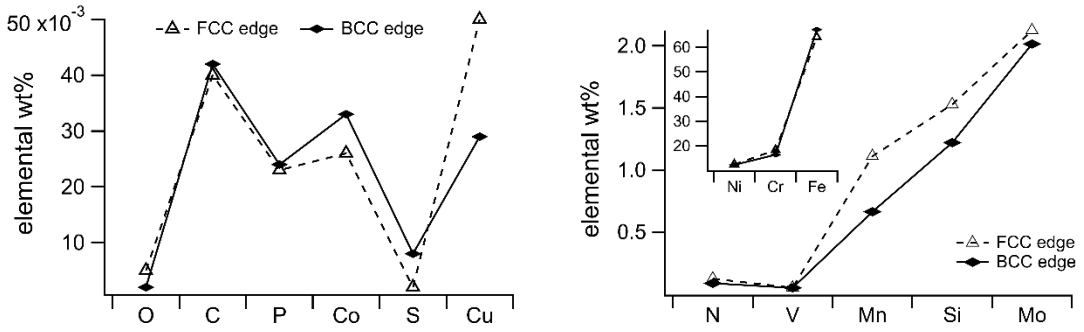

Figure 3.13: Quantitative chemical composition obtained using atom probe tomography of samples taken from an FCC and a BCC particle. Both samples were taken from as close to the edge of each particle as possible.

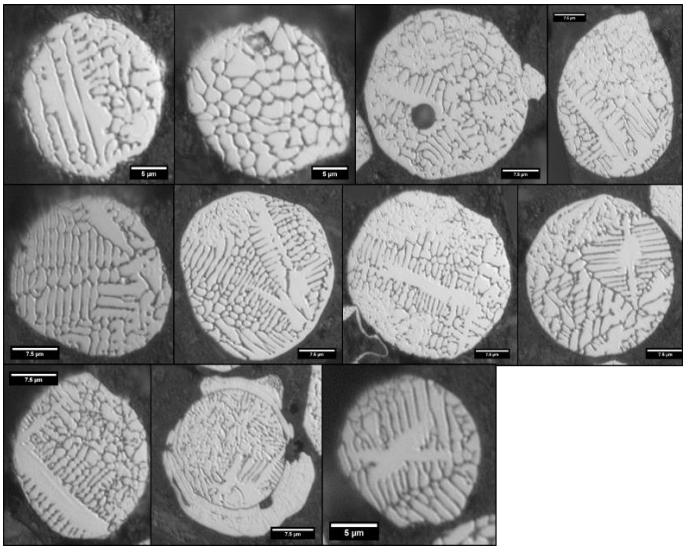

Figure 3.14: virgin powder polished and etched using 10% oxalic acid.

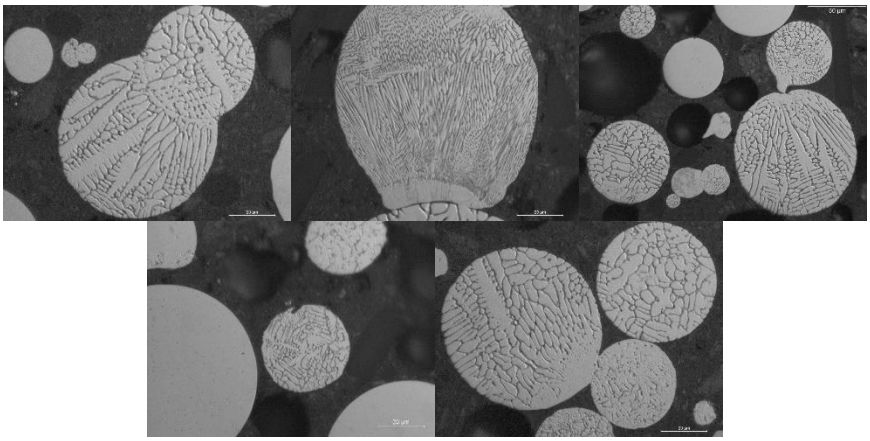

Figure 3.15: Spatter powder polished and etched using 10% oxalic acid.

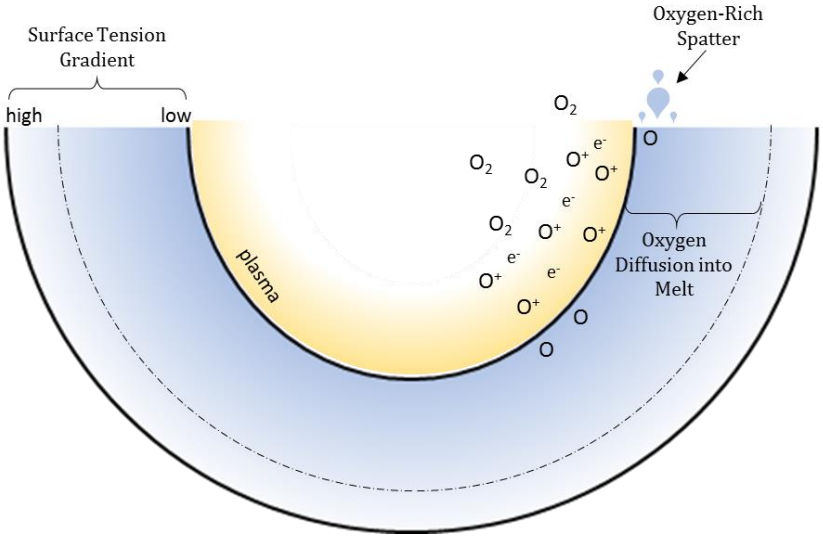

Figure 3.16: Schematic showing oxygen molecules disassociating within the plasma above a laser-induced weld pool. The resulting monatomic oxygen atoms diffuse more rapidly into the liquid melt, locally lowering the surface tension of the liquid and allowing spatter to occur.

spatter particle remains in a liquid state for at least several milliseconds, allowing enough time for all oxygen within the liquid globule to diffuse to the surface.

3.2.2. Dendrite Arm Spacing

Because single-crystal BCC particles containing no observable interdendritic solute segregation were observed, it is possible that the solidification mechanism of these particles was planar in nature. Planar solidification can take place at very low or very high solidification velocities. The range of solidification velocities possibly experienced by the spatter particles was investigated by measuring the dendrite arm spacings of the FCC spatter particles. It is assumed that FCC spatter particles experience similar cooling conditions as the BCC spatter particles.

Virgin powder and five FCC spatter particles were selected for dendrite arm spacing measurement (Figure 3.14 and Figure 3.15). The dendrite morphologies of the selected particles are different enough from that of virgin powder that the selected particles were assumed to be representative of spatter emanating from the weld pool rather than bed powder that was disturbed by pressure differentials. Between 5 and 20 PDAS and SDAS measurements were taken from each powder particle and used as inputs to Eqs. 1-1 and 1-2. The resulting calculated cooling rates for the virgin and spatter powder are plotted in Figure 3.17 and Figure 3.18. From the figures, it can be seen that for the measured dendrite arm spacings, the spatter particles potentially experienced a larger range of cooling rates when compared to the virgin powder.

Equation 3-1 demonstrates how the solidification velocity (V) can be calculated if the cooling rate (ε) and temperature gradient (G) are known. The smaller the thermal gradient and the larger the cooling rate during solidification, the larger the resulting solidification velocity.

$$V = \frac{\varepsilon}{G} \tag{3-1}$$

The temperature gradient within an ejected particle during solidification is unknown. However, a range of temperature gradients possibly experienced by the particle during solidification can be estimated based on the particle size and solidus and boiling temperatures. If solidification of the particle begins at the surface and proceeds towards the center, we can assign the liquid region of the particle a temperature value ranging from just above the FCC solidus (1635 K) all the way to the boiling point (~3000K). Equation 3-2 demonstrates how by taking the difference between an assumed liquid temperature (T_l) and the actual solidus (T_s) and dividing by the radius (r_p) of a particle, a range of thermal gradients can be calculated, as shown in Figure 3.19.

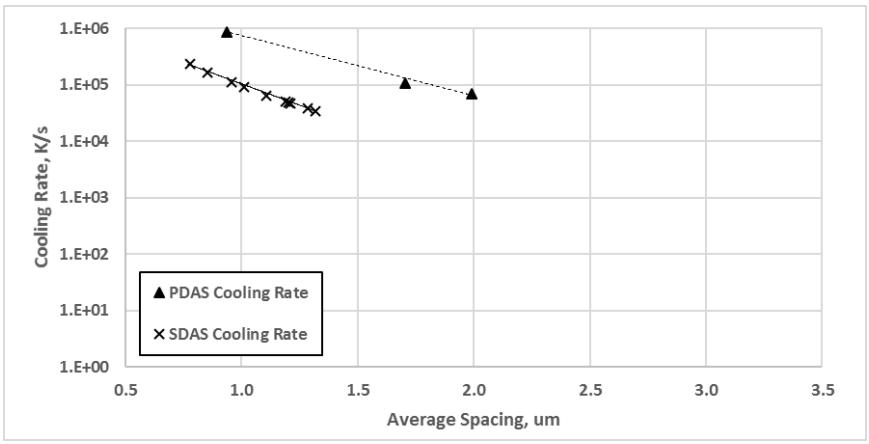

Figure 3.17: Virgin Powder Particle cooling rates (K/s) calculated from measured Primary (PDAS) and Secondary (SDAS) Dendrite Arm Spacings.

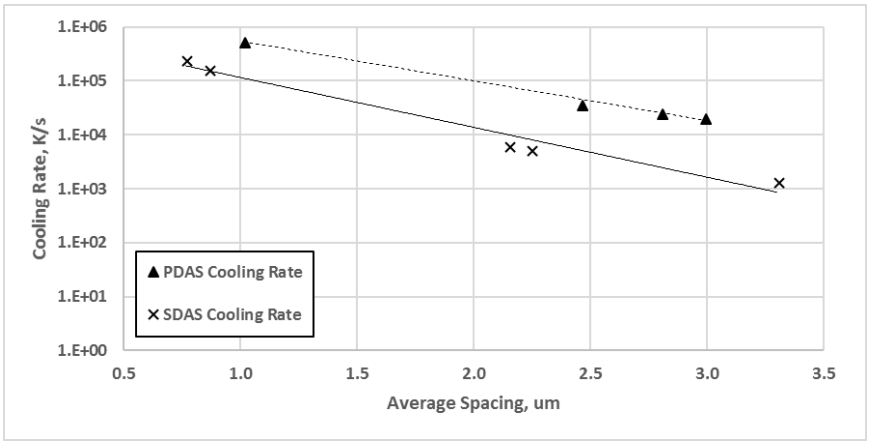

Figure 3.18: Cycle 3 DS FCC Powder Particle cooling rates (K/s) calculated from measured Primary and Secondary Dendrite Arm Spacings

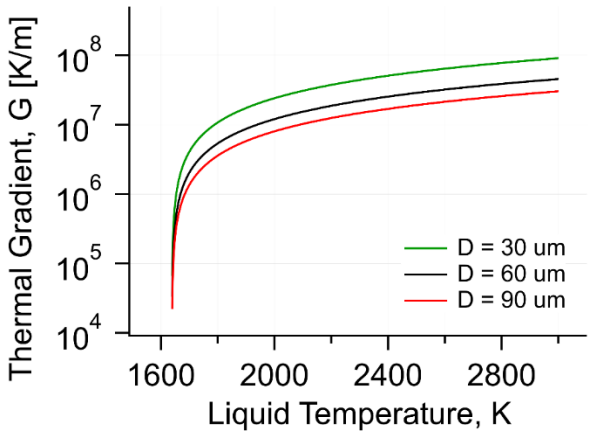

Figure 3.19: Estimated temperature gradients (G) calculated based on powder particle diameter, and possible liquid to solidus temperature difference.

$$G = \frac{T_l - T_s}{r_p} \quad (3\text{-}2)$$

Using the calculated cooling rates and estimated range of temperature gradients as inputs into Eq. 3-1, a range of solidification velocities for the spatter powder can be calculated for the spatter powder. The possible solidification velocities are plotted in Figure 3.20 and Figure 3.21.

A large range of velocities are possible based on this analysis. Solidification velocities exceeding 1 m/s are possible at thermal gradients up to approximately 1e5 K/m. High velocity planar solidification of spatter particles cannot be ruled out as part of a rationalization for the existence of single-crystal BCC spatter particles.

3.2.3. Interface Response Function

The possibility of high solidification velocities (>1 m/s) combined with the single crystal nature of the BCC spatter particles suggest that the particles may have solidified as a planar front. The KGT interphase response function was used to predict the primary solidification phase as a function of solidification velocity, using the composition obtained from the APT analysis. Code developed by Babu et al and modified by the author was used to iteratively solve for the dendrite tip/planar front temperature as a function of solidification velocity [32]. Table 3-1 and Table 3-2 show the parameters that were input into the model.

Figure 3.22 shows the output of the KGT interface response function model. BCC is predicted to form at all solidification velocities. This result is not congruent with observations since many of the spatter particles solidify as FCC. Changing the temperature gradient input only shifts the dendritic portion of the graph left or right and does not affect the calculated temperatures.

t was seen that by increasing the Gibbs-Thompson coefficient of the BCC phase by an order of magnitude, it was possible to produce a graph showing dendritic FCC solidification at lower velocities and planar BCC solidification at higher velocities (Figure 3.23).

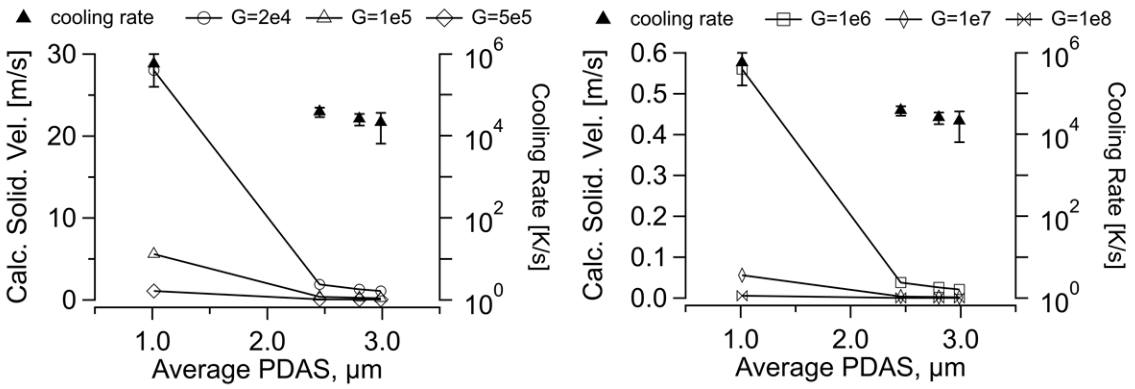

Figure 3.20: Estimated solidification velocities (V) experienced by FCC spatter particles, as a function of primary arm spacing (PDAS) and Thermal Gradient (G). Depending on the assumed thermal gradient and particle size, the estimated solidification velocity spans a large range of values (10e-3 – 10e+2 m/s)

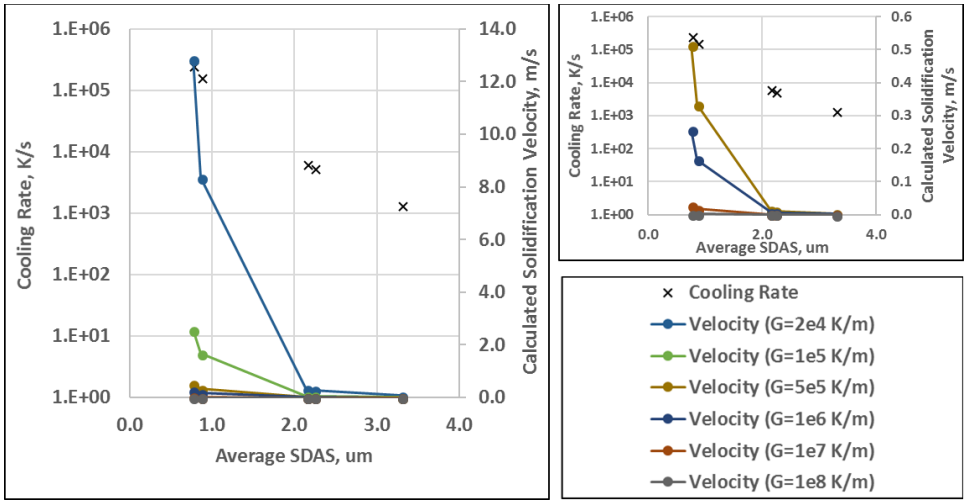

Figure 3.21: Estimated solidification velocities (V) experienced by FCC spatter particles, as a function of secondary arm spacing (SDAS) and Thermal Gradient (G). Depending on the assumed thermal gradient and particle size, the estimated solidification velocity spans a large range of values (10e-3 – 10e+2 m/s)

Table 3-1: Elemental weight fractions and associated partition coefficients (calculated using ThermoCalc) used as inputs in the KGT interface response function model developed by Babu et. al. [32]

Element	wt. fraction	partition coefficient (FCC)	partition coefficient (BCC)
Fe	6.50E-01	1.056174	1.047643
C	4.03E-05	0.256234	0.111004
Cr	1.74E-01	0.891205	1.034903
Mn	7.45E-03	0.777329	0.707756
Mo	2.16E-02	0.707863	1.138122
N	7.66E-04	0.557801	0.257526
Ni	1.28E-01	0.953171	0.724318
O	0.00E+00	0.013136	0.118146
Si	1.70E-02	0.804199	0.87937

Table 3-2: Fundamental material parameters of stainless steel used as inputs in the KGT interface response function model developed by Babu et. al. [32]

Parameter	Value
$\Gamma(\gamma)$ (m·K)	3.2×10^{-7}
$\Gamma(\alpha)$ (m·K)	2.6×10^{-7}
$D(\alpha,\gamma)$ m^2s^{-1}	5.0×10^{-9}
$\mu(\alpha,\gamma)$ $ms^{-1}K^{-1}$	10.0
$a_0(\alpha,\gamma)$ m	5.0×10^{-9}

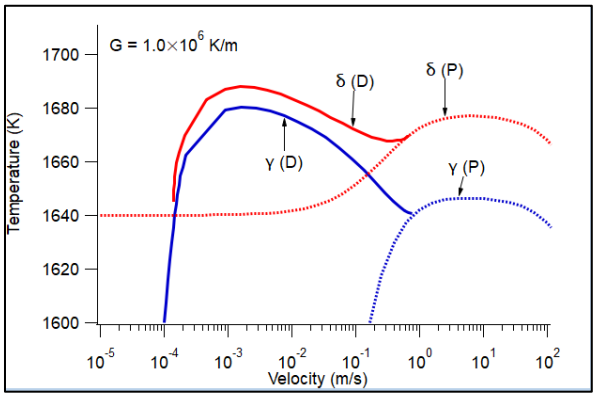

Figure 3.22: Output of interface response function model using the input values listed in Table 3-1 and Table 3-2.

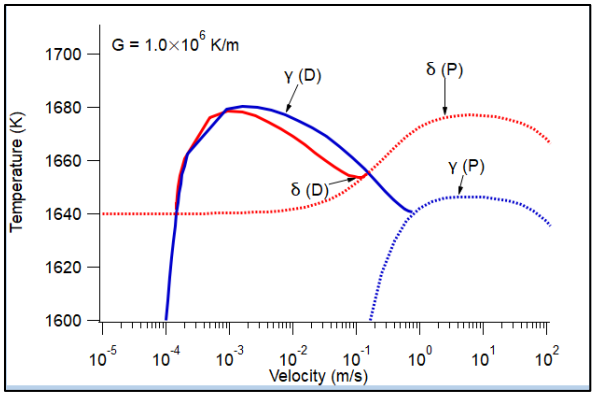

Figure 3.23: Output of the interface response function model after increasing the Gibbs Thompson coefficients of the BCC phase by an order of magnitude to 2.6×10^{-6}.

The Gibbs-Thompson coefficient is a ratio of the solid/liquid surface energy and the temperature of fusion by the solid density and latent heat of fusion. In order to understand if increasing the value of the BCC phase Gibbs-Thompson coefficient is reasonable, the Gibbs-Thompson coefficient was recalculated using surface energy, temperature, density, and latent heat of fusion values ranging from 10%, 50%, and 100% error of the values presented in Table 3-2. The results are plotted in Figure 3.24 and show that it is extremely unlikely that the default value for BCC phase Gibbs-Thompson coefficient is incorrect to the degree necessary to change the results of the interface response function to match those depicted in Figure 3.23.

3.2.4. Homogenous vs Heterogeneous Nucleation

Besides planar solidification at fast growth velocities, undercooling and nucleation kinetics could also explain the presence of single-crystal BCC particles within spatter samples. Given the appropriate conditions, a strong case can be made by which the BCC phase could nucleate and out-compete FCC growth via either homogenous or heterogeneous nucleation.

It is known that liquid melt atomization is an effective technique by which to achieve large undercoolings [33]. By dispersing the bulk liquid into small droplets, potent nucleation sites like oxides can be isolated in a fraction of the droplet population, allowing those droplets without nucleation sites to freeze at lower undercoolings. Figure 3.25 demonstrates how nucleation kinetics, undercooling, and growth velocity can combine to allow a metastable phase like BCC to form over a thermodynamically stable phase like FCC [34].

However, even in the presence of nucleating sites, Kelly et. al. calculated that in the presence of nucleating sites with large wetting angles and given sufficient undercooling, the nucleation of the metastable BCC phase is favorable over the FCC phase in 303 stainless steel. Suzuki et. al showed that the undercooling for solidification of steel on an oxide is dependent on the type of oxide used, and appeared to increase with increasing lattice misfit between the oxide and the solidifying phase [35].

Sufficient evidence exists in literature to contemplate homogeneous or heterogeneous nucleation to explain the formation of metastable BCC particles during the selective laser melting process of stainless steel 316L.

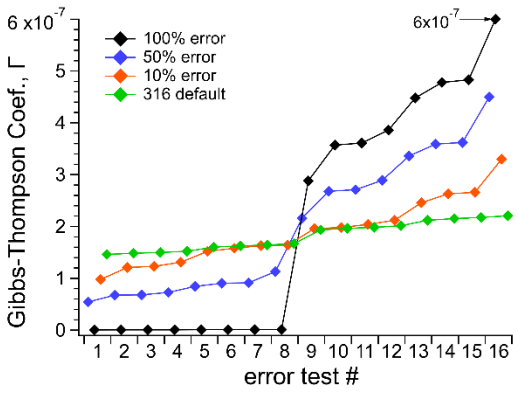

Figure 3.24: Error study of the Gibbs-Thompson coefficient for the BCC phase of stainless steel 316L, assuming 10%, 50%, and 100% error in the default parameter values that make up the coefficient.

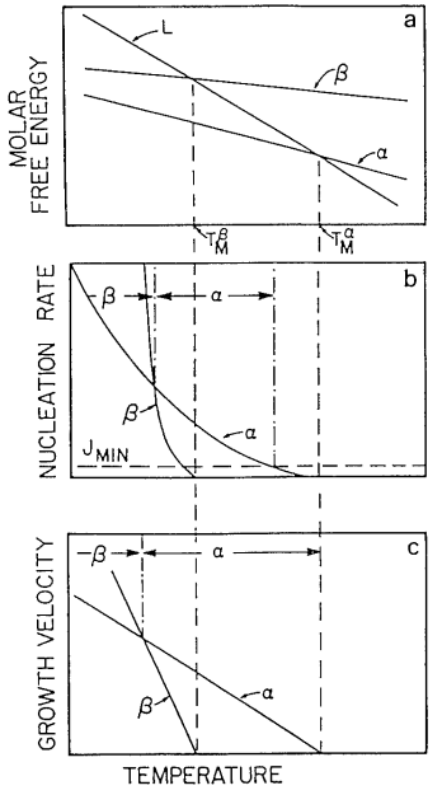

Figure 3.25: Schematic representation of competitive kinetics which favor the formation of a metastable phase β from the liquid L at low temperature in spite of (a) the thermodynamic stability of α. The temperature range for faster nucleation of the β-phase is shown in (b). The temperature range for faster growth of β is shown in (c) [34].

3.3. Conclusions

During selective laser melting processing of stainless steel 316L, an unusual phase and microstructure was discovered to exist among a fraction of the re-solidified spatter particles ejected from the melt pool during processing. The unusual phase was ferrite (BCC) and the microstructure was single-crystal spatter particles. In welding literature 316l steel almost always solidifies as primary austenite (FCC), and very high cooling rates are required in order for it to solidify as primary BCC. When it does solidify as primary BCC, the microstructure is never single crystal/non-dendritic. Also, in welding literature, BCC is always accompanied by the FCC phase to some extent. In this chapter, the single-crystal, BCC particles were characterized, and their formation mechanism was rationalized. Conclusions reached were as follows:

1. Inspection of FCC spatter particles' dendrite arm spacings revealed that fast solidification velocities (>1m/s) may exist, that are adequate to drive a planar solidification front (most likely accompanied by solute trapping).

2. An interface response function model developed by Kurtz, Giovanni, and Trivedi, and codified by Babu et. al. was implemented to see if the modeled primary solidification phase matched with what was observed experimentally. The model unrealistically predicted dendritic BCC solidification at low solidification rates, and planar BCC solidification at higher solidification rates. This is unrealistic considering that, as a number percentage, more spatter particles were observed to be composed of FCC grains than BCC grains.

3. The KGT model does not consider nucleation kinetics. It is hypothesized that the spattering mechanism during SLM processing allows for the dispersal of bulk liquid into droplets, some of which do not contain potent nucleation sites like oxides, which allows the liquid droplet to supercool to temperatures where the metastable phase can out-nucleate or out-grow a more thermodynamically stable phase.

4. The presence of an oxide shell surrounding the BCC spatter particles may also have influenced undercooling to temperatures allowing for heterogeneous nucleation of the metastable phase to out-compete that of the thermodynamically stable phase.

CHAPTER 4 DISCOVERY & MODELING OF POWDER BED HEAT-AFFECTED-ZONE

A gap currently exists in literature relating to local effects of the selective laser melting process on unmelted powder residing in the powder bed. A novel heat-affected-zone experiment was conducted to investigate any local property changes in the powder bed as a function of distance from a melt region during selective laser melting process of stainless steel 316L. Powder samples were characterized using a variety of techniques and a simple thermal cycle model based on Rosenthal's heat transfer equation was developed and used as an input to a DICTRA oxidation model. The model was compared against the data collected from the experiment. This experiment identified powder particle oxidation to be the primary mode of modification to the remaining powder bed during selective laser melting. The knowledge gained from this experiment would be beneficial in the design of future powder re-use experiments for laser powder bed additive manufacturing.

4.1. Results

Any changes in powder size distribution, chemistry, or phase fraction within the unmelted powder bed as a function of distance from a melted region was investigated and the results presented here. A description of the experiment setup and procedure is provided in section 0. A description of the data collection methods is provided in section 2.3.3.

4.1.1. Variations of Oxygen Partial Pressure During SLM

The partial pressure of oxygen inside the build chamber of the Renishaw AM250 varied as a function of time. At the start of a build O2 values of around 800 ppm and a chamber gas pressure of 20 mbar were typical. The corresponding oxygen partial pressure at this chamber pressure and oxygen ppm content was calculated to be 0.016 mbar. Due to a small leak in the system, the chamber gas pressure began at 20 mbar and slowly decreased to 6 mbar over the course of a couple of hours. Once 6 mbar was reached, the Renishaw would introduce fresh argon into the build chamber and the chamber pressure would correspondingly jump back to 20 mbar before slowly decreasing back to 6 mbar. Because of the periodic variance in the chamber gas pressure, the O2 partial pressure also cycled between 0.016 and 0.0048 mbar until about 6 hours into a build. At about 6 hours, the machine's oxygen sensors generally read 0 ppm oxygen and an oxygen partial pressure could not be calculated.

The calculated O2 partial pressures throughout the entire build for each HAZ experiment are given in Figure 4.1. The average O2 partial pressure experienced by the powder during each experiment is also given in the legend of Figure 4.1 and generally agrees between the three builds. O2 partial pressures can vary between builds but.

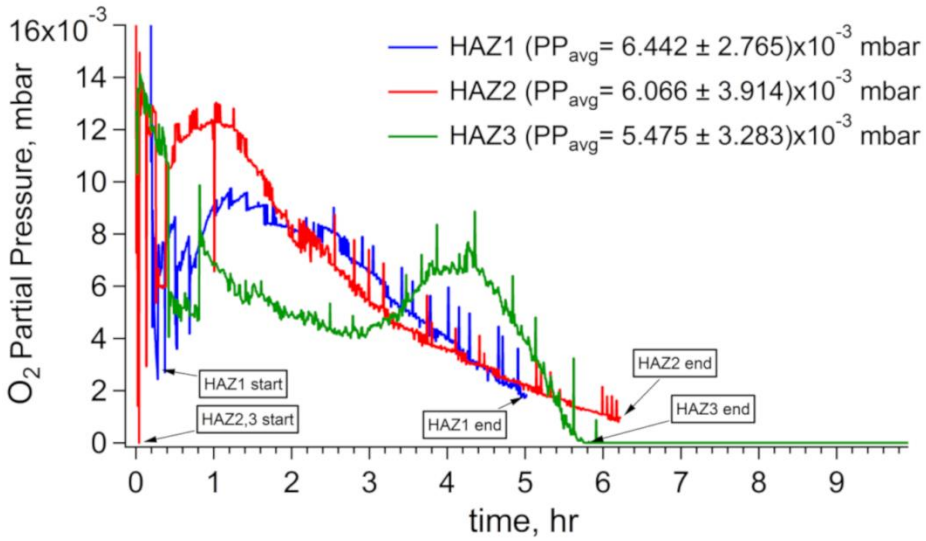

Figure 4.1: Bottom oxygen sensor values and the corresponding calculated oxygen partial pressures in an otherwise pure argon environment during processing of the three heat-affected-zone experiments.

generally stays below 0.015 mbar (1.5 Pa) due to the manually set limit of 0.02 mbar (2.0 Pa). If the Renishaw AM250 detects an O2 value greater than 0.02 mbar, it automatically pauses the SLM process and enters into vent and backfill mode until the recorded ppm value falls below 0.02 mbar. This vent and backfill cycle is evident in Figure 4.1 at the beginning of each of the HAZ experiments. HAZ1 and HAZ2 O2 partial pressures both follow a typical decrease of measured O2 over time assumed to be brought on by gettering of oxygen by the SLM material, reactions of oxygen with evaporated metal species, and the periodic introduction of argon into the chamber to bring the chamber pressure back to 20 mbar once it falls below 6 mbar. The HAZ3 O2 partial pressure exhibits an atypical rise in oxygen partial pressure at around the 3-hour mark before resuming its decrease at around the 4.3-hour mark. It is hypothesized that the initial increase in oxygen partial pressure in all three of the HAZ experiments is due to oxygen introduced from the powder hopper as it dispenses fresh powder for each new layer. Over time, all of the oxygen that was trapped in the powder within the hopper is released and O2 partial pressures are allowed to decrease again. This explanation could also explain the atypical O2 partial pressure curve observed for the HAZ3 experiment. In this case, trapped oxygen from powder within the hopper could have been released partway into the build rather than entirely at the beginning.

4.1.2. Chemical Analysis

4.1.2.1. HAZ1 & HAZ2 Chemistry

Excepting the 150µm data point from the first HAZ experiment (due to possible contamination by broken wall pieces) the oxygen content measurements from the HAZ1 and HAZ2 samples provide evidence for reproducibility within the error of measurement. Figure 4.2 shows that the powder oxygen content (wt %) decreases as a function of channel width, with a measurable increase in powder residing in the 500µm wide channel and no measurable increase in powder residing in the 5000µm wide channel. The data from these three channel spacings was deemed sufficient and the powders from the other channel width spacings were not chemically tested for oxygen content.

4.1.2.2. HAZ3 Chemistry

The HAZ3 experiment varied the channel wall thickness between 150µm and 2000µm and the channel widths between 150µm and 5000µm. Figure 4.3 shows that the thickness of the channel walls in the HAZ3 experiment did not affect the measured oxygen content of the un-melted powder within the channels themselves.

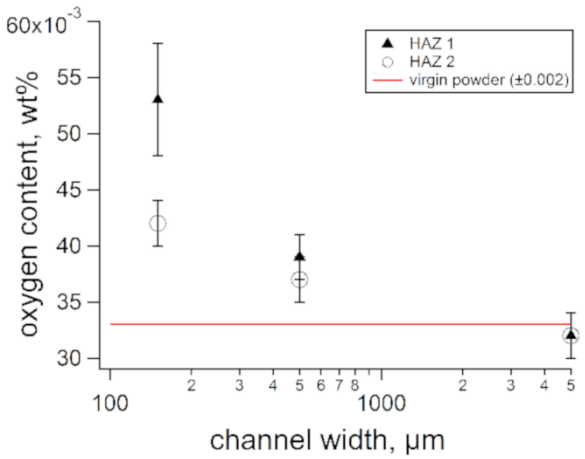

Figure 4.2: Unmelted powder oxygen content (wt %) as a function of channel width between melted walls.

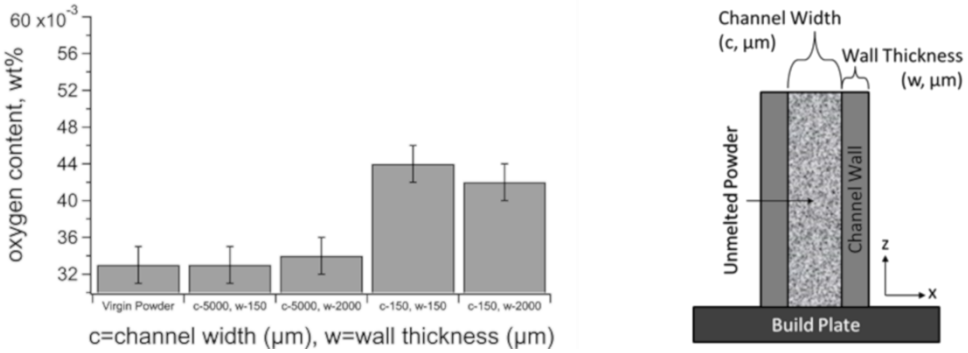

Figure 4.3: Bulk chemical analysis of powder samples taken from several sections of the third heat-affected-zone experiment. Error values of ±0.002 wt% were provided by Luvak Laboratories.

4.1.3. X-Ray Diffraction

Figure 4.4 shows the XRD results of powder samples from the virgin powder and all three heat-affected-zone experiments. All of powder samples revealed fully austenitic phase and no detectable evidence for any other phases. The bimodal peaks present in these plots correspond to the slightly different wavelengths of the x-ray radiation given off by the Cu and Mo diffractometer x-ray sources. Both Molybdenum and Copper sources each emit two characteristic k_α x-rays at differing wavelengths. The data obtained from the Mo x-ray sources was converted to Cu source values using Eq. 2-1 to facilitate comparison between the virgin powder and the HAZ experiments powder samples. The difference in peak shape between the virgin powder and HAZ powder diffraction patterns can be attributed to the difference in detector resolution between the two machines used to collect the data.

4.1.4. Powder Size Distribution

Figure 4.5 and Figure 4.6, and Table 4-1 and Table 4-2 show the powder size distribution data obtained from laser diffraction measurements from selected channels of the HAZ2 and HAZ3 experiments. A slight coarsening seems to be present in HAZ2 samples from channel widths of 150, 250, and 1000μm, and a widening of the powder size distribution exists in samples from channel widths of 250, 500, and 1000μm. The powder size distribution average is slightly smaller in the HAZ3 samples when compared to virgin powder. It is worth noting that all powder sample size distributions were only measured once, with an assumption that the uncertainty related to sampling procedures are minimal.

4.1.5. X-Ray Photoelectron Spectroscopy

Even though the depths associated with the XPS measurements shown in Figure 4.7 are calibrated using SiO_2 films instead of stainless steel, the qualitative results can be analyzed to understand aspects of the powder samples' surface chemistry. In Figure 4.7 (a-d), virgin powder contains a higher percentage of iron associated with iron oxides than do the HAZ2 and HAZ3 powder samples. Conversely, the HAZ2 and HAZ3 powder samples contain a higher percentage of chromium associated with chromium oxides than does the virgin powder sample (Figure 4.7 (a-c, e)).

Interesting peaks in Figure 4.7 (a-e) are present at distances several nanometers below the surface of the powder particles. These peaks are likely an effect of the sample surface morphology, namely that the samples are not flat but are instead composed of many spheres packed closely together. When the argon-ion beam first begins to sputter away material, what is measured is surface data of the particles. Because of the powder particles' rounded surfaces and the 45-degree angle at which the ion-gun is situated relative to the sample, individual powder particles can "shade" adjacent particles

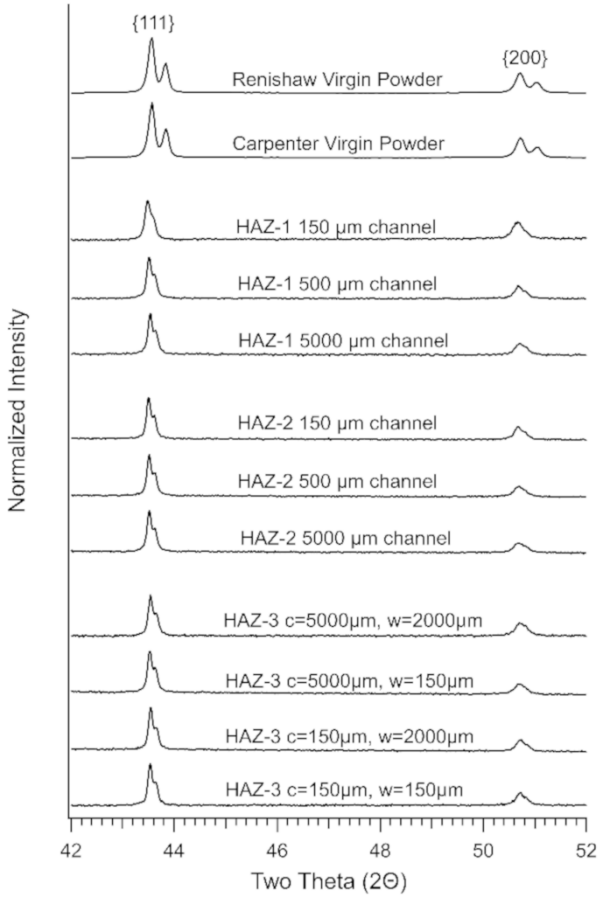

Figure 4.4: X-ray diffraction peaks of virgin powder and powder samples collected from the HAZ1, HAZ2, & HAZ3 experiments. FCC crystal structures were seen with no evidence of additional phases. A Mo x-ray source was used to collect the virgin powder data and a Cu x-ray source was used to collect the HAZ experiments data. c=channel width, w=wall thickness.

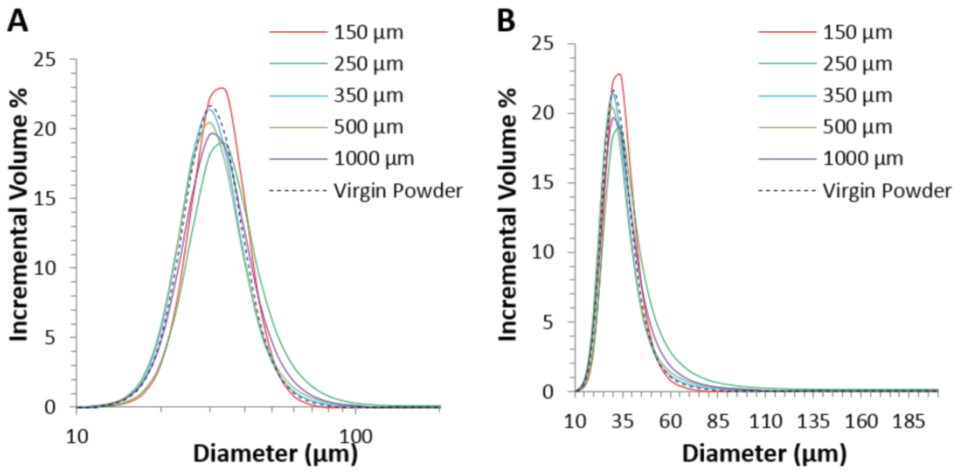

Figure 4.5: Laser diffraction results for samples collected from the HAZ2 experiment, compared to virgin powder. Presented here in log (A) and linear (B) forms.

Table 4-1: Median, mean, mode, D(v,0.1), D(v,0.5), and D(v,0.9) values for the powder size distribution samples from the HAZ2 experiment.

HAZ_2 Channel Width (µm)	Median (µm)	Mean (µm)	Mode (µm)	St. Dev. (µm)	D(v, 0.1) (µm)	D(v, 0.5) (µm)	D(v, 0.9) (µm)
150	29.99	30.76	31.41	7.44	21.95	29.99	40.52
250	31.32	34.66	31.63	17.76	21.85	31.32	48.47
350	28.13	29.46	27.93	8.59	20.25	28.13	39.95
500	28.12	30.53	27.88	15.55	20.05	28.12	41.53
1000	29.38	31.07	28.22	10.00	20.55	29.38	43.35

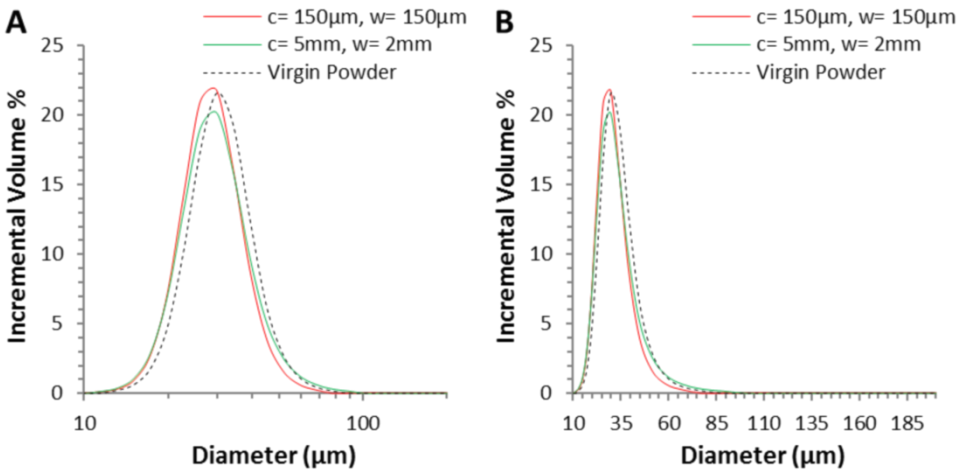

Figure 4.6: Laser diffraction results for samples collected from the HAZ3 experiment, compared to virgin powder. Presented here in log (A) and linear (B) forms. c=channel width, w=wall thickness.

Table 4-2: Median, mean, mode, D(v,0.1), D(v,0.5), and D(v,0.9) values for the powder size distribution samples from the third heat-affected zone experiment.

HAZ_3 Channel Width (c), Wall Thickness (w) (µm)	Median (µm)	Mean (µm)	Mode (µm)	St. Dev. (µm)	D(v, 0.1) (µm)	D(v, 0.5) (µm)	D(v, 0.9) (µm)
c=150, w=150	26.68	27.66	27.53	7.33	19.41	26.68	37.25
c=5000, w=2000	27.24	28.75	27.66	9.00	19.32	27.24	39.54

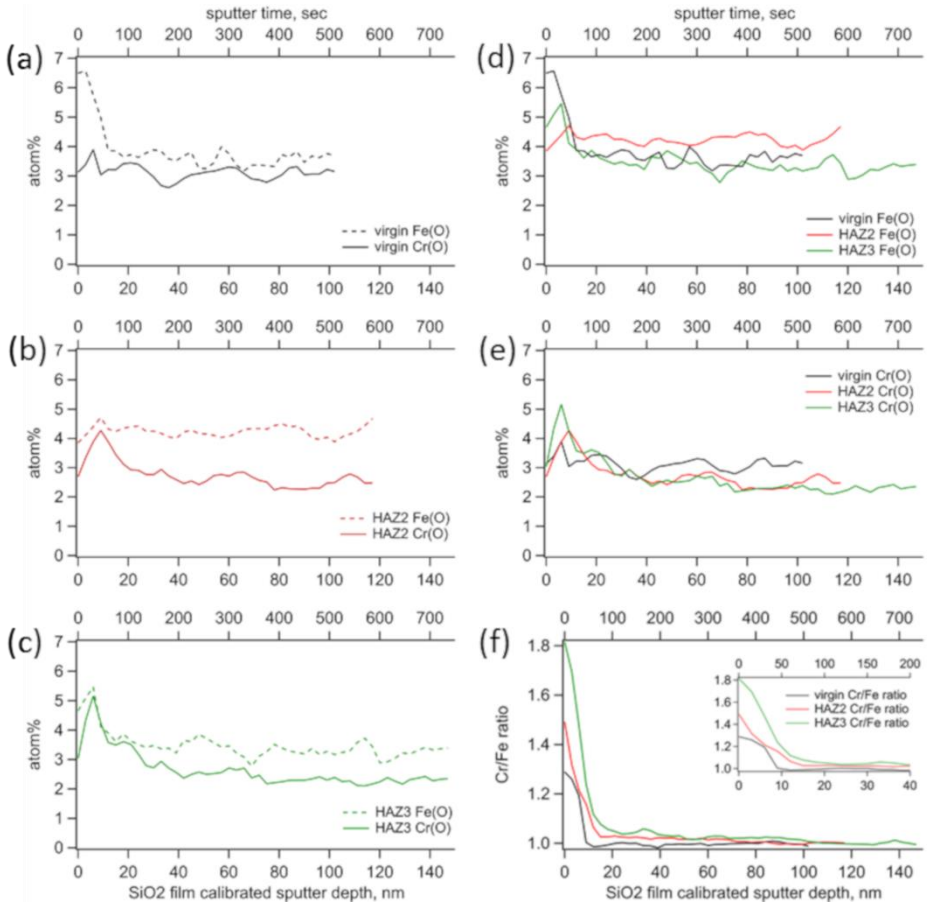

Figure 4.7: XPS measurements of iron and chromium atoms associated with oxides on the surface of (a) virgin powder, (b) HAZ2 powder, and (c) HAZ3 powder. (d) Comparison of surface iron-oxide content. (e) Comparison of surface chromium-oxide content. (f) Comparison of (Cr/Fe)/(Cr/Fe-bulk) ratio.

temporarily. Once enough material is sputtered away, the shaded adjacent particles are then exposed to the ion-beam and fresh surface area is measured. This effect continues until no more particles are shaded by their neighbors.

Figure 4.7 (f) confirms the presence of chromium in increased amounts relative to iron at the HAZ powder surfaces. The total chromium-to-iron ratio (Cr/Fe) was calculated at each measurement point. This value was compared as a ratio to the Cr/Fe ratio of the bulk material (Cr/Fe-bulk). The Cr/Fe-bulk value was taken to be the mean of the last ten data points. Figure 4.7 (f) shows that chromium enrichment at the surface of the HAZ particles is increased relative to virgin powder. The enrichment is pronounced at the surface and can be seen at deeper surface levels in the HAZ powder compared to the virgin powder. If the maximum oxide depth is taken to be the point when the slope levels off in Figure 4.7 (f), then the oxide depths for the virgin, HAZ2, and HAZ3 powders are approximately 10, 15, and 24 nm, respectively.

4.2. Discussion

XRD and PSD measurements of the heat-affected-zone powders reveal that neither the powder size nor the crystallographic structure of un-melted powder is affected by their proximity to melt regions during the SLM process. The observed oxygen wt% increase in the HAZ samples (see Figure 4.2 and Figure 4.3) cannot be explained by the dissolution in the molten state or by the loss of materials that are devoid of oxygen. At normal processing atmospheric pressures, evaporation loss of non-oxygen containing material may only occur at temperatures above the boiling point of the material or due to dissociation of oxides, e. g., 1100^{o} C for oxide to gas reactions [19]. Boiling temperatures were obviously not reached in the heat-affected-zones of interest and only a small fraction of the HAZ powder reaches high enough temperatures for oxide to gas reactions, according to a Rosenthal heat conduction model. The oxygen increases in the heat-affected-zones can be concluded to be the result of a physical mechanism, yet to be understood. Three of the most likely methods of oxygen addition, i.e., rapid oxide formation, spatter, and moisture retention are discussed in this section.

4.2.1. Role of Moisture

Water vapor has the potential to accelerate the observed oxidation kinetics in steels and other metals noticeably [19]. However, most of these effects apply to fully developed scales and are only observable after temperature exposure times far exceeding that seen by un-melted powder during SLM. It is worth noting that any pick up of moisture from the environment by the feedstock powder may contribute to the introduction of oxygen into the system. The 316L powder was stored in a climate controlled high bay area for several weeks in closed containers containing desiccant bags. However, once the powder containers were opened, the desiccant bags were removed, and the powder left exposed to air for sometimes several hours. No drying of the powders was

employed, so whatever moisture that was picked up as powder was transferred to the sieve and back to the Renishaw AM 250 hopper is likely retained prior to its use as feedstock. The oxygen chemical analysis results do not support this theory of oxygen addition to the powder bed. Figure 4.2 shows that the oxygen values for the powder samples taken from the 5000µm channel spacings in both HAZ1 and HAZ2 experiments equal the oxygen values of the fresh powder before it is processed (Figure 4.3).

Powder samples were also dried in an oven at 110^{o}C for one hour prior to oxygen analysis, and the results were compared to oxygen analysis of powders in the undried state. No difference in oxygen content could be detected between the dried and undried powder samples, further discrediting the theory of retained moisture adding measurable amounts of oxygen into the system.

4.2.2. Rapid Oxidation of Powders

Solid-state growth of a surface oxide shell surrounding a powder particle is the most likely mechanism to explain the oxygen pickup observed in the powder bed HAZ. Oxygen has a low solubility in FCC iron (0.0002 wt%) and cannot therefor exist as solute within the powder particle lattice structure. Surface moisture retention was ruled out by a heating experiment (Figure 4.3). The following sections attempt to estimate the amount of oxide shell growth by first, back-calculating from the measured bulk oxygen wt% values given in section 4.1.2 and second, comparing the back-calculated oxide growth value to that determined by thermal heat transfer model in combination with the DICTRA software. The heat transfer model is based on the Rosenthal equation and was used to estimate the accumulated time period over which the HAZ powders were exposed to oxide accelerating temperatures (>500 ^{o}C). The thermal histories output by the heat transfer model were used as inputs into a DICTRA oxide growth model to model the amount of growth experienced by the oxide shell.

4.2.2.1. Solid-State Oxidation Back-Calculation

The back-calculated oxide thicknesses in this section were calculated using the measured oxygen content of powder particles both before and after thermal cycling (0.033 $\pm$0.002 and 0.043 $\pm$0.002 wt% respectively). They were performed to estimate the extent of oxide growth experienced by powder particles during processing. The details of the back-calculation method are given in Appendix C.

The difference between the initial back-calculated average initial oxide thickness and the thermally cycled average oxide thickness is taken to be the oxide growth experienced by a single representative powder particle residing in the heat-affected-zone. Real stainless-steel oxides can be complex. To simplify the back-calculation the assumption was made that the entire oxide shell surrounding a powder particle is made up of a single oxide type (i.e. FeO, Fe_2O_3, Fe_3O_4, Cr_2O_3). As a conservative estimate, it is also assumed that all oxygen pickup by the powder bed is converted to oxide scale,

and that none of the initial oxygen or oxygen pickup is in the form of internal oxides, solutionized oxygen, or adsorbed H_2O. The back-calculated initial oxide thicknesses and heat-affected zone oxide growth values are presented in Table 4-3 and take into account the oxygen content measurement error of 0.002 wt%.

Figure 4.8 shows the calculated oxide scale growth needed to match the observed oxygen data (0.043 $\pm$0.002 wt%). Each particle in the powder bed would need to grow, on average, a FeO oxide scale of 3.49 (±1.05) nanometers, a Fe_2O_3 oxide scale of 2.83 (±0.85) nanometers, a Fe_3O_4 oxide scale of 3.12 (±0.94) nanometers, or a Cr_2O_3 oxide scale of 3.84 (±1.16) nanometers, in addition to whatever passivation layer existed before the laser welding heat cycle(s).

Figure 4.9 compares the back-calculated oxide thickness to data obtained by XPS. To estimate the oxide thickness from XPS data, a ratio of Cr to Fe as a function of depth was compared to the ratio of Cr to Fe found at a depth representative of the base metal composition of the particle. Virgin powder was found to have an initial oxide thickness of approximately 10 nm. Powder samples taken from the 150um channels in the HAZ2 and HAZ3 experiments were found to have an oxide thickness of approximately 15 to 25 nm. The XPS oxide thickness results compare favorably with the back-calculated results, showing that back calculating oxide growth from bulk chemical analysis data is feasible.

4.2.2.2. Dilution Effects

The heat-affected-zone experiments bring to light a previously unreported phenomenon in laser powder bed additive manufacturing: local changes (i.e. oxidation) can occur within the powder bed, and that these changes can escape bulk characterization detection by virtue of dilution by/with non-oxidized or virgin powder particles.

The potential diluting effects of non-oxidized powder mixed with and measured alongside oxidized powder in this experiment are represented by upper and lower limit dashed lines in Figure 4.10. Details of the method used to calculate the dilution effect can be found in Appendix D. The measured oxygen values from the HAZ2 experiment lie within the range predicted by diluting with non-oxidized powder and demonstrate how easily localized powder characteristics can be obscured during bulk powder characterization. The local oxidation effect can only be observed by sampling powder close to a melt region. The upper and lower limits of oxidation were calculated by considering the 0.002 wt% error of the processed powder oxygen content and assuming that all oxidation effects occur within 75 microns from the melted region (150-micron channel width).

Table 4-3: Back-calculated initial oxide thicknesses, heat-affected zone oxide thickness, and the resulting oxide growth values for FeO, Fe_2O_3, Fe_3O_4, and Cr_2O_3 oxide shells.

Volume averaged particle Diameter, Dv = 27.71 microns

Oxide	Initial Thickness, nm	HAZ Oxide Thickness, nm	Oxide Growth, nm
FeO	8.95 - 10.10	11.83 - 13.91	1.73 - 4.97
Fe2O3	7.26 - 8.20	9.61 - 11.30	1.41 - 4.03
Fe3O4	8.00 - 9.04	10.59 - 12.45	1.55 -4.44
Cr2O3	9.84 - 11.11	13.01 - 15.30	1.90 - 5.46

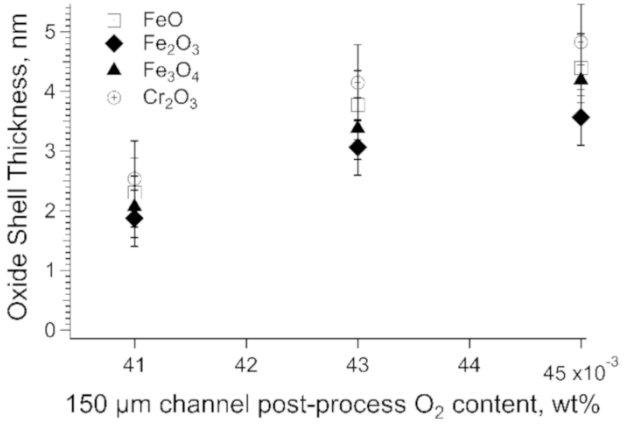

Figure 4.8: Back-calculated oxide shell thickness increase assuming FeO, Fe_2O_3, Fe_3O_4, or Cr_2O_3 oxide growth.

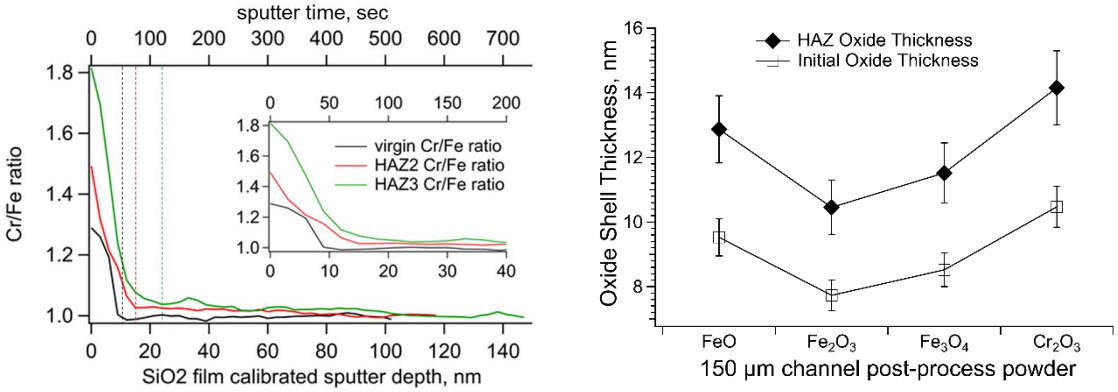

Figure 4.9: Comparison between XPS data taken from the surface of spatter particles and the total oxide thickness back-calculated from bulk chemical analysis data.

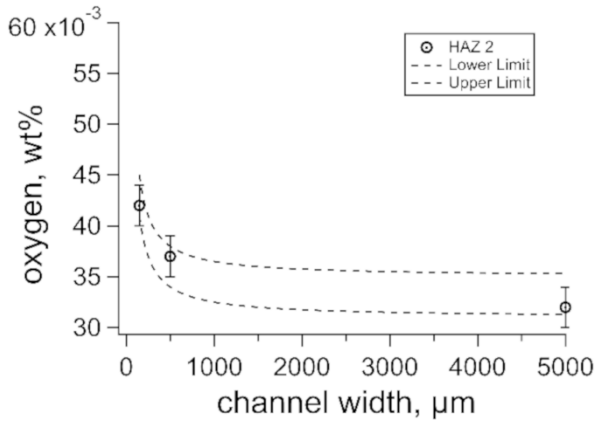

Figure 4.10: HAZ2 measured bulk oxygen content with maximum and minimum calculated dilution effects indicated by dashed lines.

4.3. Modeling Efforts

It was desired to understand if a simple thermal cycle combined with a DICTRA oxidation model could be used to model the oxidation observed during the experiment. The following sections describe the development of such a model and the comparison of the model output with the data observed.

4.3.1. Thermal Cycle Model

DICTRA was used to model the oxidation of an FCC iron substrate with an initial spinel (Fe_3O_4) oxide layer. Previous literature suggests that initial oxide layers in metal powder used for additive manufacturing are on the order of 3 nm [36], but 9.036 nm was used here in order to be consistent with the conservative, maximum value found by back-calculation in section 4.2.2.1, and does not appreciably change the DICTRA model results when compared to a 3 nm starting value. The thermal histories of the un-melted powder were obtained from a heat transfer model and input into DICTRA to calculate oxide shell growth.

While more advanced methods exist, utilizing fundamental mass, momentum, and energy transfer equation to model the thermal profile of the powder bed [37], these methods can be computationally expensive. The Rosenthal heat equation is used here in an attempt to reduce the complexity of the model as much as possible. The Rosenthal heat equation was used to model the steady state temperature field in the surrounding powder during laser processing, ignoring thermal effects of the thin wall substrate directly below the laser. Rosenthal presented his equation describing the steady-state temperature distribution for the case of a steady-state, point heat source [38]

$$T(x,R) = T_0 + \frac{\eta VI}{2\pi\lambda}\left(\frac{1}{R}\right) exp\left\{-\frac{v}{2a}(R+x)\right\}, R = \sqrt{x^2+y^2+z^2} \quad (4\text{-}1)$$

where $T(x,R)$ is the temperature as a function of radial distance (R) and linear distance (x) along the weld centerline, T_0 is the preheat or interpass temperature, V the arc voltage, I the welding current, v the welding speed, a the thermal diffusivity, η the arc efficiency, and λ the thermal conductivity. The thermophysical properties used in the conduction model are listed in Table 4-4. In laser welding the ηVI term can be replaced with an effective absorbed power ($P_{abs} = P \cdot \lambda_{abs}$). When only surface temperature distributions are of interest, one only has to omit the z variable in Eq. 4-1.

Table 4-4: Stainless steel 316L thermophysical properties and laser parameters used in Rosenthal model.

property	symbol	value	units	reference
substrate temperature	T_0	298	K	assumed
absorbed power	λ_{abs}	0.6		[39]
thermal conductivity	K	0.05-0.20	$\frac{W}{K \cdot m}$	[40]
effective weld speed	v_{eff}	6.38E-01	$\frac{m}{s}$	calculated
effective density	ρ	4315	$\frac{kg}{m^3}$	measured
specific heat	C_p	480	$\frac{J}{kg \cdot K}$	[21]
thermal diffusivity	α	2.41E - 9.66 x 10^{-8}	$\frac{m^2}{s}$	calculated

Because a pulsed laser system was used to conduct the HAZ experiments, an effective weld speed v_{eff} was used as the velocity input into Eq. 4-1. v_{eff} was calculated by adding together the total distance traveled by the laser after a large number of pulses and then dividing by the total laser travel time according to equations

$$t_{tot} = n\left(t_{exp} + t_{set}\right) + \frac{(n-1)d_{p2p}}{v_{trvl}}, \tag{4-2}$$

and

$$v_{eff} = \frac{(n-1)d_{p2p}}{t_{tot}}, \tag{4-3}$$

where t_{tot} is the total laser travel time, n is an arbitrary large number of pulses, t_{exp} the length of exposure time of each pulse (80 µs), t_{set} the settling time of the laser (2 µs), d_{p2p} the distance traveled by the laser between each pulse (60 µm), v_{trvl} the speed at which the laser travels between pulses (5 m/s), and v_{eff} the effective travel speed of the pulsed laser. Using this method, the effective laser speed in the Renishaw 250AM was calculated to be 0.638 m/s. Modifying Eq. 4-1 to produce the pulsed laser, surface-only Rosenthal solution results in the following equation

$$T(x,R) = T_0 + \frac{P_{abs}}{2\pi\lambda}\left(\frac{1}{R}\right) exp\left\{-\frac{v_{eff}}{2a}(R+x))\right\}, R = \sqrt{x^2+y^2} \tag{4-4}$$

The thermal histories of four points, located 0, 37.5, 75, and 125 µm from the melt pool edge respectively are presented in Figure 4.11. The 75 and 125 µm distances were chosen because they represent the halfway points of the 150 and 250 channels built during the HAZ experiments. The halfway points of the channels are assumed to be the points that are least affected by the thermal cycle of the passing laser. The 37.5 µm distance was chosen to represent a point close to the fusion zone.

4.3.2. Oxide Growth Model

As a conservative comparison to the oxide shell thicknesses calculated in section 4.2.2.1, the Rosenthal-calculated thermal history for a point positioned at the furthest possible distance (75µm) from the edge of the melt pool was input into DICTRA and the spinel (Fe_3O_4) oxide growth as a function of time was calculated. The thermal history of the powder bed, which was assigned an effective thermal conductivity of 0.2 W/mK, was used as a further method of conservative estimation. A higher value of powder bed thermal conductivity allows heat to dissipate faster and decreases the amount of time that a point within the powder bed experiences elevated temperatures. An initial oxide thickness of 9.036 nm was assumed and only the part of the Rosenthal-calculated

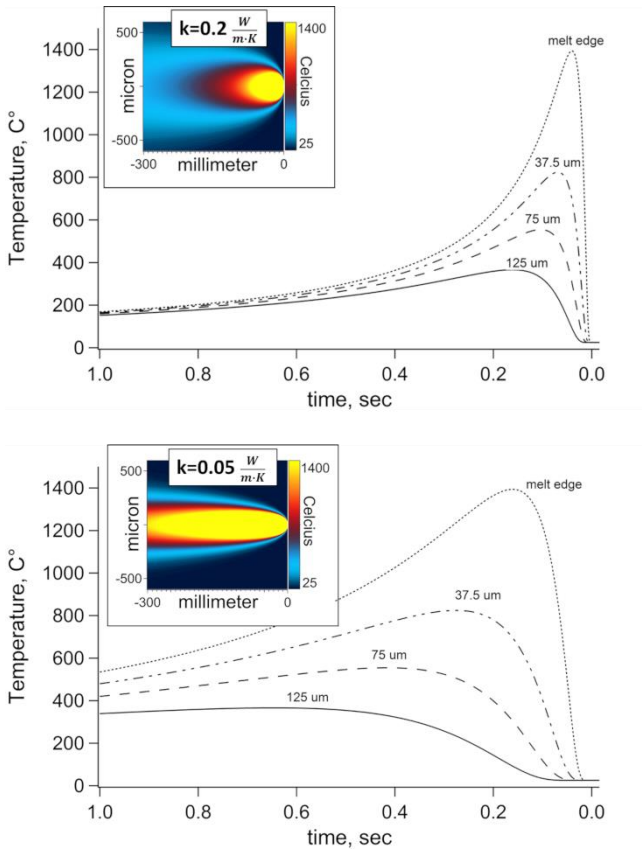

Figure 4.11: Thermal history plot of points in the powder bed located 37.5, 75, and 125 microns from the melt pool liquidus. Temperature contour map inset was generated using the Rosenthal equation. Powder bed apparent density = 4315 kg/m^3, Heat source velocity = 0.638 m/s, Absorbed Power = (200W*0.6) = 120 W.

thermal history that lies above 500 ^{o}C was used as input in the DICTRA calculation. The DCM macro files used to run the DICTRA calculation are provided in Appendix E.

The DICTRA-calculated oxide thickness (external growth) value of ~67 nm (Figure 4.12) greatly exceeds that of the 9-15 nm shell back-calculated from measured oxygen pickup data (section 4.2.2.1). While the absolute oxide depths in the powder could not be determined from the XPS data in section 4.1.5, according to Tapping et. al., the real depth values should be comparable to those reported in Figure 4.7 [41]. In comparison to the DICTRA-calculated oxide thickness, the XPS-measured values of 15-22 nm are 3 times lower than the model prediction. These results indicate that a simple, steady-state heat transfer solution may not be adequate to predict the oxide growth potential of unmelted powder experiencing thermal cycling during powder bed laser additive manufacturing processes.

4.3.3. Oxygen Contribution from Spatter Particles

Oxygen-containing spatter from the SLM process was considered as a contributing factor to the measured oxygen uptake in powder from the HAZ experiments. Two types of spatter have been found to exist during selective laser processing: liquid metal ejected from the weld pool, and unmelted powder sucked up from the surrounding powder bed. Liquid metal, or “spatter”, is routinely ejected from the weld pool during SLM processing. The spatter material is liquid at the time of its ejection from the weld pool and remains liquid for some time, Δt, as it is carried by the cover gas before solidifying in-flight and falling back down to the floor of the build chamber. Research by Bidare et al. has demonstrated that bed powder near the melt zone is removed via pressure differentials created by the rapid evaporation of liquid metal in the weld pool during selective laser melting [42]. This kind of spatter is not expected to have experienced the same amount of oxidation as liquid metal spatter that has resolidified. Figure 3.9 showed that the oxygen content of bulk measurements of spatter particles, as a mixture of the two types of spatter, can reach at least as high as 0.100 wt% (compared to virgin powder at 0.033 wt%). Even at high temperatures, the solubility of oxygen in solid Fe is low (0.003wt%) in comparison to its solubility in the molten state (0.23wt%) [43]. Therefore, it is hypothesized that most oxygen uptake in the ejected particles must occur while in the liquid state. An example of the physical disparity between ejected material and virgin powder can be seen in Figure 4.13.

4.3.3.1. Spatter Contribution Model

A MATLAB model was developed to help visualize the possible oxygen addition to the powder bed by re-introduced, oxygen rich, spatter particles. For ease of calculation, laser diffractometer measurements of two collected samples of spatter were converted into volume-averaged, monodisperse diameter particles containing the measured 0.100 (±0.002) wt% oxygen. Appendix F details the method by which the volume-averaged monodisperse diameters were calculated.

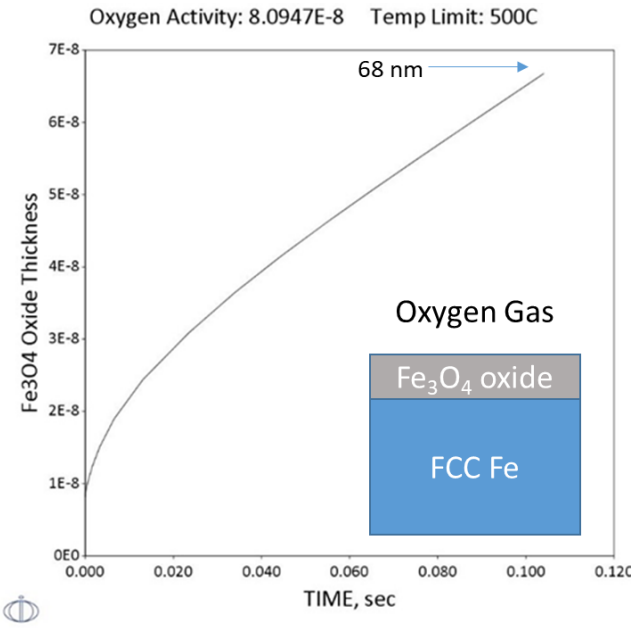

Figure 4.12: DICTRA calculated Fe_3O_4 external oxide growth on the surface of FCC iron as a function of temperature and time.

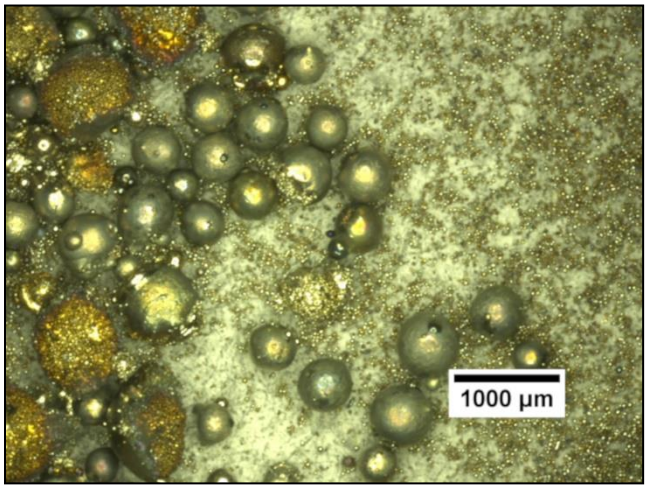

Figure 4.13: Optical microscope image of spatter powder mixed with much smaller virgin powder.

The model incrementally replaces particles of a virtual 1 cubic centimeter, monodisperse powder bed (particle diameters ranging from 30 to 70 µm) with spatter particles and outputs the total oxygen content of the powder bed in units of weight percent oxygen. Figure 4.14 shows the relationship between the bulk oxygen content of the hypothetical powder bed as a function of the number of spatter particles (containing 0.100 wt% oxygen) residing within the bed. A non-representative model of the effect of 200 µm spatter is also included to conservatively represent larger particle sizes that are sometimes seen in spatter. Both the number and size of oxygen-containing spatter particles have an impact on the predicted bulk oxygen content of the simulated powder bed.

From Figure 4.14, it can be seen that replacing 0.505% of a powder bed originally composed of virgin powder particles measuring and average 26.77µm in diameter with spatter particles 97.8µm in diameter and containing 0.100 wt% oxygen would increase the oxygen content of the bed from its original 0.033 wt% to the 0.043 wt% (±0.002) value measured in the 150µm channels of the HAZ experiments. While 0.505% may intuitively seem like a small percentage, it is actually quite large when viewed in terms of the absolute number of spatter particles.

For example, 1 cm^3 of perfectly packed (~74% full density) 26.77µm diameter monodisperse particles would equal to approximately $5.37x10^7$ particles. 0.505% of $5.37x10^7$ equates to $2.71x10^5$ spatter particles, or 5051 ppm within that 1 cm^3 powder bed. Oxygen contribution from smaller spatter particles would necessitate even larger numbers to be present in the powder bed in order to match the experimentally observed value of 0.043 wt% oxygen. These values are unlikely to be seen in actual SLM processes.

To demonstrate how unlikely it is that re-introduction of spatter particles significantly contributed to the measured oxygen content of the HAZ powders, powder distributions of samples taken from the 150 µm wide channels in HAZ2 and HAZ3 were measured by laser diffractometry. The powder size distribution results reveal that 100% of the HAZ particles measured had diameters smaller than 67.5 µm and therefore the presence of any larger spatter particles within the channels is assumed to be precluded (Figure 4.15) and not a significant source of oxygen. However, it is worth noting that the samples measured by laser diffractometry were not the same samples that were chemically tested. It lies within the realm of reason that some large spatter could have been present in the chemically tested powder samples while remaining absent from the laser diffractometer measured samples.

Observation of the spatter phenomena in the Renishaw AM250 machine was conducted using a high-speed infrared camera. A qualitative review of the amount of spatter that falls back into the powder bed supports the claim that spatter is not likely a significant source of oxygen addition to the powder bed.

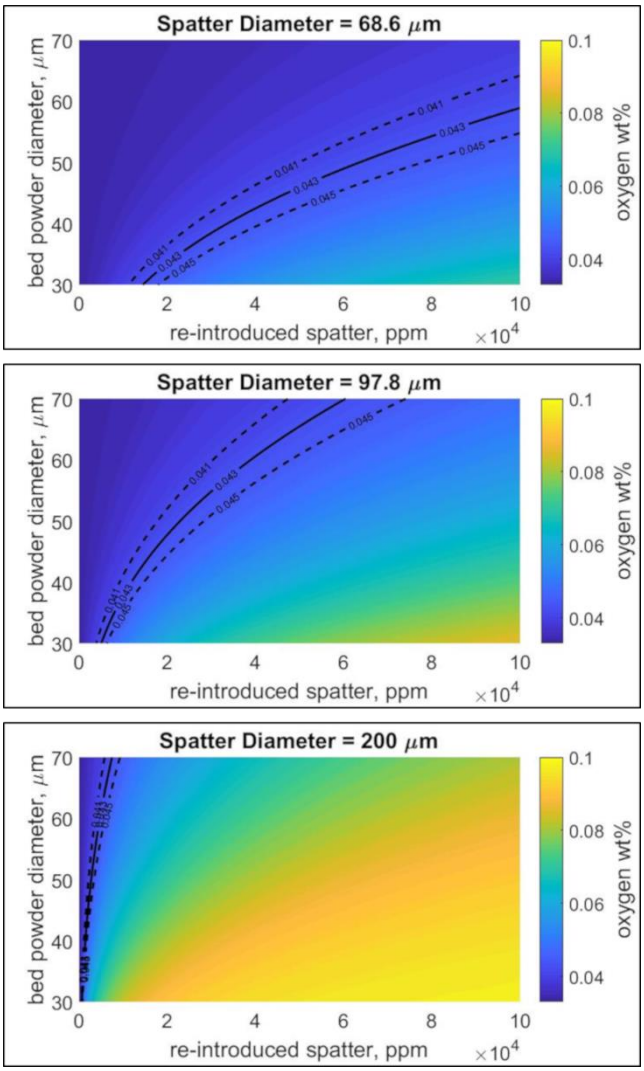

Figure 4.14: Contour plots modeling the predicated bulk powder bed oxygen content in a monodisperse, oxygen-containing (0.033 ±0.002 wt%) powder bed as a function of the addition of 68.6, 97.8, and 200 µm diameter, oxygen-containing (0.100 wt%) spatter particles, respectively.

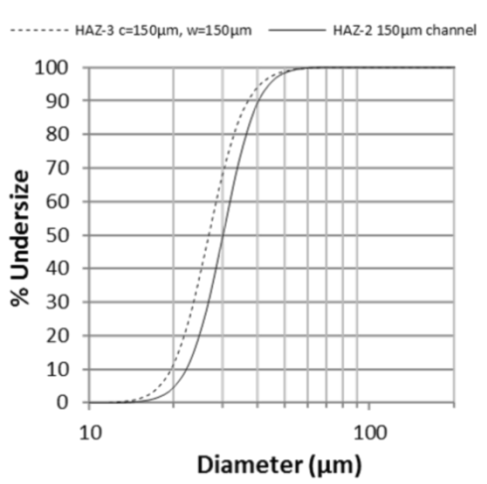

	HAZ 2	HAZ 3
Diameter (µm)	Undersize (%)	Undersize (%)
67.523	100	100
58.953	99.749	99.758
51.471	98.811	99.118
44.938	95.856	97.464
39.234	88.178	93.425
34.255	72.274	84.449
29.907	49.546	68.288
26.111	27.323	46.517
22.797	12.123	25.573
19.904	4.512	11.32
17.377	1.493	4.193
15.172	0.454	1.376
13.246	0.114	0.413
11.565	0	0.102
10.097	0	0

Figure 4.15: Laser diffraction percent undersize results from the 150µm channel in HAZ 2 and the 150µm channel in HAZ 3 showing what percentage of powder particles are smaller than the corresponding diameter. c=channel width, w=wall thickness.

4.3.4. Model Limitations

Experimental measurement verification of the predicted oxide layer growth in this study would require TEM sample preparation using the FIB technique of both a virgin powder particle and a particle collected from an area near a melted region. The HAZ experiment powder sample collection method used in this study made it impractical to attempt to find a particle by chance that resided close to the melted region and experienced enhanced oxide growth.

Limited access to appropriate oxide thermodynamic databases limited the DICTRA oxide growth model to a single oxide type (Fe_3O_4) grown on a single element (Fe). As mentioned earlier, modification of the thermodynamic and kinetic oxide data is needed to perform more relevant oxide growth calculations under non-isothermal cyclic conditions expected during selective laser melting conditions. Grain boundary effects on oxide growth were not considered in the DICTRA model. Furthermore, the model for oxide formation within DICTRA is not capable of describing the changes from Fe-rich to Cr-rich oxides.

The back-calculation of the oxide thicknesses on the processed powder was simplified by assuming single oxide types rather than the complex mix of oxides typically seen in real oxidation of steels. Further simplification of the calculations required a conversion of the real measured powder size distributions into representative, monodisperse powder distributions. The efficacy of the back-calculated estimates is limited by the lack of comparisons to real oxide thickness measurements.

4.4. Summary & Conclusions

It was found that oxygen content in un-melted 316L powder during the SLM process was found to vary as a function of its relative position to the heat source. Measurements of oxygen weight percent in powder samples located very near the melt zone (<0.25 mm) indicated increased oxygen content. The volume of melted material (i.e. thin vs thick walls) was not found to affect the degree of oxygen pickup in the un-melted powder.

The mechanism driving the oxygen pickup in powder positioned close to melted regions is likely caused by an increase in thickness of the oxide scale on the surface of the un-melted powder particles, promoted by the elevated temperatures and adequate oxygen partial pressure during processing. It was found that dilution effects become considerate even at small length scales (5 mm) and can occlude local changes in powder characteristics (i.e. oxygen pickup) when measuring bulk powder characteristics.

An oxidation model of Fe_3O_4 on FCC iron was performed using DICTRA and was found to overestimate the amount of oxidation back-calculated from oxygen content and XPS

measurements. The DICTRA model used thermal histories calculated by a simple Rosenthal conduction model. The overestimation of oxide thickness predicted by DICTRA may also be in some parts the fault of the Rosenthal model. Access to thermodynamic and kinetic data of oxides is needed to perform more relevant oxidation growth calculations.

The role of spatter and its re-introduction into the powder bed was discussed. It was determined that even though spatter may contain elevated levels of oxygen, it is not likely a significant source of oxygen pickup within the powder bed.
Future studies should include a traditional oxidation study of stainless-steel feedstock powder at temperatures and time scales associated with the SLM process. Qualitative examination of the oxide shell both before and after the oxidation studies should be able to validate the conclusions found in this study. Future powder recyclability studies should be aware of and consider the localized oxidation in the unmelted powder close to melted regions.

CHAPTER 5 VARIABLE OXYGEN ENVIROMENT STUDY

The variable oxygen environment study was conducted to investigate the effects of conducting selective laser melting of stainless steel 316L with higher than normal oxygen content within the argon cover gas. The powder bed, spatter particles, and as-built parts at each level of oxygen content were characterized and compared.

5.1. Results

A description of the variable oxygen environment experiment setup and procedure is provided in chapter 2, section 2.2.3. A description of the data collection methods is provided in chapter 2, section 2.3.4.

The oxygen levels within the build chamber were monitored during the variable oxygen environment experiment using the built-in oxygen sensor capability of the AM250 instrument and manipulated by manually opening (to introduce ambient air) or closing a needle valve connected to the gas recirculation system of the AM250. It was intended that the first set of tensile bars be built at a build chamber oxygen value of 4600 ppm, the second set at an oxygen value of 2300 ppm, and the third set at an oxygen value as close to 0 ppm as possible. The actual average build chamber oxygen values recorded during the build at each layer were 4671 ppm (±139), 2312 ppm (±71), and 0 ppm (±2).

5.1.1. X-Ray Diffraction

5.1.1.1. Room Temperature XRD

The powder samples collected from each of the three spatter receptacles in the experiment were manually separated into magnetic and non-magnetic partitions. Each partition was analyzed via powder x-ray diffraction at room temperature to determine the relative phase content of crystal phases within the powder. Based on the characterization of spatter powder in chapter 3, it can be assumed that a large fraction, if not the entirety, of BCC phase observed in powder XRD results can be attributed to the metastable BCC phase formed during solidification of spatter particles.

The powder XRD patterns of both the non-magnetic and magnetic powder samples in Figure 5.1 demonstrate that there is indeed an increased proportion of the BCC phase present in the magnetic samples. A large FCC (111) peak is also present in the magnetic powder XRD profiles. It was shown in chapter 3 that small amounts of the BCC phase can sometimes be present within primarily FCC particles. The magnet that was used to separate magnetic powder from non-magnetic powder was encased in plastic and so the possibility of collecting FCC particles via static cling instead of magnetic attraction may also exist.

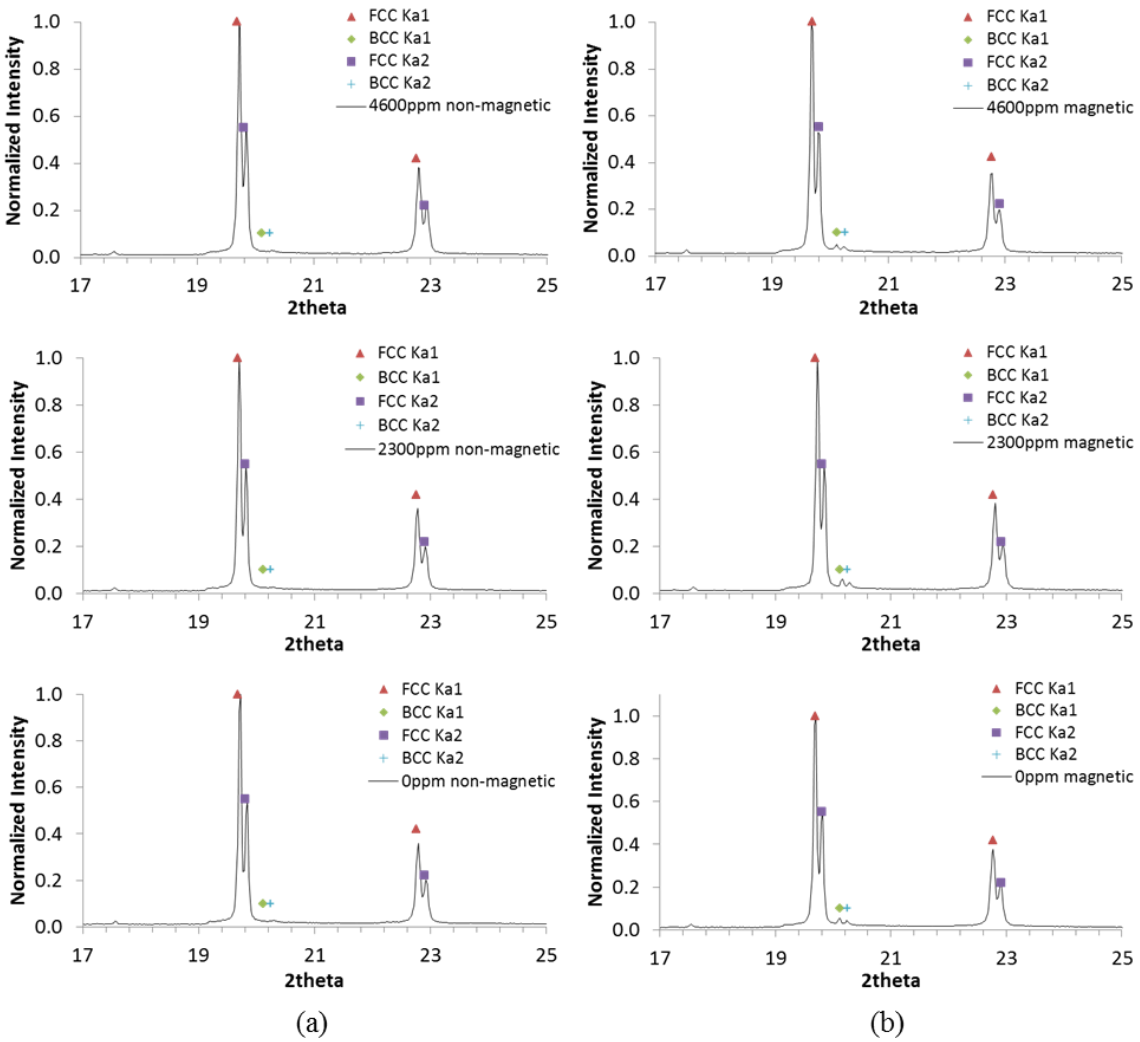

Figure 5.1: X-ray diffraction analysis of magnetic and non-magnetic partitions of powder samples collected from each of the three receptacles in the variable oxygen environment experiment.

The XRD patterns of both the non-magnetic and magnetic powder samples do not qualitatively change as a function of atmospheric (cover gas) oxygen content.

5.1.2. Magnetic Measurements

Magnetically separated powder collected from the powder bed and from the downstream area within the build chamber, as well as several versions of virgin powder were magnetically tested and subjected to differential scanning calorimetry and thermogravimetric analysis. The naming scheme and description for each tested powder sample is shown in Table 5-1.

5.1.2.1. Hysteresis Curves

Magnetic measurement of the magnetically separated powder samples was conducted at Ames Laboratory and the results are presented in Figure 5.2 and Figure 5.3. It can be seen that all of the magnetic powder samples showed stronger ferromagnetic contributions than the non-magnetic samples, but the strongest ferromagnetic reactions (saturation at 22 and 30 emu/g) were from the two magnetic spatter samples, indicating the presence of strongly ferromagnetic BCC phase within the powder. The rest of the magnetic samples collected from the powder bed had both ferromagnetic and paramagnetic contributions to the hysteresis curves and started leveling off at much lower levels of magnetization (4-6 emu/g). The magnetic samples also exhibited very low retentivity and coercivity values.

The non-magnetic samples exhibit strongly paramagnetic behavior by never reaching saturation even at exposure to high magnetic fields, up to 30kOe. The non-magnetic samples also show very low retentivity, but slightly more coercivity than the magnetic powder samples.

5.1.2.2. Differential Scanning Calorimetry

Differential scanning calorimetry of the magnetically separated powder was conducted at the Ames laboratory and the results are presented in Figure 5.4. All of the samples exhibit a dip in heat flow at approximately 1000^{o}C. The sieved spatter samples H and I have the least pronounced dips, indicating that they may have a different composition compared to the rest of the samples. The spread of data from the different samples along the y-axis is related to the masses of the samples tested. A constant energy source was used to heat the samples, and so larger sample masses cause the heat flow value to show as decreased relative to lighter sample masses. There does not seem to be much of a difference between the profiles of the magnetic vs non-magnetic powders taken from the powder bed.

Table 5-1: Naming key for the powder samples magnetically tested.

Marking		Sample Description	Magnetic vs Non-Magnetic
1	A	Spatter Experiment Virgin Powder	Virgin Powder
2	B	Oxygen Experiment Level 1	Magnetic
3	C	Oxygen Experiment Level 1	Non-Magnetic
4	D	Oxygen Experiment Level 2	Magnetic
5	E	Oxygen Experiment Level 2	Non-Magnetic
6	F	Oxygen Experiment Level 3	Magnetic
7	G	Oxygen Experiment Level 3	Non-Magnetic
8	H	Oxygen Experiment Spatter Sieved	Magnetic
9	I	Oxygen Experiment Spatter Sieved	Non-Magnetic
10	J	Oxygen Experiment Spatter Oversized	Magnetic
11	K	Renishaw Virgin Powder 2nd Batch	Virgin Powder
12	L	Carpenter Virgin Powder	Virgin Powder

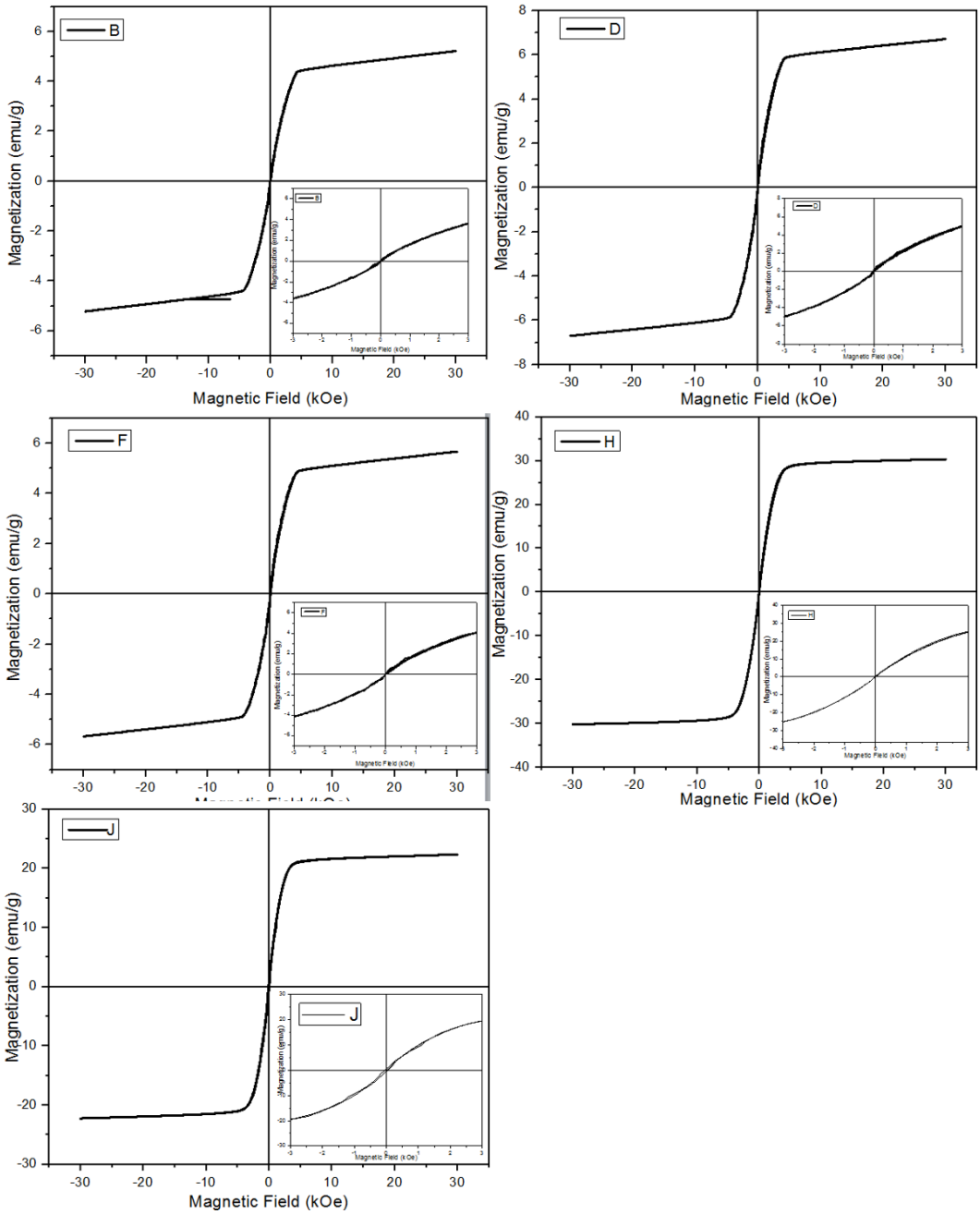

Figure 5.2: Hysteresis M-H curves of the magnetically separated, magnetic powder samples.

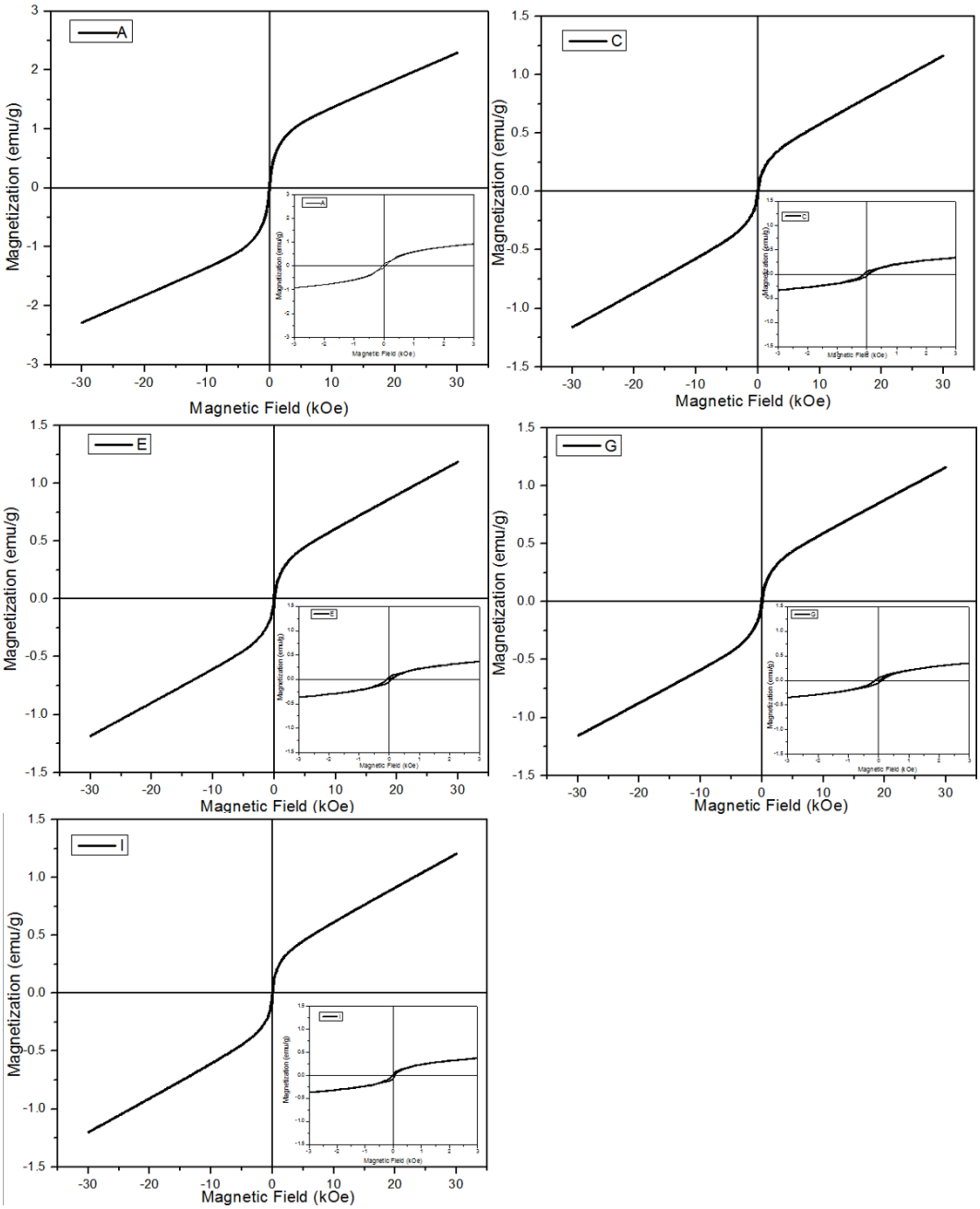

Figure 5.3: Hysteresis M-H curves of magnetically separated, non-magnetic powder samples.

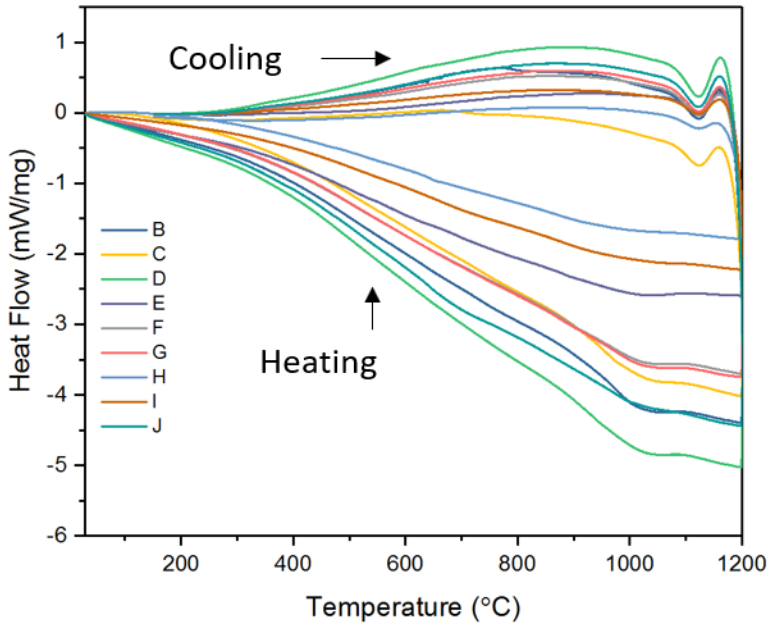

Figure 5.4: Differential scanning calorimetry results from testing of both magnetic and non-magnetic powder samples.

Some concern exists concerning the reactivity of the powders with the alumina crucible at high temperatures and affecting the results. To check if the powders are reacting with the crucible, they can be retested by heating them from room temperature to 700^{o}C, cooling back down to room temperature, heating back to 1200^{o}C, and then cooling back to room temperature.

5.1.2.3. Thermogravimetric Analysis

Thermogravimetric analysis of the magnetically separated powder was conducted at the Ames Laboratory and the results are presented in Figure 5.5. A Faraday balance was used to measure the apparent mass change of the samples during heating and cooling. Only sample F, containing magnetic powder collected from the level 3 receptacle of the oxygen-controlled atmosphere experiment (see section 2.2.3), showed evidence of a possible Curie temperature as indicated by the sharp apparent mass change at approximately T=540^{o}C. This Curie temperature most closely resembles that of iron-oxide (575-585^{o}C), indicating the presence of iron-oxide within the powder sample. This Curie temperature is not apparent in the TGA results of the other magnetic powder samples (B, D, H, & J). Samples D, G, and J show relatively large increases in mass upon cooling. This could be caused by either oxidation of the samples or by a magnetic phase change causing an increased magnetic susceptibility and increased apparent mass. If these samples were analyzed a second time with no applied magnetic field and still gained mass, oxidation of the samples during processing would likely explain the mass change.

5.1.2.4. X-ray Photoelectron Spectroscopy

Virgin stainless steel 316L feedstock powder was partitioned into magnetic and non-magnetic portions using the magnetic separation technique described in section 2.3.4.1. The major photoemission peak for each element identified during the surface composition of the as-received bed powder from the variable oxygen experiment are labelled in Figure 2.26, all other peaks are minor transitions of these same elements. The survey data for well sputtered powders is given in . It can be seen that the oxygen signature has decreased dramatically in the well-sputtered plot and a nickel peak has formed. No discernable difference between the magnetic and non-magnetic XPS spectrums can be seen in either the as-received or well-sputtered states.

The depth profile data for the magnetic powder is shown in Figure 5.8. The upper plot gives the total signals for C, Fe, Cr, Mn, Mo, and O and the lower plot gives the O 1s and the de-convoluted C 1s and Fe 2p signals. As before, the Mn profile is distorted at longer sputter times due to overlap with a Ni Auger feature but is enriched in the near surface region consisting primarily of C and metal oxides. The upper plot shows that the surface carbon is removed quickly, but that the C-signal dies more slowly as sputtering proceeds. Likewise, the outermost layer is made up primarily of Fe- and Cr-oxides.

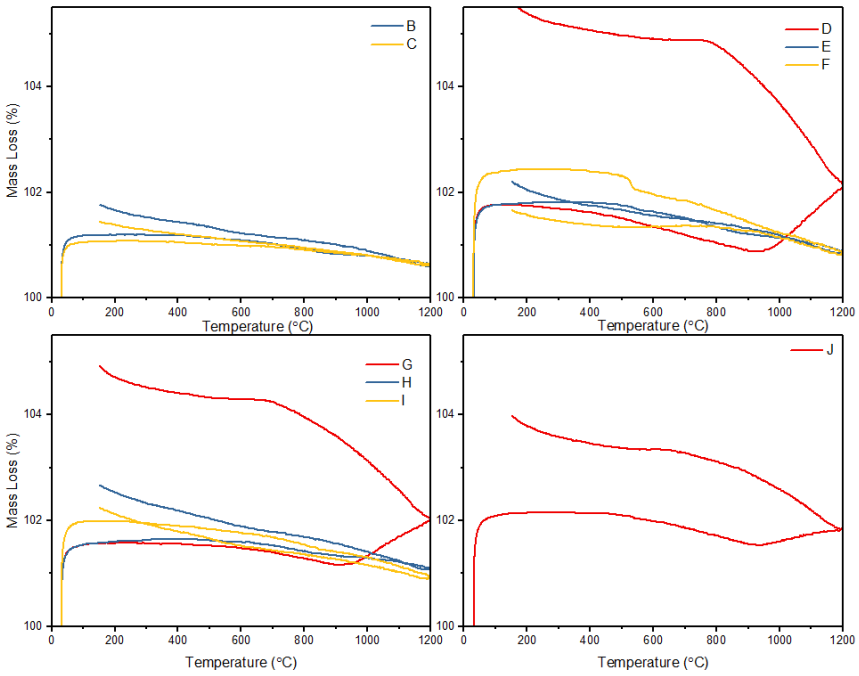

Figure 5.5: Thermogravimetric analysis results for both magnetic and non-magnetic powder samples.

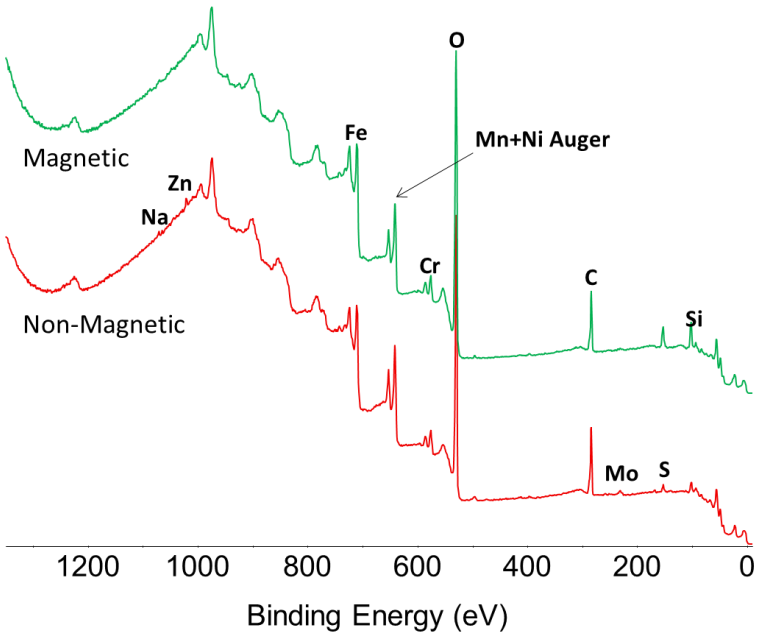

Figure 5.6: As-received XPS elemental binding energy plot of virgin powder separated into magnetic and non-magnetic batches

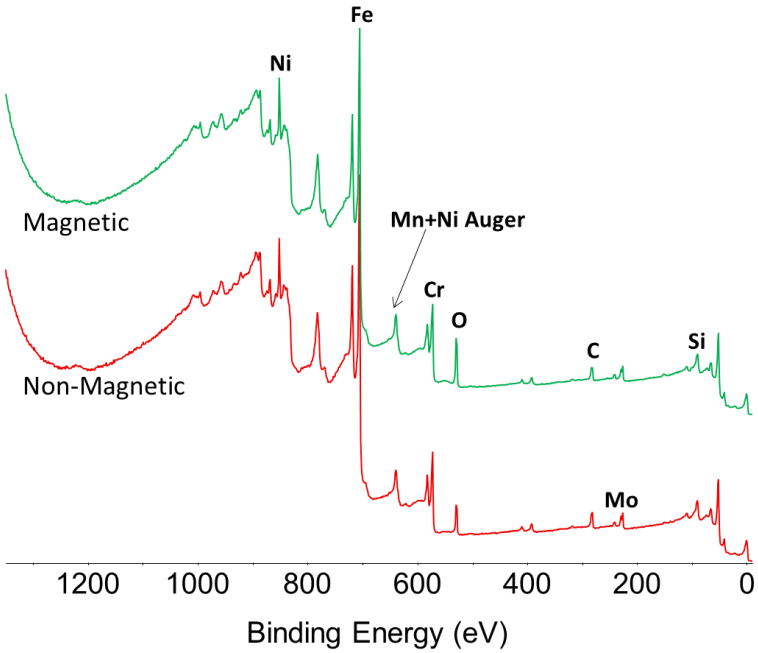

Figure 5.7: Well-sputtered XPS elemental binding energy plot of virgin powder separated into magnetic and non-magnetic batches.

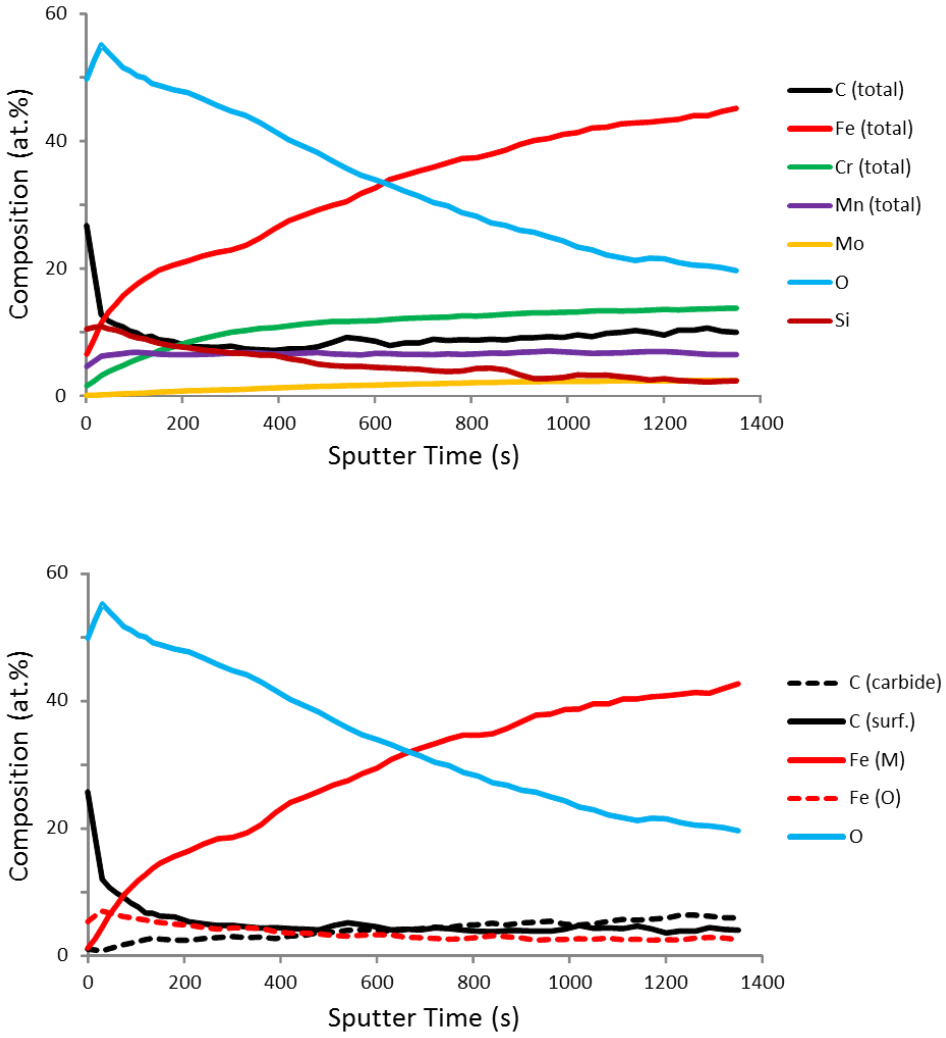

Figure 5.8: (top) Elemental depth profile of magnetic bed powder. (bottom) Elemental depth profile of magnetic powder bed oxides.

The profile was stopped at the same time as the one for the fresh powder and is just beginning to show a plateau of the Fe and Cr signals. The O signal never reaches the 20% mark as for the fresh powder in section 2.3.1.9. The lower plot shows peak fitting for both the C 1s and Fe 2p signals to de-convolute them into surface adsorbed C, carbide C, metal Fe, and oxide Fe. The O 1s signal is also re-plotted. It is clear that as the Fe metal signals exceeds the Fe-oxide signals (~60 sec) the carbide starts to grow and likely indicates that carbide is being formed by gettering C-containing species from the residual gas.

5.1.3. Transmission Electron Microscopy

Sample 1A was prepared for TEM via focused ion beam milling and was imaged using the OSU CEMAS Tecnai T20 TEM microscope. Figure 5.9 shows a TEM image of the prepared FIB foil with grains and grain boundaries marked, and Figure 5.10 shows the selected area diffraction pattern of both grains. The SAD images confirm that both grains in Figure 5.9 are FCC in phase.

ImageJ image analysis was performed on six images taken at 28,000x magnification (totaling 90.16 square microns of area). Table 5-2, Figure 5.11, and Figure 5.12 summarize the results of the analysis of all the precipitates found within the six images that were processed. The results show that the majority of precipitates/oxides are smaller than 11 nm, and that the average effective diameter of the oxides is 28 nm, which is only slightly larger than the oxides in the recyclability experiment as-built parts that were built at oxygen levels of 0 ppm. The precipitate area fraction is also similar to that of sample 2-10K.

Figure 5.13 is an overview of the sample 1A FIB foil with EDS scan areas 4 and 5 marked. Both scans focused on the characterization typical black precipitates in two different locations. The precipitates in both scans were confirmed to be rich in Mn, Si, and O and depleted in Cr, Ni, Fe, and Cu. The precipitates are most likely a mix of MnO and SiO_2.

5.1.4. Chemical Analysis

5.1.4.1. Powder

The magnetically partitioned powder samples as well as samples from the downstream pile were analyzed for bulk oxygen content by Luvak Laboratories. The results in Table 5-3 show that oxygen content alone in the powder collected by the receptacles could not predict the magnetic BCC phase present in concentration indicated in Figure 5.1. However, oxygen content in the downstream powder is markedly high, presumably due to the fact that unlike powder samples taken from the receptacles, it was not mixed with low oxygen content bed powder when analyzed. It can be seen that spatter particles

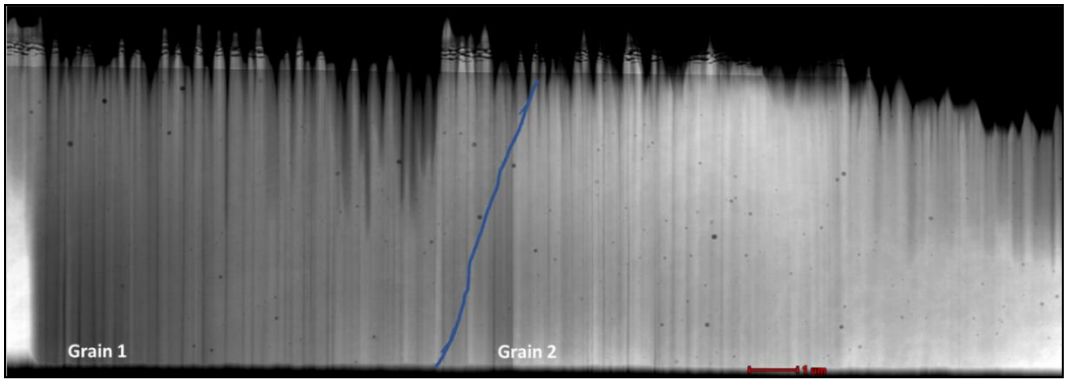

Figure 5.9: STEM image of sample 1A HAADF FIB foil with grain boundary and grains marked. Curtaining from FIB preparation is evident.

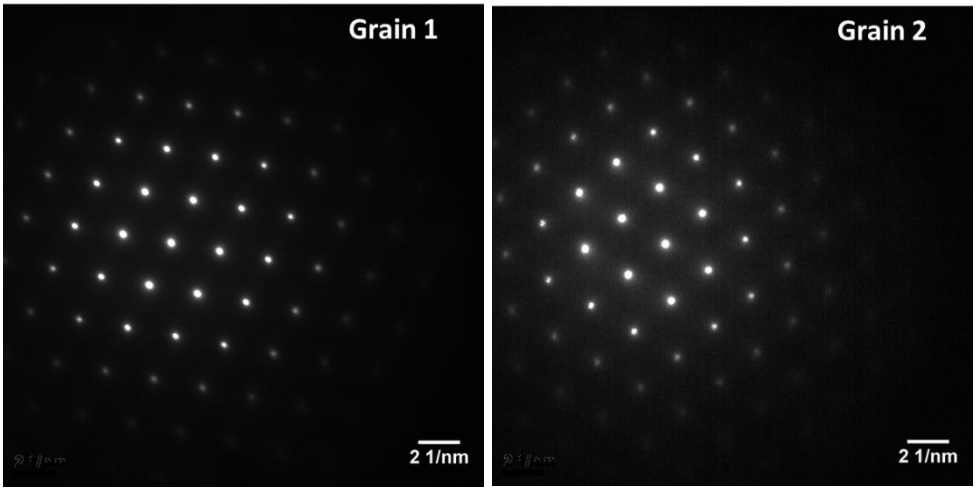

Figure 5.10: Sample 1A diffraction patterns for grains 1 & 2.

Table 5-2: Sample 1A precipitate areas and calculated average diameters.

No. of precipitates	Precipitate Area Fraction	Average Particle Area, nm^2	Average Particle Diameter, nm
785	0.55411%	632.98	28.39

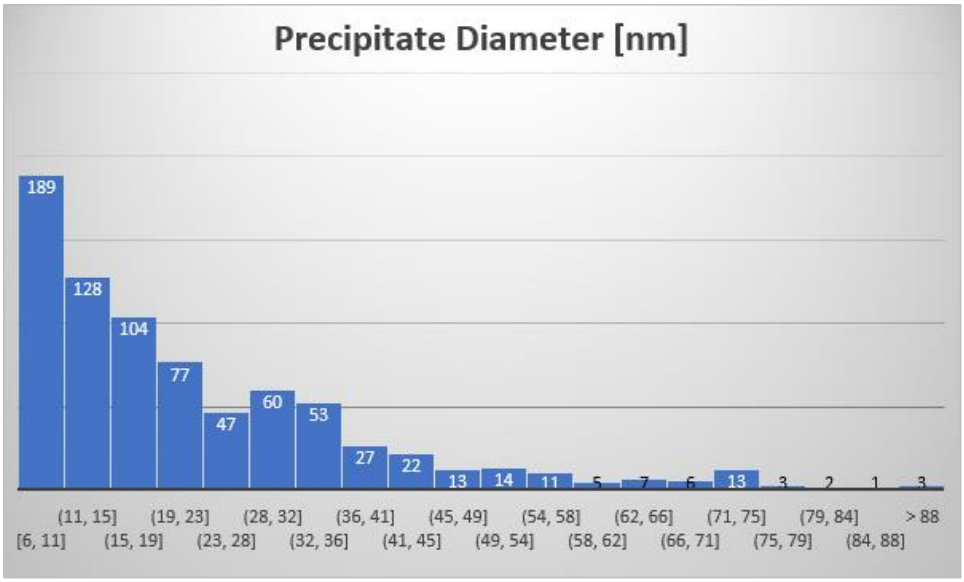

Figure 5.11: Histogram of precipitate diameters present within the 1A FIB foil

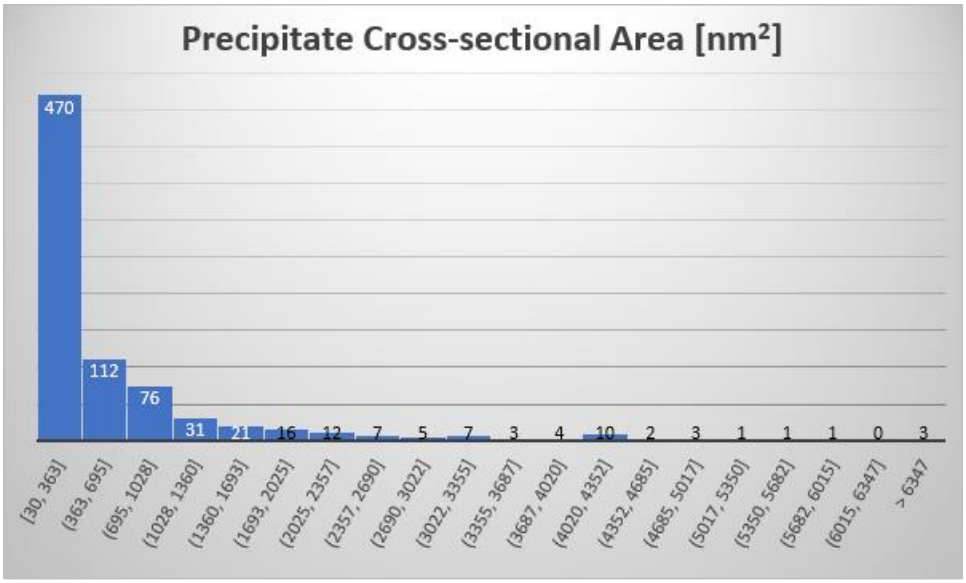

Figure 5.12: Histogram of precipitate cross-sectional areas present within the 1A FIB foil

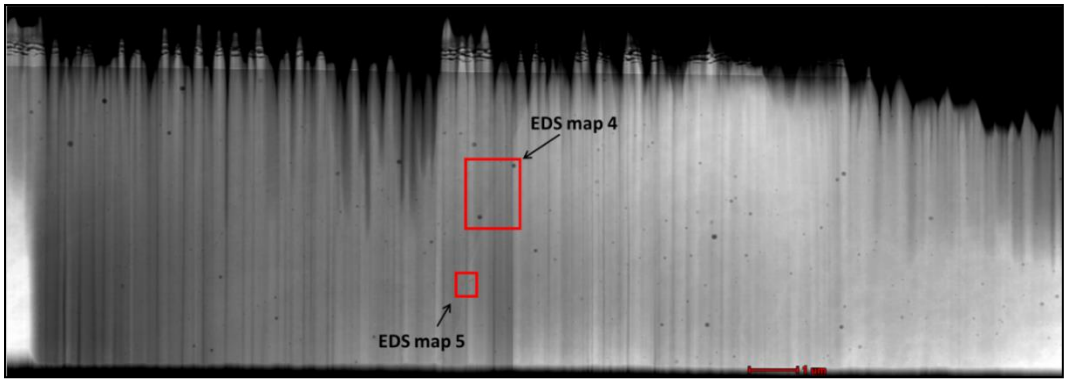

Figure 5.13: Sample 1A FIB foil with EDS scan map areas outlined.

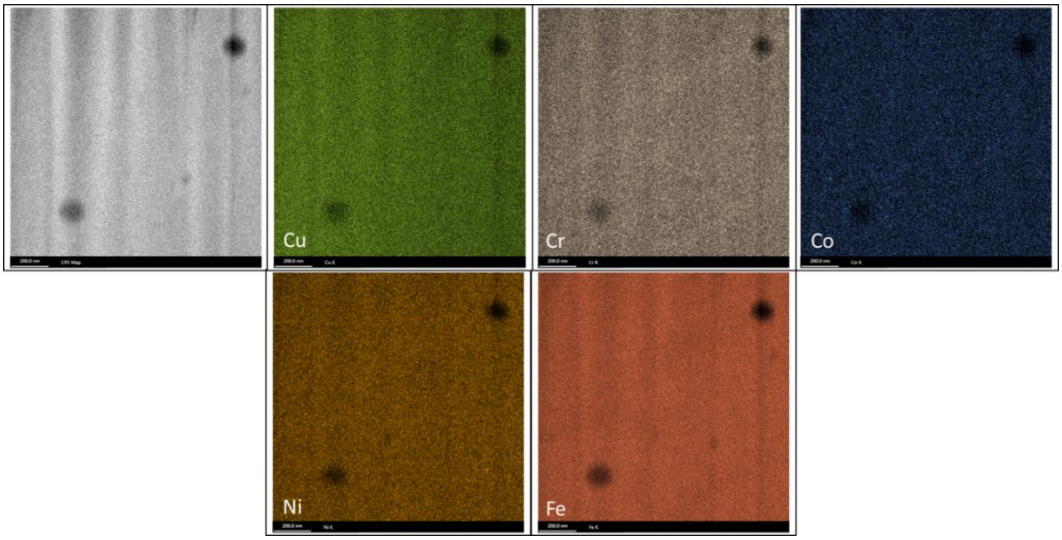

Figure 5.14: Sample 1A EDS map 4 elemental depletion

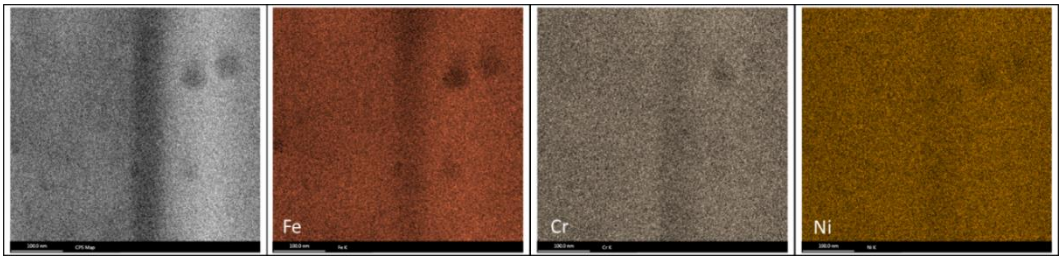

Figure 5.15: Sample 1A EDS map 5 elemental depletion.

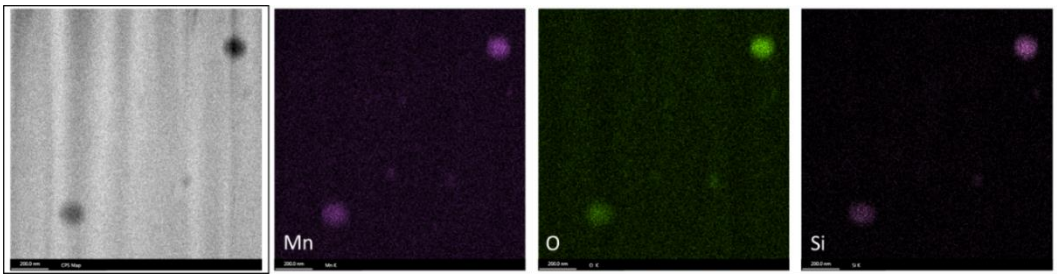

Figure 5.16: Sample 1A EDS map 4 elemental enrichment

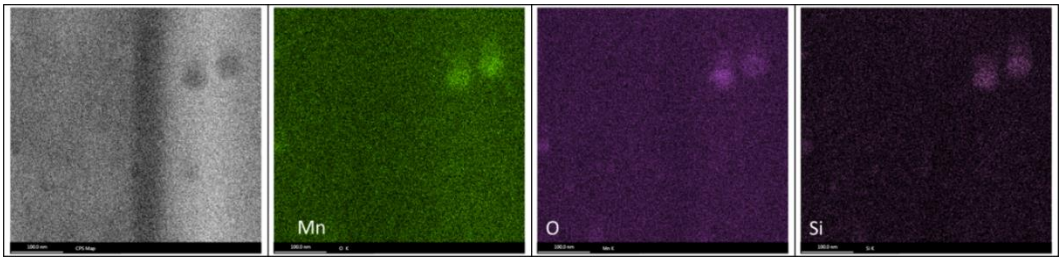

Figure 5.17: Sample 1A EDS map 5 elemental enrichment

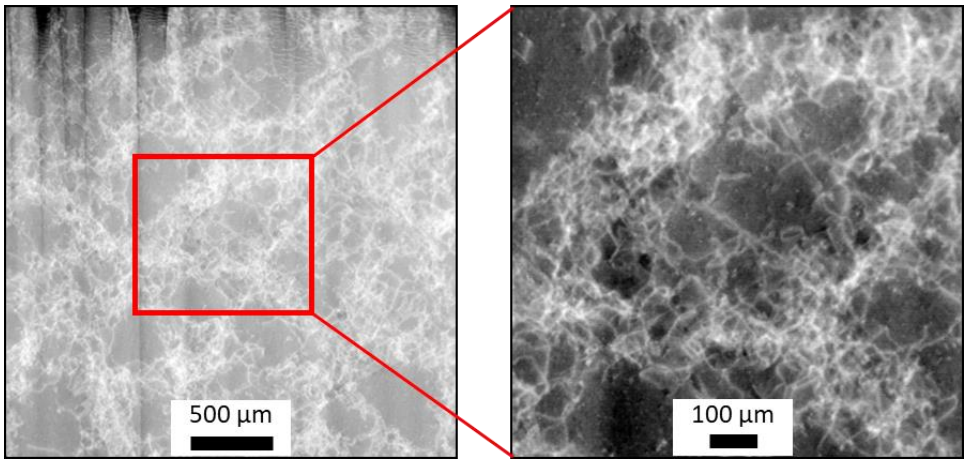

Figure 5.18: (*Left*) Sample 1A, grain 2 dislocation density. (*Right*) Magnified, grain 2 dislocation density.

Table 5-3: Oxygen content of powder collected from the controlled oxygen environment experiment.

Powder Sample	Sieved (Y/N)*	Magnetic (Y/N)	Oxygen [%]	Error [+/-]
DS	N	N	0.127	0.005
DS	Y	Y	0.100	0.005
DS Oversized	Y	Y	0.123	0.005
0 ppm	N	Y	0.036	0.002
0 ppm	N	N	0.034	0.002
2300 ppm	N	Y	0.032	0.002
2300 ppm	N	N	0.032	0.002
4600 ppm	N	Y	0.038	0.002
4600 ppm	N	N	0.034	0.002

*Sieve mesh size is 66 µm

larger than the sieve mesh size (>66 μm) contain more oxygen (0.123 ± 0.005 wt%) than smaller spatter particles (0.100 ± 0.005 wt%). This makes sense as the larger particles would have remained in the liquid state longer than the smaller particles (assuming constant cooling conditions), which would have allowed more time for environmental oxygen to diffuse into the larger particles.

To remove the chance of moisture already present on the powder affecting oxygen analysis values, the powder samples were also dried at 110^{o}C for one hour prior to chemical analysis. Table 5-4 shows that no change in oxygen content was measured between the dried and un-dried samples.

5.1.4.2. Tensile Bars

The results of the bulk chemical analysis of oxygen, nitrogen, and carbon in solid, as-built parts 1E, 2E, and 3E are presented in Figure 5.19. A slight reduction of oxygen within the part correlate with the reduction of oxygen within the build chamber atmosphere, although this effect is very minimal. Additionally, as oxygen decreases in the chamber atmosphere, a slight increase of carbon within the printed parts can be seen.

5.1.5. Mechanical Testing

5.1.5.1. Hardness Mapping

Vickers micro-hardness testing of the XZ planes of samples 1C, 1A, 1D, 1F, 3A, 3F and the XY planes of samples 1C, 1A, 1D, 1F, and 3F using a load of 200 was conducted and converted into hardness maps using an IgorPro program written by Babu [44]. Samples from groups A and F came from parts that were positioned on the build plate in such a way so that ejecta material from the build would neither contaminate the powder bed where they were built before nor after melting (see section 2.2.3). Samples from groups C and D came from parts that were positioned on the build plate in such a way that ejecta from the melting of parts in groups A, B, E, and F had a chance to land in the powder bed prior to the melting of groups C and E (see section 2.2.3). The diagonal purple spots seen in the hardness map of sample 3A coincides to where the sample was cut into two pieces with a saw, and then placed back together within the epoxy mount and is not representative of the material properties of the part at those points.

The average Vickers Hardness (HV) values obtained from the samples are presented in Table 5-5. Figure 5.20 depicts the XZ plane hardness maps with consistent hardness value ranges of 130-250 HV. The hardness values in sample 3F are consistently lower than those in sample 1F. Sample 1A is softer than the other samples in Level 1 and sample 1D seems to have an increasing hardness gradient in the build direction.

Table 5-4: Extended chemical analysis of magnetically separated, oxygen experiment powders.

Element	PB Mag Sieved	DS Mag Sieved	DS Non-Mag Non-Sieved	DS Mag Oversized	error [±]
Carbon	0.015	0.013	0.015	0.012	0.005
Copper	0.072	0.070	0.072	0.069	0.002
Hydrogen	4E-4	4E-4	4E-4	3E-4	1E-4
Manganese	1.49	1.49	1.49	1.45	0.03
Molybdenum	2.45	2.40	2.53	2.41	0.05
Nitrogen	0.099	0.094	0.099	0.093	0.005
Oxygen	**0.039**	**0.106**	**0.120**	**0.129**	**0.002**
Oxygen -DRIED	**0.040**	**0.109**	**0.118**	**0.132**	**0.002**
Silicon	0.59	0.66	0.69	0.66	0.01

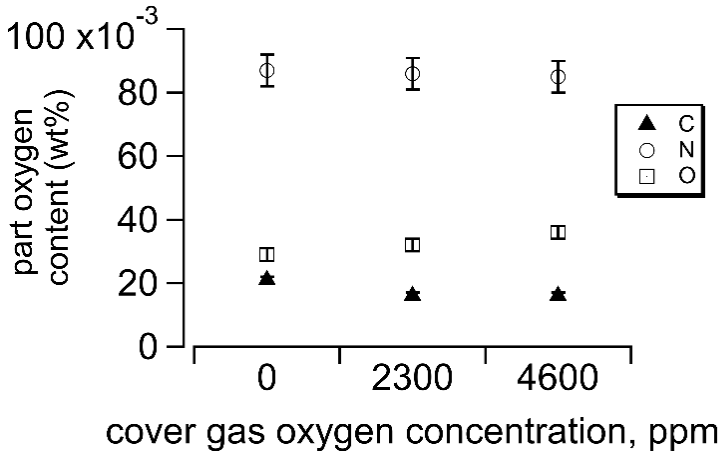

Figure 5.19: Carbon, Oxygen, and Nitrogen weight percent of samples 1E, 2E, and 3E.

Table 5-5: Oxygen Experiment average Vickers Hardness (HV) values

XZ Plane				*XY Plane*		
Sample	**Avg. HV**	**error, ±**		**Sample**	**Avg. HV**	**error, ±**
1C	236	7		1C	226	5
1A	224	9		1A	228	5
1D	239	10		1D	224	6
1F	236	8		1F	224	6
3A	222	11				
3F	223	9		3F	226	8

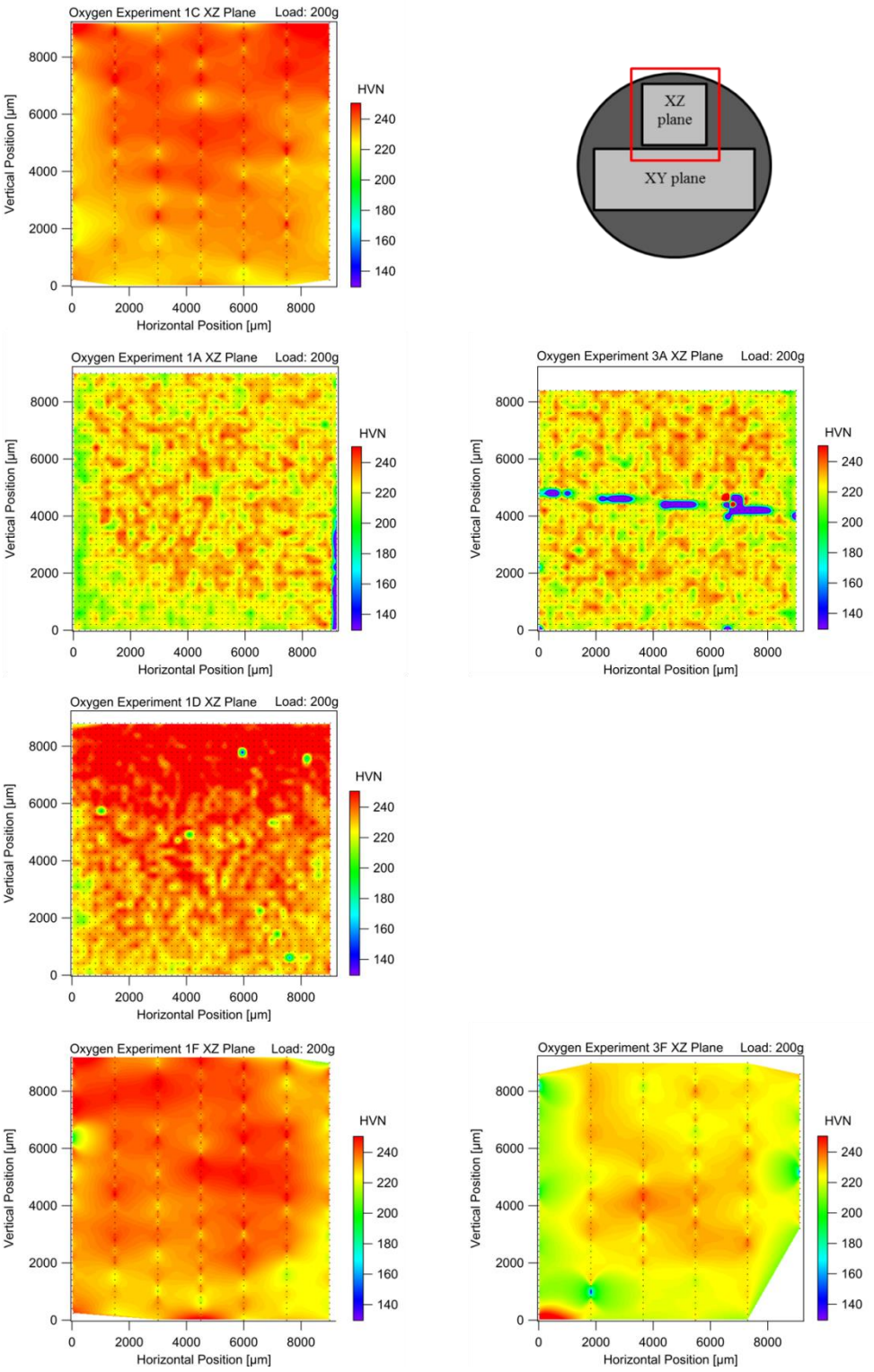

Figure 5.20: IgorPro hardness maps of the XZ plane cross-sections of oxygen experiment samples interpolated from hardness data.

Figure 5.22 shows the same Figure 5.20 hardness values with modified hardness ranges. It can be seen that there exists a trend of decreased relative hardness along the bottoms and sides of the samples compared to the interior and top surface of the samples. This trend lies in contrast to the hardness maps in the XY plane shown in Figure 5.21 which indicate slightly increased hardness along the edges and center of the samples.

5.1.5.2. Tensile Testing

Tensile data from the tensile specimens machined from the as-built tensile bars was collected at ORNL using an MTS™ tensile frame and a 1" extensometer at a strain rate of 0.001 in/sec. Figure 5.23 shows the 0.2% yield strength of the level 1 and level 3 tensile samples. These data represent the material properties of selective laser melt additively manufactured stainless steel 316L in the XY build direction, built in atmospheres of 4600 ppm and 0 ppm oxygen respectively. In order to reduce experimentation time and material feed stock cost, no specimens were built to test the XZ build direction material properties.

The average 0.2% yield strengths (4600ppm: 557(±25.6) MPa, 0ppm: 545(±26.6) MPa) for the oxygen experiment tensile samples is lower and with a larger spread than the average 0.2% yield strength (573.4(±12.6) MPa) from the recyclability experiment, but do not differ much from each other.

5.2. Conclusions

The powder XRD characterization of unmelted powder collected from the powder bed at each level of cover gas oxygen content does not qualitatively demonstrate a difference in the amount of BCC phase present in the powder bed as a function of cover gas oxygen content. Bulk chemical analysis of the same powder samples also does not suggest a correlation between powder bed particle oxygen content and cover gas oxygen content, even between magnetic and non-magnetic particles.

HTXRD shows that the BCC phase present within the spatter sample solidified as a metastable phase with an AC1 temperature of approximately 550°C.

Chemical analyses of parts built under atmospheres containing varying concentrations of oxygen suggest that reducing cover gas oxygen content reduces the oxygen content slightly within as-built parts (~0.008 wt%). TEM analysis confirmed this by finding more nano-oxides within the as-built parts built at higher concentrations of atmospheric oxygen when compared to parts built at low concentrations of atmospheric oxygen. The nano-oxides in the high oxygen atmosphere were also an average of 3 nm bigger in diameter than those inside parts built at low levels of atmospheric oxygen.

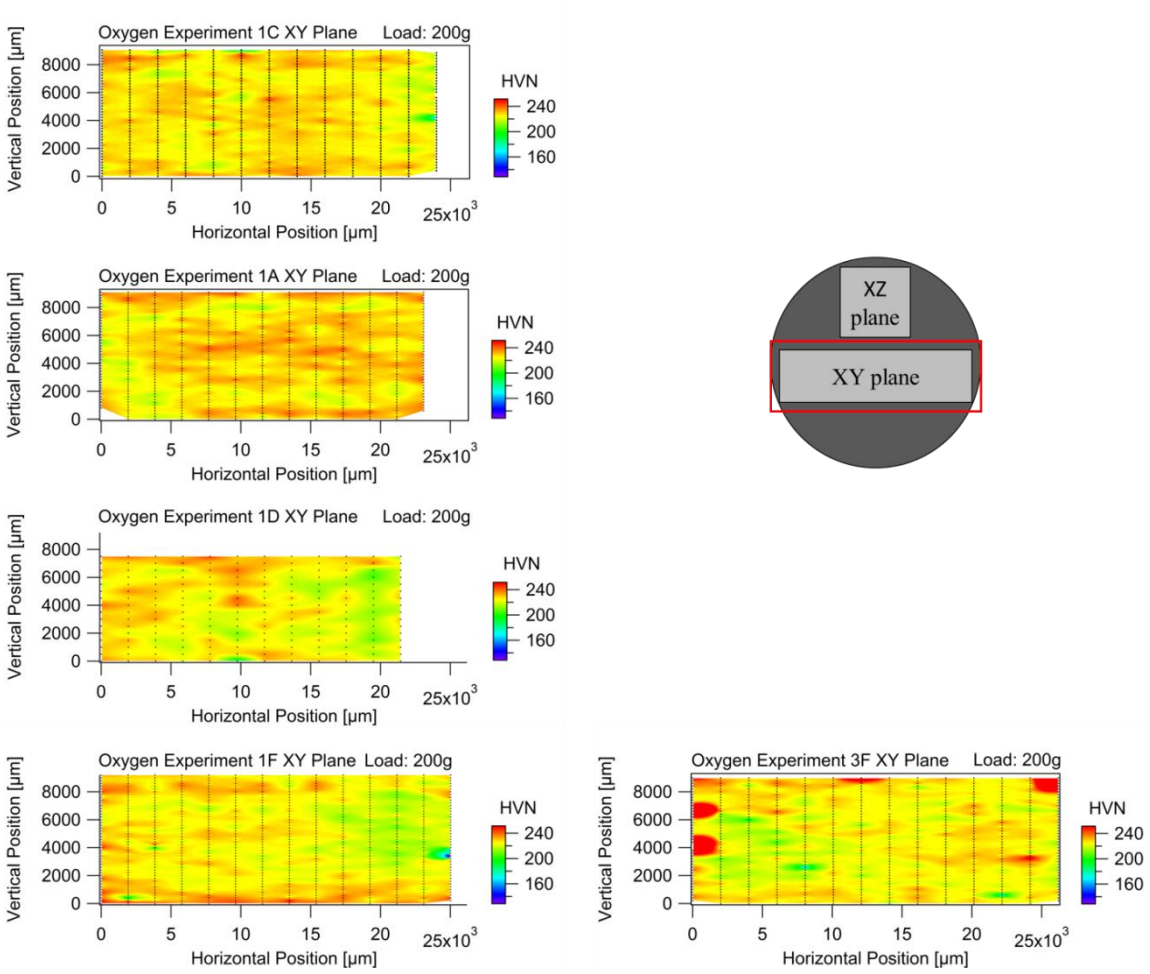

Figure 5.21: IgorPro hardness map of XY plane cross-sections of oxygen experiment samples interpolated from hardness data.

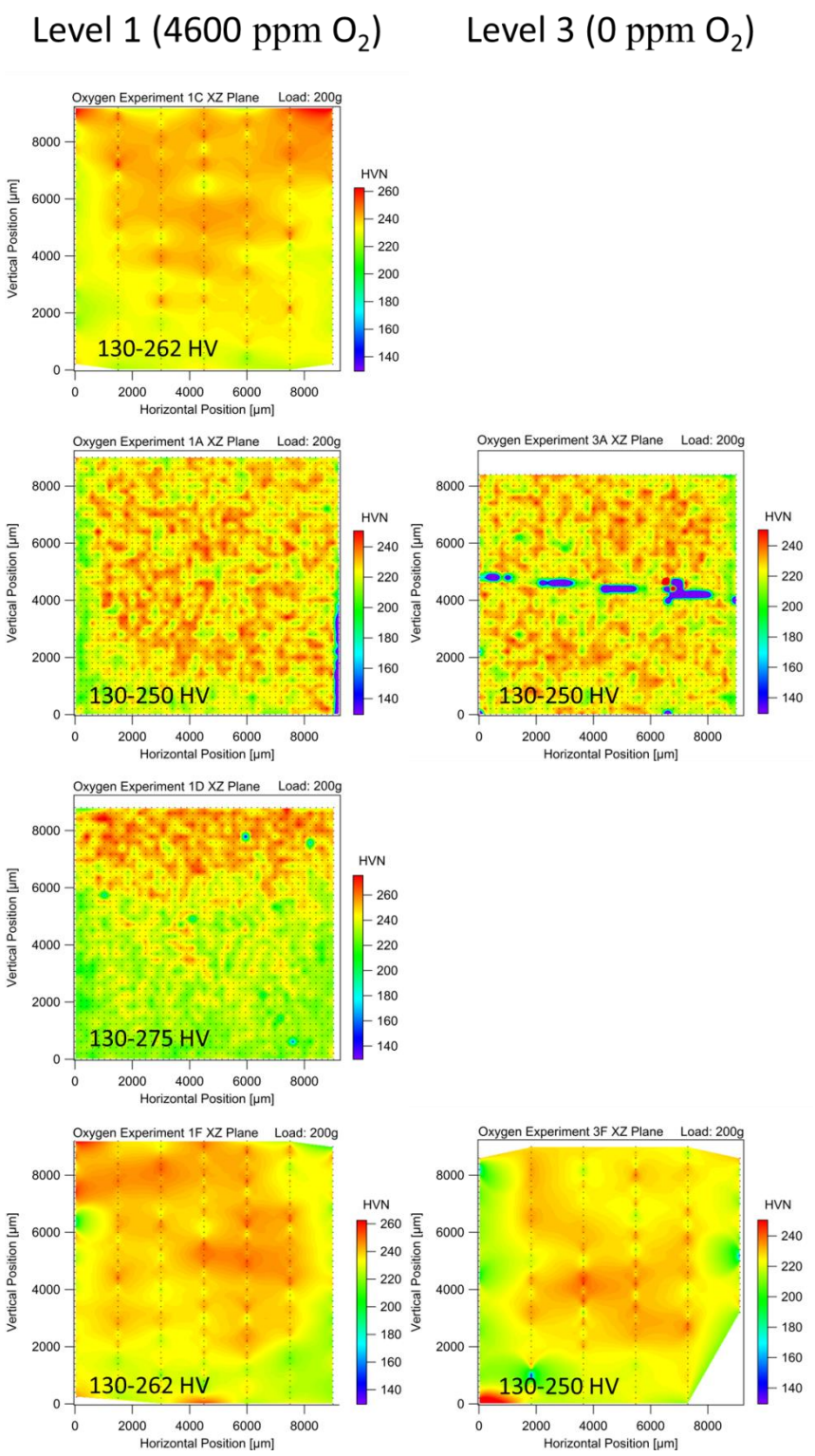

Figure 5.22: IgorPro hardness maps of the XZ plane cross-sections of oxygen experiment samples interpolated from hardness data, with modified hardness ranges to show the existing hardness trends.

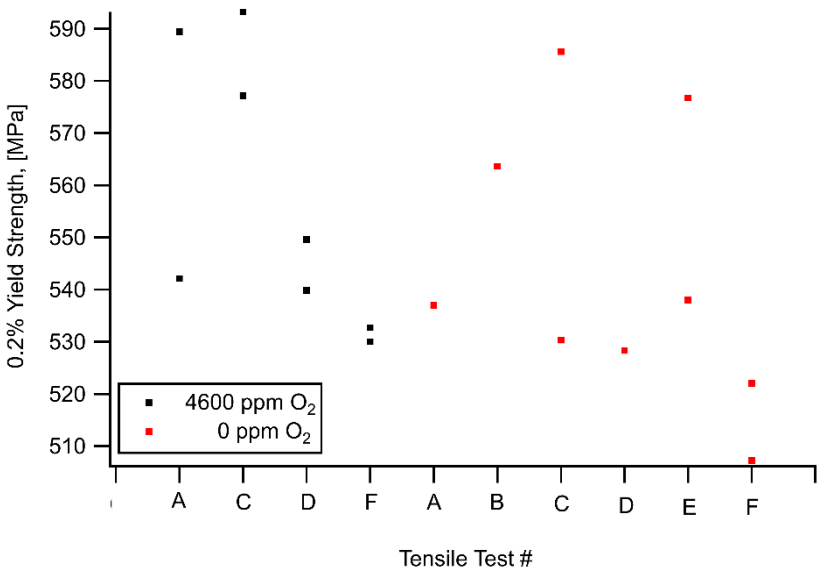

Figure 5.23: 0.2% yield stress of all tensile samples tested, plotted as a function of position on the build plate.

Despite the increase in nano-oxides, mechanical testing results (hardness mapping and tensile testing) indicate that the mechanical properties of additively manufactured 316L parts are insensitive to significant variation of cover gas O_2 concentration in the build chamber during processing.

CHAPTER 6 RECYCLABILITY STUDY

6.1. Characterization Results

6.1.1. Optical Imaging

Large amounts of lack of fusion porosity were found to reside inside of the filler bars, as can be seen in the inverted black and white XZ plane cross-sections of filler bar 1-9. Figure 6.1 shows that the lack of fusion porosity is sparser on the edges and in the top 2 mm of the part. It was observed that the beginning of the relatively pore free region at the top of the filler bar coincides with a point in time during the processing of cycle 1 when the build was paused so that the laser lens cover inside of the build chamber could be cleaned of soot. The amount of time taken to clean the soot off of the lens cover was approximately 20 minutes, during which time the paused build was cooling and exposed to atmosphere conditions. It is thought that by removing the soot from the lens cover, more power from the laser was available for melting this final region which resulted in a more dense build. Since this type of porosity was observed even in the beginning of the build, the occluding effect that soot condensation has on the laser lens must occur fairly rapidly and is assumed to be proportional to the volume of powder melted.

The relatively pore-free regions on either side of the filler bars in Figure 6.1 cannot be explained by removal of soot condensation on the laser lens cover because it is present throughout the entire height of every filler bar sample. It is thought that either the meander laser scan strategy used during the build, or the different laser parameters used for border melting are responsible for this effect. Figure 6.2 gives examples of two commonly used laser scan strategies: meander and island. The meander scan strategy guides the laser path in a straight line across the entirety of the part. When the path reaches the edge of the part, it moves at a right angle the distance of the hatch spacing and begins to melt in a straight line in the opposite direction of the first line scan. This pattern repeats until the entire area of the part for that powder layer has been covered by the beam path. It can be seen that at the turn-around point of the beam path, namely the edges of the part, the material located in those areas experiences an effective pre-heat from the previous line scan before being melted in turn. Material located at the edges of a part may also experience the insulating effects of the adjacent powder bed, which reduces thermal conductivity and allows the edges of the part to hold onto its heat longer, also contributing to the pre-heat effect.

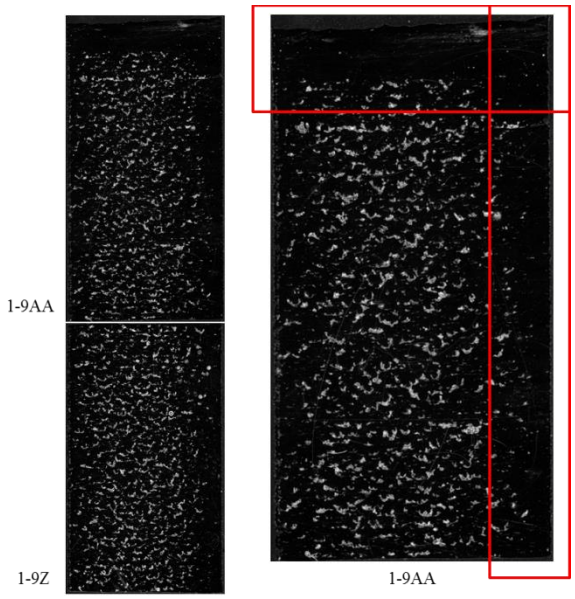

Figure 6.1: Inverted optical images of XZ plane cross-sections of samples 1-9Z and 1-9AA (see Figure 2.36) revealing reduced edge porosity.

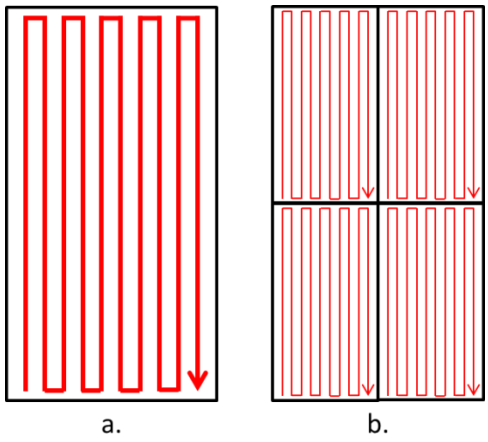

Figure 6.2: Laser beam paths for (a) "meander" melt pattern, and (b) "island" melt pattern.

The areal energy density equation of a circular weld pool created by a single pulse of the laser in the AM250 was taken to be represented by Eq. 6-1, where ρ_E is the areal energy density, P is the laser power, A_b is the cross-sectional area of the laser beam at the build surface, and t_e is the exposure time of the beam pulse.

$$\rho_E = \frac{P t_e}{A_b} \frac{J}{mm^2} \tag{6-1}$$

Varying any of the values on the right-hand side of Eq. 6-1 would have the effect of varying the areal energy density of the laser experienced by the powder bed. The machine parameter used to vary A_b in the AM250 is the focus offset value. Negative values of focus offset move the focal point of the laser beam above the build surface. Positive values of focus offset move the focal point down below the build surface, increasing the beam area at the build surface.

As can be seen in Appendix A, the laser melt parameters for melting the borders of the part were different than those used to melt the bulk volume of the part. Specifically, the border melt uses a lower power (175W compared to 200W), a closer point-to-point spacing (25µm versus 65µm), and a longer exposure time (130µs versus 110µs) than the volume melt. Using Eq. 6-1 and beam diameter of 70µm, the border melting parameters would provide an areal energy density for melting ~0.2 J/mm^2 greater than the parameters used for volume melting.

In addition to this increased areal energy density, the reduced point-to-point distance between melt spots in the border laser parameters would allow for greater overlap (i.e. remelting) of the weld pools. The remelting of an already solidified region as opposed to a purely powder region could allow previously formed lack of fusion defects to heal, resulting in the relatively defect free region seen at the edges of the parts in Figure 6.1.

6.1.2. Powder Size Distribution

The incremental volume percentage (q%) and percent undersized powder size distributions of the bed and downstream powder samples from cycles 1 through 4 are shown in Figure 6.3 and Figure 6.4. It can be seen that the powder distribution of the bed powder experiences a widening of the powder size distribution and a coarsening effect as a function of reuse. Powder size distribution measurements of the downstream powder exhibit the expected coarsening effect of large spatter particles present in the samples and does not show a clear relationship to the number of reuses.

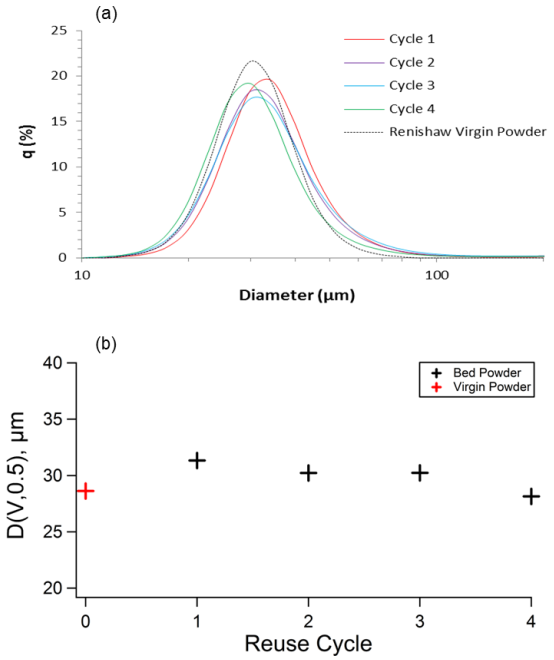

Figure 6.3: (a) Incremental volume percentage powder size distribution and (b) D(0.5) of powder samples as a function of reuse.

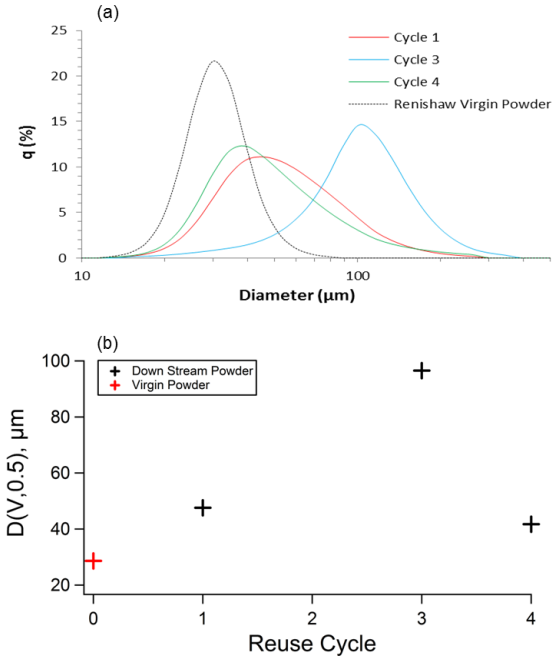

Figure 6.4: (a) Incremental volume percentage powder size distribution and (b) D(0.5) of DS powder samples as a function of reuse.

6.1.3. Chemical Analysis

6.1.3.1. Powder

Elemental chemical analysis of virgin powder and downstream powder show little change in composition except for an increase in oxygen in the downstream powder.

Figure 6.5 shows that the measured oxygen content in the bed powder varies as a function of reuse up to what seems like an equilibrium point. The difference between the upper error bar of cycle 0 and the lower error bar of cycle 4 is 0.005 wt% oxygen, or approximately 170 ppm.
Figure 6.6 shows that the oxygen content of the downstream powder, while consistently high, does not seem to be significantly affected by powder reuse.

6.1.3.2. Tensile Bars

Chemical analysis was also conducted on the tensile specimens and the results are shown in
Figure 6.8, and Table 6-2 through Table 6-5. Samples were sectioned off of the end of the machined tensile specimens as shown in Figure 6.7. Of special note in Table 6-2 and Table 6-3 are the elemental concentrations of nitrogen, silicon, phosphorous, manganese, molybdenum, and copper. Molybdenum and phosphorous both show wt. % increases in the as-built parts when compared to virgin powder; while nitrogen, silicon, and manganese show reduced weight percentages. Copper was measurably increased in all of the tested samples compared to virgin powder, and large increases were observed in both the top and bottom tensile bars from samples 2-3 and 2-6. Copper is not specified as an alloying element for stainless 316L steel and therefor its presence in both the virgin powder as well as the as-built parts is considered contamination. It is unknown where the increase in copper in the as-built parts originates.

6.1.4. Tensile Testing

6.1.4.1. As-Built, Machined

Tensile data from the tensile specimens machined from the as-built tensile bars were collected at ORNL using an MTS™ tensile frame and a 1” extensometer at a strain rate of 0.001 in/sec. The stress-strain curves collected from every sample tested from each recycle cycle are overlaid and presented in Figure 6.9. The yield stress does not vary as a function of cycle number. However, the ultimate yield strengths of all samples from cycle 4 that were tested exceed those of all other samples from other cycles. Figure 6.10 through Figure 6.16 with associated tables Table 6-6 through Table 6-10 depict the stress-strain data collected from each recycle cycle number.

Table 6-1: Virgin stainless steel 316L powder and downstream powder elemental weight percentages. Downstream powder is composed primarily of spatter particles.

Elemental ID	Virgin Powder wt%	Down Stream Powder wt%	Error [+/-]
Chromium	17.73	17.73	0.3
Nickel	12.45	12.54	0.2
Molybdenum	2.22	2.25	0.05
Sulfur	0.005	0.004	0.0005
Silicon	0.66	0.66	0.01
Oxygen	0.32	0.186	0.005
Phosphorus	0.0066	0.0054	0.001
Nitrogen	0.1	0.098	0.005
Carbon	0.015	0.014	0.005
Hydrogen	0.0009	0.0007	0.00002

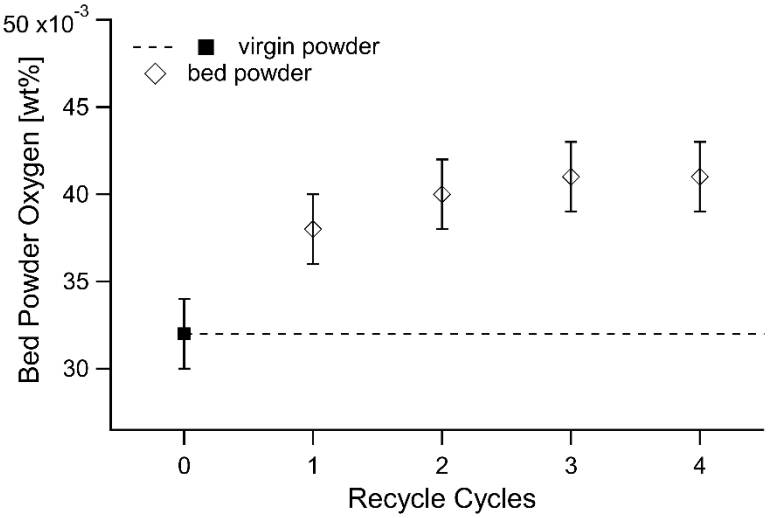

Figure 6.5: Oxygen content in the powder bed samples seems to reach an equilibrium level as a function of powder reuse. The red square corresponds to the feed stock of cycle 5, whose history is unknown but is presumed to have been recycled many times.

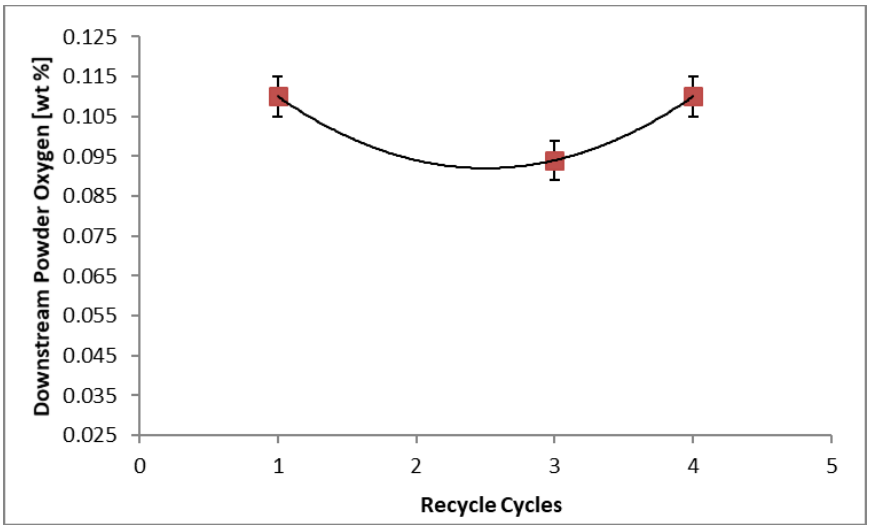

Figure 6.6: Oxygen content in downstream powder samples from cycles 1, 3, and 4 as a function of powder reuse.

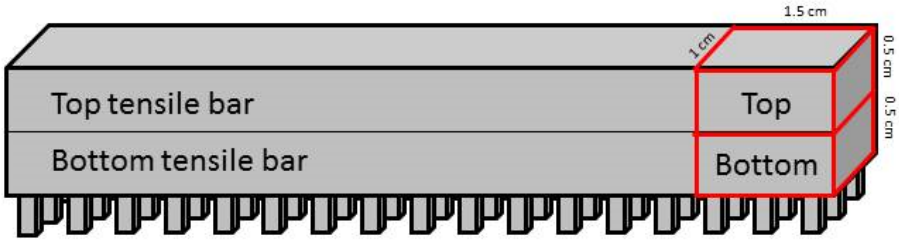

Figure 6.7: Schematic depicting how the tensile bars were sectioned for bulk chemical analysis.

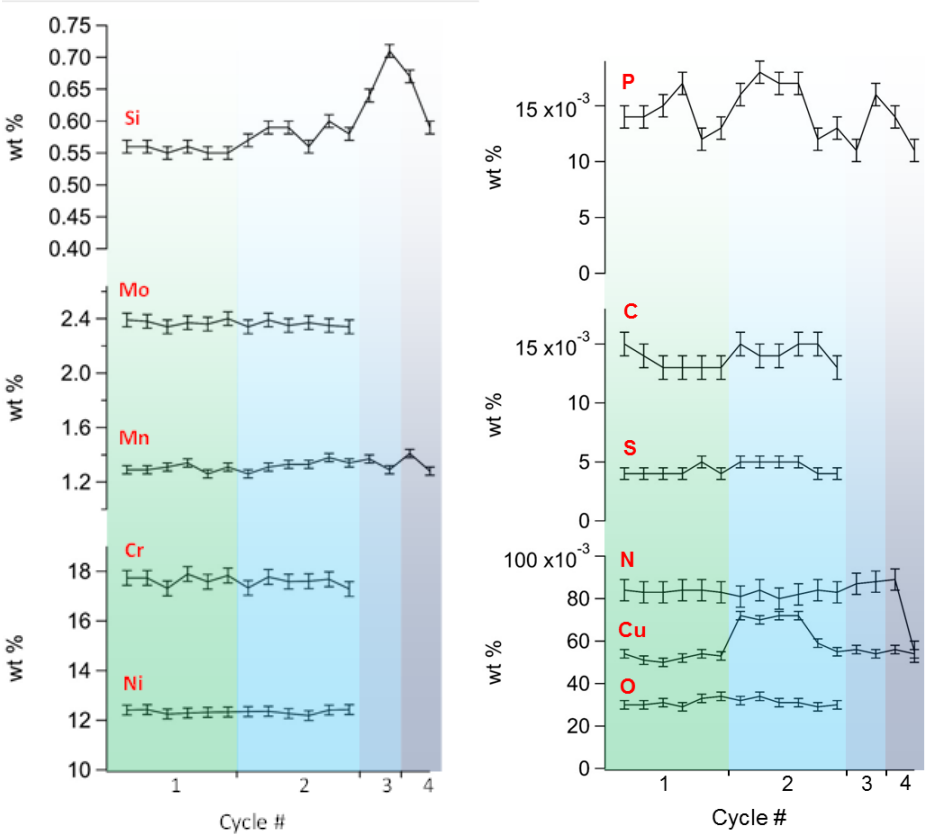

Figure 6.8: Weight percentages of elements present in the tensile bars shown in Table 6-2 through Table 6-5.

Table 6-2: Elemental weight percentages in as-built tensile bars from cycle 1 compared to virgin powder

Sample	C	N	O	Si	P	S	Cr	Ni	Mn	Mo	Cu
Virgin Powder	0.015	**0.1**	0.032	**0.66**	**0.0066**	0.005	17.73	12.45	**1.44**	**2.22**	**0.046**
1-3B	0.015	**0.084**	0.030	**0.56**	**0.014**	0.004	17.73	12.41	**1.29**	**2.39**	**0.054**
1-3T	0.014	**0.083**	0.030	**0.56**	**0.014**	0.004	17.73	12.43	**1.29**	**2.38**	**0.051**
1-6B	0.013	**0.083**	0.031	**0.55**	**0.015**	0.004	17.31	12.25	**1.31**	**2.34**	**0.050**
1-6T	0.013	**0.084**	0.029	**0.56**	**0.017**	0.004	17.89	12.29	**1.34**	**2.37**	**0.052**
1-8B	0.013	**0.084**	0.033	**0.55**	**0.012**	0.005	17.58	12.32	**1.26**	**2.36**	**0.054**
1-8T	0.013	**0.083**	0.034	**0.55**	**0.013**	0.004	17.83	12.33	**1.31**	**2.40**	**0.053**
Error [+/-]	*0.001*	***0.005***	*0.002*	***0.01***	***0.001***	*0.0005*	*0.3*	*0.2*	***0.03***	***0.05***	***0.002***
average	0.014	**0.084**	0.031	**0.56**	**0.014**	0.004	17.68	12.34	**1.30**	**2.37**	**0.052**
St. Dev.	*0.001*	***0.001***	*0.002*	***0.005***	***0.002***	*0.0004*	*0.21*	*0.07*	***0.03***	***0.02***	***0.002***

Table 6-3: Elemental weight percentages in as-built tensile bars from cycle 2 compared to virgin powder

Sample	C	N	O	Si	P	S	Cr	Ni	Mn	Mo	Cu
Virgin Powder	0.015	**0.1**	0.032	**0.66**	**0.0066**	0.005	17.73	12.45	**1.44**	**2.22**	**0.046**
2-3B	0.015	**0.081**	0.032	**0.57**	**0.016**	0.005	17.33	12.35	**1.26**	**2.34**	**0.072**
2-3T	0.014	**0.084**	0.034	**0.59**	**0.018**	0.005	17.77	12.36	**1.31**	**2.39**	**0.070**
2-6B	0.014	**0.080**	0.031	**0.59**	**0.017**	0.005	17.59	12.27	**1.33**	**2.35**	**0.072**
2-6T	0.015	**0.082**	0.031	**0.56**	**0.017**	0.005	17.60	12.19	**1.33**	**2.37**	**0.072**
2-8B	0.015	**0.084**	0.029	**0.60**	**0.012**	0.004	17.68	12.41	**1.38**	**2.35**	**0.059**
2-8T	0.013	**0.083**	0.030	**0.58**	**0.013**	0.004	17.29	12.43	**1.34**	**2.34**	**0.055**
Error [+/-]	*0.001*	***0.005***	*0.002*	***0.01***	***0.001***	*0.0005*	*0.3*	*0.2*	***0.03***	***0.05***	***0.002***
average	0.014	**0.082**	0.031	**0.58**	**0.016**	0.005	17.54	12.34	**1.33**	**2.36**	**0.067**
St. Dev.	*0.001*	***0.002***	*0.002*	***0.015***	***0.002***	*0.0005*	*0.19*	*0.09*	***0.04***	***0.02***	***0.0076***

Table 6-4: Elemental weight percentages in as-built tensile bars from cycle 3 compared to virgin powder

Sample	C	N	O	Si	P	S	Cr	Ni	Mn	Mo	Cu
Virgin Powder	0.015	**0.1**	0.032	**0.66**	**0.0066**	0.005	17.73	12.45	**1.44**	**2.22**	**0.046**
3-6T		**0.087**		**0.640**	**0.011**				**1.37**		**0.056**
3-8B		**0.088**		**0.710**	**0.016**				**1.29**		**0.054**
Error [+/-]	*0.001*	***0.005***	*0.002*	***0.01***	***0.001***	*0.0005*	*0.3*	*0.2*	***0.03***	***0.05***	***0.002***
average		**0.0875**		**0.675**	**0.0135**				**1.34**		**0.055**
St. Dev.		***0.0007***		***0.05***	***0.004***				***0.057***		***0.0014***

Table 6-5: Elemental weight percentages in as-built tensile bars from cycle 4 compared to virgin powder

Sample	C	N	O	Si	P	S	Cr	Ni	Mn	Mo	Cu
Virgin Powder	0.015	**0.1**	0.032	**0.66**	**0.0066**	0.005	17.73	12.45	**1.44**	**2.22**	**0.046**
4-3B		**0.089**		**0.670**	**0.014**				**1.410**		**0.056**
4-6B		**0.055**		**0.590**	**0.011**				**1.280**		**0.054**
Error [+/-]	*0.001*	***0.005***	*0.002*	***0.01***	***0.001***	*0.0005*	*0.3*	*0.2*	***0.03***	***0.05***	***0.002***
average		**0.072**		**0.630**	**0.013**				**1.345**		**0.055**
St. Dev.		**0.024**		**0.057**	**0.002**				**0.09**		**0.0014**

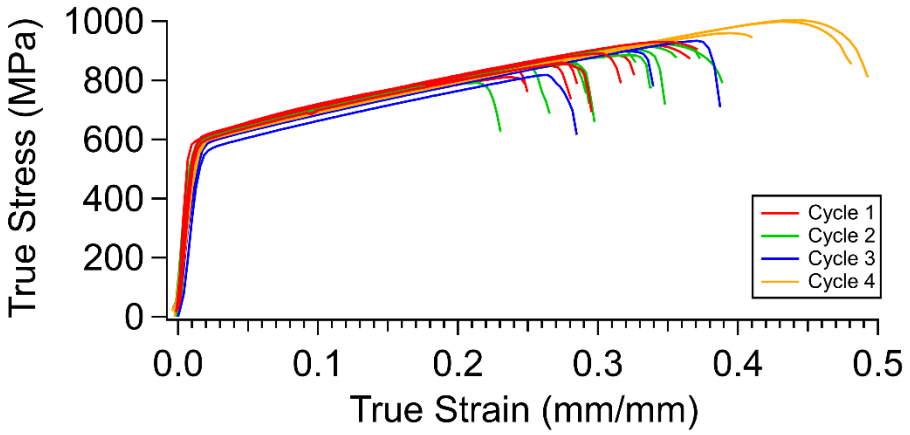

Figure 6.9: Overlaid tensile test data from cycles 1-4.

Table 6-6: Material property and curve fit data for cycle 1 tensile specimens tested in the XY build plane.

Fit name	e_0	n	K	UTS [MPa]	0.2% YP [MPa]	Elastic Modulus [GPa]	Elongation %	RA %
1-3B	0.1890	0.4445	1230.8	668.9	577.6	174.21	34.44	43.95%
1-3T	0.1776	0.4203	1222.8	670.4	587.6	173.45	39.69	47.48%
1-4B	0.1739	0.4218	1216.5	666.8	573.5	176.71	38.11	36.29%
1-4T	0.1757	0.4203	1208.4	660.6	576.1	177.60	36.13	40.20%
1-5B	0.1948	0.4433	1234.7	678.1	588.6	182.89	49.27	64.12%
1-5T	0.1783	0.4222	1216.7	666.0	582.5	185.05	31.83	34.04%
1-6B	0.1950	0.4432	1234.7	676.4	592.8	178.32	46.94	61.20%
1-6T	0.1840	0.4304	1216.9	666.2	579.7	176.08	40.67	51.08%
1-8B	0.1585	0.3962	1179.2	647.9	560.0	173.19	29.06	34.56%
1-8T	0.1769	0.4189	1209.8	663.4	578.3	178.68	34.11	37.47%

Elongation is engineering strain
n is the strain hardening exponent
K is the strength coefficient

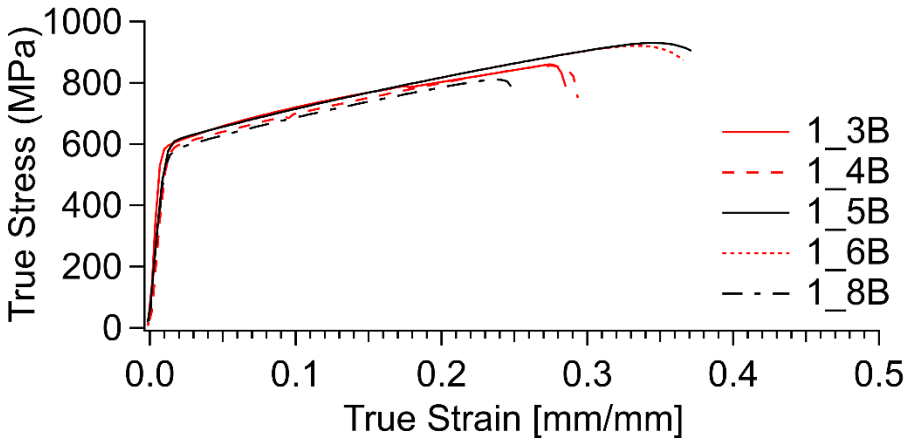

Figure 6.10: True stress true strain, cycle 1 bottom tensile specimen data. Specimens were tested in the XY build plane.

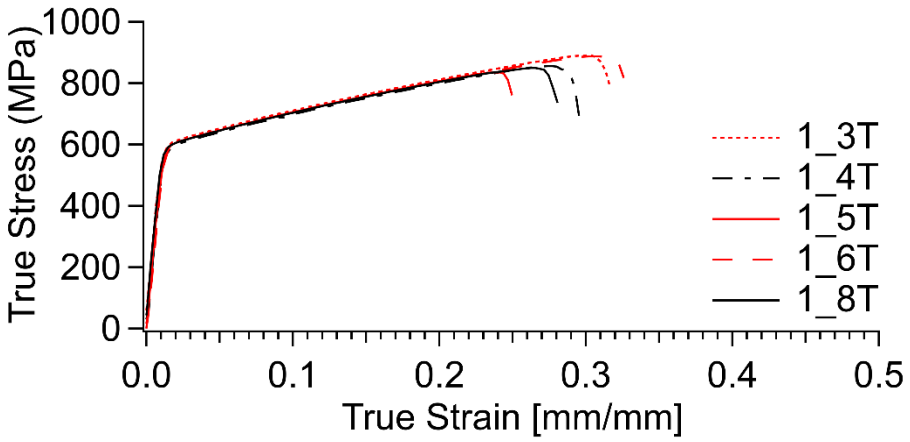

Figure 6.11: True stress true strain, cycle 1 top tensile specimen data. Specimens were tested in the XY build plane.

Table 6-7: Material property and curve fit data for cycle 2 tensile specimens tested in the XY build plane.

Fit name	e_0	n	K	UTS [MPa]	0.2% YP [MPa]	Elastic Modulus [GPa]	Elongation %	RA %
2-3B	0.1867	0.4388	1234.0	671.8	582.2	182.96	41.43	53.15%
2-3T	0.1866	0.4412	1213.5	659.3	571.4	175.72	41.59	44.79%
2-4B	0.1834	0.4314	1232.5	673.6	586.6	176.73	44.37	45.52%
2-4T	0.1713	0.4145	1209.0	662.4	573.2	173.57	35.26	41.20%
2-5B	0.1836	0.4312	1235.9	681.4	590.7	184.18	57.97	51.15%
2-5T	0.1791	0.4246	1212.0	662.0	571.5	179.76	32.81	39.70%
2-6B	0.2061	0.4654	1238.8	674.7	588.0	186.79	46.50	57.09%
2-6T	0.1857	0.4360	1209.6	660.5	570.0	177.38	35.31	35.17%
2-7B	0.1966	0.4528	1233.1	671.2	585.0	185.89	49.10	61.18%
2-7T	0.1809	0.4301	1200.7	654.8	570.8	183.71	36.51	44.90%
2-8B	0.1851	0.4261	1215.9	670.0	584.2	184.18	42.93	53.14%
2-8T	0.1379	0.3529	1154.9	647.5	566.7	178.19	28.00	36.00%

Elongation is engineering strain
n is the strain hardening exponent
K is the strength coefficient

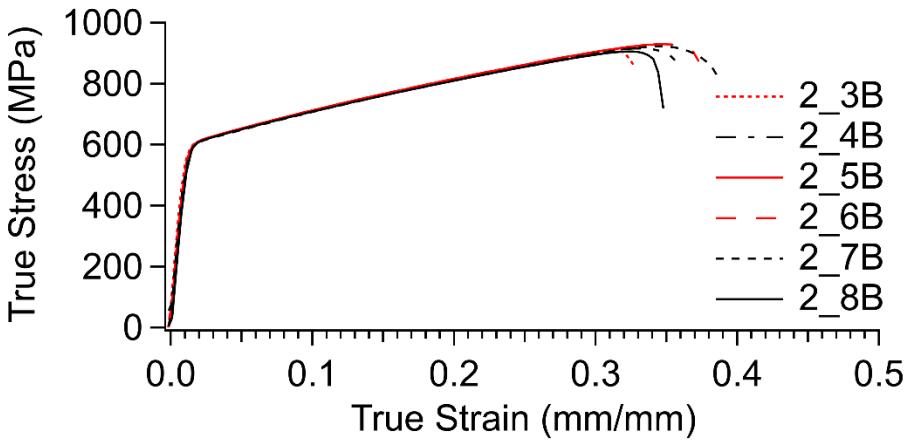

Figure 6.12: True stress true strain, cycle 2 bottom tensile specimen data. Specimens were tested in the XY build plane.

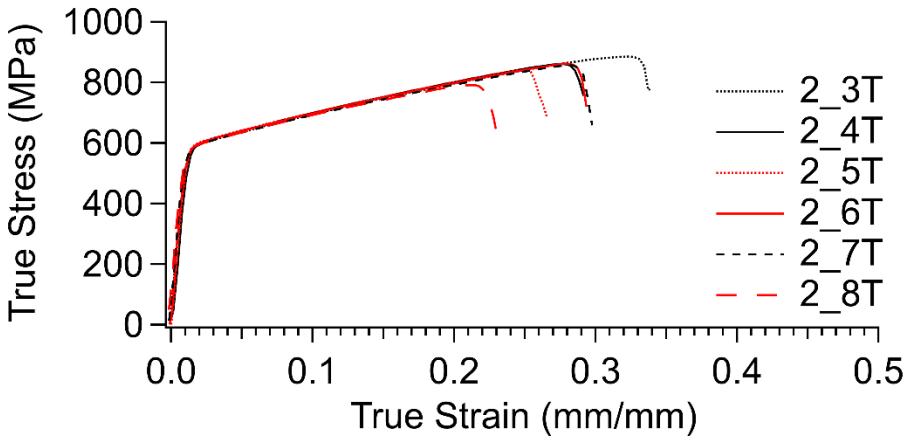

Figure 6.13: True stress true strain, cycle 2 top tensile specimen data. Specimens were tested in the XY build plane.

Table 6-8: Material property and curve fit data for cycle 3 tensile specimens tested in the XY build plane.

Fit name	e_0	n	K	UTS [MPa]	0.2% YP [MPa]	Elastic Modulus [GPa]	Elongation %	RA %
3-5T	0.1267	0.3470	1178.1	659.9	573.8	199.30	44.45	28.97%
3-8B	0.1292	0.3524	1177.3	657.6	568.6	198.80	54.01	47.76%
3-8T	0.1062	0.3199	1130.3	636.8	543.5	203.32	35.95	36.17%

Elongation is engineering strain
n is the strain hardening exponent
K is the strength coefficient

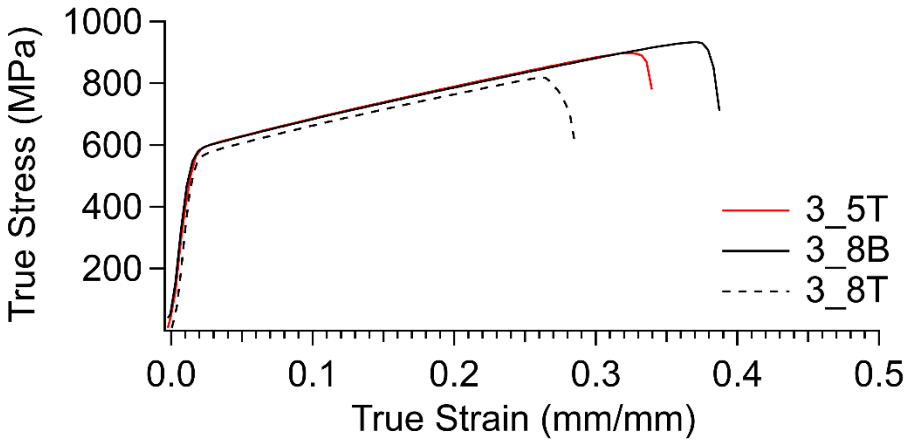

Figure 6.14: True stress true strain, cycle 3 tensile specimen data. Specimens were tested in the XY build plane.

Table 6-9: Material property and curve fit data for cycle 4 tensile specimens tested in the XY build plane.

Fit name	e_0	n	K	UTS [MPa]	0.2% YP [MPa]	Elastic Modulus [GPa]	Elongation %	RA %
4-4T	0.1582	0.1670	1211.7	666.3	578.2	216.05	64.43	64.83%
4-5T	0.1582	0.2220	1210.7	667.7	581.9	229.13	62.72	60.87%
4-8T	0.1392	0.2640	1193.1	663.2	572.2	207.98	53.10	47.49%

Elongation is engineering strain
n is the strain hardening exponent
K is the strength coefficient

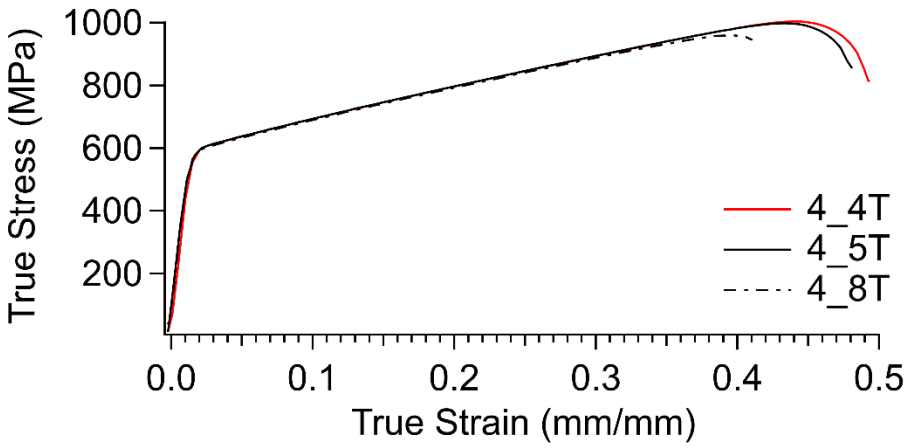

Figure 6.15: True stress true strain, cycle 4 tensile specimen data. Specimens were tested in the XY build plane.

Table 6-10: Material property and curve fit data for cycle 5 tensile specimens tested in the XY build plane.

Fit name	e_0	n	K	UTS [MPa]	0.2% YP [MPa]	Elastic Modulus [GPa]	Elongation %	RA %
5-4B	0.1139	0.2260	1182.3	668.4	583.6	211.13	55.39	62.15%
5-4T	0.1067	0.3900	1168.6	668.2	584.0	204.84	42.98	43.00%
5-5B	0.1389	0.2140	1200.4	678.6	594.8	213.73	55.63	57.06%
5-5T	0.1338	0.3845	1239.3	672.7	576.5	210.78	49.64	53.06%

Elongation is engineering strain
n is the strain hardening exponent
K is the strength coefficient

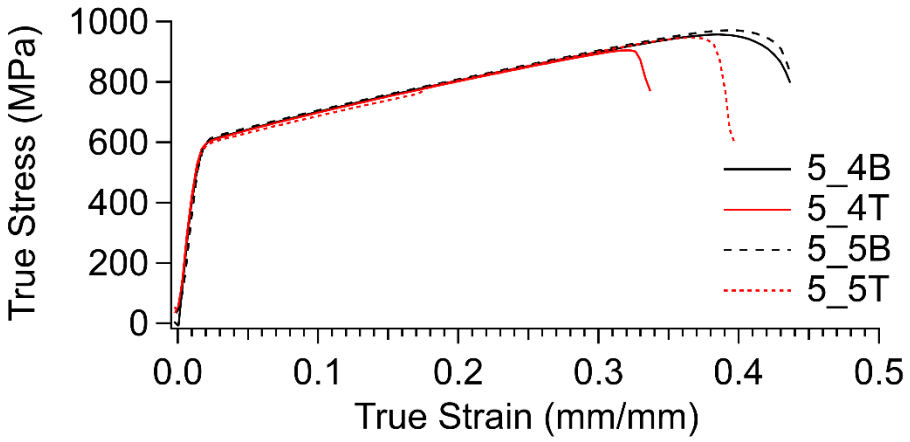

Figure 6.16: True stress true strain, cycle 5 tensile specimen data. Specimens were tested in the XY build plane.

The engineering stress strain data was converted to true stress and true strain values and fitted using IgorPro v6.37 with a cubic spline, pre-averaging to 100 nodes with 5000 destination points. An IgorPro line fit was used to obtain elastic modulus values from the elastic portions of each stress strain curve as well as to identify the 0.2% yield strengths. The IgorPro Curve Fitting function was used to fit the Datsko strain hardening equation (Eq. 6-2) to the plastic portions of the curve which allowed for the evaluation of the amount of inherent strain ε_0, strength coefficient K, and strain-hardening coefficient n [45].

$$\sigma_T = K(\varepsilon_0 + \varepsilon_T)^n \quad (6\text{-}2)$$

where σ_T is the true stress and ε_T is the true strain. The values obtained for K, n, 0.2% yield strength, UTS, elongation, reduced area percentage, the elastic modulus, and the inherent strain for the fit to Eq. 6-2 for each tensile test performed can be found in Table 6-6 through Table 6-10.

6.1.4.2. Annealed

Three tensile samples were machined and then annealed, each at a specific temperature and for a specific length of time. Details of the annealing process are provided in section 2.3.2.

Tensile data from the tensile specimens machined from the as-built tensile bars were collected at room temperature at ORNL using an MTS™ tensile frame and a 1" extensometer at a strain rate of 0.001 in/sec. The stress-strain curve of the sample annealed at 600ºC for 1 hour is presented in Figure 6.17. The stress-strain curves collected from the two other samples are overlaid onto a stress-strain curve of an un-annealed tensile sample and presented in Figure 6.18. As is typical of highly cold-worked wrought material, the yield point of the tensile samples is seen to decrease as a function of anneal time/temperature. Elongation values also increase as a function of anneal time/temperature, though it is not known if this effect can be attributed to the annealing process or some other characteristic of the tensile samples, such as pore size and location within the samples themselves.

6.1.5. Transmission Electron Microscopy

6.1.5.1. Filler Bar

Transmission electron microscopy was performed on two samples obtained from near the center of sample 2-10K. Sample 2-10K was a filler bar and was not subjected to tensile testing. The TEM sample from 2-10K was obtained from the same build height as that which the tensile specimens were built at.

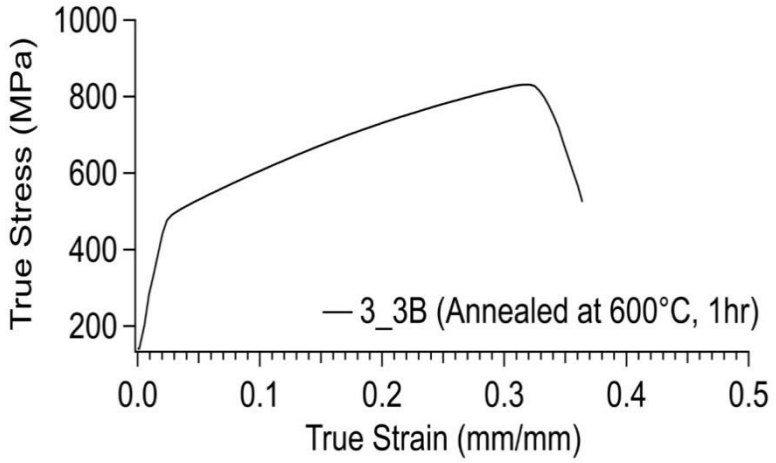

Figure 6.17: True stress true strain, cycle 3-3B tensile specimen data after annealing at 600ºC for 1 hour. Specimen was tested in the XY build plane.

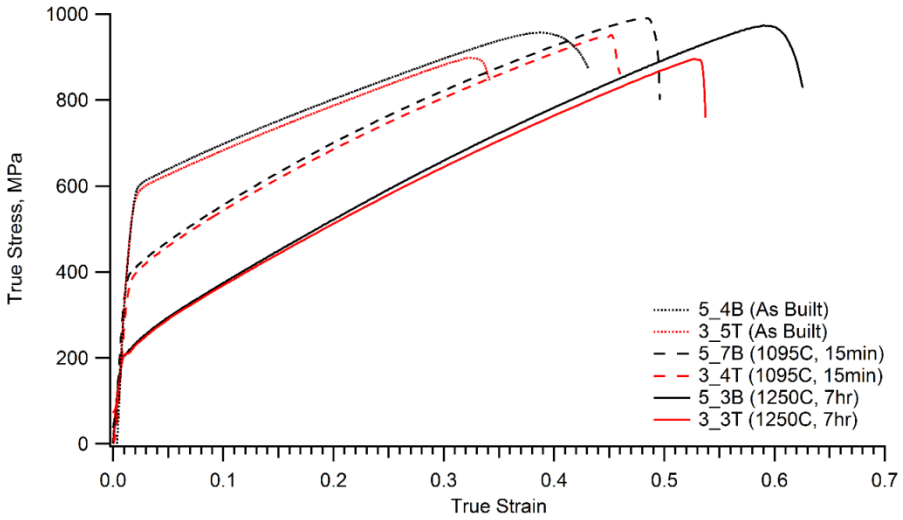

Figure 6.18: True stress true strain data of annealed additively manufacture 316L tensile specimens compared to unannealed, as-built parts. Specimens were tested in the XY build plane.

A TEM sample was electropolished and observed using the ORNL LAMBDA Talos STEM microscope. A second sample was prepared via focused ion beam milling and viewed using the OSU CEMAS Tecnai T20 TEM microscope.

High dislocation density (Figure 6.19) and nano-inclusions were found residing primarily on interdendritic grain boundaries (Figure 6.20) in the electropolished sample.

The EDS capability of the ORNL LAMBDA Talos STEM microscope allowed for elemental mapping of the inclusions, the results of which can be seen in Figure 6.21 and Figure 6.22. There seems to exist two types of inclusion: the first type is rich in silicon, manganese, and oxygen, while the second is rich in copper and carbon. A magnified view of the second type of precipitate along with its own EDS map is presented here in Figure 6.23 through Figure 6.25. This second type of inclusion is made up of a spherical core rich in silicon, manganese, oxygen, and nitrogen surrounded by a ~5 nm thick shell rich in carbon, copper, and sulfur. Tendrils rich in copper and sulfur extend away from the particle in all directions.

Figure 6.26 shows a TEM image of the prepared FIB foil and Figure 6.27 shows the selected area diffraction pattern of each grain.

Four images (totaling 47.86 square microns of area) were taken of the foil at 28,000x magnification, near the bottom edge where the sample was thinnest. Image analysis was performed using ImageJ to determine statistical knowledge of the precipitates/oxides in aggregate. Figure 6.28 gives an example of how each HAADF image was converted to a binary image highlighting the dark precipitates, and how each precipitate was numbered and analyzed individually. Table 6-11, Figure 6.29, and Figure 6.30 summarize the results of the analysis of all the precipitates found within the four images that were processed. The results show that the majority of precipitates/oxides are small (< 7 nm) and that the average effective diameter of the oxides is 26 nm.

Multiple attempts were made to obtain a diffraction pattern of the precipitates/oxides using the smallest aperture available on the Tecnai T20 instrument. Figure 6.31, Figure 6.32, and Figure 6.33 all depict attempted precipitate diffraction patterns. Secondary diffraction patterns corresponding to a precipitate were obtained in Figure 6.33 while no secondary diffraction patterns were obtained on any of the other precipitates. It is likely that the precipitate contribution to the diffraction patterns in Figure 6.31 and Figure 6.32 is small compared to the contribution from the surrounding matrix and simply cannot be resolved. While the diffraction pattern from the precipitate is visible in Figure 6.33, it is faint and difficult to index.

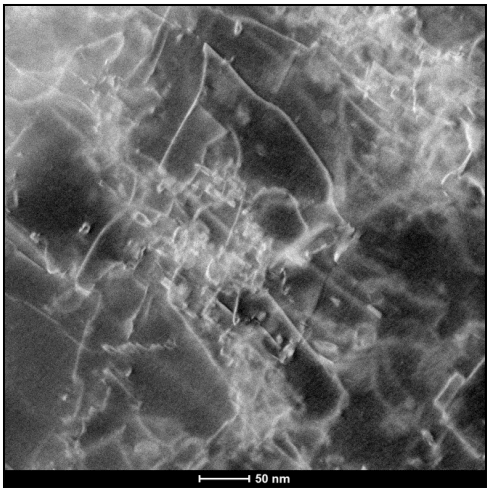

Figure 6.19: TEM image of dislocations present in sample 2-10K

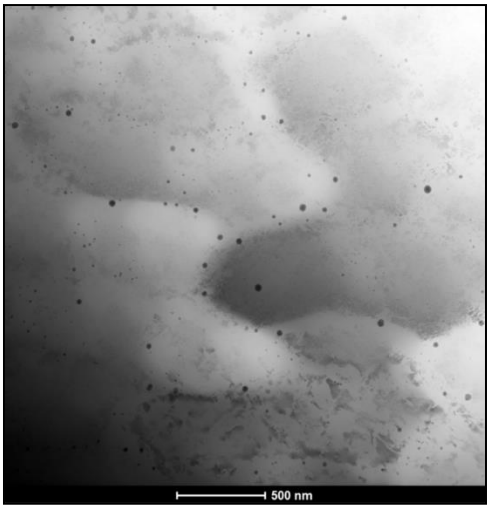

Figure 6.20: TEM image showing the presence of inclusions residing mainly on interdendritic grain boundaries of sample 2-10K. The local density of these spheroids at the grain boundaries is approximately 10^{22} particles/m^3.

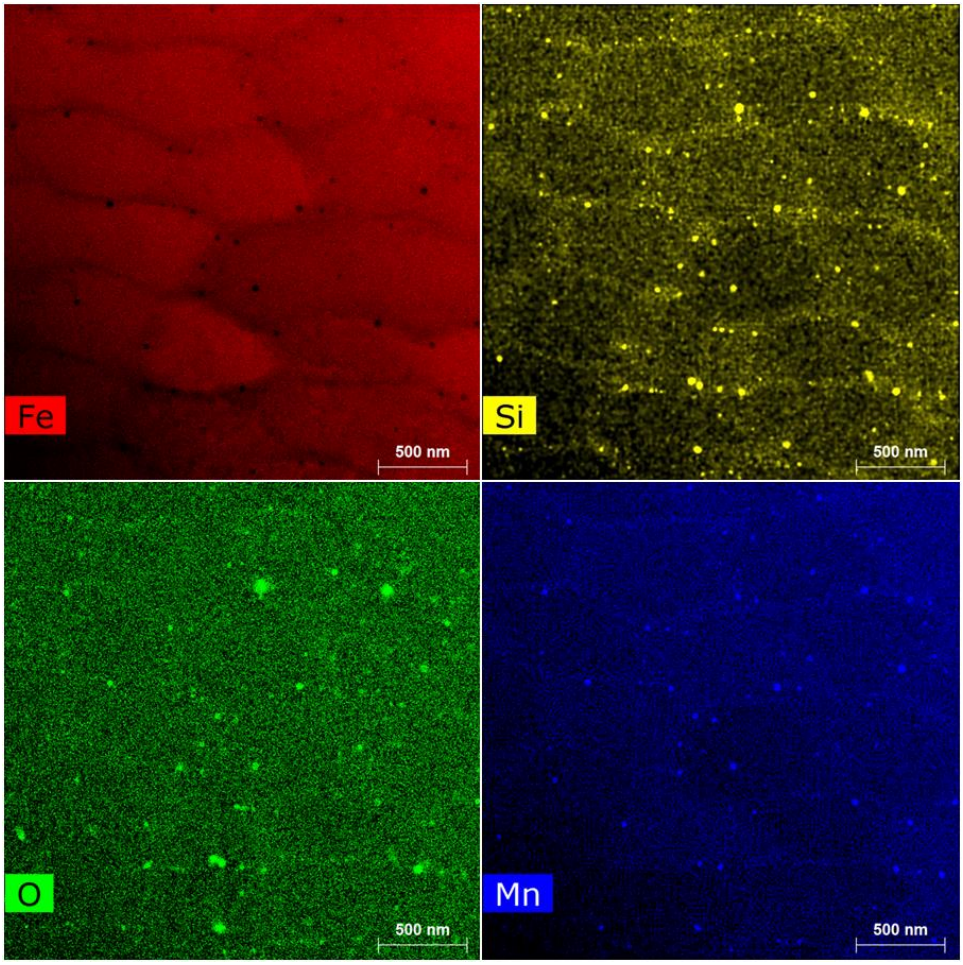

Figure 6.21: EDS elemental maps of Fe, Si, O, and Mn concentrations in TEM 2-10K filler bar sample (see Figure 6.20).

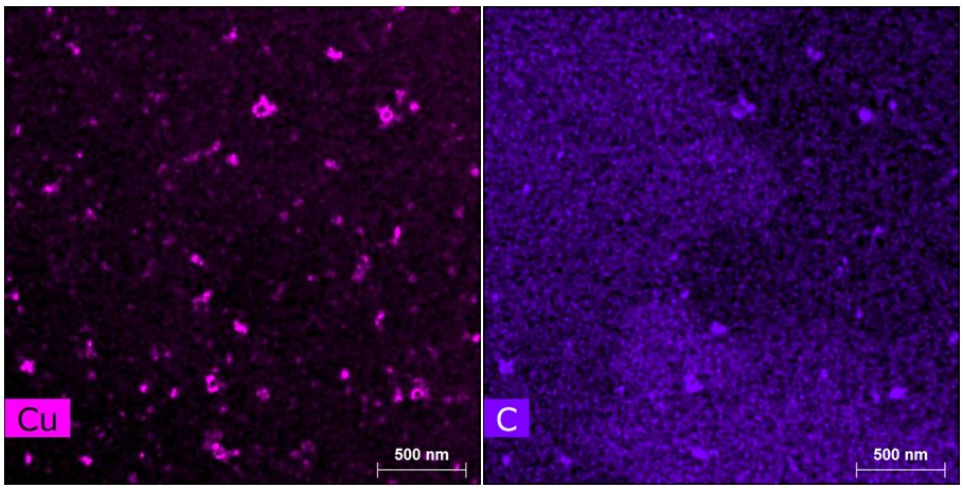

Figure 6.22: EDS elemental maps of Cu and C concentrations in TEM 2-10K filler bar sample (see Figure 6.20).

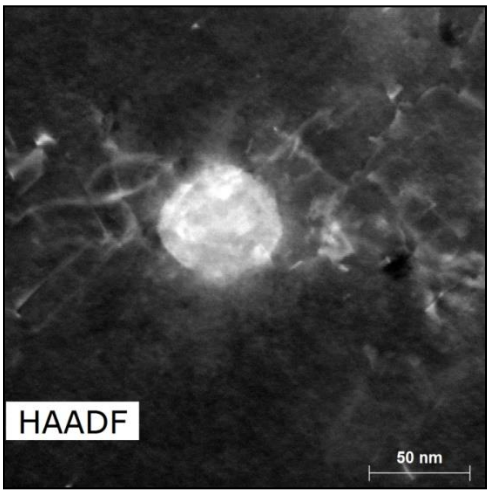

Figure 6.23: Magnification of large inclusion using TEM high angle annular dark field detector.

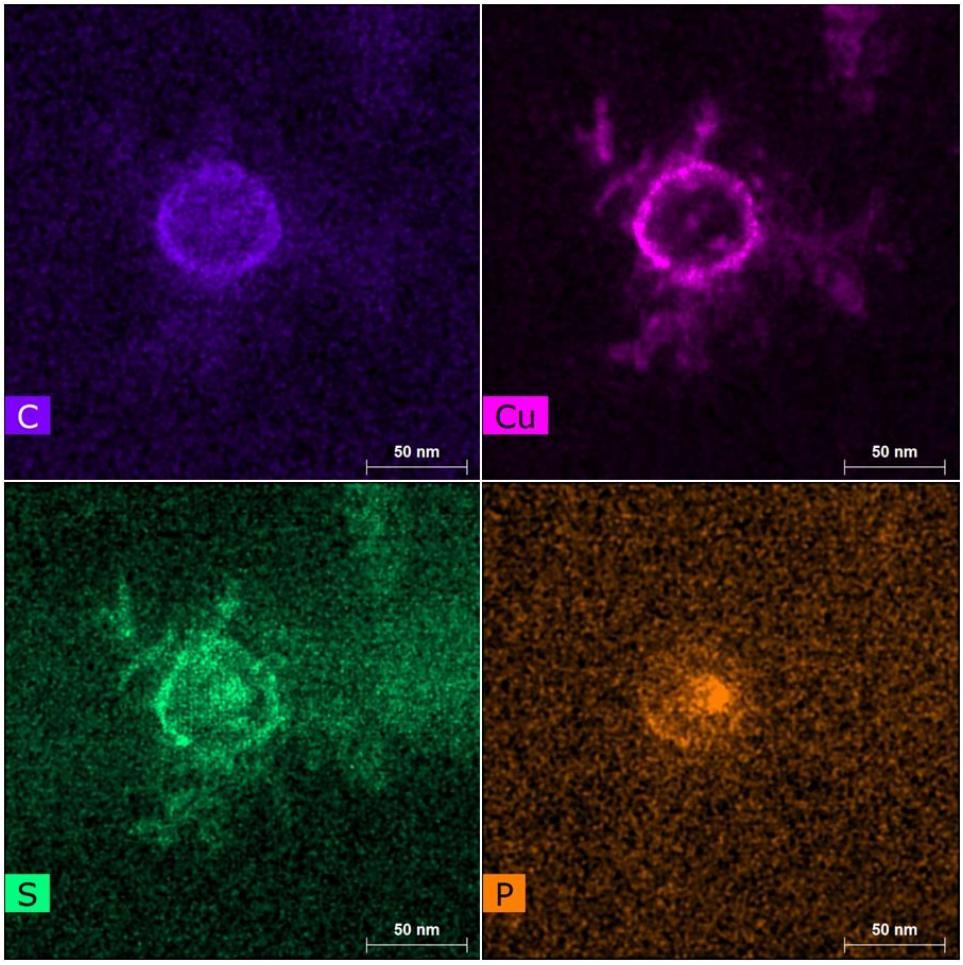

Figure 6.24: EDS elemental maps of C, Cu, S, and P concentrations in TEM 2-10K filler bar sample (see Figure 6.23).

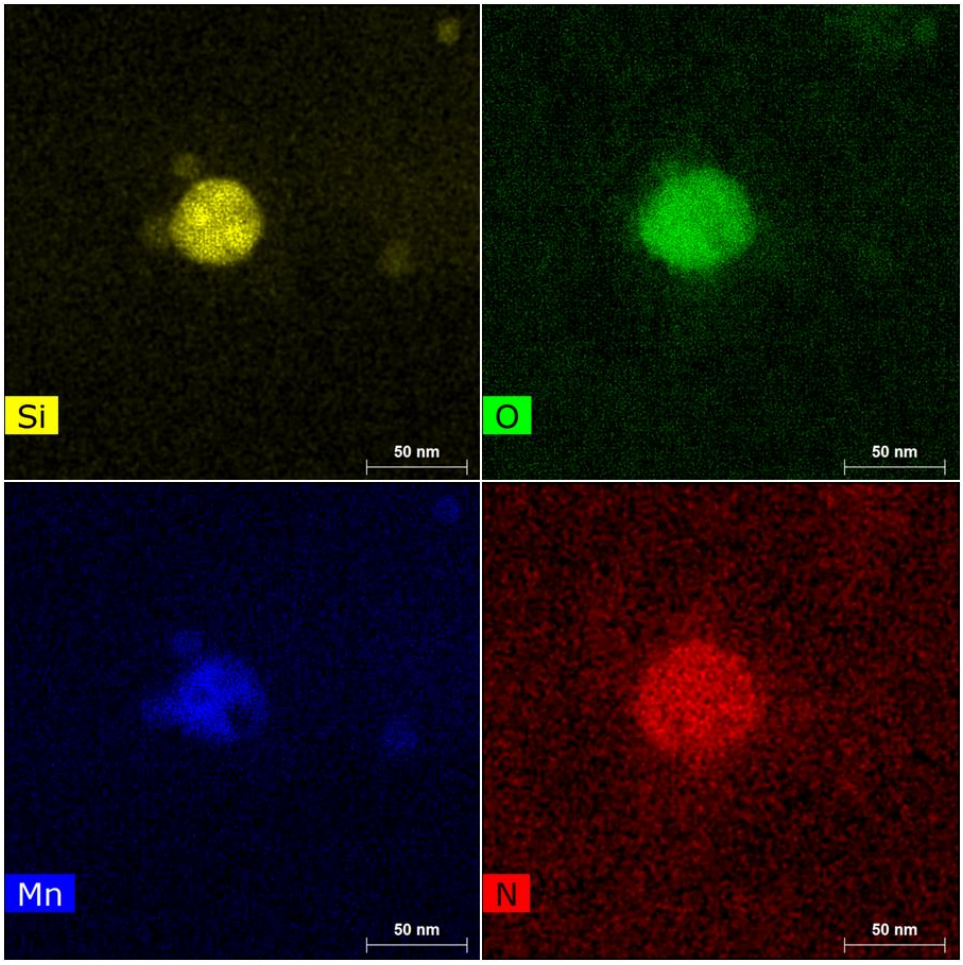

Figure 6.25: EDS elemental maps of Si, O, Mn, and N concentrations in TEM 2-10K filler bar sample (see Figure 6.23).

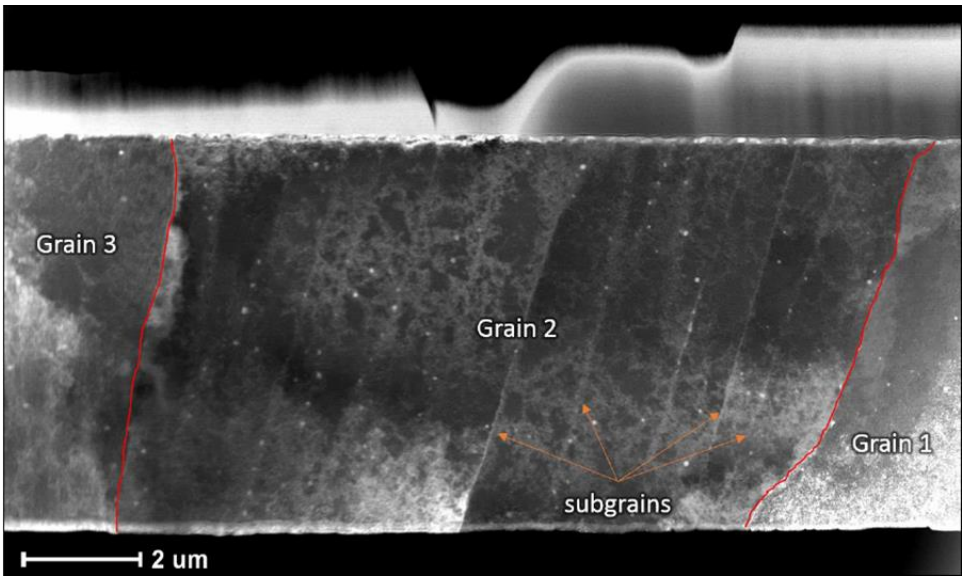

Figure 6.26: TEM image of sample 2-10K FIB foil with grains and grain boundaries marked.

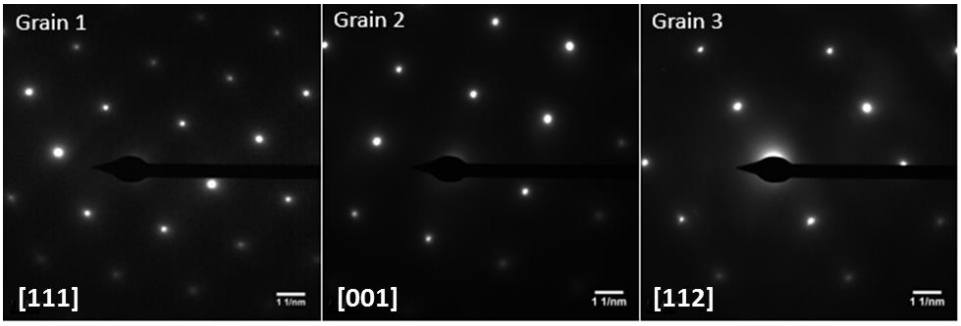

Figure 6.27: Sample 2-10K diffraction patterns of each grain within the FIB foil

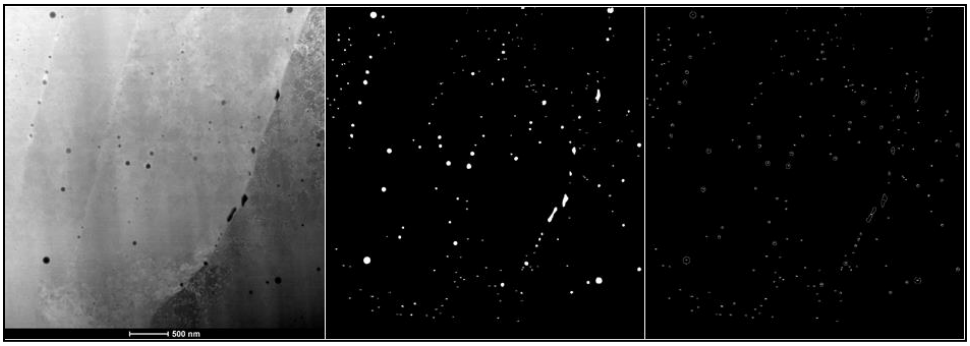

Figure 6.28: Example of ImageJ image analysis technique.

Table 6-11: Sample 2-10K precipitate areas and calculated average diameters.

No. of precipitates	Precipitate Area Fraction	Average Particle Area, nm^2	Average Particle Diameter, nm
501	0.5544 %	529.59	25.97

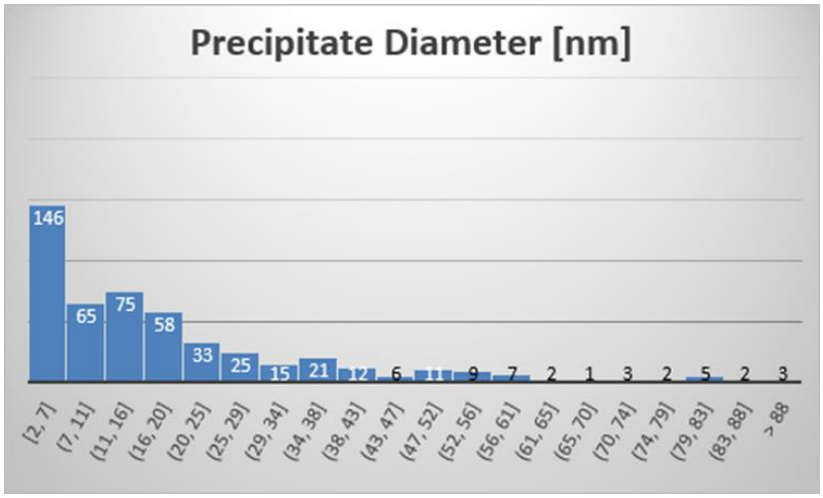

Figure 6.29: Histogram of precipitate diameters in 2-10K FIB foil.

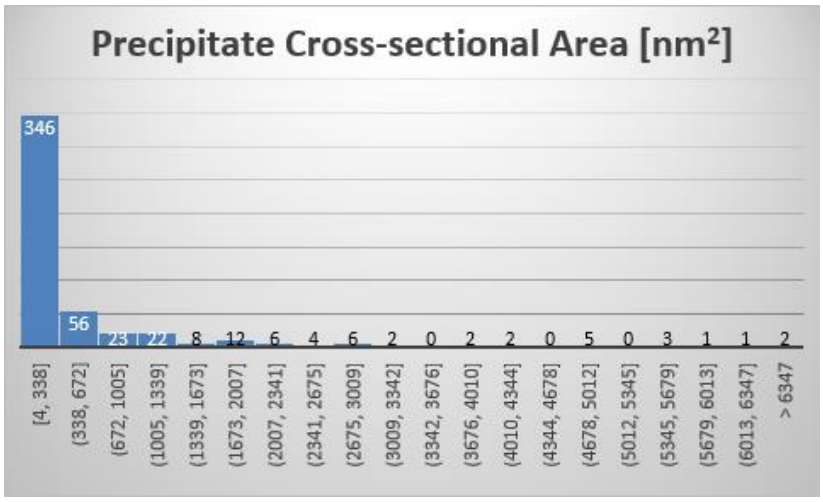

Figure 6.30: Histogram of precipitate cross-sectional area in 2-10K FIB foil.

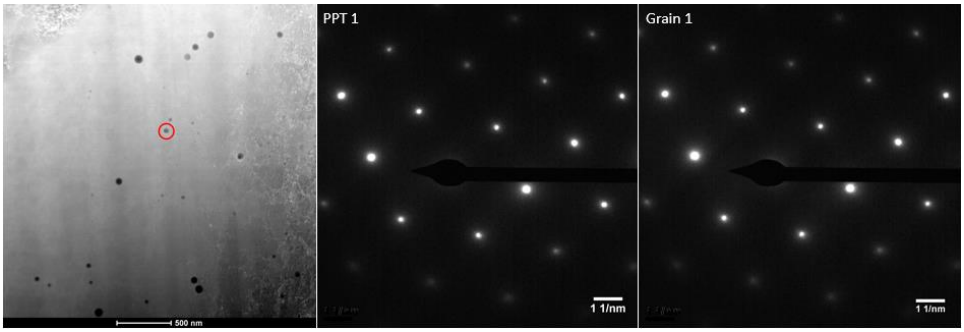

Figure 6.31: Attempted diffraction pattern of precipitate (ppt 1) alongside the diffraction pattern of the surrounding matrix. The pattern from the preciptate is not visible.

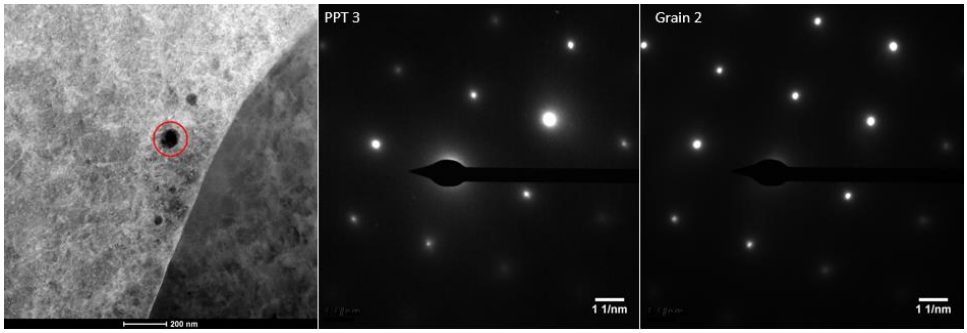

Figure 6.32: Attempted diffraction pattern of precipitate (ppt 3) alongside the diffraction pattern of the surrounding matrix. The pattern from the preciptate is not visible.

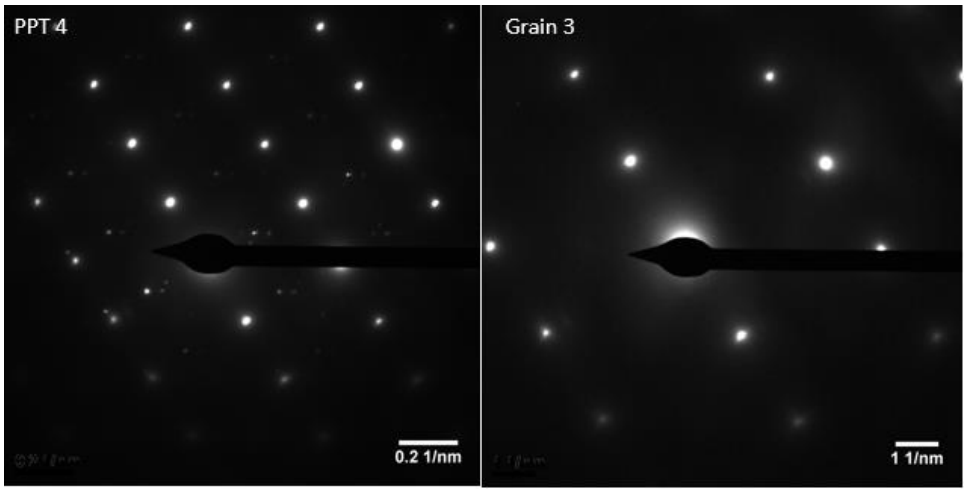

Figure 6.33: Diffraction pattern of precipitate (ppt 4) alongside the diffraction pattern of the surrounding matrix.

Figure 6.34 is an overview of sample 2-10K FIB foil with EDS scan areas 1&2 marked. EDS scan 1 lies along the grain boundary between grains 1&2. Uncharacteristically elongated oxides lie along this grain boundary and elemental characterization of these oxides as well as the grain boundary itself was desired. EDS scan 2 looks at an odd feature of two spherical precipitates connected by a bright region. This feature lies along a sub-grain boundary within grain 2. Knowledge of elemental concentrations along grain and sub-grain boundaries can help determine the solidification modes of the sample.

Scan 1 and scan 2 both show elemental depletion of metallic elements Fe, Ni, Cr, Co, Cu, and Mo in the precipitates (Figure 6.35, Figure 6.36), and elemental enrichment of Si, O, and Mn (Figure 6.37, Figure 6.38). These results strongly suggest that the precipitates are made up of $MnO \cdot SiO_2$ oxides. Some evidence of MnS precipitates forming on top of the main $MnO \cdot SiO_2$ oxides can also be seen. The white region connecting the two larger oxides in scan 2 is enriched in Cr, Mo, S, and P. The sub-grain boundary is also rich in both Cr and Mo compared to the surrounding matrix, but in less concentration than the area between the two oxides.

6.1.5.2. Tensile Bars

6.1.5.3. 1095^{O}C, 0.25 hour anneal (3-4T)

Heat treated sample 3-4T was prepared via focused ion beam milling and viewed using the OSU CEMAS Tecnai T20 TEM microscope. Figure 6.41 shows a TEM image of the prepared FIB foil and Figure 6.42 shows the selected area diffraction patterns of both grains.

ImageJ image analysis was performed on three images (totaling 77.22 square microns of area) taken of the foil. Figure 6.43 and Figure 6.44 summarize the results of the analysis of all the precipitates found within the three images that were processed. The results show that the majority of precipitates/oxides are still smaller than 7 nm after heat treatment, and that the average effective diameter of the oxides has doubled to 53 nm when compared to precipitates in the as-built part. In addition to an increased average precipitate diameter, the size spread of the oxides has increased relative to the spread in the as-built part.

Selected area diffraction was attempted on one precipitate in the thinnest region of the foil in Grain 2, as shown in Figure 6.45. Again, the diffraction pattern of the precipitate was unable to be resolved and only the diffraction pattern of the surrounding matrix could be seen.

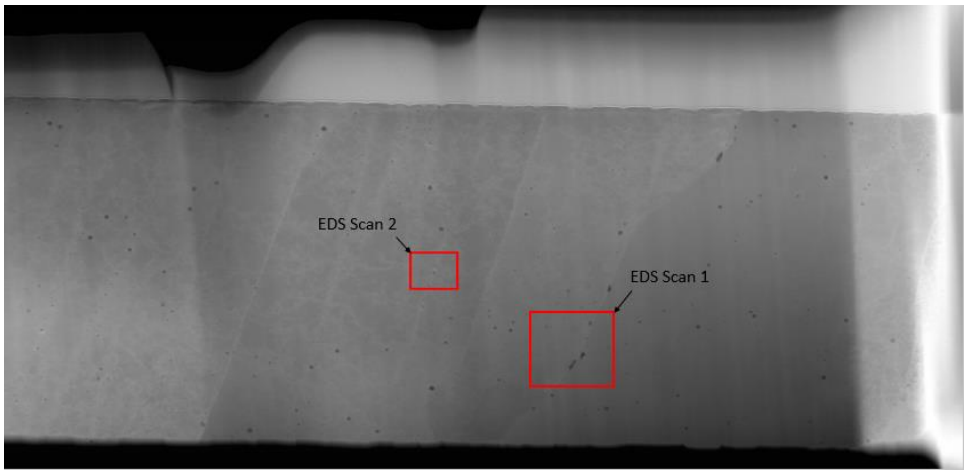

Figure 6.34: Overview HAADF image with EDS map scan areas shown.

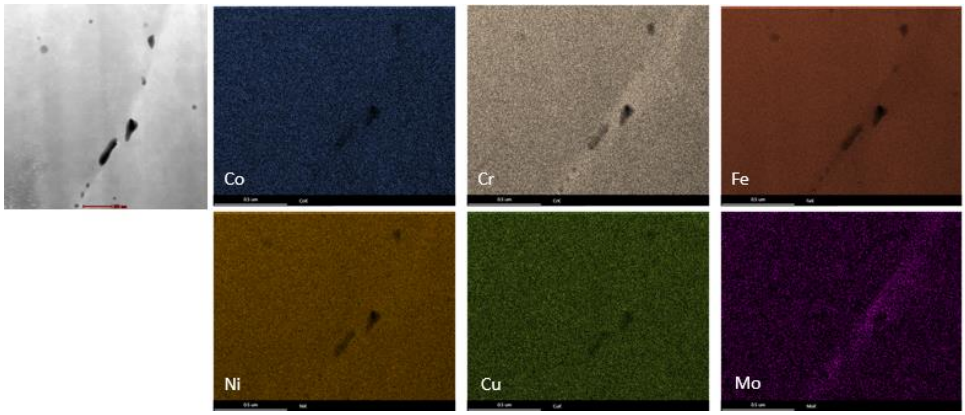

Figure 6.35: Sample 2-10K scan 1 element depletion EDS map

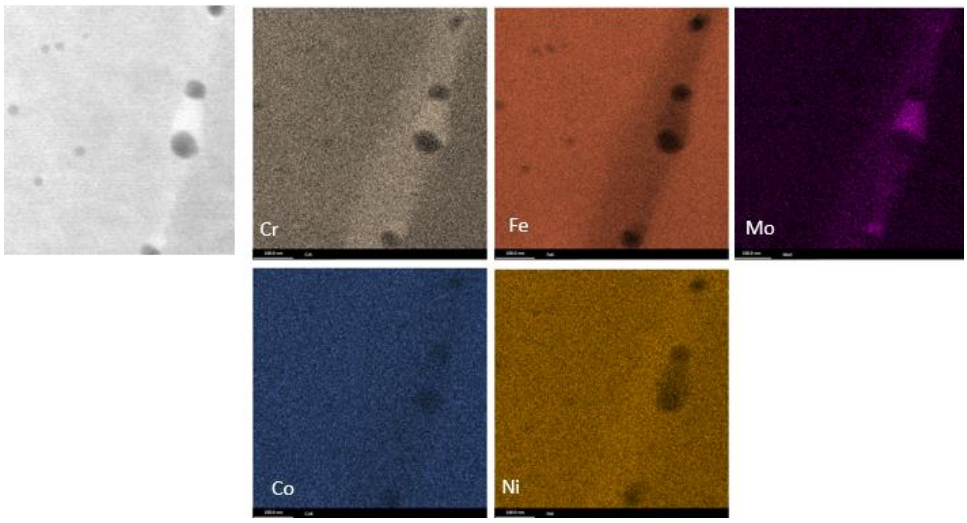

Figure 6.36: Sample 2-10K scan 2 element depletion EDS map

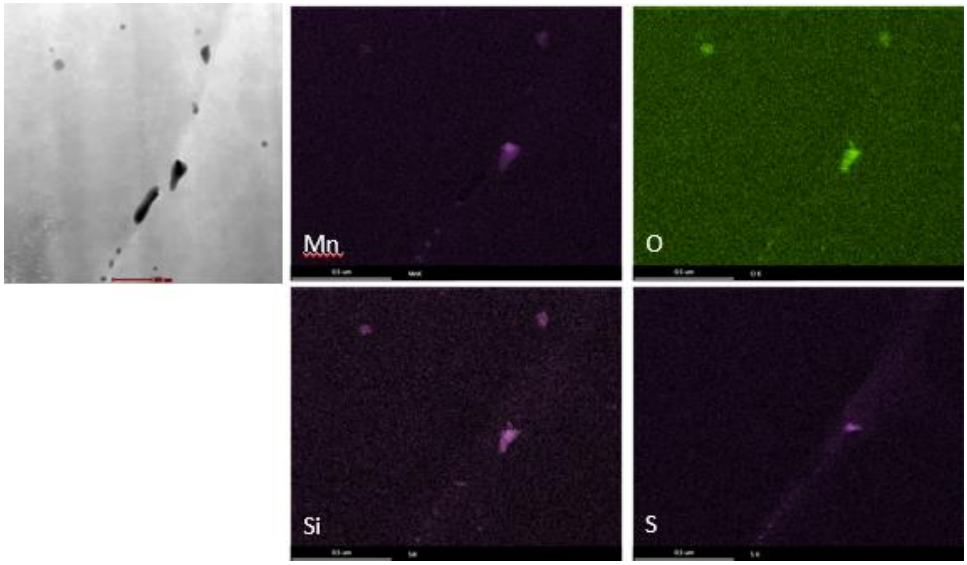

Figure 6.37: Sample 2-10K scan 1 element enrichment EDS map

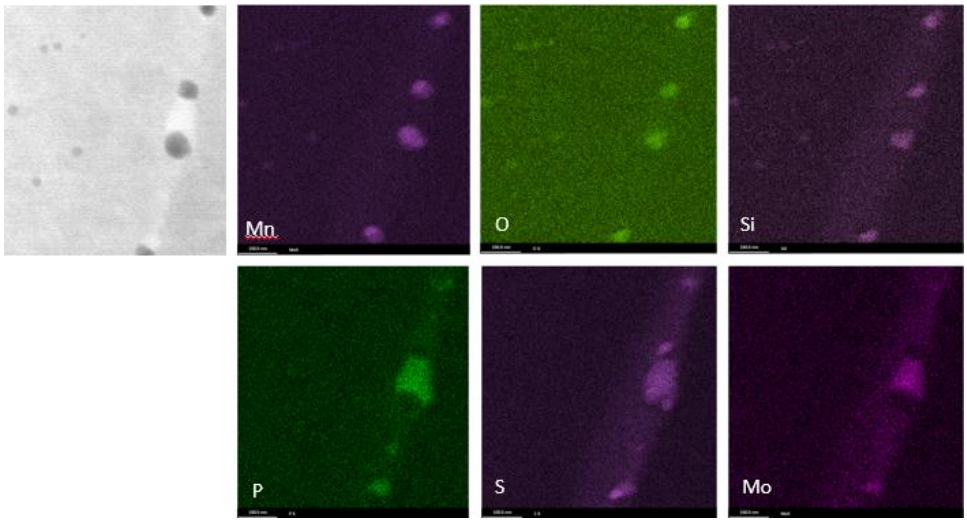

Figure 6.38: Sample 2-10K scan 2 element enrichment EDS map

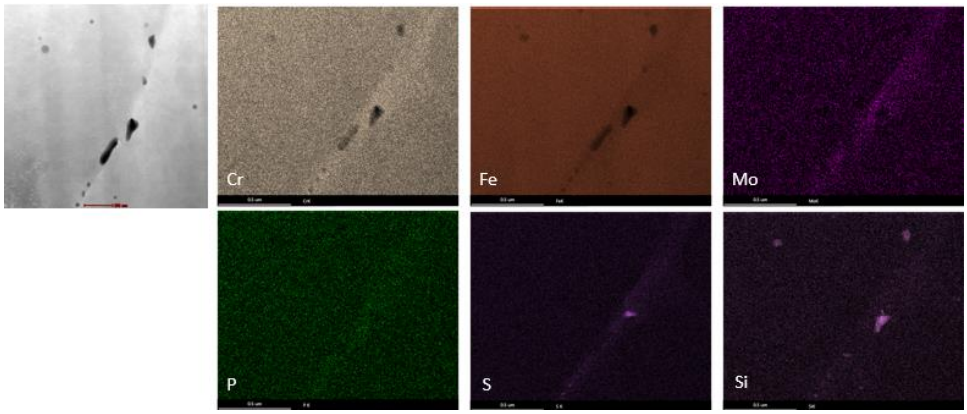

Figure 6.39: Sample 2-10K scan 1 grain boundary element enrichment/depletion EDS map

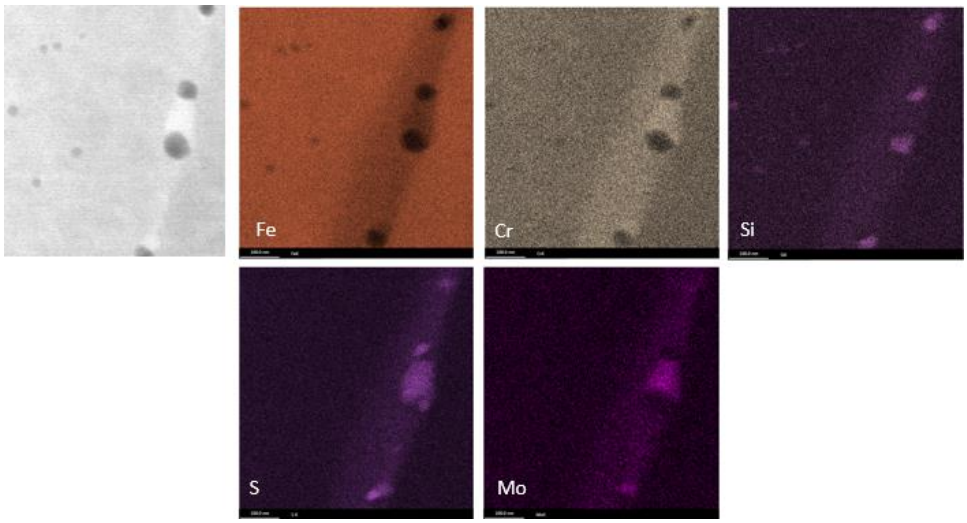

Figure 6.40: Sample 2-10K scan 2 grain boundary element enrichment/depletion EDS map

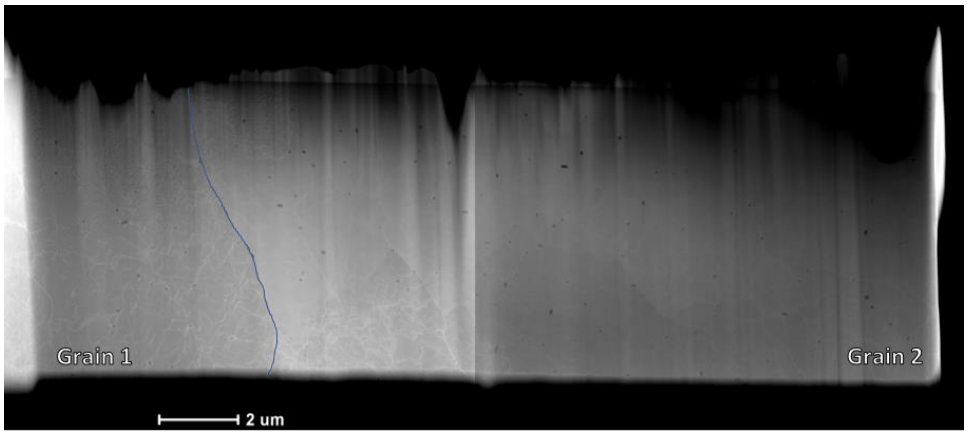

Figure 6.41: HAADF image of sample 3-4T FIB foil with grains and grain boundary marked.

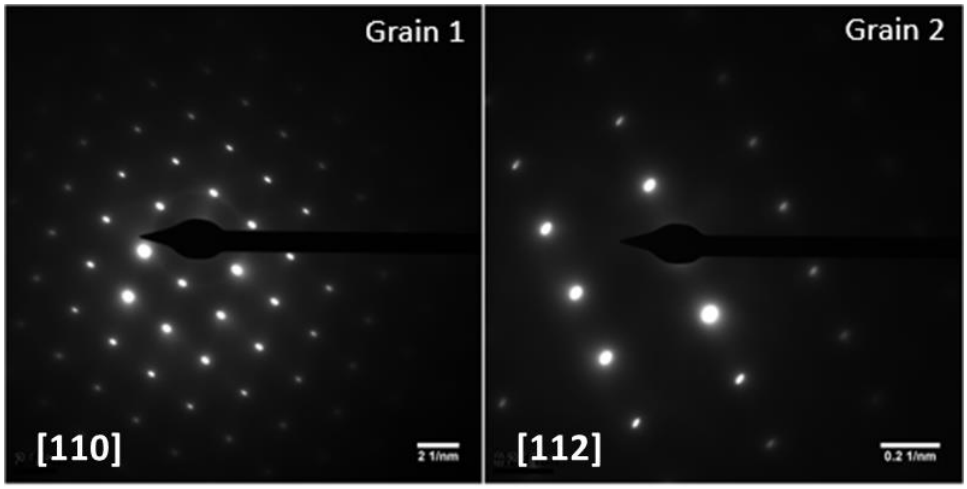

Figure 6.42: Diffraction patterns of both grains within the 3-4T FIB foil

Table 6-12: 3-4T precipitate areas and calculated average diameters.

No. of precipitates	***Precipitate Area Fraction***	***Average Particle Area, nm²***	***Average Particle Diameter, nm***
147	0.4254%	2234.38	53.34

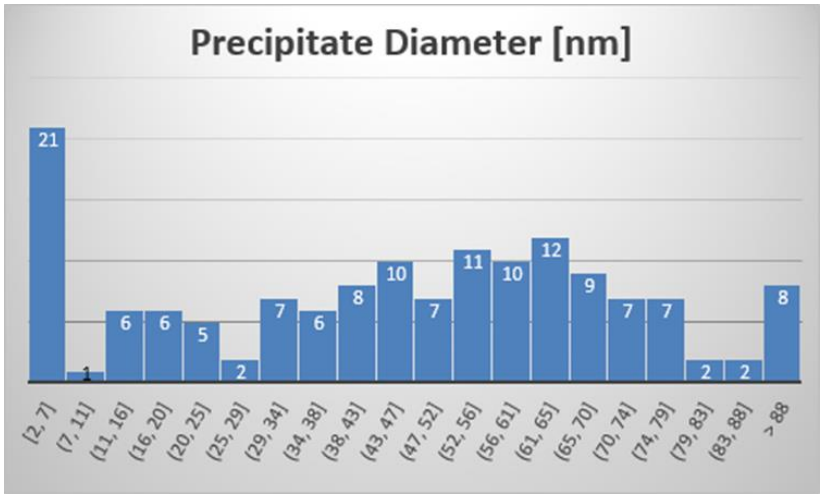

Figure 6.43: Histogram of precipitate diameters present within the 3-4T FIB foil

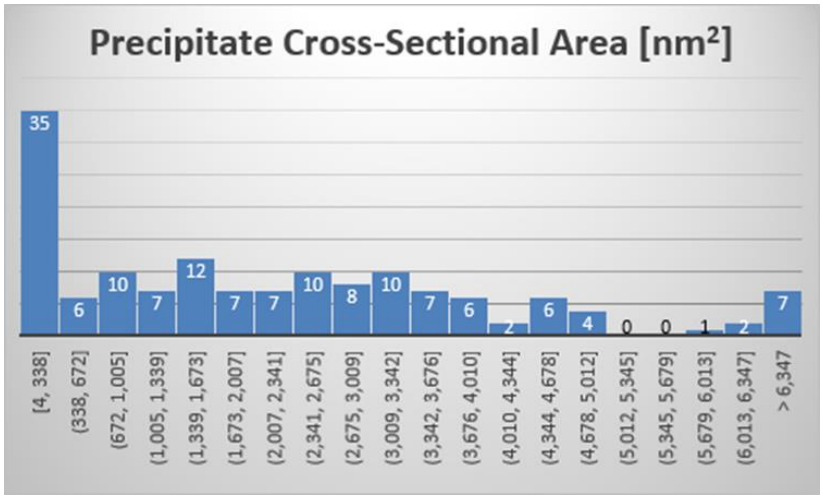

Figure 6.44: Histogram of precipitate cross-sectional areas within the 3-4T FIB foil

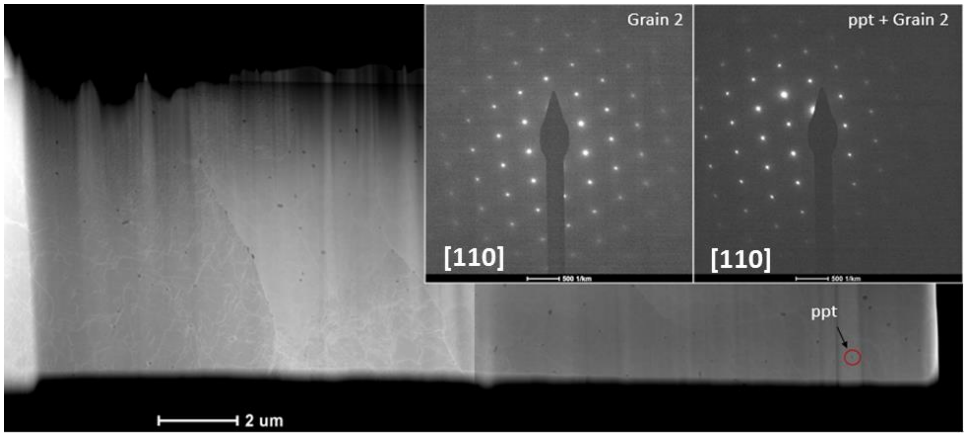

Figure 6.45: Diffraction pattern of precipitate (ppt) alongside the diffraction pattern of the surrounding matrix.

Figure 6.46 is an overview of the sample 3-4T FIB foil with EDS scan areas 1, 2, and 3 marked. EDS scan 1 focused on the characterization of an odd-looking, ‘sandwich’ precipitate. EDS scan 2 focused on the characterization of an oblong oxide, seemingly bisected by the grain boundary. EDS scan 3 focused on an oxide surrounded by dislocations. All three precipitates were confirmed to be rich in Mn, Si, and O. The concentration of these elements in scan 2 did not seem to be affected by being bisected by a grain boundary, and the concentration of these elements in scan 3 did not seem to be affected by the high density of dislocations surrounding the precipitate. An interesting feature in the ‘sandwich’ precipitate is that the EDS scan shows that wherever the precipitate is crossed by the dislocation, a higher concentration of Fe, Ni, Cr, and Cu seems to exist. The concentration of Mn, Si, and O is not affected by the dislocation crossing. Scan 3 shows some concentration of sulfur adjacent to the precipitate. This is perhaps indicative of a sulfide growth.

Figure 6.53 and Figure 6.54 demonstrate the different type and reduced density of dislocations within sample 3-4T after heat treating, as compared to dislocations that were in seen in sample 2-10K. An example of Orowan bowing can also be seen in Figure 6.54, indicating that the oxides may be contributing to the strength of the material during deformation. This would help explain the continued increase in yield strength in sample 3-4T even after heat treatment to relieve strain buildup from the SLM process.

6.1.5.4. 1250^{O}C, 7-hour anneal (3-3T)

Heat treated sample 3-3T was prepared via focused ion beam milling and viewed using the OSU CEMAS Tecnai T20 TEM microscope. Figure 6.55 shows a TEM image of the prepared FIB foil and Figure 6.56 shows the selected area diffraction patterns of both grains. It was seen that no oxides of any size were present within the foil, excepting the three large oxides shown. Two of the oxides lie on the grain boundary while the third, smallest oxide remains embedded within the matrix.

ImageJ image analysis was performed on the three oxides and the results area shown in Table 6-13. Assuming a spherical shape, the total volume of the three precipitates is enough to encompass the total volume of all of the precipitates in the sample 2-10K foil. Selected area diffraction of precipitate 1 is shown in Figure 6.57. The diffraction pattern indicates a multi-crystalline structure.

Figure 6.58 is an overview of the sample 3-3T FIB foil with EDS scan areas 1 and 2 marked. EDS scan 1 focused on the characterization of the two large precipitates located on the grain boundary, while EDS scan 2 focused on the characterization of the smaller precipitate located in the matrix. All of the precipitates remain rich in Mn, Si, and O and depleted of Cr, Fe, and Ni. However, strong evidence exists showing the presence of MnS growing on the largest precipitate, and on the smaller matrix-trapped precipitate.

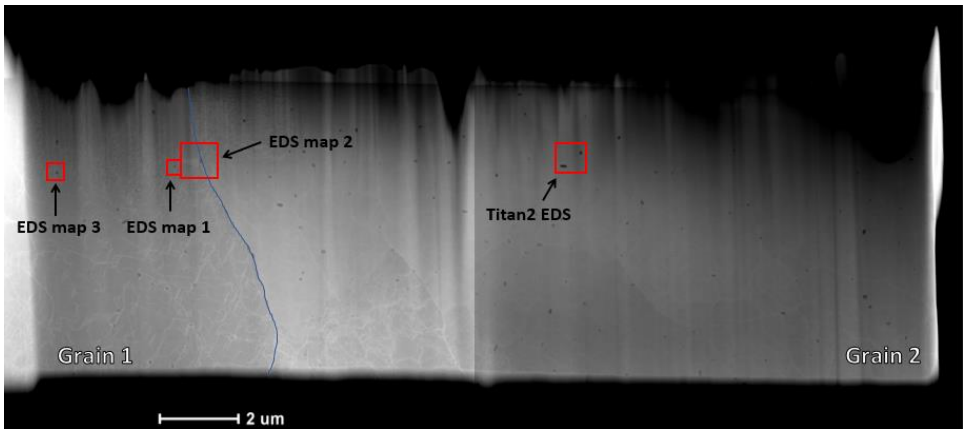

Figure 6.46: Sample 3-4T FIB foil overview with EDS scan map areas outlined.

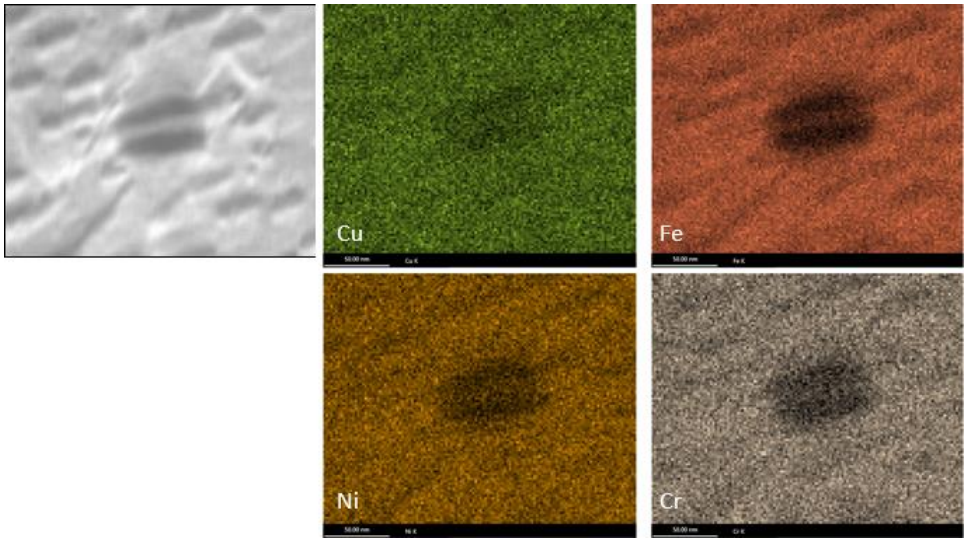

Figure 6.47: Sample 3-4T scan 1 element depletion EDS map

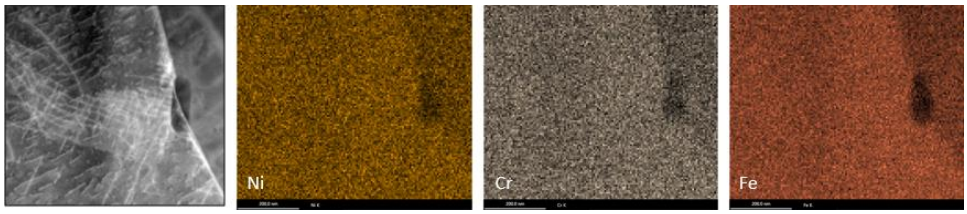

Figure 6.48: Sample 3-4T scan 2 element depletion EDS map

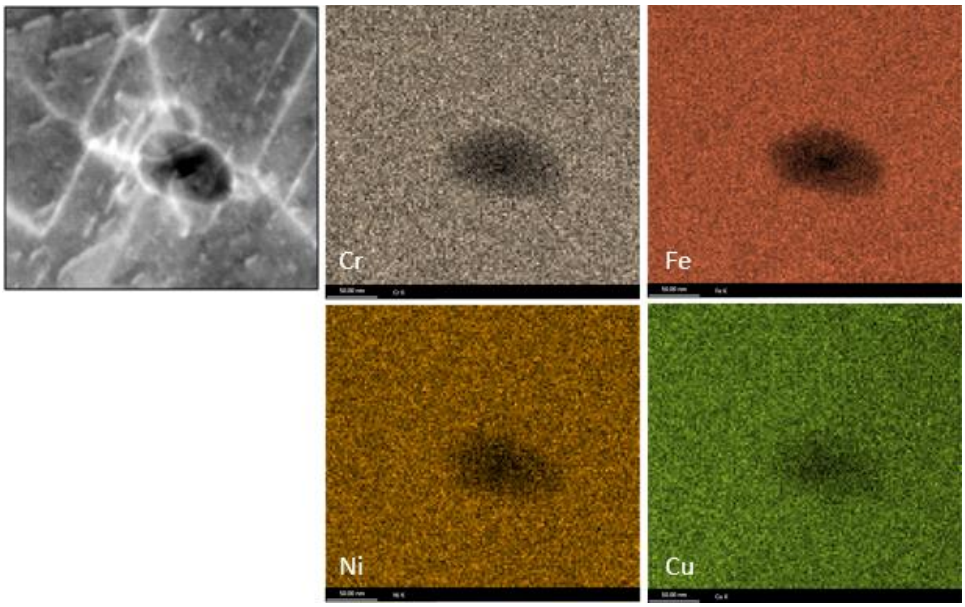

Figure 6.49: Sample 3-4T scan 3 element depletion EDS map

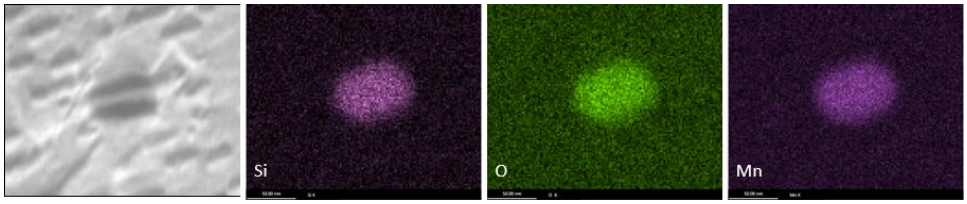

Figure 6.50: Sample 3-4T scan 1 element enrichment EDS map

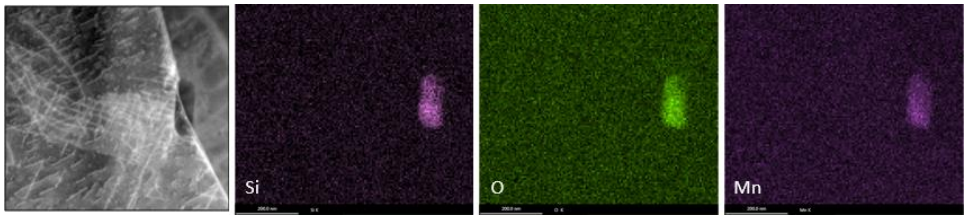

Figure 6.51: Sample 3-4T scan 2 element enrichment EDS map

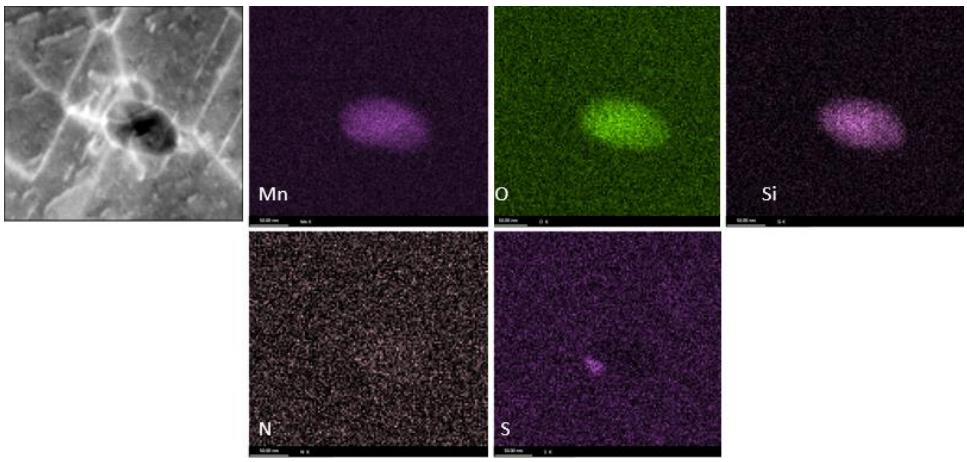

Figure 6.52: Sample 3-4T scan 3 element enrichment EDS map

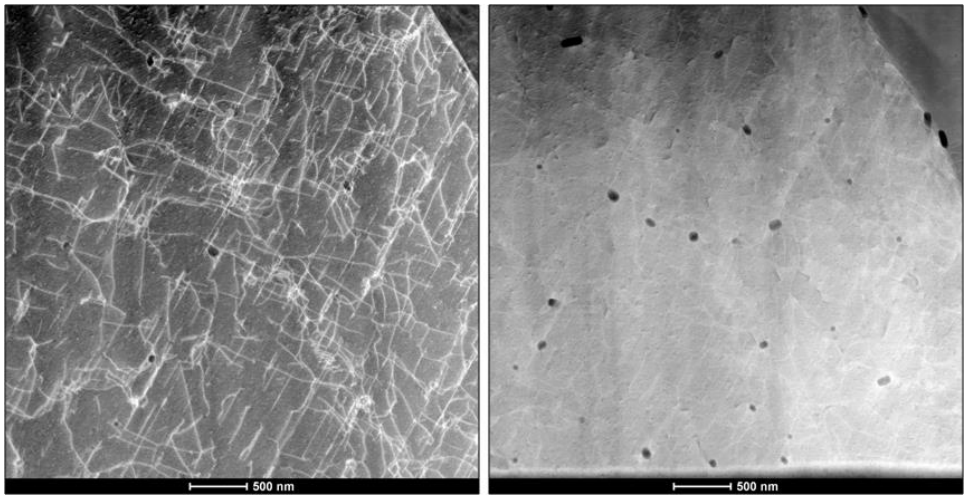

Figure 6.53: (left) Sample 3-4T on-zone dislocation distribution within grain 1. (Right) Sample 3-4T precipitate distribution within grain 1

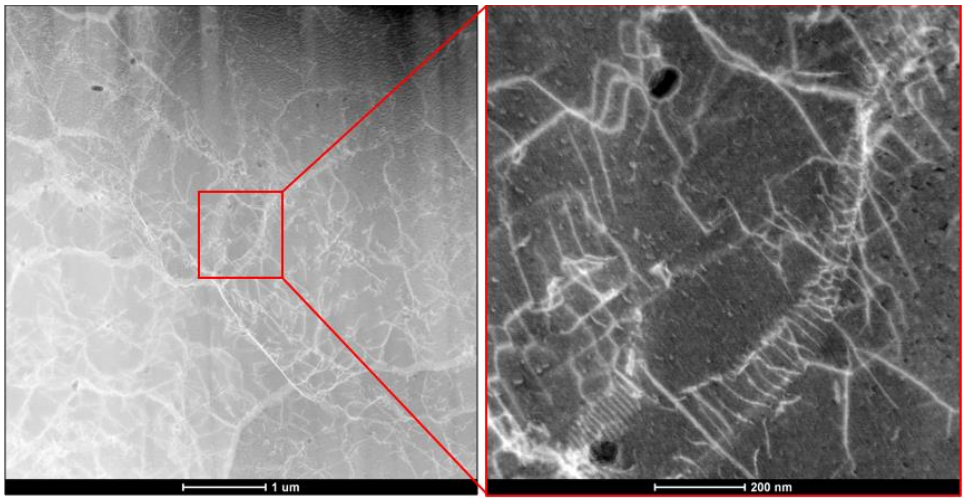

Figure 6.54: (Left) Sample 3-4T on-zone dislocation distribution within grain 2. (Right) Magnified region showing dislocations bowing around precipitate

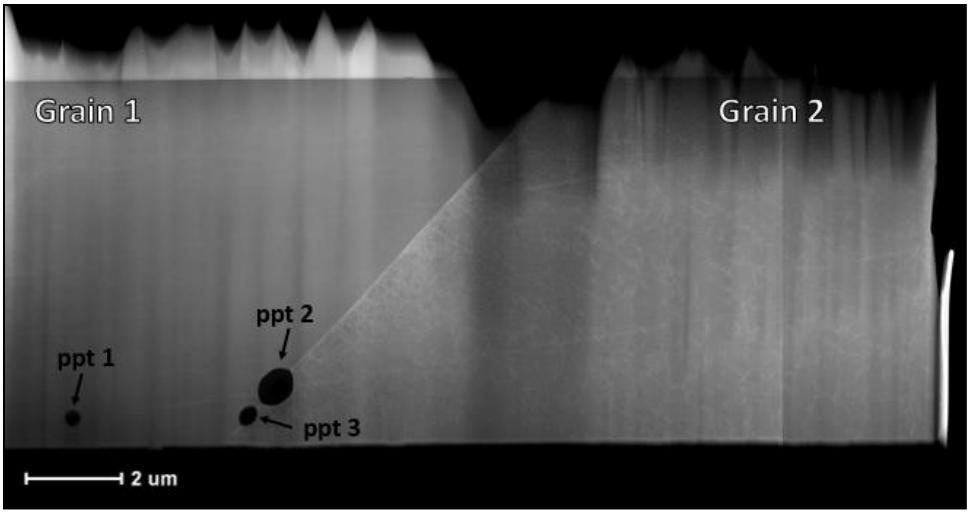

Figure 6.55: Sample 3-3T FIB foil overview with grains and precipitates marked.

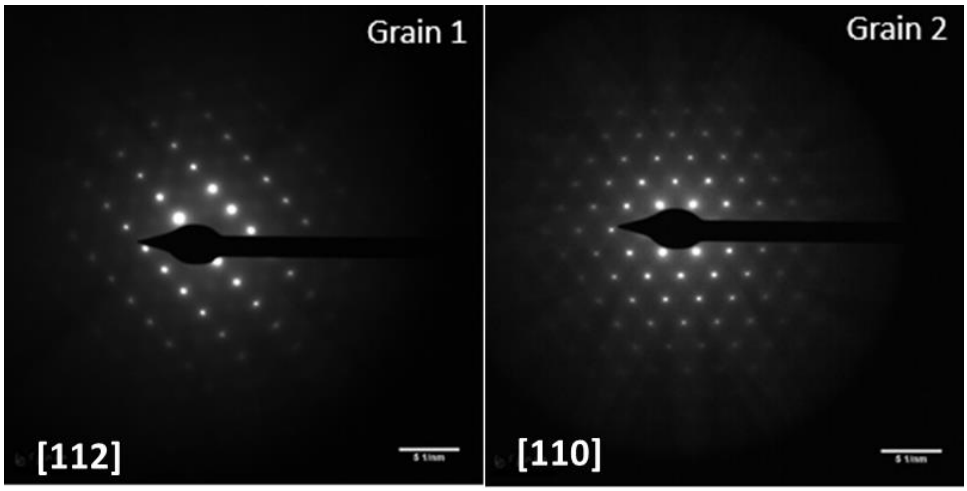

Figure 6.56: Sample 3-3T grain 1 and grain 2 diffraction patterns.

Table 6-13: Sample 3-3T precipitate areas and calculated effective diameters

Precipitate	***Area, nm²***	***Diameter, nm***
1	93,251.12	344.57
2	423,613.44	734.41
3	118,341.93	388.17

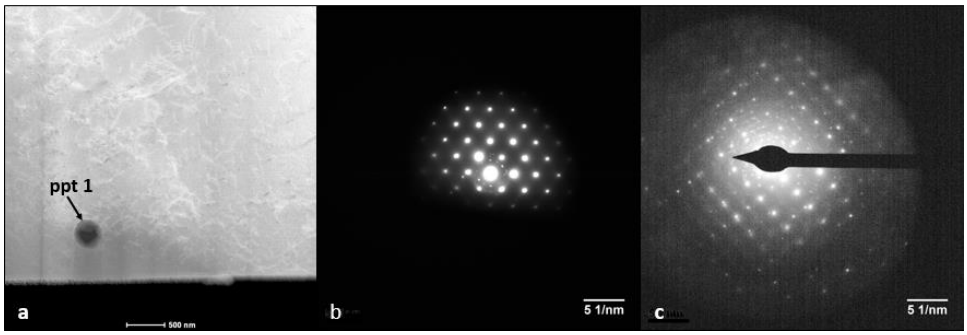

Figure 6.57: (a) HAADF image of precipitate 1. (b) Precipitate (ppt 1) diffraction pattern alongside (c) ImageJ enhanced diffraction pattern.

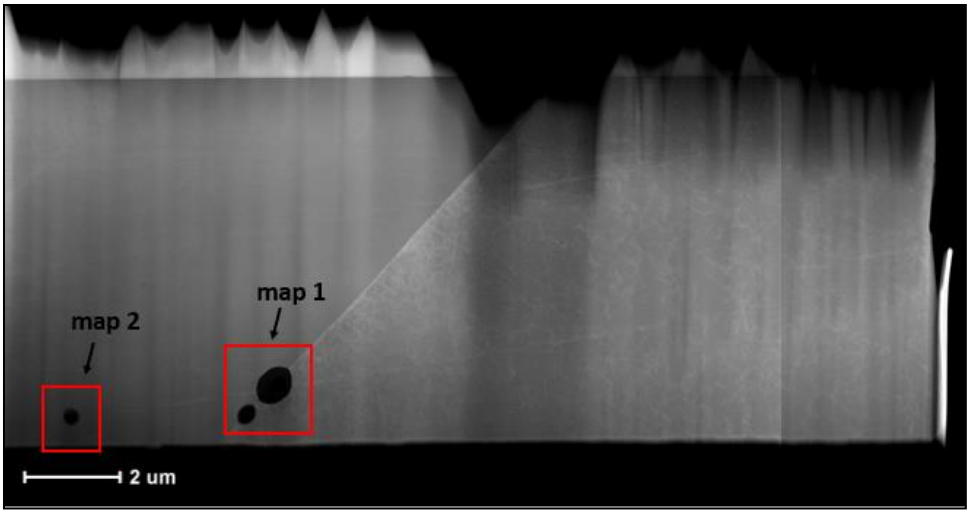

Figure 6.58: Sample 3-3T FIB foil with EDS scan map areas outlined.

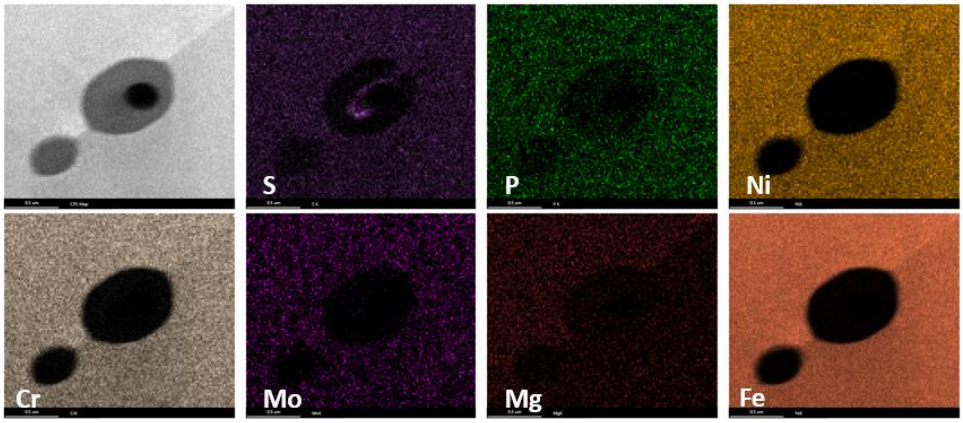

Figure 6.59: Sample 3-3T map 1 element depletion EDS map.

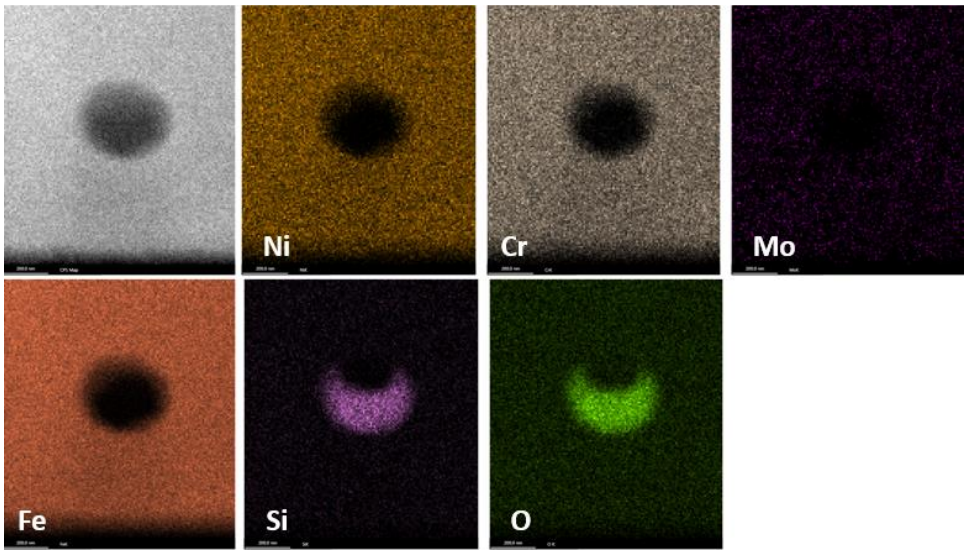

Figure 6.60: Sample 3-3T map 2 element depletion EDS map

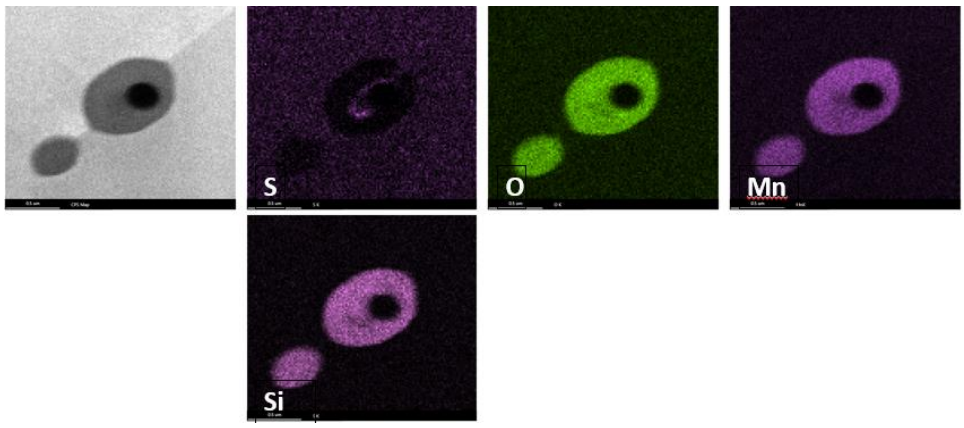

Figure 6.61: Sample 3-3T map 1 element enrichment EDS map

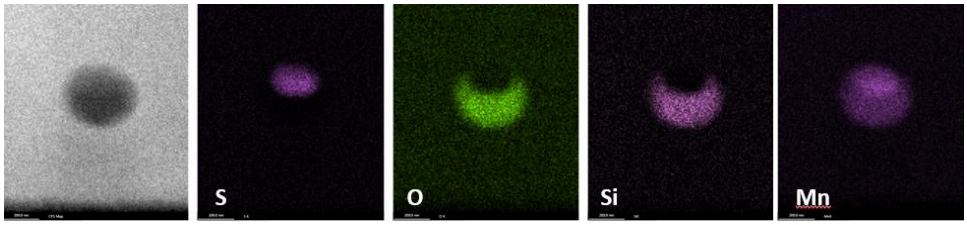

Figure 6.62: Sample 3-3T map 2 element enrichment EDS map

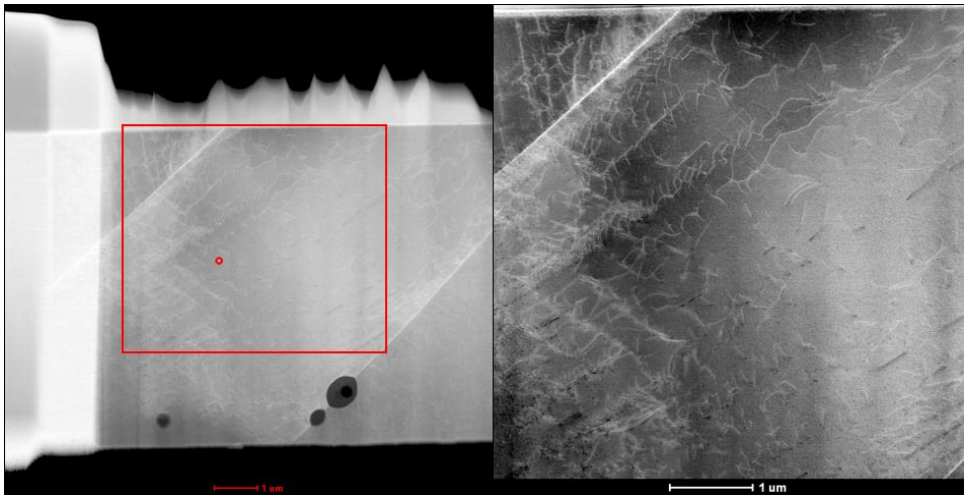

Figure 6.63: Sample 3-3T dislocation density present in grain 1.

6.2. Discussion

Figure 6.64 shows the average values obtained for 0.2% yield strength, ultimate tensile strength, elongation, and reduced area measured, and compares the average 0.2% yield strength and elongation to material minimum standards found in ASTM A276/A276M-16a. These data represent the material properties of selective laser melt additively manufactured stainless steel 316L in the XY build direction. It can be seen that the average values for all four material properties meet or exceed the minimum standards for multiple conditions and finishes of stainless steel 316L. The increased yield strength in the additively manufactured samples is of special interest because it represents values typically seen in strain-hardened 316L steels, which are typically only available from manufacturers in simple geometries such as bars, plate, or cylinders whereas the SLM process is capable of producing parts of considerable complexity with superior strength.

Figure 6.65 through Figure 6.69 show the values of 0.2% yield strength, inherent strain, strength coefficient, elastic modulus, and strain hardening exponent for all of the recyclability experiment tensile tested samples plotted as a function of powder re-use cycle. It should be noted that Cycle 5 did not re-use powder from Cycle 4, but rather was built from a separate stock of well-worked powder. While yield strength and strength coefficient remain consistent, calculated inherent strain, elastic modulus, and strain hardening exponent all either trend upwards or downwards as a function of re-use. An elastic modulus of 200 MPa is expected of steel. The upward trend of elastic modulus seen in Figure 6.67 could be attributed to a decrease in porosity of the samples as a function of re-use. This is supported by the elongation data of Cycles 3-5, which show increased elongation when compared to Cycles 1-2. Cycle 4 showed the best elongation which corresponds to the highest values obtained for elastic modulus.

The stress-strain curves of annealed sample overlaid onto the stress-strain curves of annealed parts built during the recyclability experiment in Figure 6.18 are similar to the stress-strain curves collected by Gibbs and Wyatt from incrementally cold-worked 316 stainless steel, shown in Figure 6.70 [46]. This similarity combined with the heavy dislocation density in unannealed samples point towards strain hardening as the main contributing factor to additively manufactured 316L stainless steel's high yield strength. Classic dislocation theory related to strain hardening states that the yield stress of a metal is proportional to the square root of the dislocation density as described in Eq. 6-3 [47].

$$\sigma_0 = \sigma_i + \alpha G b \rho^{1/2} \quad (6\text{-}3)$$

where σ_0 is the yield stress off the metal, σ_i represents the overall resistance of the crystal lattice to dislocation movement, α is a numerical constanct between 0.3 and 0.6, G is the bulk modulus of the metal, b is the burgers vector of a dislocation, and ρ is the dislocation density.

Condition	Dia./ Thick. [in.]	0.2% Yield [MPa]	UTS [MPa]	Elongation %	RA [%]
SLM AM	0.20	573.4 (±12.6)	665.4 (±9.6)	43.45 (±9.6)	47.34 (±10.14)

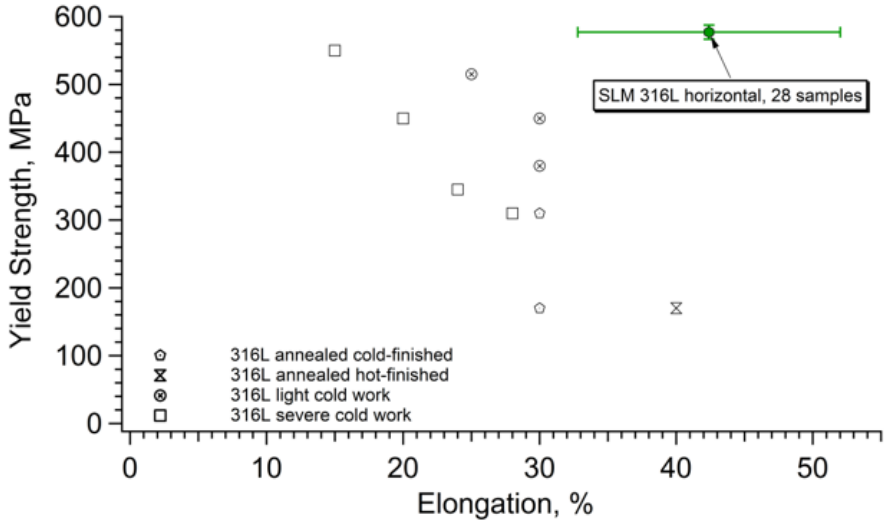

Figure 6.64: Comparison of selective laser melted 316L material properties in the XY build direction to ASTM A276/A276M-16a standard minimum values for 316L bars and plates.

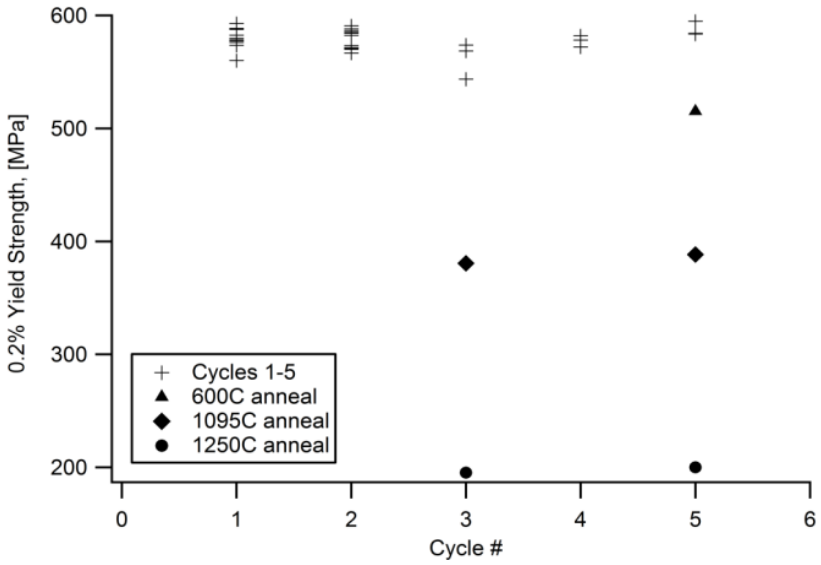

Figure 6.65: 0.2% yield stress of all as-built and heat-treated tensile samples plotted as a function of re-use cycle. Cycle 5 did not re-use powder from cycle 4, but rather was built from a separate stock of well-worked powder.

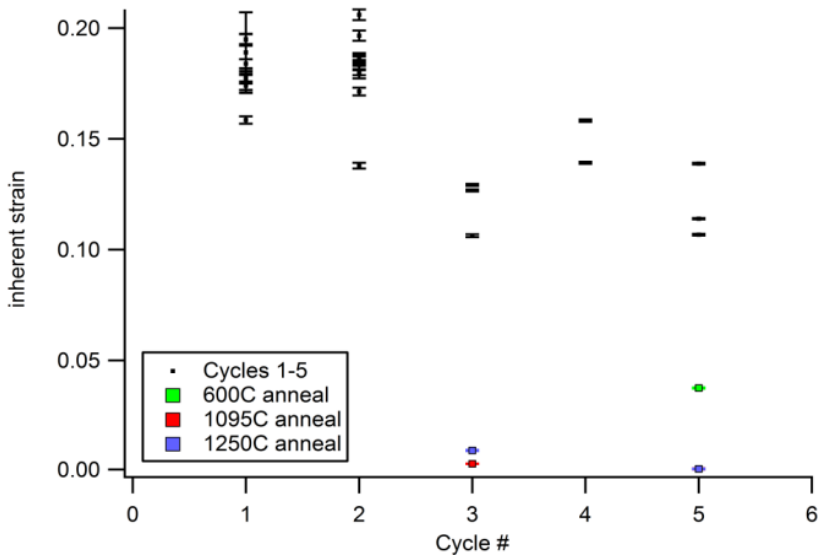

Figure 6.66: Inherent strain of all as-built and heat-treated samples, as calculated by Eq. 6-2, plotted as a function of re-use cycle. Cycle 5 did not re-use powder from cycle 4, but rather was built from a separate stock of well-worked powder.

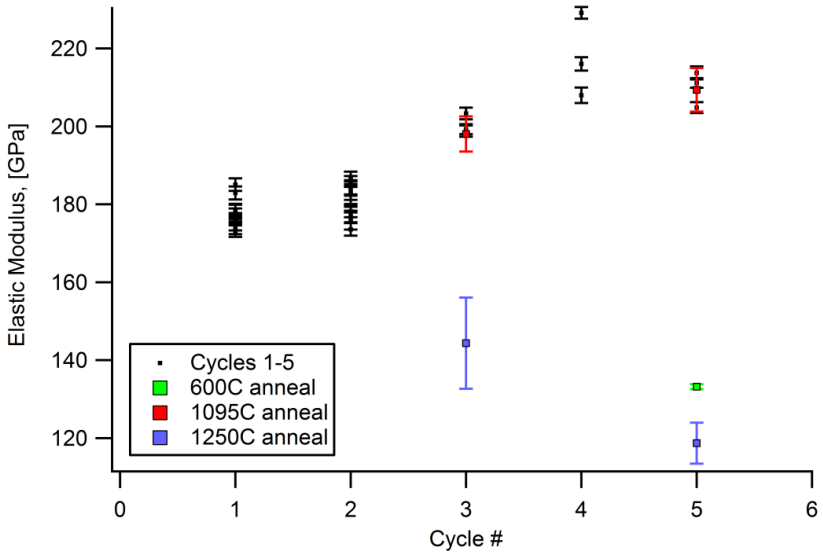

Figure 6.67: Elastic modulus of all as-built and heat-treated samples plotted as a function of re-use cycle. Cycle 5 did not re-use powder from cycle 4, but rather was built from a separate stock of well-worked powder.

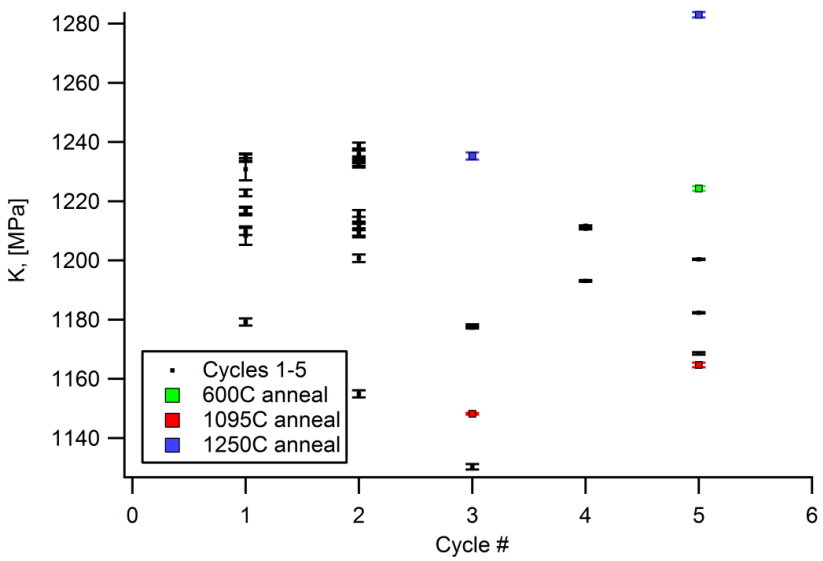

Figure 6.68: Strength coefficient of all as-built and heat-treated samples, as calculated by Eq. 6-2, plotted as a function of re-use cycle. Cycle 5 did not re-use powder from cycle 4, but rather was built from a separate stock of well-worked powder.

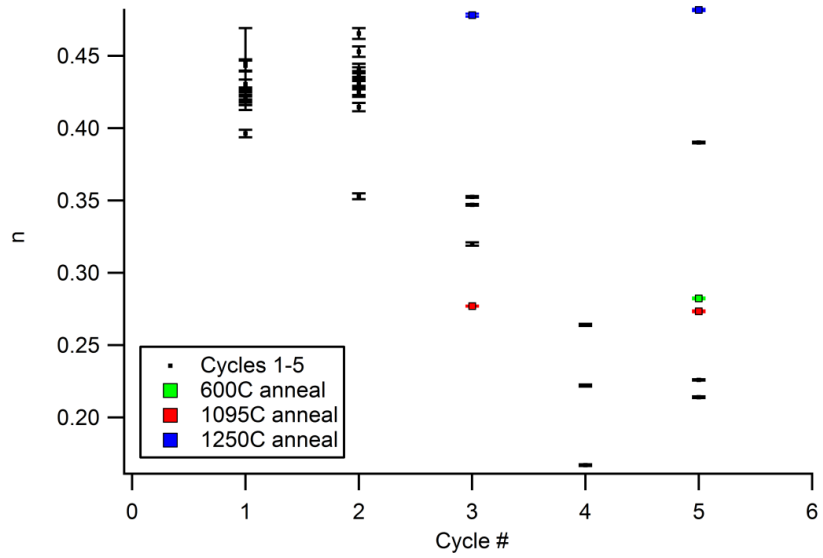

Figure 6.69: Strain hardening exponent of all as-built and heat-treated samples, as calculated by Eq. 6-2, plotted as a function of re-use cycle. Cycle 5 did not re-use powder from cycle 4, but rather was built from a separate stock of well-worked powder.

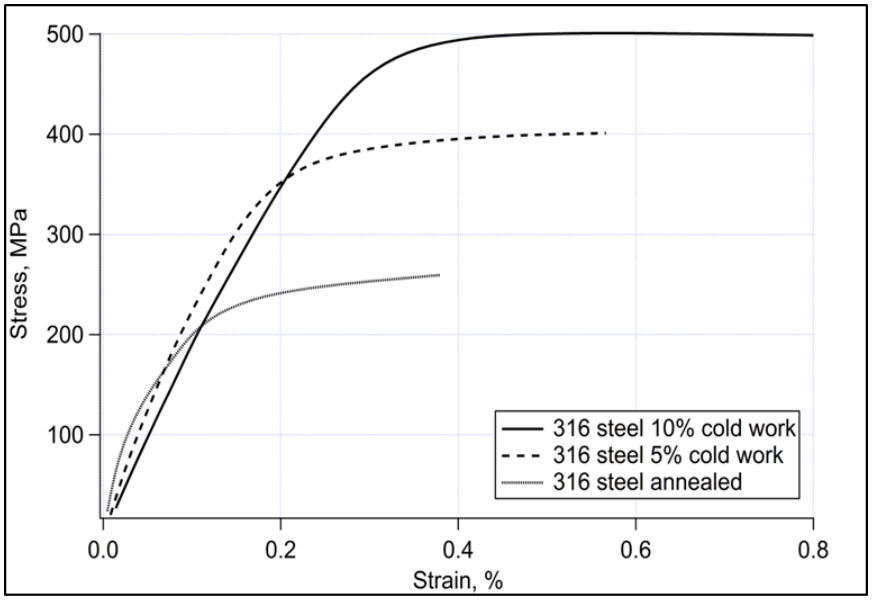

Figure 6.70: 316 annealed and cold-worked stainless-steel sheet, stress-strain curves. Reproduced from [46].

TEM observations of the annealed samples built during the recyclability experiment reveal decreased dislocation density after annealing, which supports the strain hardening conclusion. According to Eq. 6-3, and the observed yield stresses of as-built parts (~600MPa) and parts annealed for 15 min. at 1095ºC (~400MPa), dislocation densities within as-built parts should be $\sqrt{2}$ times the dislocation density within the annealed sample if strain hardening is the sole mechanism driving the increased strength in as-printed parts.

Sochalski-Kolbus et. al. used neutron diffraction to measure residual stresses in parts built using SLM (Figure 6.71) and found increased residual stresses in these parts when compared to parts built using electron beam manufacturing techniques [48]. This increased residual stress is attributed to the lower operating temperatures used during SLM processing. Lower operating temperatures means that thermal gradients between peak melting temperature and the surrounding part/powder bed temperature may be increased.

6.3. Summary & Conclusions

Despite high porosity content, the mechanical properties of parts built during the powder recyclability study are increased relative to standards for wrought stainless 316L steel. Increased yield strength (575MPa) and ductility (0.42) were observed. This yield strength is comparable to severely cold-worked wrought material. Part ductility is much increased compared to standards for stainless steel 316L but is not consistent. Fractographic analysis suggests that the variability in ductility correlates with porosity positioning within each specimen. Tensile specimens with porosity located at stress-concentrating corners failed earlier than specimens with similarly sized porosity located within the interior of the specimen.

Heat treatment (1095ºC for 15 min., 1250ºC for 420 min., 600ºC for 1 hour) and subsequent tensile testing and TEM analysis of recyclability parts reveal that heat treatment reduces the strain dislocation density within the parts, which correlates with reduced yield strength. It is concluded that the increased tensile properties observed in SLM as-built parts is due to high amounts of residual stress within the parts resulting from the exposure to multiple heat cycles and high thermal gradients experienced during the SLM process.

TEM analysis of as-built parts revealed the presence of Si and Mn rich oxides residing primarily on the interdendritic and grain boundaries. It is concluded that these oxides form as a result of solute segregation during the solidification process. Heat treatment caused these oxides to grow in size and reduce in number.

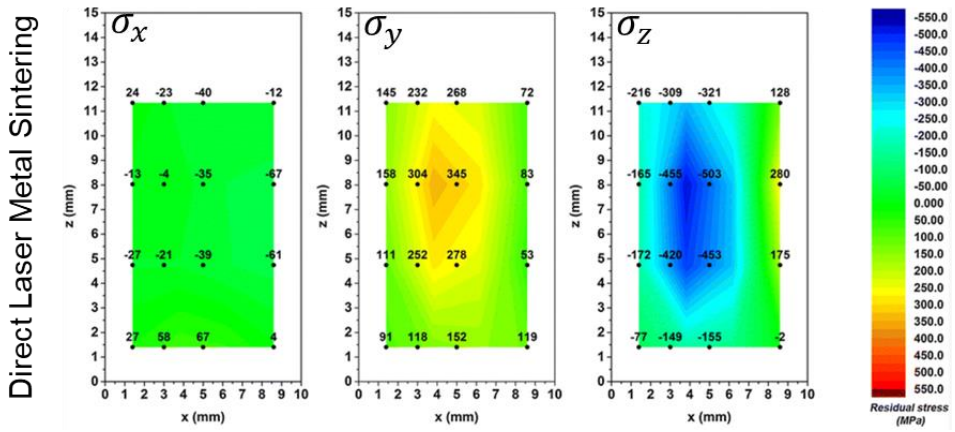

Figure 6.71: Neutron diffraction measured residual stress in SLM processed IN718 [48].

CHAPTER 7 POWDER BED COOLING RATE STUDY

The powder bed cooling rate study was conducted with the intent of manipulating the cooling rates of as-built parts as well as possibly affect the melting conditions during the selective laser melting of stainless steel 316L. The study was conducted by applying preheat scans to the powder prior to a melt scan using a default melt parameter set known to normally produce defect-free parts. The preheat scans used parameter sets differing by power, focus offset, hatch spacing, and the number of preheat scan employed prior to melting (1 or 2). Details of the experiment setup can be found in section 2.2.4.

7.1. Results

The picture on the left side of Figure 7.1 shows a top-down view of the final build after completion of the study, while the schematic to the right shows which parts were analyzed using IR data.

In the two rows where 200 W was used in the preheat scan, several of the cylinders are surrounded by sintered powder. In 100 um hatch preheats scan sections (salmon and blue sections), the sintered powder effect is more pronounced around cylinders where the focus offset was set closer to the default value of 0. Also, more powder remains adhered to the ±25 and ±15 focus offset cylinders built using two preheat scans than to the cylinders build with 1 preheat scan.

The sintered powder effect is even more pronounced in the areas than employed a 60-um hatch spacing parameter during the preheat scans (green and beige sections). In these sections, in both the single preheat and the double preheat sections, powder is adhered to all the cylinders within the row regardless of focus offset parameter value.

It was hypothesized that the preheat scans would affect the build quality of the as-built parts, but an unexpected variable emerged as the build progressed: in Figure 7.2 the infrared intensity of the powder bed prior to processing can be seen to increase as a function of layer height. This observation suggests that for this build and others like it, heat can build up within the powder bed, effectively acting as another preheat parameter. Materials that are sensitive to being held at temperature may experience unexpected microstructural changes as a result of this type of preheating.

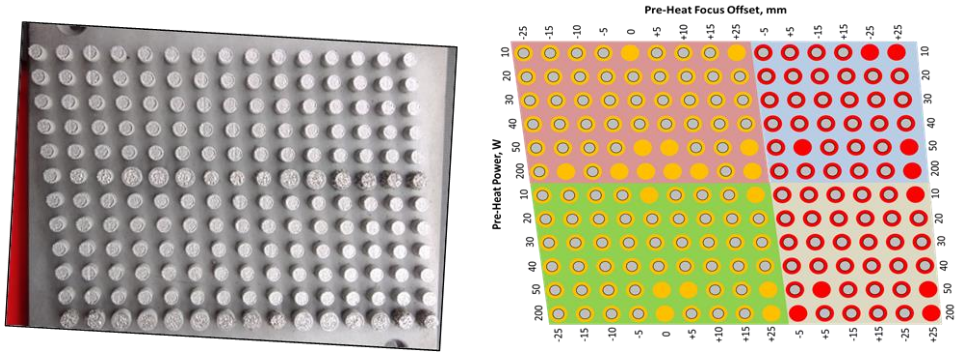

Figure 7.1: (left) top-down view of as-built parts still attached to the build plate. (right) schematic of the experiment setup with filled in circles marking which parts were analyzed using infrared data.

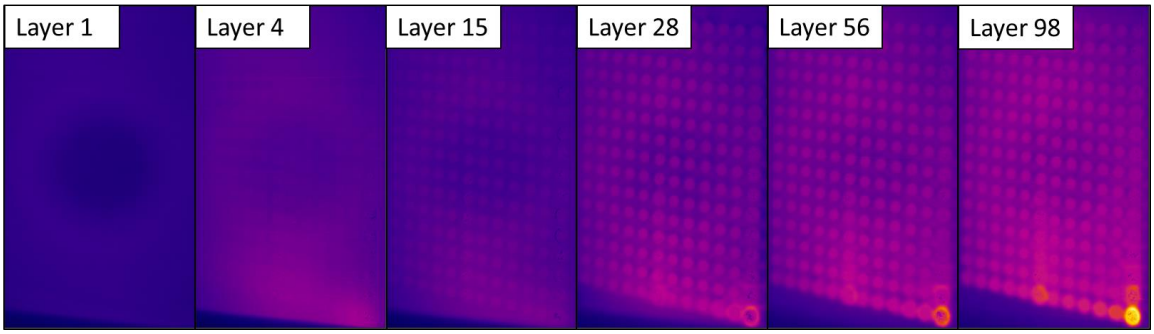

Figure 7.2: Infrared snapshots of the powder bed surface, collected the frame before building of the layer began.

Figure 7.3 shows the build plate schematic with optical images of XZ cross-sections of the cylinders overlaid onto their corresponding cylinder positions. A general pattern can be seen wherein parts that were built with preheat scans utilizing large focus offsets contain more porosity defects than parts built with preheat scans utilizing focus offset values closer to the 0 default. When comparing optical images of parts built with 1 preheat scan versus 2 preheat scans, an increase in porosity content can be seen. For example, the 200W, ±5 focus offset parts built using a 100-um hatch spacing parameter and only 1 preheat scan contain visibly less porosity compared to the same parts built using 2 preheat scans. These trends are seen primarily at preheat scans utilizing the highest power, 200W. Parts built with preheat scans utilizing lower power wattages up to 50W do not seem to contain varying amounts of porosity as a function of preheat parameters.

Figure 7.4 shows the same build plate schematic as in Figure 7.3 but with micro hardness values taken from the same XZ cross-sections and overlaid onto their corresponding cylinder positions. The micro hardness grid for each part was placed to avoid porosities so that all values would be representative of the material.

A general trend of increasing micro hardness values from the top surface of the parts going down to where the parts connect to the baseplate seems to exist across all sets of preheat parameters. Parts that exhibit large amounts of porosity do not exhibit this pattern as it is assumed that any accumulated stresses in these parts can relieve themselves by expanding into a nearby porous region.

It is interesting to note however, that although the part built with the preheat parameter set 200W, 0 FO, 60um hatch, and 1 preheat scan exhibit a similar porosity content as the parts built with the preheat parameter set 200W, ±5 FO, 100um hatch, and 1 preheat scan, it exhibits less internal stresses than those other two parts. This could be a direct result of reducing the hatch spacing. By reducing the hatch spacing, the number of spots is increased, and more energy is deposited in to the powder bed during the preheat. This continuous local preheating may have provided enough energy to relax some of the internal stresses within the part.

7.2. Discussion

In addition to collecting information about the hardness and porosity content of the as-built cylinders, the IR data collected during the builds was analyzed using homegrown code developed in MatLab. Frames recorded by the FLIR high speed IR container were 864x512 pixels in size. Each build layer video was comprised of approximately 25-30k frames.

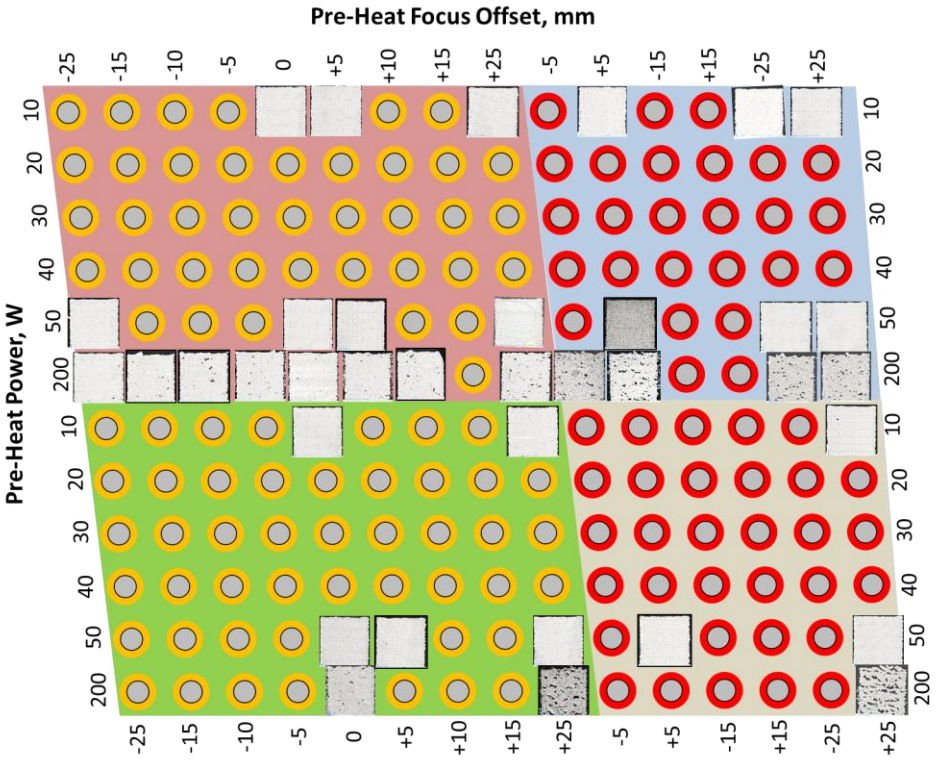

Figure 7.3: Build plate schematic with optical images of XZ cross-sections of the cylinder parts overlaid onto their respective positions on the build plate.

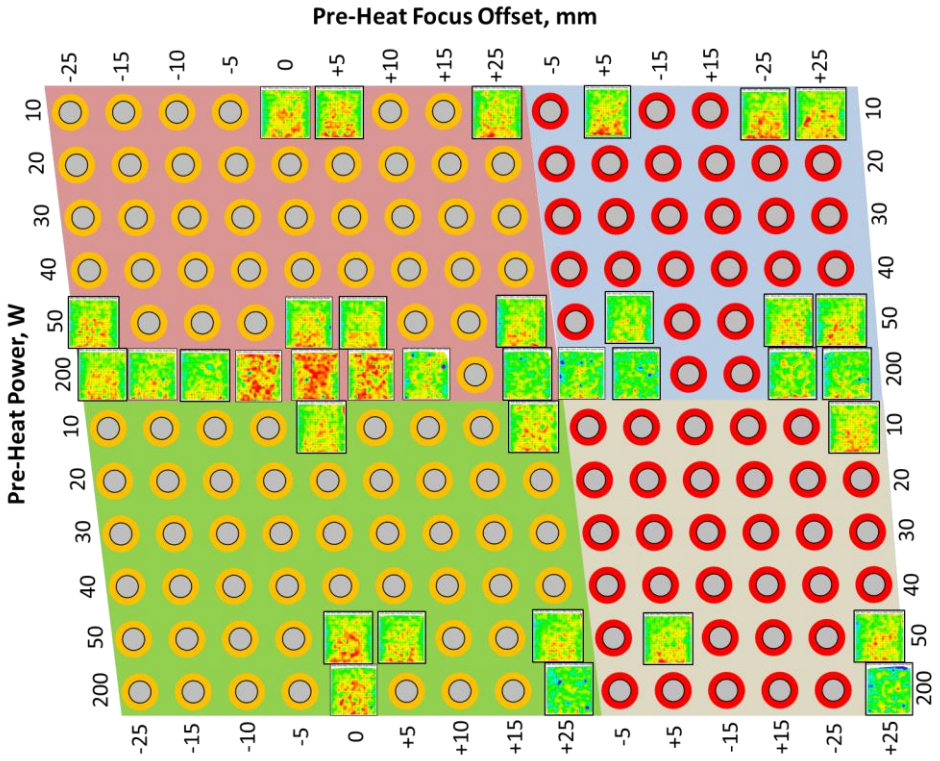

Figure 7.4: Build plate schematic with microhardness values of the XZ cross-sections of the cylinder parts overlaid onto their respective positions on the build plate.

To determine the cooling rate of a single pixel, the approximation was made that the IR intensity scaled with temperature. Several factors other than temperature can affect the intensity of the IR signal and over large differences in temperature, temperature and IR intensity do not scale linearly. However, the approximation made here is assumed to be valid for the purpose for obtaining general trends in temperature fluctuations within the powder bed.

To determine the cooling rate of a single pixel, the IR intensity signal from every frame for that pixel was collected a one-dimensional vector. The unrefined signal contained many small peaks corresponding to spatter particles intersecting the pixel or nearby laser passes. For ease of calculation, infrared signal contributions from moving spatter particles were removed and the raw signal was filtered using a 55-pixel moving average smoothing function. It was assumed that the peak intensity value within the vector correlated with a melt event at that point. Once the peak intensity value of the smoothed curve was determined, the curve was integrated beginning at the peak value frame and ending at a frame two seconds later (2sec*217frames/sec = 434 frames) in the pixel history. The value resulting from the integration is defined as the integrated area of that pixel and represents the cooling rate to a first degree. This process is shown pictorially in Figure 7.5.

In order to evaluate the cooling rate of a particular cylindrical part from the build, a region of interest containing the integrated areas of many pixels was defined, as shown in Figure 7.6a. Since the diameter of the cylinders was designed to be 5mm, and the resolution per pixel was set as 200 um/pixel, it was possible to define a new, circular region of interest 25 pixels in diameter within the original region of interest, as shown in Figure 7.6b. The rest of the original region of interest is comprised of the powder bed surrounding the part (Figure 7.6c).

By plotting the integrated areas of each pixel as a function of distance from the center of the original region of interest, patterns emerge describing specific events such as spatter presence in the powder bed, cool spots, and the level of preheat experienced by the powder bed as a function of build layer number. Figure 7.7 demonstrates how these plots can differ as a function of build height for a single cylinder (50W, +25 FO, 60um hatch, 1 preheat pass). Figure 7.8 depicts the micro hardness data and optical imaging of the cross-section of the cylinder.

In layers 15 and 56, bright spots can be seen in the powder bed representing spatter particles that landed in the powder bed and cooled. This event can be seen in the plots represented as thinner peaks offset from the main peak. The IR intensity in the part itself can also be tracked as a function of layer height and can be seen to rise significantly in layer 99 compared to layers 15 and 56.

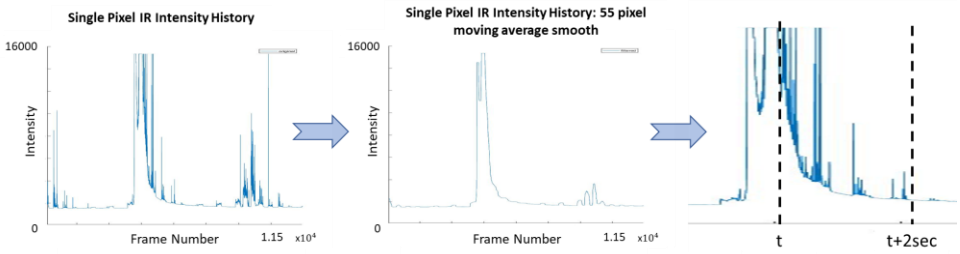

Figure 7.5: Figure describing the steps of infrared data analysis for a single pixel.

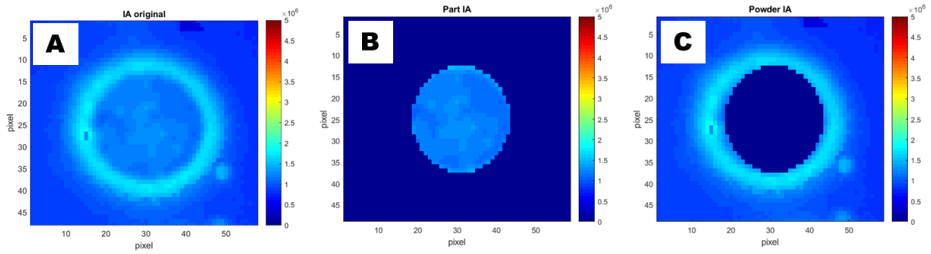

Figure 7.6: (a) a region of interest containing a top-down view of a cylinder part. Each pixel shows the integrated area intensity calculated for that pixel. (b) The same as a, except that the part has been isolated. (c) The same as a, except that the surrounding powder bed has been isolated.

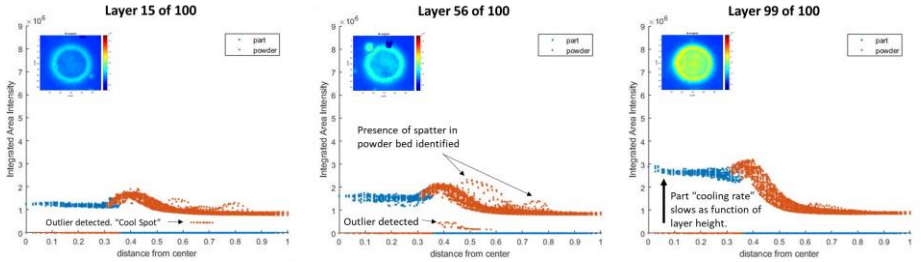

Figure 7.7: Integrated area calculated cooling rates for each pixel in the inlaid image are plotted as a function of distance from the center of the image. Comparisons of data from the same part, experiencing 1 preheat before melting, taken at three different layer heights can be made.

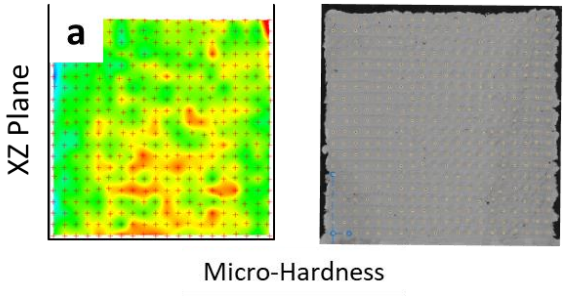

Figure 7.8: The micro hardness plot and optical image of the polished cross-section of the part whose IR data is analyzed in Figure 7.7.

As a comparison to Figure 7.7, the integrated intensities for pixels comprising another cylinder built with almost identical preheat parameters is presented in Figure 7.9. The micro hardness map and optical image of the cross-section of the part are given in Figure 7.10. The only difference is that the part in Figure 7.9 experience two preheat passes before melting instead of one. While this parts hardness values and optical image are not much different from its 1 preheat pass twin, the IR signal is significantly different. In particular, the peak is wider indicating a larger area of heat diffusion through the powder bed. The integrated area values of the melt region are higher at layer 15 and reach their highest value much faster, by layer 56. Distinct intensity rings formed around the part, and in layer 99 the main peak seems to divide into 2 peaks of equal intensity, but one shifted to the right of the other. This event seems to correlate with the heterogeneous intensity seen in the surface of the part, where the left side reads as "warmer" than the right side.

7.3. Summary & Conclusions

Laser preheat scans were employed during selective laser processing of stainless steel 316L prior to the final melting scan to influence the cooling rates of additively manufactured parts. Cylinders 5 mm in diameter and 5 mm in height were manufactured and infrared data was collected using a high speed FLIR IR camera operating at 217 Hz. Post build, destructive evaluation was performed XZ cross-sections of selected parts. The IR data collected from each pixel within a selected region of interest were converted into representative cooling rates using MatLab code and correlations were made between the IR cooling rate signatures and the micro-hardness data and porosity content of the as-built parts.

1. The powder bed prior to melting at each layer was observed to increase in overall IR emittance as a function of build height. This suggests that there exists some level of preheat within the powder bed and parts prior to melting that was not planned in the experiment. The observation that the pre-melt conditions vary as a function of build height suggest that a standard default build parameter set may not be appropriate and that a more responsive, sensory feedback-based parameter set selection process may be desired to produce parts of optimal quality.

2. In contrast with micro hardness data collected from as-built parts in the variable oxygen experiment, hardness maps of the cylinders exhibited increased hardness at the base of the parts becoming softer as a function of build height.

3. A general trend of increased amounts of lack-of-fusion porosity existed within parts build with 2 versus 1 preheat scans prior to melting. It is thought that by overly preheating the powder bed surface prior to melting, too much energy is deposited into the melt pool during the melt scan, resulting in unstable key-holing welding phenomenon to occur.

4. Pixel-level cooling rates based off of IR intensity over time were proven to be a feasible data analysis technique. Features that can be detected include: spatter particles that fall back into the powder bed, powder bed cooling rates as a function of position, variations within the cooling rate of the surface of as-built parts, the degree to which a part of the powder bed is preheated prior to melting.

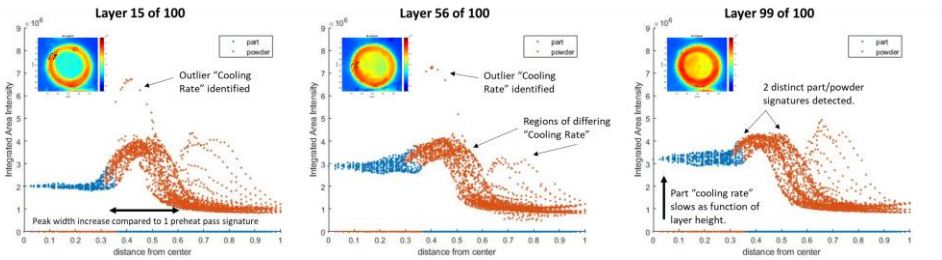

Figure 7.9: Integrated area calculated cooling rates for each pixel in the inlaid image are plotted as a function of distance from the center of the image. Comparisons of data from the same part, experiencing 2 preheats before melting, taken at three different layer heights can be made.

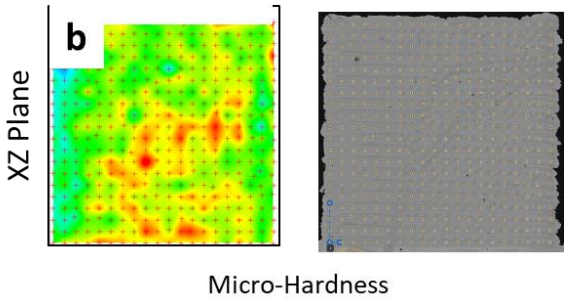

Figure 7.10: The micro hardness plot and optical image of the polished cross-section of the part whose IR data is analyzed in Figure 7.9.

CHAPTER 8 CONCLUSIONS & FUTURE WORK

8.1. Conclusions

8.1.1. Spatter Characterization & Rationalization

1. Inspection of FCC spatter particles' dendrite arm spacings revealed that fast liquid/solid interface velocities (>1m/s) may exist during solidification, that are adequate to drive a planar solidification front (most likely accompanied by solute trapping).

2. An interface response function model developed by Kurtz, Giovanni, and Trivedi, and codified by Babu et. al. was implemented to see if the modeled primary solidification phase matched with what was observed experimentally. The model unrealistically predicted dendritic BCC solidification at low solidification rates, and planar BCC solidification at higher solidification rates. This is unrealistic considering that, as a number percentage, more spatter particles were observed to be composed of FCC grains than BCC grains.

3. The KGT model does not consider nucleation kinetics. It is hypothesized that the spattering mechanism during SLM processing allows for the dispersal of bulk liquid into droplets, some of which do not contain potent nucleation sites like oxides, which allows the liquid droplet to supercool to temperatures where the metastable phase can out-nucleate or out-grow a more thermodynamically stable phase.

4. The presence of an oxide shell surrounding the BCC spatter particles may also have influenced undercooling to temperatures allowing for heterogeneous nucleation n of the metastable phase to out-compete that of the thermodynamically stable phase.

8.1.2. Heat Affect Zone Experiments

It was found that oxygen content in un-melted 316L powder during the SLM process was found to vary as a function of its relative position to the heat source. Measurements of oxygen weight percent in powder samples located very near the melt zone (<0.25 mm) indicated increased oxygen content. The volume of melted material (i.e. thin vs thick walls) was not found to affect the degree of oxygen pickup in the un-melted powder.

The mechanism driving the oxygen pickup in powder positioned close to melted regions is likely caused by an increase in thickness of the oxide scale on the surface of the un-melted powder particles, promoted by the elevated temperatures and adequate oxygen partial pressure during processing. It was found that dilution effects become considerate

even at small length scales (5 mm) and can occlude local changes in powder characteristics (i.e. oxygen pickup) when measuring bulk powder characteristics.

An oxidation model of Fe3O4 on FCC iron was performed using DICTRA and was found to overestimate the amount of oxidation back-calculated from oxygen content and XPS measurements. The DICTRA model used thermal histories calculated by a simple Rosenthal conduction model. The overestimation of oxide thickness predicted by DICTRA may also be in some parts the fault of the Rosenthal model. Access to thermodynamic and kinetic data of oxides is needed to perform more relevant oxidation growth calculations.

The role of spatter and its re-introduction into the powder bed was discussed. It was determined that even though spatter may contain elevated levels of oxygen, it is not likely a significant source of oxygen pickup within the powder bed.
Future studies should include a traditional oxidation study of stainless-steel feedstock powder at temperatures and time scales associated with the SLM process. Qualitative examination of the oxide shell both before and after the oxidation studies should be able to validate the conclusions found in this study. Future powder recyclability studies should be aware of and take into account the localized oxidation in the unmelted powder close to melted regions.

8.1.3. Variable Oxygen Environment Experiment

The powder XRD characterization of unmelted powder collected from the powder bed at each level of cover gas oxygen content does not qualitatively demonstrate a difference in the amount of BCC phase present in the powder bed as a function of cover gas oxygen content. Bulk chemical analysis of the same powder samples also does not suggest a correlation between powder bed particle oxygen content and cover gas oxygen content, even between magnetic and non-magnetic particles.

HTXRD shows that the BCC phase present within the spatter sample solidified as a metastable phase with an AC1 temperature of approximately 550oC.

Chemical analyses of parts built under atmospheres containing varying concentrations of oxygen suggest that reducing cover gas oxygen content reduces the oxygen content slightly within as-built parts (~0.008 wt%). TEM analysis confirmed this by finding more nano-oxides within the as-built parts built at higher concentrations of atmospheric oxygen when compared to parts built at low concentrations of atmospheric oxygen. The nano-oxides in the high oxygen atmosphere were also an average of 3 nm bigger in diameter than those inside parts built at low levels of atmospheric oxygen.

Despite the increase in nano-oxides, mechanical testing results (hardness mapping and tensile testing) indicate that the mechanical properties of additively manufactured 316L

parts are insensitive to significant variation of cover gas O2 concentration in the build chamber during processing.

8.1.4. Powder Recyclability Experiment

Despite high porosity content, the mechanical properties of parts built during the powder recyclability study are increased relative to standards for wrought stainless 316L steel. Increased yield strength (575MPa) and ductility (042) were observed. This yield strength is comparable to severely cold-worked wrought material. Part ductility is much increased compared to standards for stainless steel 316L but is not consistent. Fractographic analysis suggests that the variability in ductility correlates with porosity positioning within each specimen. Tensile specimens with porosity located at stress-concentrating corners failed earlier than specimens with similarly sized porosity located within the interior of the specimen.

Heat treatment (1095oC for 15 min., 1250oC for 420 min., 600oC for 1 hour) and subsequent tensile testing and TEM analysis of recyclability parts reveal that heat treatment reduces the strain dislocation density within the parts, which correlates with reduced yield strength. It is concluded that the increased tensile properties observed in SLM as-built parts is due to high amounts of residual stress within the parts resulting from the exposure to multiple heat cycles and high thermal gradients experienced during the SLM process.

TEM analysis of as-built parts revealed the presence of Si and Mn rich oxides residing primarily on the interdendritic and grain boundaries. It is concluded that these oxides form as a result of solute segregation during the solidification process. Heat treatment caused these oxides to grow in size and reduce in number.

8.1.5. Cooling Rate Experiment

1. The powder bed prior to melting at each layer was observed to increase in overall IR emittance as a function of build height. This suggests that there exists some level of preheat within the powder bed and parts prior to melting that was not planned in the experiment. The observation that the pre-melt conditions vary as a function of build height suggest that a standard default build parameter set may not be appropriate and that a more responsive, sensory feedback-based parameter set selection process may be desired to produce parts of optimal quality.

2. In contrast with micro hardness data collected from as-built parts in the variable oxygen experiment, hardness maps of the cylinders exhibited increased hardness at the base of the parts becoming softer as a function of build height.

3. A general trend of increased amounts of lack-of-fusion porosity existed within parts build with 2 versus 1 preheat scans prior to melting. It is thought that by overly preheating the powder bed surface prior to melting, too much energy is deposited into the melt pool during the melt scan, resulting in unstable key-holing welding phenomenon to occur.

4. Pixel-level cooling rates based off of IR intensity over time were proven to be a feasible data analysis technique. Features that can be detected include: spatter particles that fall back into the powder bed, powder bed cooling rates as a function of position, variations within the cooling rate of the surface of as-built parts, the degree to which a part of the powder bed is preheated prior to melting.

8.2. Future Work

During the course of the work presented in this thesis, a number of areas were identified that merit further analysis or additional investigation. This final section discusses ways in which the research already conducted could be enhanced and better understanding of the findings achieved

First, the theory of homogeneous nucleation of the BCC phase in the solidification rationalization of the single-crystal BCC spatter particles relies on the assumption that the particles do not contain potent nucleation sites. TEM analysis of the BCC particles would confirm if there are the same number and type of nano-oxides present within the BCC matrix as in the FCC matrices already observed. If nano-oxides are present within the BCC particles homogeneous nucleation of the BCC phase is not likely to be a convincing explanation.

Second, if in fact the solidification of single-crystal BCC particles is driven by extremely fast cooling rates, an experiment could be performed to increase the cooling rates in spatter particles. A cover gas with a higher thermal conductivity than argon could be used to promote faster cooling in more particles. A higher number percentage of particles would be expected to form as BCC, single-crystal than under normal argon cover gas. A more extreme experiment could employ the use of liquid nitrogen to rapidly quench spatter particles as soon as they are emitted from the weld pool. Again, a higher number proportion of particles should solidify as BCC under these conditions, if cooling rate is the driving factor behind BCC solidification.

Third, APT data was only collected for one FCC particle in this study. Because of the sampling method, it is possible that the FCC particle analyzed was not ejected from the weld pool and resolidified, rather it could have originated from the powder bed as the second type of spatter that is displaced by pressure variations caused by evaporating gases over the weld pool. A surer sampling technique of spatter, perhaps of a particle

too large to have fit through the sieve, and more data collected from FCC particles would help elucidate the differences between how FCC and BCC particles solidify.

Fourth, a new type of powder recyclability study should be designed and carried out utilizing the findings of the HAZ experiment, namely that local oxidation of the powder bed near a melted region occurs. This finding naturally suggests that the powder feedstock for builds with more surface area will “age” faster than feedstock for builds of a simpler geometry like the recyclability studies that have been carried out to date.

Fifth, the code for the pixel cooling rate calculated from IR data is not fast enough to be performed in-situ during the build process. Increased camera frame rates and more IR data would exacerbate this problem. Also, the code in its current form is optimized to analyze simple geometries like squares, circles, etc. A more flexible code that can translate the features seen within the plots in section 7.2 into simple weighted indicators is desired.

REFERENCES

[1] R. Dehoff and W. Peter, “unpublished research,” 2014.
[2] A. Strondl, O. Lyckfeldt, H. Brodin, and U. Ackelid, “Characterization and Control of Powder Properties for Additive Manufacturing,” *JOM*, vol. 67, no. 3, pp. 549–554, 2015.
[3] H. P. Tang, M. Qian, N. Liu, X. Z. Zhang, G. Y. Yang, and J. Wang, “Effect of Powder Reuse Times on Additive Manufacturing of Ti-6Al-4V by Selective Electron Beam Melting,” *JOM*, vol. 67, no. 3, pp. 555–563, 2015.
[4] Renishaw, “Investigating the effects of multiple re-use of Ti6Al4V powder in additive manufacturing,” 2016.
[5] Y. Liu, Y. Yang, S. Mai, D. Wang, and C. Song, “Investigation into spatter behavior during selective laser melting of AISI 316L stainless steel powder,” *Mater. Des.*, vol. 87, pp. 797–806, Dec. 2015.
[6] R. K. Blandford, D. K. Morton, S. D. Snow, and T. E. Rahl, “Tensile Stress-Strain Results for 304L and 316L Stainless Steel Plate at Temperature,” 2007.
[7] P. Nandwana *et al.*, “Recyclability Study on Inconel 718 and Ti-6Al-4V Powders for Use in Electron Beam Melting,” *Metall. Mater. Trans. B*, vol. 47, no. 1, pp. 754–762, Oct. 2015.
[8] P. Nandwana and R. Dehoff, “unpublished research,” 2014.
[9] B. Strauss and M. E., “Die hochlegierten Chromnickelstahle als nichtrostende Stahle,” *Kruppsche Monatshefte*, vol. 1, no. 8, pp. 129–146, 1920.
[10] J. C. Lippold and D. J. Kotecki, *Welding Metallurgy and Weldability of Stainless Steels*. Hoboken: John Wiley & Sons, Inc., 2005.
[11] D. J. Kotecki and T. A. Siewert, “WRC-1992 Constitution Diagram for Stainless Steel Weld Metals : A Modification of the WRC-1988 Diagram,” *AWS Annu. Meet.*, pp. 171–178, 1992.
[12] S. A. David, J. M. Vitek, and T. L. Hebble, “Effect of Rapid Solidification on Stainless Steel Weld Metal Microstructures and Its Implications on the Schaeffler Diagram,” *Weld. Res. Suppl.*, no. October, pp. 289–300, 1987.
[13] J. W. Elmer, S. M. Allen, and T. W. Eagar, “Microstructural development during solidification of stainless steel alloys,” *Metall. Trans. A*, vol. 20, no. 10, pp. 2117–2131, 1989.
[14] J. M. Vitek, S. A. David, and C. R. Hinman, “Improved Ferrite Number Prediction Model that Accounts for Cooling Rate Effects-Part1: Model Development.”
[15] J. M. Vitek, S. A. David, and C. R. Hinman, “Improved Ferrite Number Prediction Model that Accounts for Cooling Rate Effects – Part 2: Model Results,” *Welding Journal*, 2003. [Online]. Available: file:///C:/Users/gdg/Downloads/Improved Ferrite Number Prediction Model that Accounts for Cooling Rate Effects-Part1 Model Development.pdf. [Accessed: 06-Apr-2016].
[16] W. Kurz and D. J. Fisher, “Dendrite growth at the limit of stability: tip radius and spacing,” *Acta Metall.*, vol. 29, no. 1, pp. 11–20, 1981.
[17] W. Kurz, B. Giovanola, and R. Trivedi, “Theory of Microstructural Development During Rapid Solidification,” vol. 34, no. 5, 1986.

[18] University of Cambridge, “The Ellingham diagram.” [Online]. Available: https://www.doitpoms.ac.uk/tlplib/ellingham_diagrams/ellingham.php. [Accessed: 01-Jan-2016].
[19] N. Birks, G. H. Meier, and F. S. Pettit, *Introduction to the high-temperature oxidation of metals*, 2nd ed. New York: cambridge university press, 2006.
[20] E. Fromm, *Kinetics of Metal-Gas Interactions at Low Temperatures*. berlin: Springer-Verlag, 1998.
[21] R. Guillamet, J. Lopitauz, B. Hannoyer, and M. Lenglet, “Oxidation of stainless steels (AISI 304 and 316) at high temperature. Influence on the metallic substratum,” *Le J. Phys.*, vol. 3, pp. 349–356, 1993.
[22] K. A. Habib, M. S. Damra, J. J. Saura, I. Cervera, and J. Bellés, “Breakdown and evolution of the protective oxide scales of AISI 304 and AISI 316 stainless steels under high-temperature oxidation,” *Int. J. Corros.*, vol. 2011, 2011.
[23] M. F. McGuire, “Oxidation,” in *Stainless Steels for Design Engineers*, ASM International, 2008, pp. 57–68.
[24] J. Tarabay *et al.*, “Oxidation of stainless steel powder,” vol. 80, pp. 311–322, 2013.
[25] T. Debroy and S. A. David, “Physical processes in fusion welding,” 1995.
[26] T. Hibiya and S. Ozawa, “Effect of oxygen partial pressure on the marangoni flow of molten metals,” *Cryst. Res. Technol.*, vol. 48, no. 4, pp. 208–213, 2013.
[27] E. Louvis, P. Fox, and C. J. Sutcliffe, “Selective Laser Melting of aluminum components,” *J. Mater. Process. Technol.*, vol. 2311, pp. 275–284, 2011.
[28] R. C. Nederland, “A profile refinement method for nuclear and magnetic structures,” *J. Appl. Cryst.*, vol. 2, pp. 65–71, 1969.
[29] B. H. Toby and R. B. Von Dreele, “GSAS-II : the genesis of a modern open-source all purpose crystallography software package,” *J. Appl. Cryst.*, vol. 46, pp. 544–549, 2013.
[30] T. A. Palmer and T. DebRoy, *Physical modeling of nitrogen partition between the weld metal and its plasma environnment*. 1996.
[31] T. A. Palmer and T. Debroy, “Numerical modeling of enhanced nitrogen dissolution during gas tungsten Arc welding,” *Metall. Mater. Trans. B*, vol. 31, no. December, pp. 1371–1385, 2000.
[32] S. S. Babu, J. W. Elmer, J. M. Vitek, and S. A. David, “Time-resolved X-ray diffraction investigation of primary weld solidification in Fe-C-Al-Mn steel welds,” *Acta Mater.*, vol. 50, pp. 4763–4781, 2002.
[33] J. H. Perepezko, “Nucleation in Undercooled Liquids,” *Mater. Sci. Eng.*, vol. 65, pp. 125–135, 1984.
[34] J. H. Perepezko and M. J. Uttormark, “Undercooling and nucleation during solidification,” *ISIJ Int.*, vol. 35, no. 6, pp. 580–588, 1995.
[35] T. Suzuki, J. Inoue, and T. Koseki, “Solidification of Iron and Steel on Single-crystal Oxide,” *ISIJ Int.*, vol. 47, no. 6, pp. 847–852, 2007.
[36] C. Oikonomou, D. Nikas, E. Hryha, and L. Nyborg, “Evaluation of the thickness and roughness of homogeneous surface layers on spherical and irregular powder particles,” *Surf. Interface Anal.*, vol. 46, no. 10–11, pp. 1028–1032, Oct. 2014.

[37] B. Almangour, D. Grzesiak, J. Cheng, and Y. Ertas, “Thermal behavior of the molten pool , microstructural evolution , and tribological performance during selective laser melting of TiC / 316L stainless steel nanocomposites : Experimental and simulation methods,” *J. Mater. Process. Tech.*, vol. 257, no. November 2017, pp. 288–301, 2018.
[38] D. Rosenthal, “The Theory of Moving Sources of Heat and Its Application to Metal Treatments,” *Trans. Am. Soc. Mech. Eng.*, vol. 68, pp. 849–866, 1946.
[39] C. D. Boley, S. A. Khairallah, and A. M. Rubenchik, “Calculation of laser absorption by metal powders in additive manufacturing.,” *Appl. Opt.*, vol. 54, no. 9, pp. 2477–82, Mar. 2015.
[40] M. R. Alkahari, T. Furumoto, T. Ueda, A. Hosokawa, R. Tanaka, and M. S. Abdul Aziz, “Thermal Conductivity of Metal Powder and Consolidated Material Fabricated via Selective Laser Melting,” *Key Eng. Mater.*, vol. 523–524, pp. 244–249, 2012.
[41] R. L. Tapping, R. D. Davidson, and T. E. Jackman, “Calibration of argon ion sputter rates using nuclear microanalysis and Auger spectroscopy,” *Surf. Interface Anal.*, vol. 7, no. 2, pp. 105–108, 1985.
[42] P. Bidare, I. Bitharas, R. M. Ward, M. M. Attallah, and A. J. Moore, “Fluid and particle dynamics in laser powder bed fusion,” *Acta Mater.*, vol. 142, pp. 107–120, 2018.
[43] O. Kubaschewski, “Fe-O Phase Diagram,” in *IRON - Binary Phase Diagrams*, 1982, pp. 79–82.
[44] S. S. Babu, S. A. David, J. M. Vitek, and R. W. Reed, “Solidication and microstructure modelling of welds in aluminium alloys 5754 and 6111,” *Sci. Technol. Weld. Join.*, vol. 6, no. 1, pp. 31–40, 2001.
[45] J. Datsko, *Material Properties and Manufacturing Processes*. New York: John Wiley & Sons, Inc., 1966.
[46] V. Weiss, J. G. Sessler, W. F. Brown, and S. S. Manson, Eds., *Aerospace Structural Metals Handbook: Volume 1 Ferrous Alloys*. Syracuse: Syracuse University Press, 1963.
[47] G. E. Dieter, “Strengthening Mechanisms,” in *Mechanical Metallurgy*, 3rd ed., New Delhi: McGraw Hill Education (India) Private Limited, 2013, p. 191.
[48] L. M. Sochalski-Kolbus *et al.*, “Comparison of Residual Stresses in Inconel 718 Simple Parts Made by Electron Beam Melting and Direct Laser Metal Sintering,” *Metall. Mater. Trans. A*, vol. 46, no. 3, pp. 1419–1432, Jan. 2015.
[49] Bruker AXS GmbH, “D2 Phaser 2nd Generation.” [Online]. Available: https://www.bruker.com/fileadmin/user_upload/8-PDF-Docs/X-rayDiffraction_ElementalAnalysis/XRD/Brochures/D2_PHASER_2ndGen_Brochure_DOC-B88-EXS017-V2_web.pdf. [Accessed: 13-Sep-2015].
[50] Bruker AXS GmbH, “Spec Sheet XRD 27 LYNXEYE-Super Speed Detector for X-ray Powder Diffraction,” 2015. [Online]. Available: https://www.bruker.com/fileadmin/user_upload/8-PDF-Docs/X-rayDiffraction_ElementalAnalysis/XRD/ProductSheets/LYNXEYE_DOC-S88-EXS027_V4_high.pdf.

APPENDICES

Appendix A – build parameters

Recyclability and HAZ Experiments
Scan Strategy: MEANDER

Hull and Core overlap	0.4	mm	
Wire Structure Shape: Minimal segment length	0.2	mm	
Layer path organization	inside to outside		
	Volume Area	Volume of Offset Hatch	Volume border
Power Output (W)	200	180	175
Focus Offset (mm)	0	0	0
Point distance (µm)	60	65	25
Exposure time (µs)	80	110	130
	Overhang border	Skin area	Wire structure
Power Output (W)	50	125	0
Focus Offset (mm)	0	0	0.2
Point distance (µm)	25	65	200
Exposure time (µs)	65	60	400

Contour		
Layer Spot Composition	45	µm
Edge Factor	1.2	
Following distances	200	µm
Offset Hatch general offset number	1	
Offset Hatch general offset space	50	µm
Volume Area		
Angle	0	deg
Angle increment	67	deg
Hatch Space	110	µm
Contour Space	100	µm
Skin Area		
Angle	0	deg
Angle increment	0	deg
Hatch Space	175	µm
Contour Space	100	µm

Variable Oxygen Environment Study and Spatter Experiment Baseplate
Scan Strategy: STRIPE

Stripe Width	5	mm
Stripe Offset	-0.05	mm
Repetition Limit	10	
Merge Vectors	yes	
Optimize Jumps	yes	
layer path organization	inside to outside	

	Volume Area	Volume Border	Downskin	Upskin
Power Output (W)	200	110	100	160
Focus Offset (mm)	0	0	0	0
Point distance (µm)	60	20	40	50
Exposure time (µs)	80	100	80	110

Border		
Borders	2	
beam compensation	250	µm
border distance	100	µm
blocked path	yes	
Volume Area		
Angle	0	deg
Angle increment	67	deg
Hatch spacing	110	µm
hatch offset	60	µm
filter length	10	µm
Downskin		
Exposure Number	1	
Angle	0	deg
Angle increment	67	deg
Hatch spacing	60	µm
Pattern	meander	
skin area tolerance	61	µm
Upskin		
Exposure Number	1	
Angle	0	deg
Angle increment	67	deg
Hatch spacing	110	µm
filter length	10	µm
Pattern	meander	
offset to volume	-50	µm

Powder Bed Cooling Rate Study
Scan Strategy: MEANDER

layer path organization	inside to outside	
Number of Borders	0	
Downskin	No	
Upskin	No	
Volume Area		
Power Output	200	W
Focus Offset	0	mm
Point distance	60	µm
Exposure time	80	µs
Hatch spacing	100	µm
Hatch Offset	-60	µm
Filter length	10	µm
Angle	0	deg
Angle increment	0	deg

Appendix B – build log files

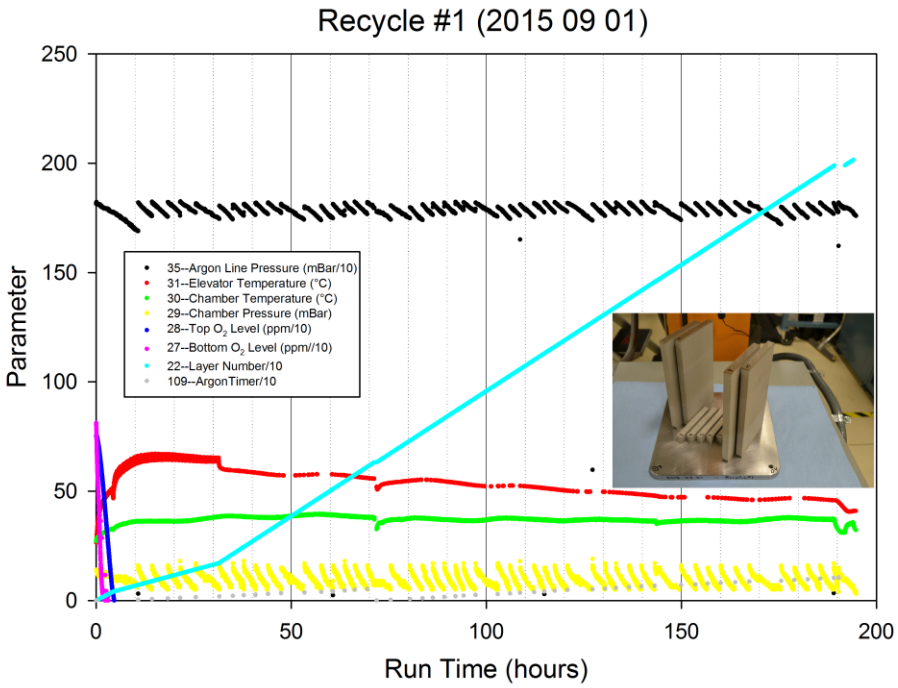

Data log of the first build cycle of the recyclability experiment.

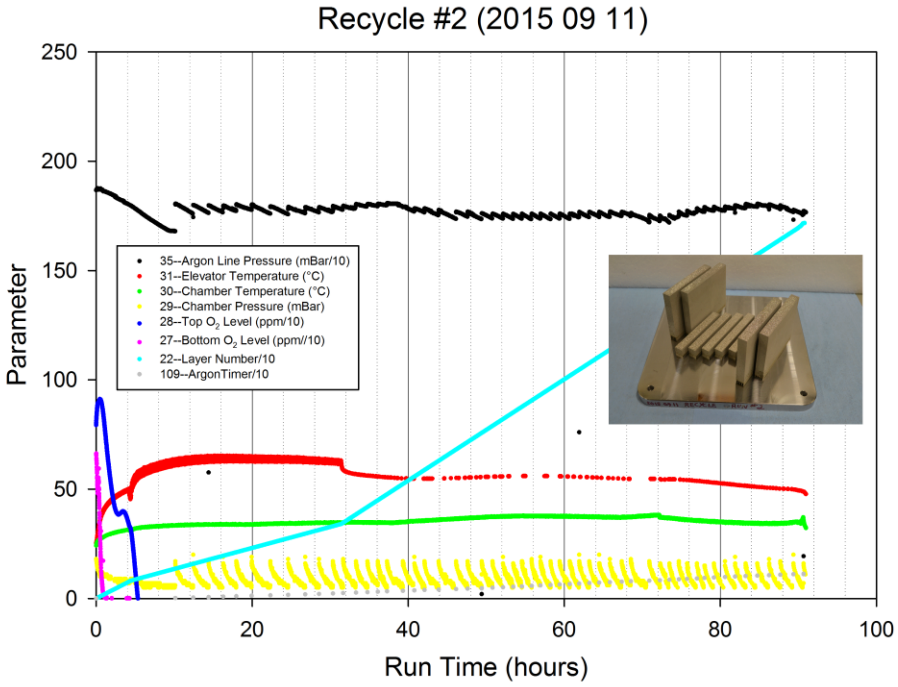

Data log of the second build cycle of the recyclability experiment.

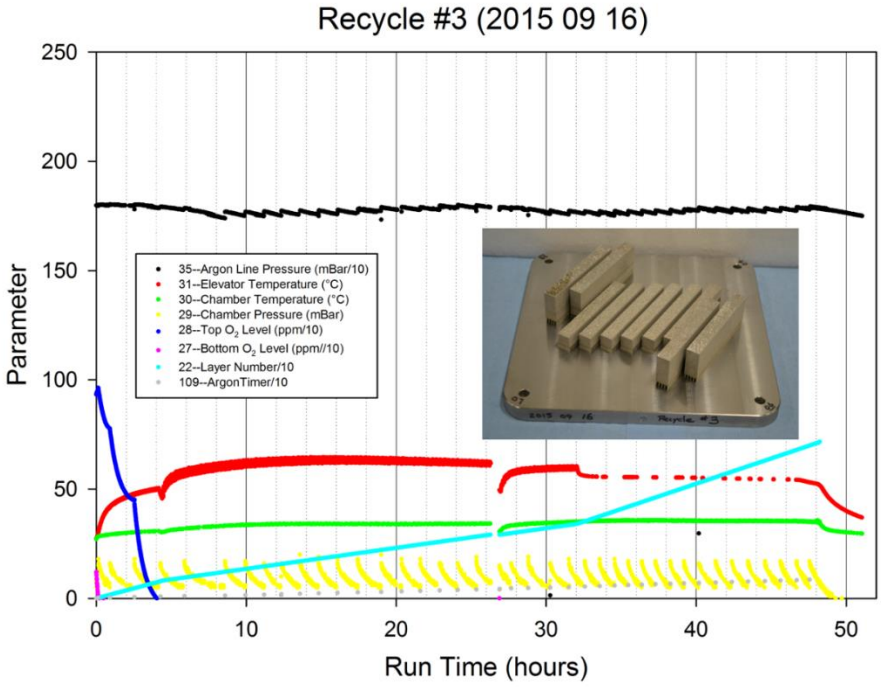

Data log of the third build cycle of the recyclability experiment. The discontinuity at hour 27 is attributed to an unexpected loss of power to the machine. The machine sat in shutdown mode for approximately 30 minutes before it was restarted and continued to build.

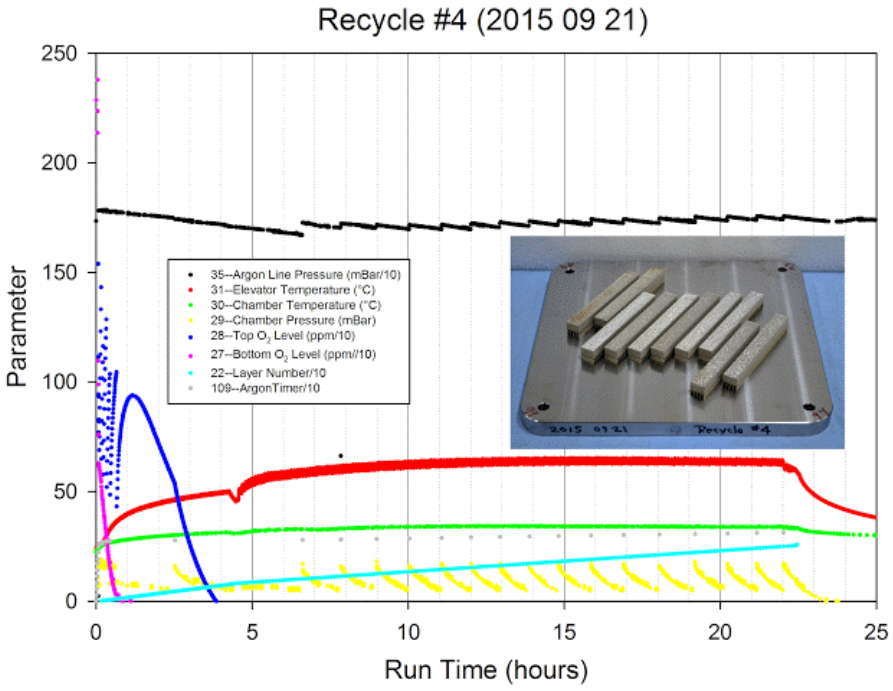

Data log of the fourth build cycle of the recyclability experiment.

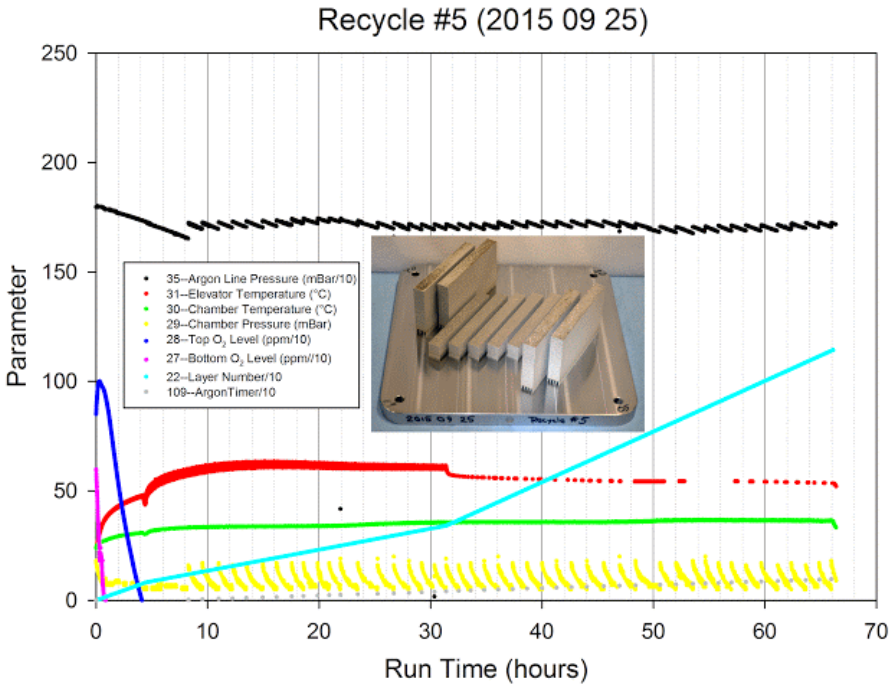

Data log of the fifth build cycle of the recyclability experiment.

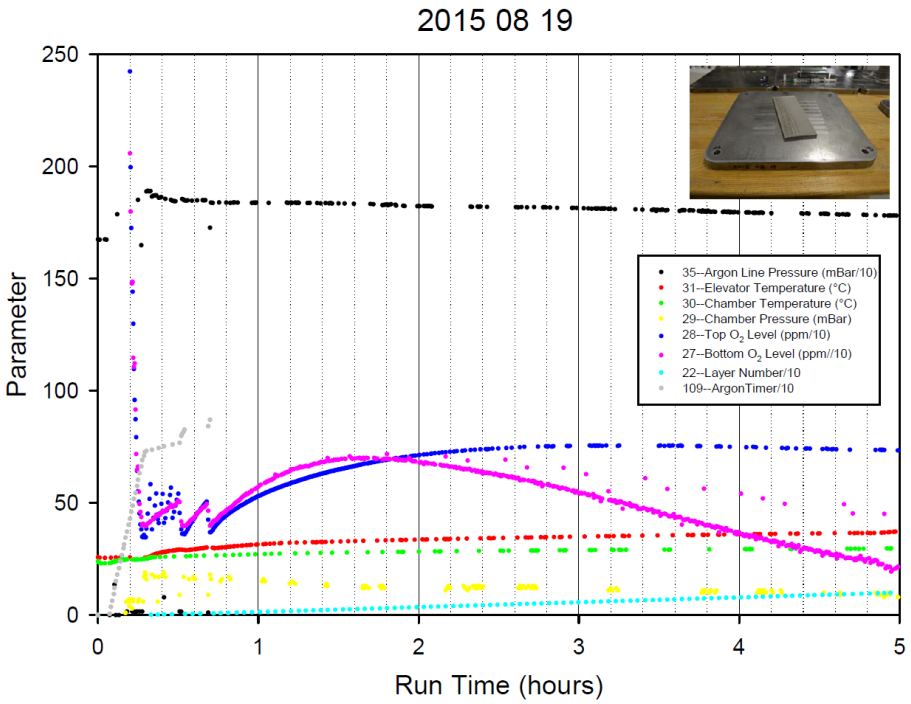

Data log of the first heat affected zone experiment.

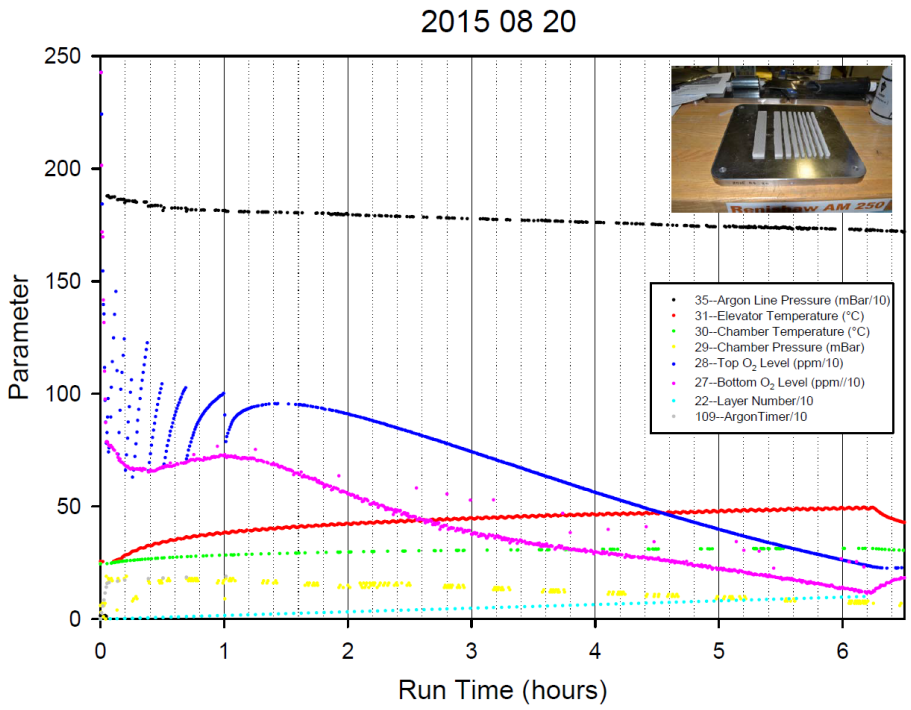

Data log of the second heat affected zone experiment.

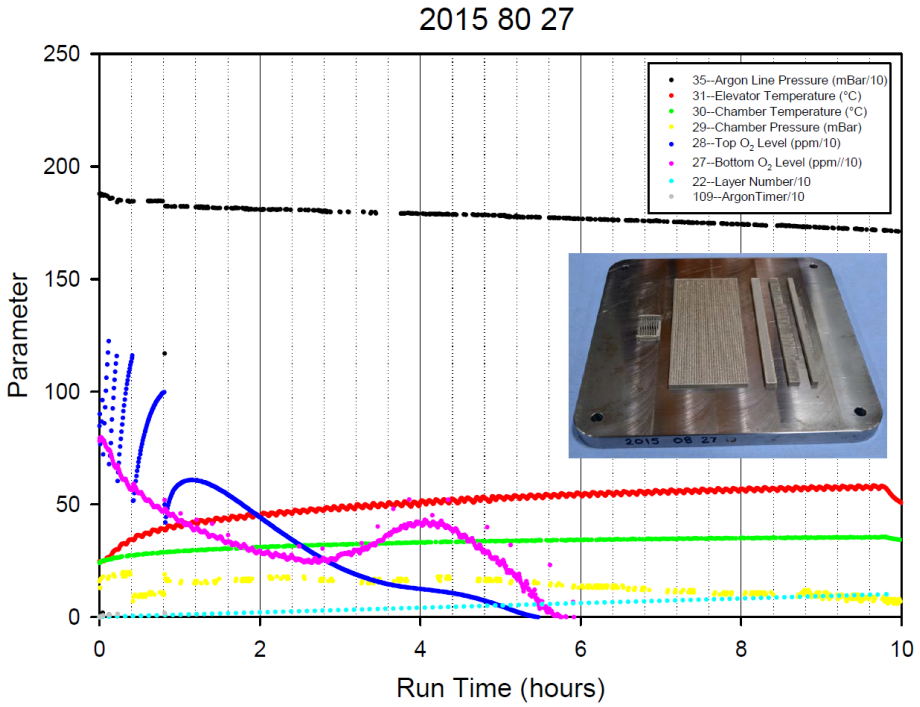

Data log of the third heat affected zone experiment.

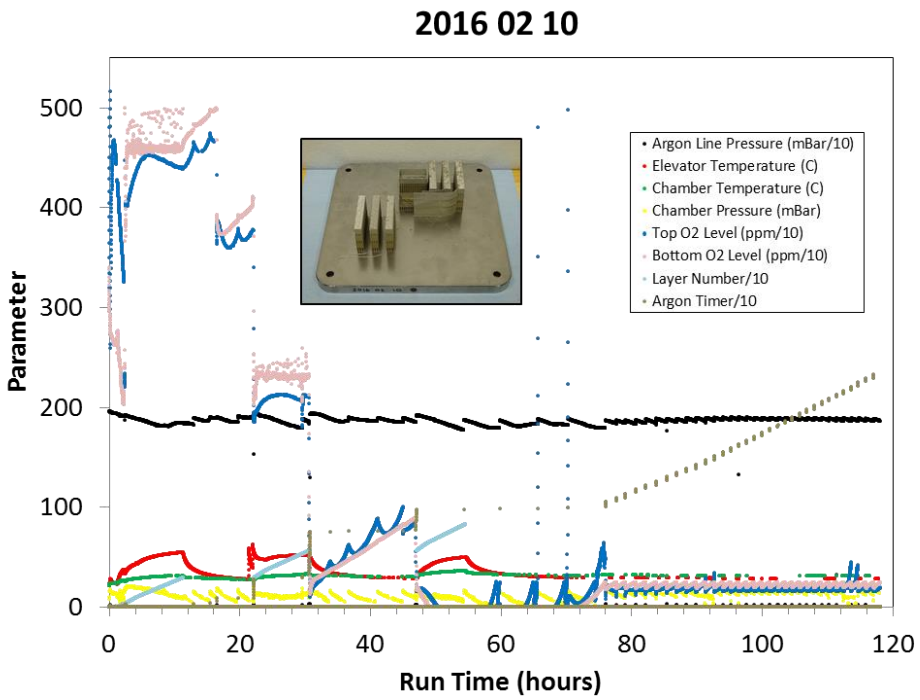

Data log of the variable oxygen environment experiment.

Appendix C – oxide scale thickness calculations

This appendix describes the methodology used to arrive at estimated initial and heat-affected-zone oxide thicknesses on a representative powder bed particle. A schematic of a representative steel particle encased in an oxide shell is provided in the schematic below.

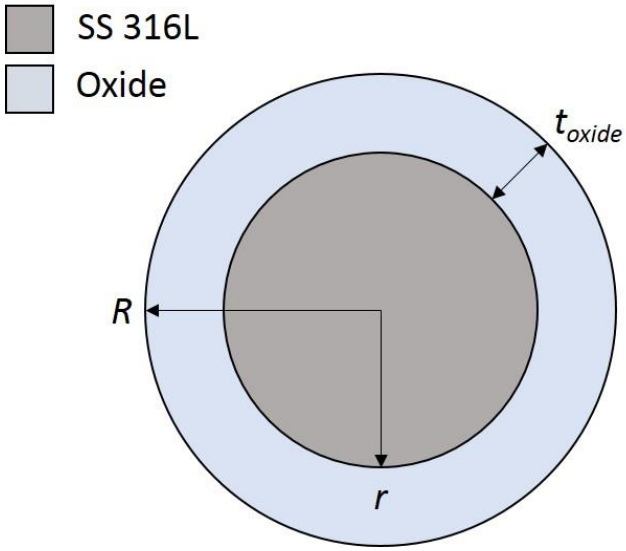

Schematic showing the oxide shell surrounding a stainless-steel powder particle.

To back calculate the initial Fe_3O_4 oxide thickness on an average particle, the following variables must be known: the measured oxygen content of the virgin powder ($wt\%_O$ = 0.033 $\pm$ 0.002 wt%), the density of 316L steel ($\rho_{316L} = 7.99$ g/cm^3), the density of the oxide ($\rho_{Fe_3O_4} = 5.17$ g/cm^3), the stoichiometry of Fe and O within the oxide ($s_{Fe} = 3, s_O = 4$), the molar mass of Fe and O ($MM_{Fe} = 55.845$ g/mol, $MM_O = 15.999$ g/mol), the molar mass of the oxide ($MM_{Fe_3O_4} = 231.533$ g/mol), and Avogadro's Number ($N_A = 6.022x10^{23}$ mol^{-1}). It follows that the wt% of the oxygen within the oxide shell can be determined by equations

$$wt\%_O = 100 \cdot \frac{m_O}{m_p + m_O} \quad \text{(C1)}$$

$$m_p = \rho_{316L} * V_p \quad \text{(C2)}$$

$$V_p = \frac{\pi}{6}(r)^3 \quad \text{(C3)}$$

where m_O is the mass of the oxygen contained in the oxide layer, m_p is the mass of a single powder particle with no oxide layer, V_p is the volume of a single powder particle

with no oxide layer, and r is the radius of a single powder particle with no oxide layer. The virgin powder size distribution (see section 2.3.1.3) was used to calculate an average particle radius, r = D_V/2, based on the average particle volume (D_V = 27.71 μm). It is assumed that the Fe needed to form the oxide is supplied by the base material and is therefore included in m_p value of Eq. C1. The mass of the oxygen within the initial oxide layer, m_O, can be determined by the equations

$$m_O = \frac{m_{oxide} N_A s_O MM_O}{MM_{oxide} N_A} \quad \text{(C4)}$$

$$m_{Oxide} = V_{Oxide} * \rho_{Fe_3O_4} \quad \text{(C5)}$$

$$V_{Oxide} = \frac{4\pi}{3}((r + t_{Oxide})^3 - r^3) \quad \text{(C6)}$$

where m_{oxide} is the mass of the oxide layer, V_{Oxide} is the volume of the oxide layer, and t_{Oxide} is the thickness of the oxide layer. Since the oxygen content in wt% is known, it is possible to back-calculate using Eqs. C1–C6 to determine the initial oxide thickness, t_{Oxide}, that will achieve the initial measured wt% value of 0.033 ($\pm$0.002). Microsoft Excel's Goal Seek function works well for this task. It is a simple matter to repeat the calculations above to find the average oxide thicknesses in the HAZ powder after being thermally cycled, using this time the oxygen content value of 0.043 ($\pm$0.002) wt%, measured from the powder contained in the 150 μm channels of the HAZ experiments.

Appendix D – powder bed dilution calculations

To calculate the dilution effects of an ever-increasing ratio of non-oxidized powder to oxidized powder, it was assumed that all the measured oxygen pickup is evenly distributed between the powder particles residing within a 150 µm wide channel, which is the narrowest channel in the heat-affected-zone experiments. For simplification purposes, a powder particle diameter (D_V) of 30 µm is assigned to all particles residing within the 150 µm channel. Furthermore, it is assumed that the powder particles are arranged in rows of stacked columns as shown in the schematic below. The oxygen content measured in the heat-affected powder sampled from the 150 µm channels ($wt\%_{HAZ}$) is 0.043 (+0.002) wt% and is represented by solid black outlines in the figure. Diluting powder is assumed to contain the measured oxygen content of the virgin powder ($\text{wt\%}_{\text{virgin}}$ = 0.033 + 0.002 wt%) and is represented by red dashed outlines.

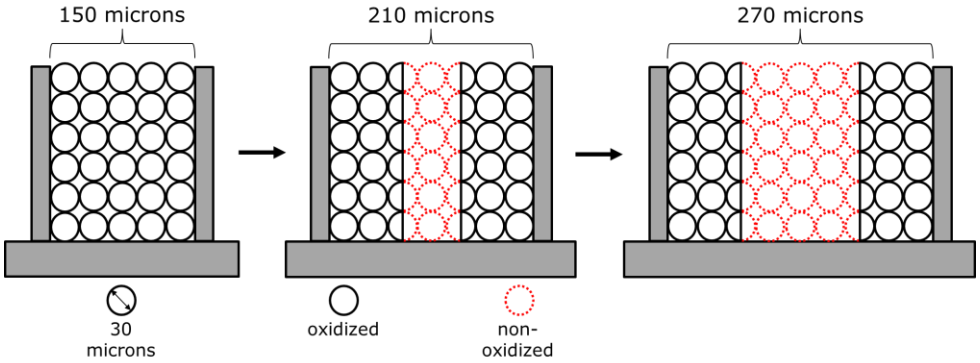

Schematic demonstrating the diluting effect of non-oxidized powder on locally oxidized powder as channel width is increased.

As the channel width is increased from 150 microns and more un-oxidized powder is added to fill the space between the channel walls, the total oxygen content wt% of the powder within the channel ($wt\%_{bed}$) begins to decrease as described by Equations D1-D3.

$$wt\%_{bed} = \frac{m_O}{m_{bed}} \quad \text{(D1)}$$

$$m_O = V_p \rho_{316L} (N_{HAZ} wt\%_{HAZ} + N_{virgin} wt\%_{virgin}) \quad \text{(D2)}$$

$$m_{bed} = V_p \rho_{316L} (N_{HAZ} + N_{virgin}) \quad \text{(D3)}$$

where m_O is the mass of oxygen in powder within the channel, m_{bed} is the total mass of the powder within the channel, V_p is the volume of a powder particle with diameter D_V, ρ_{316L} is the density of stainless steel 316L (7.99 g/cm^3), N_{HAZ} is the number of powder

particles within the heat-affected zone of the channel (black outlines), and N_{virgin} is the number of non-heat-affected powder particles within the channel (red, dashed outlines). N_{HAZ} and N_{virgin} can be determined by assuming any arbitrary height and length for the channel walls and calculating the number of powder particles of diameter D_V, arranged in the above geometry, that would fit between them. N_{HAZ} is the number of those particles that reside within 75 microns of either channel wall. The remaining particles after subtracting out N_{HAZ} from the total particles are N_{virgin}. By performing the above calculations using several increasing channel widths, as well as the upper and lower error bounds of the virgin powder oxygen content (0.035 & 0.031 wt%) and the upper and lower bounds of the HAZ powder oxygen content (0.045 & 0.041 wt%), a bounding area of oxygen wt% as a function of channel width can be produced as shown in the figure below.

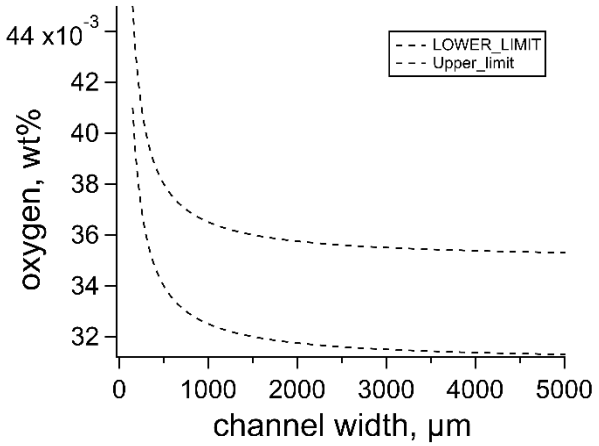

Plot of the bounded area of the dissolution effect as a function of channel width.

Appendix E – DICTRA macros

This appendix contains the text form of the DCM macro files used to 1) set up the DICTRA calculation, 2) Run the DICTRA calculation, and 3) Plot the thermal history and oxide thickness as functions of time on two separate plots. ThermoCalc version 2017b was used to perform the following calculations.

1. DICTRA Calculation Set-Up

```
@@ 05/25/2017
@@ Daniel Galicki
@@ Diffusion in complex phases.
@@ Oxidation of FCC iron sample and consequent growth of an oxide layer.

@@ fcc_oxidation.DCM
@@ WE START BY GOING TO THE DATABASE MODULE
goto-module
database-retrieval

@@ WE SELECT A USER DATABASE FOR READING THE THERMODYNAMIC
DATA
switch-database
TCFE8
define-system fe o
reject species *
restore species fe fe+2 fe+3 o o2 o-2 va
reject phases *
restore phases gas fcc spinel
get-data

@@ SWITCH TO A MOBILITY DATABASE TO RETRIEVE MOBILITY DATA FOR FCC
PHASE
append-database
MOBFE3
define-system fe o
reject species *
restore species fe o o2 va
reject phases *
restore phases FCC_A1
get-data

@@ SWITCH TO A USER DEFINED MOBILITY DATABASE TO RETRIEVE
MOBILITY DATA
append-database
```

```
user FeOmob.TDB
define-system fe o
reject species *
restore species fe fe+2 fe+3 o o2 o-2 va
reject phases BCC_A2
get-data

@@ ENTER THE DICTRA MONITOR
goto-module
dictra-monitor

@@ ENTER GLOBAL CONDITION TEMPERATURE
set-condition
global
T
0
775.29+(3529.04*TIME)+(-76661.26*(TIME**2))+(602228.84*(TIME**3))+(-
1857433.07*(TIME**4));
*
N

@@ SET REFERENCE STATE FOR O TO O2 (GAS)
set-reference-state
o
gas
323
100000

@@ ENTER REGIONS gam AND sp
enter-region
gam
enter-region
sp
gam
yes

@@ ENTER PHASES INTO REGIONS
enter-phase-in-region
active
gam
matrix
fcc
enter-phase-in-region
active
```

```
sp
matrix
spinel

@@ ENTER GRIDS INTO THE REGIONS
@@ Enter a size for the austenite
enter-grid-coordinates
gam
4.99999e-3
linear
50

@@ Enter a thin initial size for the oxide
enter-grid-coordinates
sp
9.036e-9
linear
50

@@ ENTER INITIAL COMPOSITIONS IN FCC
enter-compositions
gam
fcc
mole-fraction
o
linear
1e-9
1e-9

@@ ENTER INITIAL COMPOSITIONS IN THE OXIDE
enter-compositions
sp
spinel
mole-fraction
fe
linear
4.28771e-01
4.28549e-01
@@ ENTER A BOUNDARY CONDITION "GAS" ON THE UPPER (RIGHTMOST)
INTERFACE
@@ OF THE OXIDE. THIS WILL ALLOW THE SYSTEM TO EXPAND AND THE
OXIDE LAYER
@@ TO GROW EXTERNALY. FOR THIS EXAMPLE WE HAVE SPECIFIED AN
OXYGEN ACTIVITY
```

@@ THAT IS LOW ENOUGH IN ORDER NOT TO FORM CORUNDUM (FE2O3). WE ALSO
@@ SPECIFY THAT THERE IS NO FLUX OF FE ACROSS THIS INTERFACE, I.E. NO FE
@@ IS ALLOWED TO ENTER OR LEAVE THE SYSTEM.
set-condition
boundary
upper
gas-interface
zero-flux
activity
0
8.0947E-8;
*
N

@@ ENTER START VALUES FOR INITIAL INTERFACE VELOCITIE
set-all-start-values
-1e-5
1e-5
yes

@@ SIMULATE FOR 24 HOURS
set-simulation-time
0.104017526004381
yes
0.01040175260
1e-07
1e-07

@@ SPECIFY THAT POTENTIALS AND NOT ACTIVITIES ARE VARIED AT THE PHASE
@@ INTERFACE, AND ALSO USE A FULLY IMPLICIT SCHEME FOR TIME INTEGRATION.
set-simulation-condition
0
1
1
yes
potentials
yes
yes
1
2

no
yes
no

@@ SAVE THE SETUP ON A NEW STORE FILE AND EXIT
save 0.2WmK_75um_tempfunc_fcc_oxidation_500C_acr(O)=8.0947e-8_9.036nm.DIC
Y
set-interactive

2. Running the DICTRA Calculation

```
@@ Daniel Galicki
@@ 05/25/2017

@@ fcc_oxidation.DCM
@@ FILE FOR RUNNING fcc_oxidation

@@ ENTER THE DICTRA MONITOR AND READ THE STORE RESULT FILE
@@
goto-module dictra-monitor
read fcc_oxidation

@@ Start the simulation
simulate y
set-interactive
```

3. Plotting the DICTRA-Calculated Results

```
@@ Daniel Galicki
@@ 05/25/2017

@@ fcc_oxidation.DCM
@@ FILE FOR GENERATING GRAPHICAL OUTPUT FOR fcc_oxidation

@@ GO TO THE DICTRA MONITOR AND READ THE STORE RESULT FILE
goto-module
dictra-monitor
read-workspaces
fcc_oxidation

@@ ENTER THE POST PROCESSOR
post-processor

@@ LET'S PLOT THE THERMAL CYCLE THAT WE ENTERED
set-plot-condition
interface
sp
upper
set-diagram-axis
x
time
set-diagram-axis
y
temperature-celsius
plot-diagram

@@ SELECT A NEW PLOT WINDOW
select-plot
new

@@ LET'S PLOT THICKNESS OF THE OXIDE LAYER GROWING AT THE
SURFACE.
@@ FOR THIS PURPOSE, WE NEED TO ENTER A FUNCTION ACCORDING TO
BELOW.
enter-symbol
function
oxideth
poi(sp,upper)-poi(sp,lower);

@@ WE PUT THIS FUNCTION ON Y-AXIS
set-diagram-axis
```

y
oxideth
plot-diagram
set-interactive
exit

Appendix F – conversion of laser diffraction measurements into a representative, volume-averaged, monodisperse particle diameter

This appendix describes in detail the calculations used to convert typical laser diffraction measurements of a powder sample into a more easily workable, single, particle diameter value representing every particle in the measured powder sample. An example of laser diffraction measurement values is provided in Figure 4.15. The "Diameter" and "Undersized" headings in Figure 4.15 are represented in the following equations by D_p^i and V_I^i, respectively.

Equations F1-F4 were used to convert the laser diffraction incremental volume-percent value (V_I^i) into an incremental number-percent value (N_I^i).

$$V_p^i = \frac{4\pi}{3}\left(\frac{D_p^i}{2*(10{,}000)}\right)^3 \quad \text{(F1)}$$

$$N_p^i = \frac{V_{hyp}*V_I^i}{V_p^i} \quad \text{(F2)}$$

$$N_p^T = \sum_{i=1}^{m} N_p^i \quad \text{(F3)}$$

$$N_I^i = \frac{N_p^i}{N_p^T} \quad \text{(F4)}$$

where V_p^i is the volume of a single spherical particle with diameter D_p^i, N_p^i is the number of particles with diameter D_p^i residing within a hypothetical measured sample volume (V_{hyp}), N_p^T is the sum total number of particles within the hypothetical sample, and m is the number of particle size bins output by the laser diffractometer. In Figure 4.15, m is equal to 15 for example.

For any size sample of powder particles (n_{sample}), the volume (V_f^i) of the sample contributed by the number fraction of particles with diameter D_p^i can be calculated using Eq. F5.

$$V_f^i = V_p^i * \left(n_{sample} * N_I^i\right) \quad \text{(F5)}$$

The monodisperse, volume-averaged, particle diameter (D_{mon}) of a laser diffractometer measured powder sample can be calculated using equation F6.

$$D_{mon} = 2 * \frac{3}{4\pi}\left[\left(\left(\frac{\sum_{i=1}^{m} V_f^i}{n_{sample}}\right)^{1/3}\right) * 10{,}000\right] \quad \text{(F6)}$$

The above equations were used in this paper to convert laser diffraction measurements for virgin powder and spatter samples. The below table contains data from the measurement of one such spatter sample, and the values obtained from the application of Eqs. F1-F6.

Example of calculation of monodisperse, volume-averaged particle diameter from laser diffractometer measured data.

	n_{sample}	1,000,000				r_{mon} 31.13	
	V_{hyp}	1				D_{mon} 62.26	
i	D_p^i	V_I^i	V_p^i	N_p^i	N_I^i	$n_{sample} * N_I^i$	V_f^i
1	344.21	0.307	2.14E-05	1.44E+04	0.0018%	18.17	3.88E-04
2	300.52	0.552	1.42E-05	3.88E+04	0.0049%	49.09	6.98E-04
3	262.38	0.993	9.46E-06	1.05E+05	0.0133%	132.69	1.25E-03
4	229.08	1.847	6.29E-06	2.93E+05	0.0371%	370.85	2.33E-03
5	200.00	3.209	4.19E-06	7.66E+05	0.0968%	968.15	4.06E-03
6	174.62	5.219	2.79E-06	1.87E+06	0.2366%	2,365.92	6.60E-03
7	152.45	7.928	1.86E-06	4.27E+06	0.5400%	5,400.33	1.00E-02
8	133.10	11.011	1.23E-06	8.92E+06	1.1270%	11,270.11	1.39E-02
9	116.21	13.585	8.22E-07	1.65E+07	2.0893%	20,892.67	1.72E-02
10	101.46	14.629	5.47E-07	2.68E+07	3.3806%	33,806.09	1.85E-02
11	88.58	12.240	3.64E-07	3.36E+07	4.2501%	42,500.61	1.55E-02
12	77.34	8.738	2.42E-07	3.61E+07	4.5589%	45,589.45	1.10E-02
13	67.52	5.976	1.61E-07	3.71E+07	4.6851%	46,851.15	7.55E-03
14	58.95	4.083	1.07E-07	3.81E+07	4.8098%	48,097.94	5.16E-03
15	51.47	2.768	7.14E-08	3.88E+07	4.8994%	48,994.03	3.50E-03
16	44.94	1.928	4.75E-08	4.06E+07	5.1278%	51,277.95	2.44E-03
17	39.23	1.402	3.16E-08	4.43E+07	5.6031%	56,030.58	1.77E-03
18	34.26	1.076	2.10E-08	5.11E+07	6.4611%	64,610.81	1.36E-03
19	29.91	0.827	1.40E-08	5.90E+07	7.4619%	74,619.41	1.05E-03
20	26.11	0.616	9.32E-09	6.61E+07	8.3517%	83,517.03	7.78E-04
21	22.80	0.439	6.20E-09	7.08E+07	8.9433%	89,432.69	5.55E-04

22	19.90	0.300	4.13E-09	7.27E+07	9.1826%	91,825.86	3.79E-04
23	17.38	0.199	2.75E-09	7.24E+07	9.1536%	91,536.34	2.51E-04
24	15.17	0.130	1.83E-09	7.11E+07	8.9842%	89,842.06	1.64E-04
				N_p^T	7.91E+08	1,000,000	

Appendix G – polishing procedures

MATERIAL	SOLID SS SAMPLES			
ABRASIVE	SiC	SiC	SiC	SiC
GRAIN SIZE	#80	#120	#220	#600
ROTATION	Complimentary	Complimentary	Complimentary	Complimentary
LUBRICANT	Water	Water	Water	Water
SPEED RPM	150	150	150	150
FORCE	30N	30N	30N	30N
MINUTES	Until plane	1:00 min	1:00 min	1:00 min
CLOTH	Allegro	Largo	DP-DAC	DP-NAP
ABRASIVE	Diamond	Diamond	Diamond	Diamond
GRAIN SIZE	6 micron	6 micron	3 micron	1 micron
ROTATION	Complimentary	Complimentary	Complimentary	Complimentary
LUBRICANT	DP - LUB	DP - LUB	DP - LUB	DP - LUB
SPEED RPM	150	150	150	150
FORCE	30N	15N	30N	30N
MINUTES	8:00 MINS	8:00 MINS	8:00 MINS	8:00 MINS

MATERIAL	POWDER SS SAMPLES			
ABRASIVE	SiC	SiC		
GRAIN SIZE	#1200	#2400		
ROTATION	Complimentary	Complimentary		
LUBRICANT	Water	Water		
SPEED RPM	150	150		
FORCE	20N	20N		
MINUTES	1:00 min	1:00 min		
CLOTH	Allegro	Largo	DP-DAC	DP-DUR
ABRASIVE	Diamond	Diamond	Diamond	Diamond
GRAIN SIZE	6 micron	6 micron	3 micron	1 micron
ROTATION	Complimentary	Complimentary	Complimentary	Complimentary
LUBRICANT	DP - LUB	DP - LUB	DP - LUB	DP - LUB
SPEED RPM	150	150	150	150
FORCE	25N	15N	30N	30N
MINUTES	4:00 MINS	5:00 MINS	8:00 MINS	8:00 MINS

Appendix H – characterization details

Powder density/flow: The apparent density of powder was measured by following the standards set forth in ASTM B212-13: A 20 mL vessel was zeroed on a scale and then powder was allowed to flow through a calibrated Hall Flowmeter into the vessel. Excess powder was carefully scraped off of the top of the vessel and the powder-containing vessel was weighed. The resulting mass divided by the volume of the vessel gave an apparent density for the uncompacted powder.

The method for obtaining the tapped density was identical to that for the apparent density except that once the vessel was full, it was firmly tapped several times by raising it into the air by hand and bringing the bottom surface of the vessel into contact with a hard surface. As the powder compacted from tapping, more powder was added, and the tapping process was repeated. This continued until no further decrease in volume could be visually observed. Excess powder was then scraped from the top of the vessel and the powder-containing vessel was weighed. The resulting mass divided by the volume of the vessel gave a tapped density for the compacted powder.

X-ray photoelectron spectroscopy: Powder samples were placed on a double-sided strip of carbon tape. A monochromatic Al k-alpha x-ray source, angled 54 degrees relative to the x-ray detector was used. The photo-electron detector was positioned normal to the surface sample. An argon ion gun, positioned 45 degrees relative to the detector, was operated at 2kV and had a calibrated sputtering rate of 12 nm/min. The sputtering rate was calibrated using SiO_2 films. Measurements were taken over an elliptical area measuring 375μm along the semi-major axis and 175μm along the semi-minor axis. Assuming 2D circle packing and a mean particle size of 30 microns, the measured area encompassed anywhere from ~145 (50% packing density) to ~260 (90% packing density) powder particles. Samples were not rotated during data collection.

Electron backscatter diffraction: Powder and parts were prepared for EBSD by mounting in conductive epoxy and polishing to a 0.25 micron finish. EBSD microscopy was performed using the ORNL's Material Science & Technology Division's JEOL 6500 SEM microscope.

Powder size distribution: The powder size distributions of all powder samples were characterized by suspension in a water and glycol solution followed by applying laser diffraction analysis using the Horiba La950 V2 instrument at the Materials Science & Technology Division at ORNL.

X-ray diffraction: Continuous θ-2θ scans of all powder, expect for samples collected from the HAZ experiments, were performed using the ORNL's Materials Science & Technology Division's Panalytical X'pert diffractometer. Scans were performed from nominally 5º to 45° 2θ in 1-hour scans using a generator voltage of 55 kV, a tube current of 40 mA, MoKα radiation (λ=0.709319 Å), and the X'Celerator detector. ¼° fixed slits, ½° anti-scatter slit, and 0.02 soller slits coupled with a 10 mm mask (beam length) were used during the measurements. The powder samples were loaded into deep wells and a spinner stage (4s/rev) with an automated sample changer.

Powder samples from the HAZ experiments were analyzed using a Bruker D2Phaser desktop diffractometer [49]. This instrument utilizes a Cu x-ray source which is filtered with Ni foil to limit beam output to only the Cu $K\alpha_1$ (1.540562 Å) and $K\alpha_2$ (1.54439 Å) wavelengths. The detector used was a LYNEYE™ 1-dimensional area detector based on Bruker AXS' compound silicon strip technology [50]. Data from the powder was collected using a beam voltage and amperage of 30 kV and 10 mA respectively. A detector dwell time of 0.5 seconds was used.

High-temperature x-ray diffraction: During heating/cooling, continuous θ-2θ scans were performed from 41.5 to 45° 2theta in 2.5-minute scans using CuKα radiation (λ=1.5406 Å) and the PIXcel detector. A θ-2θ scan from 15 to 100° 2theta was performed at room temperature both before and after thermal cycling. A ¼° fixed divergence slit, a ½° anti-scatter slit, and 0.04 radian soller slits were used during the measurements. The powder samples were loaded into alumina sample holders with a thermocouple attached beneath the sample holder to measure temperature. Once vacuum was achieved, the powder was heated from 25ºC to 250ºC at a rate of 5ºC per minute, then from 250ºC to 550ºC at a rate of 3ºC per minute, then from 550ºC to 700ºC at a rate of 2ºC per minute, then cooled from 700ºC back to 550ºC at a rate of 2ºC per minute, then from 550ºC to 25ºC at a rate of 5ºC per minute.

Single-crystal x-ray diffraction: SCXRD was conducted using ORNL's Neutron Scattering Division's Rigaku XtaLAB PRO diffractometer equipped with graphite monochromated Mo Kα radiation, a Dectris Pilatus 200K detector, and the Rigaku Oxford Diffraction CrysAlisPro software. The flat-plate detector center, distance, and orientation, as well as the peak shape parameters were calibrated using the NIST LaB_6 Standard Reference Material 660C powder on the same style mounting loop.

VITA

The author was born in Clear Lake, Texas on November 9, 1989 to his parents Peter and Pamela Galicki. The majority of his elementary schooling was conducted at Dickinson Elementary in Sugar Land, Texas before attending 5th and 6th grade at Cavalry Episcopal School in Richmond, Texas. Grades 7 and 8 were attended at Lamar Consolidated Junior High School before completing four years of high school at Lamar Consolidated High School, also located in Richmond, Texas.

After graduating high school in 2008, he was accepted into the College of Engineering at Texas A&M University in College Station, Texas, where he began majoring in Aerospace Engineering. Shortly after beginning college, he changed his major to Wildlife and Fisheries, and then to Nuclear Engineering where he received his B.S. in 2012. Also in 2012 the author began graduate school at Texas A&M University under the tutelage of Professor Sean M. McDeavitt and completed a Master of Science degree in Nuclear Engineering in 2014.

In January of 2015, the author was admitted to the Doctoral program in the Materials Science & Engineering department, with a focus in metallurgy, at the University of Tennessee in Knoxville, Tennessee under the guidance of Professor Sudarsanam Suresh Babu. His future plans are to apply his knowledge in both the fields of nuclear engineering and additive manufacturing in an industrial setting with a long-term goal of teaching the students of tomorrow.